Dissertation zur Erlangung des Doktorgrades
der Fakultät für Chemie und Pharmazie
der Ludwig-Maximilians-Universität München

Mineralizer-Assisted High-Pressure High-Temperature Synthesis and Characterization of Novel Phosphorus Nitride Imides and Luminescent Alkaline Earth Metal (Oxo)Nitridophosphates

Alexey Marchuk

aus
Kiew, Ukraine

2016

Erklärung

Diese Dissertation wurde im Sinne von §7 der Promotionsordnung vom 28. November 2011 von Herrn Prof. Dr. Wolfgang Schnick betreut.

Eidesstattliche Versicherung

Diese Dissertation wurde eigenständig und ohne unerlaubte Hilfe erarbeitet.

München, 14.4.2016

.....

(Alexey Marchuk)

Dissertation eingereicht am	22.01.2016
1. Gutachter:	Prof. Dr. Wolfgang Schnick
2. Gutachter:	Prof. Dr. Oliver Oeckler
Mündliche Prüfung am	11.04.2016

To my family

Our greatest weakness lies in giving up. The most certain way to succeed is always to try just one more time.

(Thomas A. Edison)

Danksagung

Mein ganz besonderer Dank gilt meinem Doktorvater Herrn Prof. Dr. Wolfgang Schnick für die Aufnahme in seinen Arbeitskreis und für die Möglichkeit meine Dissertation in seinem Arbeitskreis anzufertigen. Die Freiheit das Thema der Dissertation eigenständig zu entwickeln war für die Anfertigung dieser Arbeit unverzichtbar. Außerdem bedanke ich mich für viele lehrreiche Fachgespräche und Anregungen.

Weiter gilt mein besonderer Dank Herrn Prof. Dr. Oliver Oeckler für die Bereitschaft das Koreferat für diese Dissertation zu übernehmen sowie für die erfolgreichen Kooperationen.

Bei Herrn Dr. Thomas Bräuniger bedanke ich mich für die zahlreichen Fachgespräche und weitere Unterhaltungen.

Herr Dr. Constantin Hoch verdient besondere Anerkennung für seine stetige Hilfsbereitschaft bei allen möglichen Fragestellungen. Mit zahlreichen Tipps und Anregungen hat er mich auch in schwierigen Phasen kontinuierlich unterstützt und hatte immer ein offenes Ohr für mich.

Mein besonderer Dank gilt meinem Vorgänger Herrn Florian Pucher, der mich in die Thematik eingeführt hat und viele Stunden damit verbracht hat, mir die Tipps und Tricks für die Hochdruckpresse beizubringen.

Außerdem danke ich meinen Praktikanten Herrn Sebastian Wendl und Frau Nedzada Imamovic, die mich während meiner Zeit mit viel Einsatz unterstützt haben.

Herrn Christian Minke gilt besonderer Dank für die vielen Messungen am NMR-Spektrometer und seine Geduld bei unseren zahlreichen gemeinsam verbrachten Stunden im EDX-Raum. Ohne ihn wären die wunderschönen REM-Aufnahmen undenkbar.

Herrn Prof. Dr. Jörn Schmedt auf der Günne und Herrn Vinicius Ribeiro Celinski danke ich sehr für die umfangreiche und erfolgreiche Kooperation.

Herrn Thomas Miller danke ich für die Betreuung der Pulverdiffraktometer sowie für das Messen vieler Einkristalle und Hochtemperatur-Pulverdiffraktogramme.

Herrn Wolfgang Wünschheim danke ich für die Instandhaltung der Rechner und seine ständige Hilfsbereitschaft.

Frau Olga Lorenz danke ich ganz herzlich für ihre geniale organisatorische Tätigkeit und außergewöhnliche Hilfsbereitschaft bei allen Arten von Problemen. Ohne sie wäre der Arbeitskreis im Chaos versunken.

Ich danke Herrn Lukas Neudert, Herrn Dr. Tobias Rosenthal und Herrn Dr. Felix Fahrnbauer für die zahlreichen Stunden die sie mit meinen Proben am TEM und Synchrotron verbracht haben und die damit verbundene strukturelle Aufklärung einiger verzwickter Nitidophosphate.

Weiterhin bedanke ich mich bei Herrn Peter Schultz für seine Hilfe bei der Aufklärung der modulierten Strukturen.

Außerdem gilt mein besonderer Dank dem Lumileds-Team, darunter Herrn Dr. Peter J. Schmidt, Herrn Detlef Wiechert, Frau Petra Huppertz und Frau Cora Hecht, für die zahlreichen Fluoreszenz-Messungen, fachlichen Diskussionen und die daraus resultierenden hervorragenden Publikationen.

Herrn Dr. Peter Mayer danke ich für die Messung unendlich vieler sehr kleiner Einkristalle, Frau Marion Sokoll danke ich für die Aufnahme der IR-Spektren.

Mein besonderer Dank gilt dem Pressenteam, darunter Herrn Florian Pucher, Herrn Dr. Dominik Baumann, Herrn Dr. Sebastian Schneider, Herrn Simon Kloß und Frau Eva-Maria Bertschler für die angenehme Zusammenarbeit.

Meinen ehemaligen und aktuellen Laborkollegen Herrn Florian Pucher, Herrn Dr. Dominik Baumann, Frau Cora Hecht, Herrn Dr. Sebastian Schneider, Herrn Frank Tambornino, Herrn Matthias Wörsching, Frau Eva-Maria Bertschler und Herrn Simon Kloß danke ich für die unvergessliche Zeit im besten Labor aller Zeiten D2.110.

Ich danke natürlich auch allen bisher nicht erwähnten Mitgliedern der Arbeitskreise Schnick, Johrendt, Lotsch, Schmedt auf der Günne, Oeckler und Hoch für die großartige Arbeitsatmosphäre im zweiten Stock.

Zum Schluss bedanke ich mich noch bei meinen Eltern Frau Tetyana Marchuk und Herrn Vladimir Marchuk sowie meinen Großeltern Frau Stalina Yesipenko und Herrn Vasili Yesipenko. Ohne Euch wäre ich zweifellos nicht da, wo ich jetzt bin. Vor allem die Unterstützung von meiner Mutter und meiner Großmutter war für mich unverzichtbar.

Contents

List of Figures

1 Introduction

Since the beginning of mankind, materials science has always been one of the main driving forces behind technological progress. Materials do not just characterize the main ages in the development of the human race, they also give them their names, e.g. Stone, Bronze and Iron Age. Nowadays, as global markets gear towards clean energy sources, the demand for new functional materials increases exponentially. Quality requirements regarding functional materials are becoming stricter and pose a new challenge for solid-state chemists and material scientists. Thus, it has become vital to systematically investigate new compounds capable of meeting these requirements, while being able to replace long standing industry applications, as well as to create brand new ones.

One of the prominent compound classes among non-metallic high performance materials is that of oxosilicates. It represents one of the most abundant and varied compound classes, containing more than 1000 minerals.[1,2] SiO_2 alone shows a remarkably rich polymorphism, including more than 30 stable and metastable polymorphs, some of them being abundant in nature.[3,4] This binary parent compound of silicates is simultaneously one of the most fundamental oxides in terms of crystal structure, structural phase transitions, physical, and chemical properties.[2,5,6] Thus, it is not unexpected that it plays a major role in industrial manufacturing processes serving as a functional material in microelectronics, optical fibers, catalysis et cetera.[1,7–9] Accordingly, the indispensability of its deriving class, silicates, has become tangible within almost every industrial sector, as well as in daily life.

Oxosilicates are in almost all cases built up of SiO_4 tetrahedra, which may be interconnected by common corners. The structural variety, however, is limited to terminal ($O^{[1]}$) and singly bridging ($O^{[2]}$) oxygen atoms connecting up to two SiO_4 tetrahedra. The aim of solid-state chemists is, therefore, focused on the expansion of these limits in order to achieve new structural possibilities, and, subsequently, new and improved properties of the resulting materials.

The compound class of nitridosilicates, where oxygen atoms are formally substituted by nitrogen atoms, clearly illustrates such a procedure. Similar to oxosilicates, consisting almost exclusively of SiO_4 tetrahedra, nitridosilicates are built up of SiN_4 tetrahedra. Despite this analogy, the SiN_4 tetrahedra may also be edge-sharing. Furthermore, the nitrogen atoms provide significant advantages concerning its increased valency. Compared to oxygen atoms in oxosilicates, nitrogen atoms in nitridosilicates

may occur not only as terminal ($N^{[1]}$) or twofold ($N^{[2]}$)-bridging atoms, but also as threefold ($N^{[3]}$) or even fourfold ($N^{[4]}$) atoms, which may connect up to four neighboring tetrahedral centers.

A prominent example for the implementation of the threefold bridging nitrogen atoms in nitridosilicates is the binary parent compound Si_3N_4. It represents one of the most important non-oxidic functional materials, exhibiting extraordinary properties. Si_3N_4-based ceramics are well known for their high-performance applications as cutting tools and anti-friction bearings due to their high fracture toughness, hardness and wear resistance.[11–13] A representative example of its application is the use of Si_3N_4 bearings in the main engines of the NASA Space Shuttle.[14,15] Besides the ambient pressure phases α-Si_3N_4 and β-Si_3N_4, one high-pressure polymorph of silicon nitride is known, namely γ-Si_3N_4.[16–20] While the structures of α-Si_3N_4 and β-Si_3N_4 consist exclusively of threefold linked SiN_4 tetrahedra, the cubic polymorph γ-Si_3N_4 additionally exhibits SiN_6 octahedra combined with four-bonded nitrogen atoms $N^{[4]}$, crystallizing in the spinel structure type.[20] Furthermore, the so-called "star-shaped unit" $N^{[4]}(SiN_3)_4$, which consists of four SiN_4 tetrahedra sharing a common central nitrogen atom ($N^{[4]}$), has also been observed in compounds $MM'[Si_4N_7]$ with M = Ca, Sr, Ba, Eu and M' = Y, Yb, Sm (see Figure 1.1).[10,21–24]

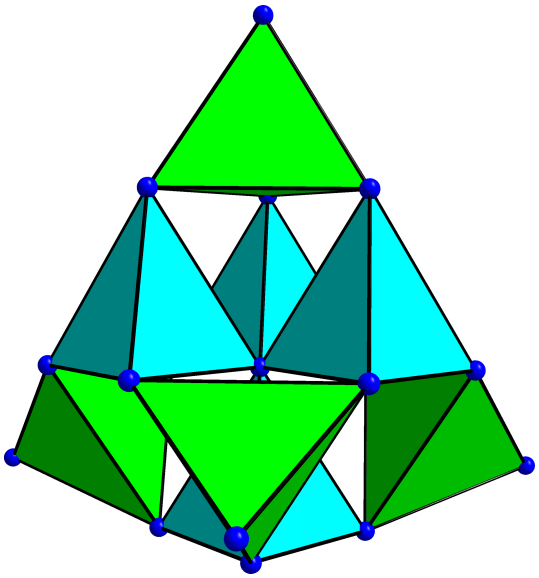

Figure 1.1: Selected section of the structure of $Ca_3Yb_3Si_9N_{17}$ showing the star-shaped unit $N^{[4]}(SiN_3)_4$ (cyan tetrahedra).[10]

Over the last years, nitridosilicates have made headlines, particularly with regard to their application in lighting industry. Considering the fact that lighting supply nowadays represents one of the largest shares within the total amount of energy consumption, research of new energy efficient light emitting devices has become one of the most imperative interdisciplinary scientific domains during the 21st century. In this context, especially phosphor-converted light-emitting diodes (pc-LEDs) have been successfully established in the market replacing energy-wasting light sources such as incandescent light bulbs.[25–27] The Nobel Prize in Physics 2014 awarded to Akasaki, Amano and Nakamura "*for the invention of efficient blue light-emitting diodes which has enabled bright and energy-saving white light sources*" underlines this fact.[28] Besides already established garnet-type phosphors, e.g. $Y_{3-x}Gd_xAl_{5-y}Ga_yO_{12}:Ce^{3+}$ (YAG:Ce)[29,30] and $Lu_3Al_5O_{12}:Ce^{3+}$ (LuAG:Ce),[31] Eu^{2+}-doped nitridosilicates like $M_2Si_5N_8:Eu^{2+}$ and $MSi_2O_2N_2:Eu^{2+}$ (M = Ca, Sr, Ba)[3,27,32] have proven

to be excellent luminescent materials. $Sr[Mg_3SiN_4]:Eu^{2+}$ represents a luminophor exhibiting the narrowest-band red emission so far identified within Eu^{2+}-doped phosphors.[33]

However, the upgrade of oxosilicates in order to obtain new structural alterations is not only limited to the substitution of the oxygen atoms. The formal exchange of the tetrahedra centers by such elements as aluminum, gallium or phosphorus leads to a great variety of compound classes (e.g. nitridoaluminates,[34] nitridogallates,[35,36] nitridophosphates[37]), which exhibit a wide range of intriguing properties. A prominent example is the narrow-band red-emitting nitridoaluminate $Sr[LiAl_3N_4]:Eu^{2+}$ which represents a next-generation LED phosphor material.[38]

The main focus of this thesis lies on the synthesis, identification, and structural characterization of novel (oxo)nitridophosphates and phosphorus nitrides. The compound class of nitridophosphates can be derived from oxosilicates by the formal substitution of Si by P and O by N. A partial substitution of O by N leads to the respective compound class of oxonitridophosphates. These compounds are expected to be structurally related to oxosilicates. On the one hand, replacing O with N leads to the atom combination P-N, which is isoelectronic and isosteric to the atom combination Si-O. On the other hand, both silicon and phosphorus form mostly covalent bonds to O and N, and, similar to nitridosilicates, exhibit almost exclusively a tetrahedral coordination at ambient pressure. This similarity can be furtherly expanded when substituing O^{2-} with the isosteric NH^{2-}, leading to the compound class of nitridoimidophosphates.[39,40]

Within the class of (oxo)nitridophates there are two pseudobinary parent compounds, namely PON and HPN_2, both being isoelectronic to silica and exhibiting a valence electron concentration (VEC) of 16/3. Considering this fact, it is not surprising that both compounds show close structural similarities to SiO_2. Both HPN_2 and PON adopt the β-cristobalite structure type under ambient pressure, which also appears as high-temperature phase of SiO_2.[41–44] Further analogies of PON to SiO_2 are its high pressure phases crystallizing in quartz-type,[45] moganite-type,[46] and coesite-type PON structures.[47]

Metal ion-containing (oxo)nitridophosphates also display a variety of structures that are comparable to those of silicates. The lowest degree of condensation $\kappa = n(P):n(N) = 1/4$ is found for Li_7PN_4, which contains isolated PN_4 tetrahedra.[48] Nitridophosphates with chain substructures M_2PN_3 (M = Mg, Ca, Zn),[49,50] as well as the oxonitridophosphate Li_2PO_2N[51] correspond to a degree of condensation $\kappa = 1/3$ and are very similar to single chain inosilicates like diopside, $MgCaSi_2O_6$.[2] An increase in the degree of condensation leads to (oxo)nitridophosphates with three-dimensional networks like cristobalite-related MPN_2 (M = Li, Na, Cu),[52–54] phenakite-type BeP_2N_4[55] or megakalsilite MP_2N_4 (M = Ca, Sr, Cd),[56–58] exhibiting $\kappa = 1/2$. The degree of condensation in nitridophosphates is, indeed,

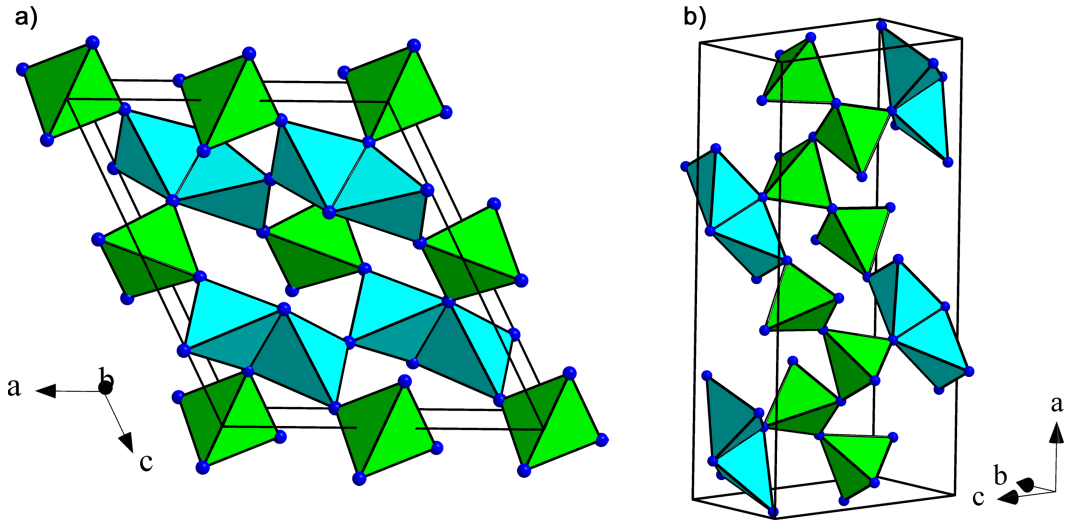

Figure 1.2: Crystal structures of α-P_3N_5 (a) and α-HP_4N_7 (b). Vertex-sharing PN_4-tetrahedra green, edge-sharing PN_4-tetrahedra cyan, P atoms green, N atoms blue.

expanded ($0.25 \leq \kappa \leq 0.6$) when compared to silicates ($0.25 \leq \kappa \leq 0.5$).[37] Representatives of such nitridophosphates are MP_4N_7 (M = Na, K, Rb, Cs) and $M_3P_6N_{11}$ (M = Rb, Cs) with $\kappa = 0.55$.[59,60] P_3N_5 exhibits the maximum degree of condensation $\kappa = 0.6$.

Hence, from the structural point of view, nitridophosphates may exhibit an even higher structural diversity. Compared to oxosilicates, consisting exclusively of corner-sharing SiO_4 tetrahedra, PN_4 tetrahedra in nitridophoshates may be also edge-sharing, similar to nitridosilicates. This situation occurs in the binary phosphorus(V) nitride α-P_3N_5,[61] as well as in the pseudobinary phosphorus nitride imide α-HP_4N_7.[62] The structures consist of both corner- and edge-sharing PN_4 tetrahedra (see Figure 1.2). Moreover, compared to Si in nitridosilicates which mostly exhibits fourfold coordination by N, in nitridophosphates P may be coordinated by up to five N atoms. This feature significantly expands the range of potential structures. Noteworthy examples for the fivefold coordination of phosphorus are the high-pressure polymorphs γ-P_3N_5 and γ-HP_4N_7.[63–65] While γ-P_3N_5 displays square PN_5 pyramids in addition to PN_4 tetrahedra, phosphorus atoms in γ-HP_4N_7 are coordinated by nitrogen atoms forming trigonal PN_5 bipyramids (see Figure 1.3).

Even if the increased valence of nitrogen atoms and the possibility of edge sharing of the $P(O,N)_4$ tetrahedra, as well as possible fivefold coordination of phosphorus atoms are not taken into account, some (oxo)nitridophosphates still exhibit unusual network structures. These have already been predicted for silicates and silica, respectively, but have only been observed in nitridic compounds so far. Excellent examples for this are δ-PON, the nitridic clathrate $P_4N_4(NH)_4(NH_3)$ and the zeolite-like oxonitridophosphates $Li_xH_{12-x-y+z}[P_{12}O_yN_{24-y}]X_z$ (X = Cl, Br) and $Ba_{19}P_{36}O_{6+x}N_{66-x}Cl_{8+x}$($x \approx 4.54$).[66–71]

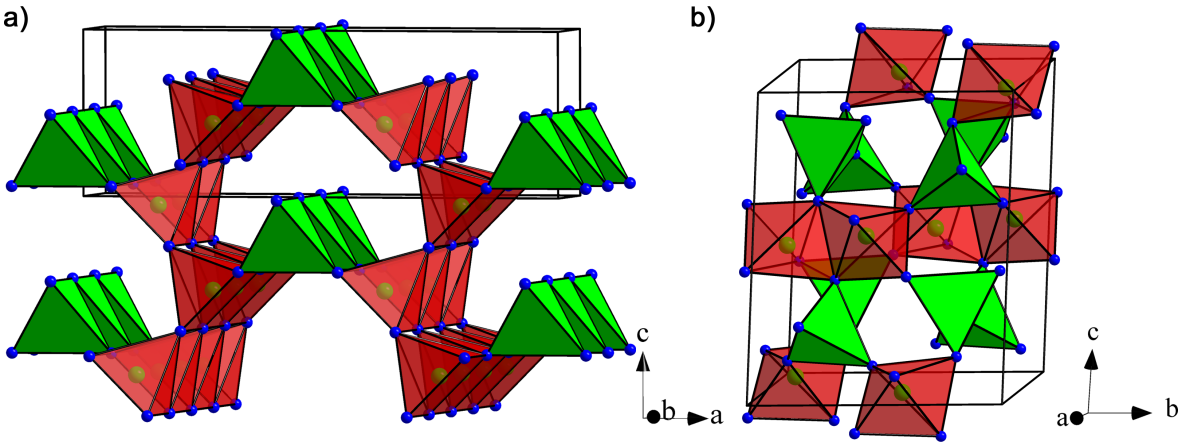

Figure 1.3: Crystal structures of γ-P_3N_5 (a) and γ-HP_4N_7 (b). Corner-sharing PN_4-tetrahedra green, PN_5-square pyramids and PN_5-trigonal bipyramids red, P atoms green, N atoms blue.

Nitridophosphates are of great importance to material scientists, not only because of the wide range of structural options, but also due to their great potential as functional materials. The nitridic clathrate $P_4N_4(NH)_4(NH_3)$ exhibits high thermal and chemical stability and contains encapsulated molecules of ammonia, trapped inside 4^28^4 cages. It has been considered as a potential material for catalysis, gas storage and separative membrane reactor material.[72] Vitreous compounds in the system Li-Ca-P-N exhibit remarkable refractive indices and hardness values.[73,74] Furthermore, Li-ion conductivity has been observed in (oxo)nitridophosphates $LiPN_2$, Li_7PN_4, and $Li_xH_{12-x-y+z}[P_{12}O_yN_{24-y}]X_z$ (X = Cl, Br),[69,75,76] rendering these materials candidates for battery applications. Amorphous LiPON thin films already enjoy application as lithium ion conductors.[24]

Phosphorus(V) nitride, P_3N_5, is used industrially as flame retardant and as getter material for the elimination of oxygen during the production of incandescent and tungsten halogen light sources. Furthermore, it exhibits a high band gap and has consequently been used as a gate insulator material in metal-insulator semiconductor field-effect transistors (MISFETs).[77–79] Due to the high band gap of P_3N_5 ($\sim$ 5.1 eV), it is reasonable to assume that ternary and higher nitridophosphates exhibit high band gap values as well and could thus serve as appropriate host compounds for new luminescent materials. However, no luminescence properties of (oxo)nitridophosphates have been published prior to this work. Considering this fact and due to their remarkable thermal and chemical stability, as well as their characteristic transparency and colorlessness, nitridophosphates may become promising host compounds for new luminescent materials, similar to nitridosilicates.

All these facts lead to the assumption that the compound class of (oxo)nitridophosphates is not only viable for numerous applications, but also a potentially fruitful research subject.

Compared to nidridosilicates, the synthesis of highly condensed nitridophosphates requires a much higher effort. This stems from the comparatively low thermal stability of common starting materials like phosphorus(V) nitride P_3N_5, tending to decompose into elements already at temperatures above 850°C, while the typical synthesis temperature of highly condensed nitridophosphates lies within the range of 1100°C. Therefore the application of standard synthetic approaches under ambient pressure like syntheses in silica ampoules or in a high-frequency furnace often turn out to be inadequate. This problem can be avoided if elevated pressures are applied during synthesis. Following Le Chatelier's principle, an elevated pressure suppresses decomposition of nitridophosphates under evolution of nitrogen. Thus, high-pressure high-temperature synthesis employing multianvil technique became a universally applicable synthesis approach in order to synthesize highly condensed alkaline earth nitridophosphates. Additionally, the use of metal azides as starting materials besides phosphorus(V) nitride P_3N_5 helps to prevent thermal bond dissociation by increasing nitrogen partial pressure. Not only metal azides but also metal nitrides can be used as starting materials. The described synthesis principle can also be transferred to synthesis of highly condensed (oxo)nitridophosphates.

Compared to oxosilicates, only few (oxo)nitridophosphates have been synthesized so far. The main reason for this lack of compounds is rooted in the fundamental difficulties concerning both their synthesis and their characterization. The reaction products almost exclusively show very poor crystallinity. In those cases where the reaction products happen to crystallize, the resulting single crystals are typically far too small to be suitable for conventional single-crystal X-ray structure determination. Most samples are microcrystalline or even nanocrystalline powders. Thus, the successful characterization of new compounds requires phase-pure synthesis of the samples on the one hand and a combination of different analytical methods such as powder X-ray diffraction, solid-state NMR spectroscopy or electron microscopy on the other hand. Compared to (oxo)nitridophosphates, oxosilicates and nitridosilicates crystallize far better, most likely due to the bond situation. With a molar bonding energy (MBE) of 290 kJ·mol^{-1}, the P−N bonding strength is significantly smaller than that of oxosilicates (MBE = 444 kJ·mol^{-1}) and nitridosilicates (MBE = 335 kJ·mol^{-1}),[1,80] which in turn results in a much better crystallization of the latter.

Consequently, it becomes apparent that the development of new synthetic strategies aiming at an increase of the crystallinity of (oxo)nitridophosphates is of great relevance. The possibility of growing single crystals would significantly accelerate structure determination. Moreover, it would target a broad spectrum of unknown phases, enabling a systematic study not only of main phase compounds but also of minority phases with potentially unprecedented properties.

In order to improve crystallinity of nitride compounds, several approaches can be applied. Often the reactions are carried out in alkali metal fluxes such as Na flux or Li flux, which can be separated from the product by sublimation *in vacuo*. This technique is applied, for example, in the synthesis of nitridogallates.[35,36] In the case of high-pressure high-temperature reactions, this approach may be problematic. On the one hand, the melting of alkali metals is combined with increasing volume,[81] which would lead to preparative problems when used in a multianvil setup. On the other hand, alkali metals would react with most starting compounds for the synthesis of (oxo)nitridophosphates, leading to the undesired side phases. Above all, the melting curves of alkali metals rise with increased pressure, thus preventing them from fulfilling their functions as fluxes.[82]

Another approach that aims to increase crystallinity of nitridic compounds is the addition of a mineralizer to the starting mixture. An example that demonstrates the effectiveness of this technique is the ammonothermal growth of large GaN crystals,[83] where basic mineralizers with a $[NH_2]^-$ group (e.g. KNH_2)[84–86] or acidic mineralizers with a $[NH_4]^+$ group (e.g. NH_4Cl, NH_4Br, NH_4I) are suitable candidates.[87,88] Ammonobasic mineralizers like KNH_2 are well known from the synthesis of binary metal amides in liquid ammonia. An example for this synthesis is the formation of $Cd(NH_2)_2$ from $Cd(SCN)_2$. The main problem when using KNH_2 is the formation of ternary alkali metal amides during synthesis.[84] Therefore it can be assumed that similar problems may occur during the synthesis of (oxo)nitridophosphates when using this mineralizer. Compared to ammonobasic KNH_2, acidic NH_4Cl does not contain any additional cations, leading to the formation of side phases. Furthermore, NH_4Cl was already successfully used in the formation of P_3N_5 from hexachlorocyclotriphosphazene $(PNCl_2)_3$, leading, however, to a microcrystalline product.[37,89] It is assumed that HCl is intermediately formed during thermal decomposition of NH_4Cl and presumably enables reversible and reconstructive $P-N$ bond cleavage and reformation, thus facilitating conditions for the growth of single crystals. NH_4Cl could therefore be a potential candidate in order to serve as a mineralizer during high-pressure high-temperature syntheses.

The main objectives of this thesis were the synthesis, identification and structural characterization of new alkaline earth metal (oxo)nitridophopshates and phosphorus nitrides. Furthermore, luminescence properties of the resulting materials should be investigated and a connection between these properties and the respective structures should be established. For this purpose, a range of synthesis strategies was employed, including conventional solid-state syntheses in silica ampoules and high-pressure high-temperature syntheses using the multianvil technique. The emphasis of the synthetic part of this thesis lies on the development of new synthetic strategies in order to increase crystallinity of

alkaline earth metal (oxo)nitridophosphates and thus accelerate their structure determination. This involves the selection of a suitable mineralizer and the investigation of its interaction with the respective starting materials. In addition, the analytical methods applied in this thesis in order to identify and characterize the compounds are just as essential as the synthesis strategies. X-ray diffraction on single crystals and on powders was carried out as the main analytical method while being supported by quantitative and qualitative ^{1}H and ^{31}P solid-state NMR measurements, FTIR and energy-dispersive X-ray (EDX) spectroscopy, as well as electron microscopy methods including both imaging and diffraction techniques. Implied by the large number of novel structures investigated, theoretical studies including topological analysis, calculations of lattice energies and bond-valence sums also played a major role in this thesis. Optical analysis methods such as reflectance spectroscopy, luminescence microscopy and photoluminescence measurements helped to determine the luminescence properties of some of the presented compounds.

1.1 References

[1] A. F. Holleman, N. Wiberg, E. Wiberg, *Lehrbuch der Anorganischen Chemie*, *Vol. 202*, Walter de Gruyter, Berlin, New York, **2007**.

[2] F. Liebau, *Structural Chemistry of Silicates*, Springer, Berlin, **1985**.

[3] M. Zeuner, S. Pagano, W. Schnick, *Angew. Chem. Int. Ed.* **2011**, *50*, 7754; *Angew. Chem.* **2011**, *123*, 7898.

[4] F. Liebau, *Angew. Chem. Int. Ed.* **1999**, *38*, 1733, *Angew. Chem.* **1999**, *111*, 1845.

[5] P. J. Heaney, *Rev. Mineral.***1994**, *29*, 1.

[6] R. J. Hemley, C. T. Prewitt, K. J. Kingma, *Rev. Mineral.* **1994**, *29*, 41.

[7] T. Demuth, Y. Jeanvoine, J. Hafner, J. G. Angyan, *J. Phys. Condens. Matter.* **1999**, *11*, 3833.

[8] A. M. Smith, *Opt. Laser Technol.* **1980**, *12*, 25.

[9] T. Ung, L. M. Liz-Marzán, P. Mulvaney, *J. Phys. Chem. B* **1999**, *103*, 6770.

[10] H. Huppertz, O. Oeckler, A. Lieb, R. Glaum, D. Johrendt, M. Tegel, R. Kaindl, W. Schnick, *Chem. Eur. J.* **2012**, *18*, 10857.

[11] F. L. Riley, *J. Am. Ceram. Soc.* **2000**, *83*, 245.

[12] H. Lange, G. Wötting, G. Winter, *Angew. Chem. Int. Ed. Engl.* **1991**, *30*, 1579; *Angew. Chem.* **1991**, *103*, 1606.

[13] D. W. Freitag, D. W. Richerdson, *Opportunities for Advanced Ceramics to Meet the Needs of the Industries of the Future*, Oak Ridge National Laboratora, **1998**.

[14] W. L. Vaughn, H. G. Maahs, *J. Am. Ceram. Soc.* **1990**, *73*, 1540.

[15] R. S. Ryan, *Space* **1994**, *31*, 53.

[16] J. Liang, L. Topor, A. Navrotsky, M. Mitomo, *J. Mater. Res.* **1999**, *14*, 1959.

[17] P. S. Kislyi, Ya. A. Kryl', A. A. Svirid, V. I. Chulakin, V. N. Troitskii, *Neorg. Mater.* **1991**, *27*, 1646.

[18] M. Billy, J. C. Labbe, A. Selvaraj, *Mater. Res. Bull.* **1983**, *18*, 921.

[19] M. Schwarz, G. Miehe, A. Zerr, E. Kroke, B. T. Poe, H. Fuess, R. Riedel, *Adv. Mater.* **2002**, *12*, 883.

[20] A. Zerr, G. Miehe, G. Serghiou, M. Schwarz, E. Kroke, R. Riedel, H. Fueß, P. Kroll, R. Boehler, *Nature* **1999**, *400*, 340.

[21] H. Huppertz, W. Schnick, *Angew. Chem. Int. Ed. Engl.* **1996**, *35*, 1983; *Angew. Chem.* **1996**, *108*, 2115.

[22] H. Huppertz, W. Schnick, *Z. Allg. Anorg. Chem.* **1997**, *623*, 212.

[23] H. Huppertz, W. Schnick, *Acta Crystallogr. Sect. C: Struct. Chem.* **1997**, *53*, 1751.

[24] C. M. Fang, Y. Q. Li, H. T. Hintzen, G. De With, *J. Mater. Chem.* **2003**, *13*, 1480.

[25] M. Born, T. Jüstel, *Chem. Unserer Zeit* **2006**, *40*, 294.

[26] C. Feldmann, *Z. Anorg. Allg. Chem.* **2012**, *638*, 2169.

[27] R. Mueller-Mach, G. Mueller, M. R. Krames, H. A. Höppe, F. Stadler, W. Schnick, T. Juestel, P. Schmidt, *Phys. Status Solidi A* **2005**, *202*, 1727.

[28] J. Heber, *Nat. Phys.* **2014**, *10*, 791.

[29] A. A. Setlur, *Electrochem. Soc. Interface* **2009**, *18*, 32.

[30] T. Moriguchi, Y. Noguchi, K. Sakano,Y. Shimizu, U.S. 5998925, July 29, **1997**.

[31] H. L. Li, X. J. Liu, L. P. Huang, *Opt. Mater.* **2007**, *29*, 1138.

[32] H. A. Höppe, H. Lutz, P. Morys, W. Schnick, A. Seilmeier, *J. Phys. Chem. Solids* **2000**, *61*, 2001.

[33] S. Schmiechen, H. Schneider, P. Wagatha, C. Hecht, P. J. Schmidt, W. Schnick, *Chem. Mater.* **2014**, *26*, 2712.

[34] P. Pust, A. Wochnik, E. Baumann, P. J. Schmidt, D. Wiechert, C. Scheu, W. Schnick, *Chem. Mater.* **2014**, *26*, 3544.

[35] F. Hintze, F. Hummel, P. J. Schmidt, D. Wiechert, W. Schnick, *Chem. Mater.* **2012**, *24*, 402.

[36] F. Hintze, N. W. Johnson, M. Seibald, D. Muir, A. Moewes, W. Schnick, *Chem. Mater.* **2013**, *25*, 4044.

[37] W. Schnick, *Angew. Chem. Int. Ed. Engl.* **1993**, *32*, 806; *Angew. Chem.* **1993**, *105*, 846.

[38] P. Pust, P. J. Schmidt, W. Schnick, *Nat. Mater.* **2015**, *14*, 454.

[39] H. Jacobs, S. Pollok, F. Golinski, *Z. Anorg. Allg. Chem.* **1994**, *620*, 1213.

[40] F. Golisnki, H. Jacobs, *Z. Anorg. Allg. Chem.* **1995**, *621*, 29.

[41] J. M. Léger, J. Haines, C. Chateau, G. Bocquillon, M. W. Schmidt, S. Hull, F. Gorelli, A. Lesauze, R. Marchand, *Phys. Chem. Miner.* **2010**, *28*, 388.

[42] L. Boukbir, R. Marchand, Y. Laurent, P. Bacher, G. Roult, *Ann. Chem.* **1989**, *14*, 475.

[43] W. Schnick, J. Lücke, *Z. Anorg. Allg. Chem.* **1992**, *610*, 121.

[44] N. Jacobs, R. Nymwegen, S. Doyle, T. Wroblewski, W. Kockelmann, *Z. Anorg. Allg. Chem.* **1997**, *623*, 1467.

[45] J. M. Léger, J. Haines, L. S. de Oliveira, C. Chateau, A. L. Sauze, R. Marchand, S. Hull, *J. Phys. Chem. Solids* **1999**, *60*, 145.

[46] J. Haines, C. Chateau, J. M. Léger, A. L. Sauze, N. Diot, R. Marchand, S. Hull, *Acta Crystallogr. Sect. B: Struct. Sci.* **1999**, *55*, 677.

[47] D. Baumann, W. Schnick, *Angew. Chem. Int. Ed.* **2015**, *54*, 4388; *Angew. Chem.* **2015**, *127*, 4463.

[48] W. Schnick, J. Lücke, *J. Solid State Chem.* **1990**, *87*, 19.

[49] V. Schultz-Coulon, W. Schnick, *Z. Anorg. Allg. Chem.* **1997**, *623*, 69.

[50] S. J. Sedlmaier, M. Eberspächer, W. Schnick, *Z. Anorg. Allg. Chem.* **2011**, *637*, 362.

[51] K. Senevirathne, C. S. Day, M. D. Gross, A. Lachgar, N. Holzwarth, *Solid State Ionics* **201**, *233*, 95.

[52] W. Schnick, J. Lücke, *Z. Anorg. Allg. Chem.* **1990**, *588*, 19.

[53] K. Landskron, S. Schmid, W. Schnick, *Z. Anorg. Allg. Chem.* **2001**, *627*, 2469.

[54] F. J. Pucher, F. Hummel, W. Schnick, *Eur. J. Inorg. Chem.* **2015**, 1886.

[55] F. J. Pucher, R. S. Römer, F. W. Karau, W. Schnick, *Chem . Eur. J.* **2010**, *16*, 7208.

[56] F. W. Karau, L. Seyfarth, O. Oeckler, J. Senker, K. Landskron, W. Schnick, *Chem . Eur. J.* **2007**, *13*, 6841.

[57] F. J. Pucher, A. Marchuk, P. J. Schmidt, D. Wiechert, W. Schnick, *Chem. Eur. J.* **2015**, *21*, 6443.

[58] F. W. Karau, *Dissertation*, Ludwig-Maximilians-Universität München, **2007**.

[59] K. Landskron, E. Irran, W. Schnick, *Chem. Eur. J.* **1999**, *5*, 2548.

[60] K. Landskron, W. Schnick, *J. Solid. State. Chem.* **2001**, *156*, 390.

[61] S. Horstmann, E. Irran, W. Schnick, *Z. Anorg. Allg. Chem.* **1998**, *624*, 620.

[62] S. Horstmann, E. Irran, W. Schnick, *Z. Anorg. Allg. Chem.* **1998**, *624*, 221.

[63] K. Landskron, H. Huppertz, J. Senker, W. Schnick, *Z. Anorg. Allg. Chem.* **2002**, *628*, 1465.

[64] K. Landskron, H. Huppertz, J. Senker, W. Schnick, *Angew. Chem. Int. Ed.* **2001**, *40*, 2643; *Angew. Chem.* **2001**, *113*, 2713.

[65] D. Baumann, W. Schnick, *Angew. Chem. Int. Ed.* **2014**, *53*, 14490; *Angew. Chem.* **2014**, *126*, 14718.

[66] D. Baumann, S. J. Sedlmaier, W. Schnick, *Angew. Chem. Int. Ed.* **2012**, *51*, 4707; *Angew. Chem.* **2012**, *124*, 4785.

[67] F. Karau, W. Schnick, *Angew. Chem. Int. Ed.* **2006**, *45*, 4505; *Angew. Chem.* **2006**, *118*, 4617.

[68] S. Correll, O. Oeckler, N. Stock, W. Schnick, *Angew. Chem. Int. Ed.* **2003**, *42*, 3549; *Angew. Chem.* **2003**, *115*, 3674.

[69] S. Correll, N. Stock, O. Oeckler, J. Senker, T. Nilges, W. Schnick, *Z. Anorg. Allg. Chem.* **2004**, *630*, 2205.

[70] S. J. Sedlmaier, M. Döblinger, O. Oeckler, J. Weber, J. Schmedt auf der Günne, W. Schnick, *J. Am. Chem. Soc.* **2011**, *133*, 12069.

[71] C. Baerlocher, L. B. McCusker, *Database of Zeolites Structures*: http://www.iza-structure.org/databases/, accessed October 2014.

[72] M. Puchard, *Nature* **2006**, *442*, 878.

[73] T. Grande, J. R. Hollowa, P. F. McMillan, C. A. Angell, *Nature* **1994**, *369*, 43.

[74] T. Grande, S. Jacob, J. R. Holloway, P. F. McMillan, C. A. Angell, *J. Non-Cryst. Solids* **1995**, *184*, 151.

[75] W. Schnick, J. Lücke, *Acta Crystallogr. (Suppl.)* **1990**, *A46*, C-363.

[76] W. Schnick, J. Lücke, *Solid State Ionics* **1990**, *38*, 271.

[77] M. S. Choudhary, J. K. Fink, K. Lederer, H. A. Krässig, *J. Appl. Polym. Sci.* **1987**, *34*, 863.

[78] a) Y. H. Jeong, J. H. Lee, Y. T. Hong, *Appl. Phys. Lett.* **1990**, *57*, 2680; b) Y. H. Jeong, G. T. Kim, K. I. Kim, U. J. Jeong, *J. Appl. Phys.* **1991**, *69*, 6699; c) Y. Hirota, T. Hisaki, O. Mikami, *Electron. Lett.* **1985**, *21*, 690.

[79] J. A. Graves, U.S. Patent 3475072, **1969**.

[80] G. H. Aylward, T. J. Findlay, *Datensammlung Chemie*, Verlag Chemie, Weinheim, **1975**.

[81] A. M. Nikolaenko, I. N. Makarenko, S. M. Stishov, *Solid State Commun.* **1978**, *27*, 475.

[82] P. W. Bridgman, *Phys. Rev.* **1926**, *27*, 68.

[83] D. Ehrentraut, E. Meissner, M. Bockowski, *Technology of Gallium Nitride Crystal Growth*, Springer Material Sciences, Berlin Heidelberg, Germany, **2010**.

[84] R. Juza, *Z. Anorg. Allg. Chem.* **1937**, *231*, 121.

[85] G. V. Karas, *Focus on Crystal Growth Research*, Nova Science Publishers Inc., New York **2006**.

[86] D.R. Ketchum, J.W. Kolis, *J. Crystal Growth* **2001**, *222*, 431.

[87] A. P. Purdy, R. J. Jouet, C. F. George, *Cryst. Growth Des.* **2002**, *2*, 141.

[88] A. P. Purdy, *Chem. Mater.* **1999**, *11*, 1648.

[89] W. Schnick, J. Lücke, F. Krumeich, *Chem. Mater.* **1996**, *8*, 281.

2 A High-Pressure Polymorph of Phosphorus Nitride Imide

Alexey Marchuk,[a] Florian J. Pucher,[a] Friedrich W. Karau,[a] and Wolfgang Schnick*[a]

[a] *Department of Chemistry, University of Munich (LMU), Butenandtstraße 5–13, 81377 Munich, Germany*

published in: *Angew. Chem.* **2014**, *126*, 2501-2504. DOI: 10.1002/ange.201309020

published in: *Angew. Chem. Int. Ed.* **2014**, *53*, 2469-2472. DOI: 10.1002/anie.201309020

Abstract

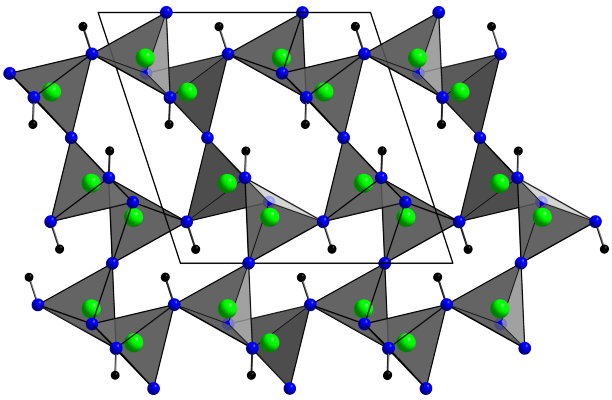

Phosphorus nitride imide, HPN_2, is of great scientific importance because it is isosteric with silica, SiO_2. Accordingly, a varied structural diversity could be expected. However, only one polymorph of HPN_2 has been reported thus far. Herein, we report on the synthesis and structural investigation of the first high-pressure polymorph of phosphorus nitride imide, β-HPN_2; the compound has been synthesized using the multianvil technique. By adding small amounts of NH_4Cl as a mineralizer, it became possible to grow single crystals of β-HPN_2, which allowed the first complete structural elucidation of a highly condensed phosphorus nitride from single-crystal X-ray diffraction data. The structure was confirmed by FTIR and ^{31}P and ^{1}H solid-state NMR spectroscopy. We are confident that high-pressure high-temperature reactions could lead to new polymorphs of HPN_2 containing five-fold- or even six-fold-coordinated phosphorus atoms and thus rivaling or even surpassing the structural variety of SiO_2.

2.1 Introduction with Results and Discussion

With more than 1000 minerals, silicates are the largest, the most important, and the most varied class of minerals.[1,2] More than 90% of the earth's crust is composed of silicate materials. SiO_2 is the binary parent compound of silicates, and simultaneously one of the most fundamental oxides in terms of crystal structure, structural phase transitions, and physical, and chemical properties.[2–4] It shows a remarkably rich polymorphism, including more than 30 stable and metastable polymorphs, with some of them being abundant in nature.[5,6] The wide range of applications in ceramic and glass industries, as well as great potential in microelectronics, optical fibers, and catalysis makes SiO_2 an irreplaceable material in modern industry.[1,7–9] Accordingly, the great structural variety of silica, and the resulting diversity of properties, makes structures that are analogous to silica an important research target. The replacement of Si and O by P and N may lead to nitridophosphates in which the $[PN_2]^-$ substructure is isoelectronic to SiO_2. From a structural point of view, nitridophosphates could exhibit a higher structural diversity than silica. In comparison to vertex-sharing SiO_4 tetrahedra in SiO_2, the PN_4 tetrahedra in nitridophosphates can be edge-sharing as well. For silica, edge-sharing has only been postulated for fibrous SiO_2. However, existence and true nature of this material has not been unequivocally proven to date.[10] Substitution of O by N provides significantly increased structural possibilities. Whereas the structures of oxosilicates are limited to terminal ($O^{[1]}$) or singly-bridging oxygen ($O^{[2]}$) positions, N in nitridophosphates may occur as $N^{[1]}$, $N^{[2]}$, $N^{[3]}$, or even ammonium-like $N^{[4]}$ atoms, which can connect up to four neighboring tetrahedral centers.[11] An even greater structural variety can be obtained by substituting Si by P, which may be coordinated by up to five nitrogen atoms. This situation has been found in the high-pressure polymorph γ-P_3N_5, the network of which is built up of vertex-sharing PN_4 tetrahedra and distorted PN_5 pyramids.[12] The nitridic clathrate $P_4N_4(NH)_4(NH_3)$ is also an excellent example for the increased structural possibilities of nitridophosphates in comparison to oxosilicates.[1,13] The framework structure of this compound has been predicted for silicates, however it has thus far only been observed in this nitridophosphate. The $P_4N_4(NH)_4(NH_3)$ clathrate contains encapsulated molecules of ammonia, which are trapped inside a phosphorus nitride framework. Consequently, it has been discussed as a possible gas storage material.[14] Phosphorus(V) nitride, P_3N_5, is the binary parent compound of nitridophosphates. It is used industrially as flame retardant, as a gate insulator material in metal-insulator semiconductor field-effect transistors (MISFETs) and as a getter material for the elimination of oxygen during the production of incandescent and tungsten halogen lamps.[15–17] Within the class of nitridophosphates and phosphorus nitrides, two cationless compounds that are isosteric to silica (valence electron

concentration VEC = 16/3), namely PON and HPN_2, have been described. Four modifications of PON are known: β-cristobalite-type,[18,19] quartz-type[20] and moganite-type PON,[21] as well as δ-PON.[22] The imide group in HPN_2 is isolobal with O in PON. However, only one polymorph of HPN_2, which crystallizes in the β-cristobalite-type of structure, has been described in the literature.[23,24] Accordingly, it may be possible that further modifications of HPN_2 do exist. Actually, the existence of a high-pressure phase of HPN_2 was discussed in earlier experiments, however, no complete crystal structure or specific properties have been investigated thus far.[13,25,26]

Herein, we report on the synthesis and structural investigation of the first high-pressure polymorph of HPN_2. Because this is the second known modification of this compound, we propose the name β-HPN_2. We succeeded in growing single crystals of β-HPN_2, which enabled structure determination of an uncharged highly condensed phosphorus nitride on the basis of single-crystal X-ray diffraction data.

β-HPN_2 was synthesized by a high-pressure high-temperature reaction using a Walker-type multianvil assembly at 6 GPa and 1000 °C.[27] Amorphous HPN_2 was used as starting material. By adding small amounts of NH_4Cl to the starting material, colorless platelet single crystals of β-HPN_2 were obtained and isolated. This is the first known synthesis of microscopic single crystals of a highly condensed phosphorus nitride (atomic ratio $P:N \geq 1:2$), which had, until now, been considered unattainable. HCl, which is intermediately formed by the dissociation of NH_4Cl, presumably enables reversible and reconstructive bond cleavage and reformation, and thus facilitates conditions for the growth of single crystals.[11] In order to remove NH_4Cl from the product, it was washed with water and ethanol. The crystal structure of β-HPN_2 was solved and refined from single-crystal X-ray diffraction data in monoclinic space group $P2/c$ (no. 13).[28] The hydrogen atom positions were unequivocally determined from difference Fourier syntheses and were refined isotropically using restraints for N−H distances. All non-hydrogen atoms were refined anisotropically. The structure elucidation was additionally confirmed by Rietveld refinement (Figure 2.1). Furthermore, the product was characterized by EDX, FTIR and solid-state NMR spectroscopy.

The crystal structure of β-HPN_2 is built up of a three-dimensional network of PN_4 tetrahedra that share vertices on all sides, and in which the hydrogen atoms are covalently bound to half of the N atoms (Figure 2.2). Owing to a pseudo-twofold screw axis along [010], the structure can almost be described in space group $P2_1/c$ (Figure A.1). The framework of β-HPN_2 may be compared to that of α-HPN_2, high and low cristobalite.[23,24,29,30] To characterize the ring sized in the structure topologically, the cycle class sequence for β-HPN_2 was calculated using the program TOPOLAN.[31] It specifies the

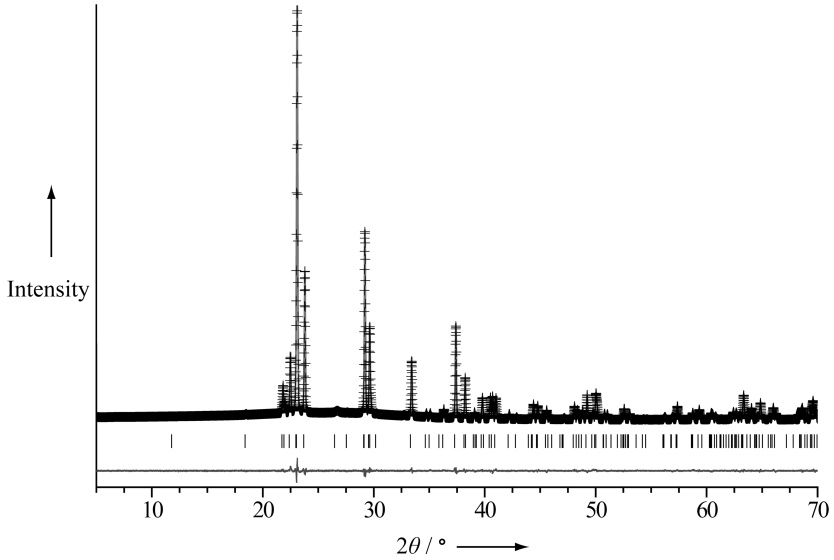

Figure 2.1: Observed (crosses) and calculated (light gray line) X-ray powder diffraction pattern. Positions of Bragg reflections (vertical lines), difference profile for the Rietveld refinement of β-HPN_2 (dark gray line).

relative abundance of P_nN_n ring sizes per unit cell. The results, which are identical with the results for the isotopological frameworks of α-HPN_2, high and low cristobalite, are summerized in Table A.9 in the Supporting Information. The secondary building units of β-HPN_2 are six-membered rings, P_6N_6, which are also those with the smallest ring size in this compound.

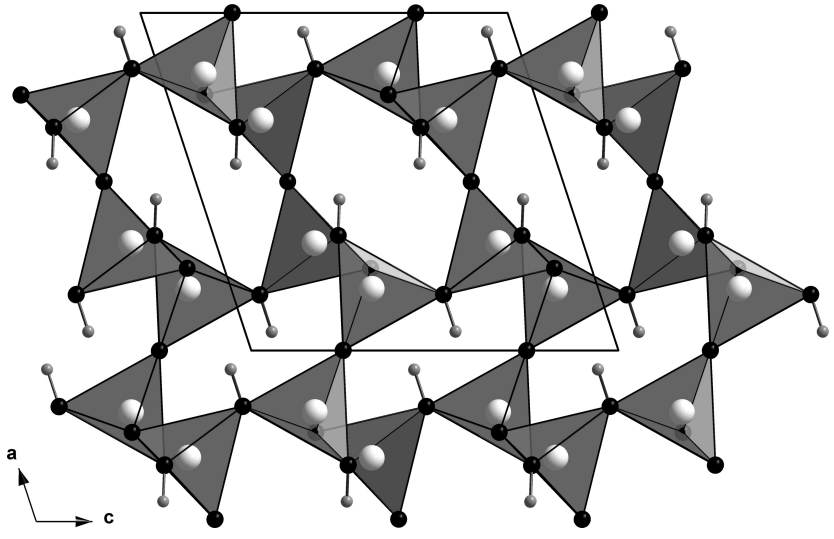

Figure 2.2: Crystal structure of β-HPN_2, viewed along [010]. H gray, N black, P white.

The differences between the structures of high cristobalite, low cristobalite, α-HPN_2 and β-HPN_2 become readily apparent when regarding the hexagonal layers in these structures (Figure 2.3). The

crystal structures of cubic cristobalite and α-HPN_2 consist of only one type of six-membered rings (Figure 2.3, a, b). In contrast, they differentiate upon transition from high over low cristobalite (two types of six-membered rings; Figure 2.3, c) up to β-HPN_2 (three types of six-membered rings; Figure 2.3, d). Additionally, the six-membered rings adopt a regular chair conformation in high cristobalite, which is significantly distorted in low cristobalite and β-HPN_2. These distortions, which are caused by the tilting of the PN_4 tetrahedra, induce increasing undulations in their respective structures.

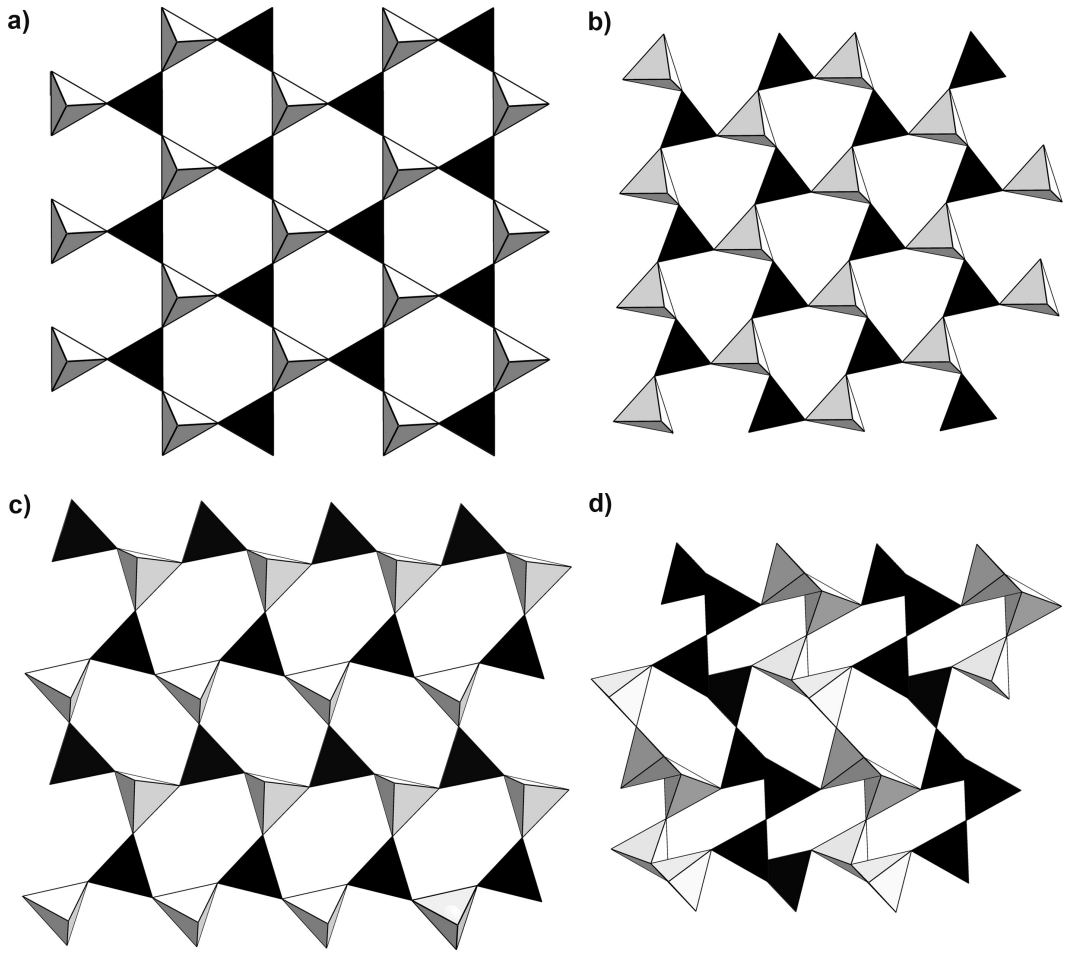

Figure 2.3: Comparison of hexagonal layers in: a) high cristobalite (view along [-111]), b) α-HPN_2 (view along [-4-12]), c) low cristobalite (view along [0-1-1]),and d) β-HPN_2 (view along [010]). For clarity, tetrahedra with vertices up are depicted in light gray, whose with vertices down are depicted in black.

The ranges of the P−N bonds (157−167 pm) and the P−$N^{[2]}$−P angles (126−147°) in the structure of β-HPN_2 are consistent with corresponding values for the low-pressure polymorph α-HPN_2 (160 pm, 130°), and are typical for those in other known phosphorus(V) nitrides. As expected, the P−$N^{[3]}$ bond lengths in the P−NH−P group (167 pm) are significantly longer than the P−$N^{[2]}$ bond lengths in the

P−N−P group (157−159 pm), which corroborates the positions of the imide groups. The values for tetrahedral angles vary between 104 and 120°, and thus differ slightly from the regular tetrahedral angle. Detailed information on bond lengths and angles can be found in Tables A.3−A.4. To verify the electrostatic consistency of the determined crystal structure, the program MAPLE (Madelung part of lattice energy) was used.[32] The partial MAPLE values of the P atom sites (14320−14440 kJ·mol^{-1}), as well as the overall MAPLE value for β-HPN_2 (23913 kJ·mol^{-1}) are consistent with the corresponding values for α-HPN_2 (MAPLE value of P atom sites: 14390 kJ·mol^{-1}, overall MAPLE value: 23825 kJ·mol^{-1}) with a minor deviation of 0.37%.

The analytical composition of β-HPN_2 was analyzed by energy-dispersive X-ray (EDX) spectroscopy. It showed no elements other than P and N. Chemical composition estimated from EDX analysis is in excellent agreement with the predicted composition of the product. The results of the EDX measurements are summarized in Tabe A.10.

The FTIR spectrum of β-HPN_2 (Figure A.3) resembles that of the tetragonal polymorph α-HPN_2.[23] It exhibits a significant broad absorption band at 2245−2217 cm^{-1}, which can be assigned to the N−H valence modes of both imide groups of the framework. Furthermore, absorption bands at 808−1261 cm^{-1} are observed and are characteristic for nitridophosphates.[13,23,33] The first group of bands, which occurs at 1070−1261 cm^{-1}, can be assigned to the assymetric stretching of the PN_4 tetrahedra ν_{as}(PNP). The second group is found at 808−951 cm^{-1}, and is caused by the symmetric valence mode of PN_4 tetrahedra ν_s(PNP).

To confirm the determined structure of β-HPN_2, the product was additionally characterized by solid-state NMR spectroscopy. The ^{31}P solid-state NMR spectrum (Figure A.4) shows one sharp signal at a chemical shift of δ_{iso} = -18.7 ppm, with a small shoulder at around δ_{iso} = -12 ppm. These two signals correspond to the two crystallographically distinct P atoms in the unit cell. Additionally, the ^{1}H solid-state NMR spectrum (Figure A.5) shows two individual signals with chemical shifts of δ_{iso} = -6.2 and 7.1 ppm, which correspond to the two different crystallographic H atoms.

2.2 Conclusion

In summary, we have synthesized β-HPN_2, a high-pressure polymorph of HPN_2. It crystallizes in a distorted cristobalit-type of structure. Moreover, by adding NH_4Cl as a mineralizer, we succeeded in growing single crystals of this compound, which allowed for a complete crystal structure elucidation of β-HPN_2. This novel synthetic approach to growing single crystals of phosphorus nitrides under high-pressure high-temperature conditions may significantly accelerate investigation of new phosphorus

nitrides in the future. Taking into account the fact that four modifications of PON are already known, it is reasonable to suggest that further polymorphs of HPN_2 may exist. Consequently, further high-pressure high-temperature experiments will probably lead to new modifications of HPN_2 containing five-fold- or even six-fold-coordinated phosphorus atoms, and thus rival or even surpass the structural variety of SiO_2. Accordingly, a wide range of interesting properties can be expected.

2.3 References

[1] A. F. Holleman, N. Wiberg, E. Wiberg, *Lehrbuch der Anorganischen Chemie*, *Vol. 202*, Walter de Gruyter, Berlin, New York, **2007**.

[2] F. Liebau, *Structural Chemistry of Silicates*, Springer, Berlin, **1985**.

[3] M. Zeuner, S. Pagano, W. Schnick, *Angew. Chem. Int. Ed.* **2011**, *50*, 7754; *Angew. Chem.* **2011**, *123*, 7898.

[4] F. Liebau, *Angew. Chem. Int. Ed.* **1999**, *38*, 1733, *Angew. Chem.* **1999**, *111*, 1845.

[5] P. J. Heaney, *Rev. Mineral.* **1994**, *29*, 1.

[6] R. J. Hemley, C. T. Prewitt, K. J. Kingma, *Rev. Mineral.* **1994**, *29*, 41.

[7] T. Demuth, Y. Jeanvoine, J. Hafner, J. G. Angyan, *J. Phys. Condens. Matter.* **1999**, *11*, 3833.

[8] A. M. Smith, *Opt. Laser Technol.* **1980**, *12*, 25.

[9] T. Ung, L. M. Liz-Marzán, P. Mulvaney, *J. Phys. Chem. B* **1999**, *103*, 6770.

[10] A. Weiss, A. Weiss, *Z. Anorg. Allg. Chem.* **1954**, *276*, 95.

[11] W. Schnick, *Angew. Chem. Int. Ed. Engl.* **1993**, *32*, 806; *Angew. Chem.* **1993**, *105*, 846.

[12] a) K. Landskron, H. Huppertz, J. Senker, W. Schnick, *Angew. Chem. Int. Ed.* **2001**, *40*, 2643; *Angew. Chem.* **2001**, *113*, 2713; b) K. Landskron, H. Huppertz, J. Senker, W. Schnick, *Z. Anorg. Allg. Chem.* **2002**, *628*, 1465.

[13] F. Karau, W. Schnick, *Angew. Chem. Int. Ed.* **2006**, *45*, 4505; *Angew. Chem.* **2006**, *118*, 4617.

[14] M. Puchard, *Nature* **2006**, *442*, 878.

[15] M. S. Choudhary, J. K. Fink, K. Lederer, H. A. Krässig, *J. Appl. Polym. Sci.* **1987**, *34*, 863.

[16] a) Y. H. Jeong, J. H. Lee, Y. T. Hong, *Appl. Phys. Lett.* **1990**, *57*, 2680; b) Y. H. Jeong, G. T. Kim, K. I. Kim, U. J. Jeong, *J. Appl. Phys.* **1991**, *69*, 6699; c) Y. Hirota, T. Hisaki, O. Mikami, *Electron. Lett.* **1985**, *21*, 690.

[17] J. A. Graves, U.S. Patent 3475072, **1969**.

[18] J. M. Léger, J. Haines, C. Chateau, G. Bocquillon, M. W. Schmidt, S. Hull, F. Gorelli, A. Lesauze, R. Marchand, *Phys. Chem. Miner.* **2110**, *28*, 388.

[19] L. Boukbir, R. Marchand, Y. Laurent, P. Bacher, G. Roult, *Ann. Chem.* **1989**, *14*, 475.

[20] J. M. Léger, J. Haines, L. S. de Oliveira, C. Chateau, A. L. Sauze, R. Marchand, S. Hull, *J. Phys. Chem. Solids* **1999**, *60*, 145.

[21] J. Haines, C. Chateau, J. M. Léger, A. L. Sauze, N. Diot, R. Marchand, S. Hull, *Acta Crystallogr. Sect. B: Struct. Sci.* **1999**, *55*, 677.

[22] D. Baumann, S. J. Sedlmaier, W. Schnick, *Angew. Chem. Int. Ed.* **2012**, *51*, 4707; *Angew. Chem.* **2012**, *124*, 4785.

[23] W. Schnick, J. Lücke, *Z. Anorg. Allg. Chem.* **1992**, *610*, 121.

[24] N. Jacobs, R. Nymwegen, S. Doyle, T. Wroblewski, W. Kockelmann, *Z. Anorg. Allg. Chem.* **1997**, *623*, 1467.

[25] F. Karau, *Dissertation*, Ludwig-Maximilians-Universität München, **2007**.

[26] K. J. Kingma, R. Pacalo, P. K. MacMillan, *Eur. J. Solid State Chem.* **1997**, *34*, 679.

[27] a) N. Kawai, S. Endo, *Rev. Sci. Instrum.* **1970**, *41*, 1178; b) D.Walker, M. A. Carpenter, C. M. Hitch, *Am. Mineral.* **1990**, *75*, 1020; c) D. Walker, *Am. Mineral.* **1991**, *76*, 1092; d) D. C. Rubie, *Phase Transitions* **1999**, *68*, 431; e) H. Huppertz, *Z. Kristallogr.* **2004**, *219*, 330.

[28] Crystal structure data for β-PN(NH): STOE IPDS, Mo-Kα (71.073 pm), $2\sigma_{\max}$ = 63.4°, crystal size 0.11 × 0.07 × 0.02 mm^3, monoclinic, space group *P*2/*c* (no. 13), *a* = 7.8853(16), *b* = 4.8278(10), *c* = 8.1456(16) Å, β = 108.19(3)°, *V* = 294.6(1) Å^3, *Z* = 8, ρ_{calcd} = 2.706 g cm^{-3}, μ = 1.222 mm^{-1}, 2371 measured reflections, 676 of which are independent, R_{int} = 0.049, least-squares refinement of F^2 (G. M. Sheldrick, SHELXL-97, program for the refinement of crystal structures, Universität Göttingen, Göttingen (Deutschland), 1997); no absorption correction, R-values (all data / $F_0^2 \geq 2\sigma(F_0^2)$) R_1 = 0.0392 / 0.0298, wR_2 = 0.0785 / 0.0762, GooF = 1.018 for 534 observed reflections ($F_0^2 \geq 2\sigma(F_0^2)$ and 64 refined parameters. Further details on crystal structure investigations may be obtained from the Fachinformationszentrum Karlsruhe, 76344 Eggenstein-Leopoldshafen, Germany (fax: (+ 49)7247-808-666; e-mail: crysdata@fiz-karlsruhe.de), on quoting the depository number CSD-426003.

[29] R. T. Downs, D. C. Palmer, *Am. Mineral.* **1994**, *79*, 9.

[30] D. R. Peacor, *Z. Kristallogr.* **1973**, *138*, 274.

[31] a) W. E. Klee, *Z. Kristallogr.* **1987**, *179*, 67; b) A. Beukemann, W. E. Klee, *Z. Kristallogr.* **1994**, *209*, 709.

[32] a) R. Hoppe, *Angew. Chem. Int. Ed. Engl.* **1966**, *5*, 95; *Angew. Chem.* **1966**, *78*, 52; b) R. Hoppe, *Angew. Chem. Int. Ed. Engl.* **1970**, *9*, 25; *Angew. Chem.* **1970**, *82*, 7.

[33] S. Horstmann, E. Irran, W. Schnick, *Angew. Chem. Int. Ed. Engl.* **1997**, *36*, 1873; *Angew. Chem.* **1997**, *109*, 1938.

3 M_2PO_3N (M = Ca, Sr) – *ortho*-Oxonitridophosphates with β-K_2SO_4 Structure Type

Alexey Marchuk,[a] Peter Schultz,[b] Constantin Hoch,[a] Oliver Oeckler,*[b] and Wolfgang Schnick*[a]

[a] *Department of Chemistry, University of Munich (LMU), Butenandtstraße 5–13, 81377 Munich, Germany*

[b] *Institute of Mineralogy, Crystallography and Materials Science, Faculty of Chemistry and Mineralogy, Leipzig University, Scharnhorststraße 20, 04275 Leipzig, Germany*

published in: *Inorg. Chem.* **2016**, *55*, 974-982. DOI: 10.1021/acs.inorgchem.5b02647

Abstract

Two novel oxonitridophosphates M_2PO_3N with M = Ca, Sr were synthesized under high-pressure high-temperature (7 GPa, 1100 °C) using the multianvil technique or by solid-state reaction in the silica ampoules (1100 °C) from amorphous phosphorus oxonitride PON and the respective alkaline earth oxides MO (M = Ca, Sr). The products represent the first examples of alkaline earth *ortho*-oxonitridophosphates containing non-condensed $[PO_3N]^{4-}$ ions. The crystal structures were elucidated by single-crystal X-ray diffraction. Sr_2PO_3N (space group *Pnma*, no. 62,

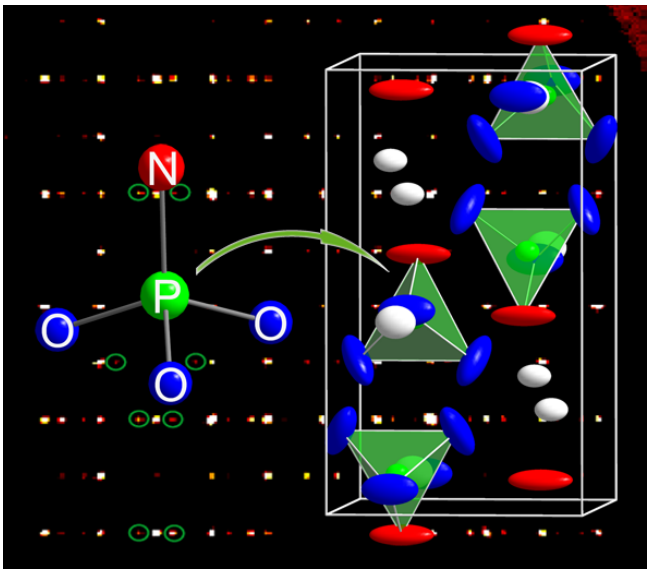

Z = 4, a = 7.1519(5), b = 5.5778(3), c = 9.8132(7) Å, $R1$ = 0.020, $wR2$ = 0.047) crystallizes in the β-K_2SO_4 structure type. The structure of Ca_2PO_3N was solved and refined in the (3+1)D superspace group $Pnma(\alpha 00)0ss$ (Z = 4, a = 6.7942(7), b = 5.4392(6), c = 9.4158(11) Å, $R1$ = 0.041, wR = 0.067). It exhibits an incommensurate modulation along [100] with a modulation vector q = (0.287(5), 0, 0). Rietveld refinements support the structural models as well as the phase purity of the products. Upon doping with Eu^{2+}, Ca_2PO_3N exhibits luminescence in the green range (λ_{em} = 525 nm) of the visible spectrum, if excited by near-UV light (λ_{exc} = 400 nm).

3.1 Introduction

The β-K_2SO_4 structure type is very widespread among sulfates, selenates, vanadates, manganates, fluoroborates etc.; at least 150 different representatives have been described.[1] However, not only the abundance of this structure type, but also the great variety of the properties of the corresponding compounds make this structure class intriguing.

Eu^{2+}-doped $A^{I}B^{II}PO_4$ (A = Li, K; B = Sr, Ba) with β-K_2SO_4 structure type have received much attention concerning potential applications as new luminescent materials for white-light emitting diodes (LEDs).[2] For example, $KSrPO_4:Eu^{2+}$ exhibits blue luminescence and shows a better thermal stability than $YAG:Ce^{3+}$ (i.e. $Y_3Al_5O_{12}:Ce^{3+}$).[3] Furthermore, $KBaPO_4$ doped with Eu^{2+}, Tb^{3+} and Sm^{3+} have been reported by Lin *et al.* as phosphors exhibiting blue, green and orange-red luminescence, respectively.[4] Similarly, alkaline-earth oxosilicates with β-K_2SO_4 structure type activated with Eu^{2+} are important and highly efficient luminescent materials as well.[5] A prominent example is the *ortho*-silicate $Ba_2SiO_4:Eu^{2+}$, which exhibits green luminescence if excited with UV light. This phosphor was used for the production of LEDs for a broad range of applications.[6–8]

Contrary to the plethora of compounds crystallizing in the β-K_2SO_4 structure type, there are only few representatives in the substance class of nitrides. Marchand *et al.* reported on rare-earth oxonitridosilicates LnEuSiO$_3$N with Ln = La, Nd, Sm.[9] Most recently, oxonitridosilicates LaMSiO$_3$N with M = Sr, Ba were presented which exhibit red luminescence upon doping with Eu^{2+} and Ce^{3+},[10] which underlines their potential as host lattices for luminescent materials in analogy to the efficient phosphors $M_2SiO_4:Eu^{2+}$ but with longer emission wavelengths caused by the introduction of one nitride anion and one trivalent cation per formula unit.

(Oxo)nitridophosphates often display structural features similar to those of silicates as both PON and PN_2^- are isoelectronic to SiO_2.[11] Thus, many well-established structures of SiO_2 have been found for PON and $PN(NH)_2$ as well, e.g. quartz-type PON,[12] cristobalite-type PON and PN(NH) and coesite-type PON.[13–16] Furthermore, there are representatives of layered oxonitridophosphates (e.g. $Sr_3P_6O_6N_8$)[17] and framework nitridophosphates (e.g. $Ba_3P_5N_{10}X$, X = Cl, Br, I),[18,19] whose structures show similarities to those of silicates. However, in contrast to the broad diversity of *ortho*-oxosilicates, there are only two representatives of (oxo)nitridophosphates containing non-condensed tetrahedra, namely Li_7PN_4 and $Li_{14}(PON_3)_2O$.[20,21] Presumably, Li^+ ions are able to stabilize the highly negative charges of non-condensed $[PN_4]^{7-}$ and $[PON_3]^{6-}$ ions.

In this contribution we present the first examples of β-K_2SO_4-type alkaline earth *ortho*-oxonitridophosphates containing discrete $[PO_3N]^{4-}$ ions.

3.2 Experimental Section

Synthesis of Amorphous PON

Amorphous PON was synthesized by heating a mixture of $PO(NH_2)_3$ and NH_4Cl in ratio 1:3 in a silica glass flow tube under continuous nitrogen flow at 680 °C for 48 h.[17] The mixture results from reaction of $POCl_3$ with liquid NH_3, as described by Klement *et al.*[22] The product was characterized by FTIR spectroscopy.

Synthesis of CaO

CaO was obtained by thermal decomposition of $Ca(NO_3)_2 \cdot 4H_2O$ ($\geq$ 99.0%, Sigma Aldrich) at 800 °C for 8 h. Phase purity of the product was confirmed by powder X-ray diffraction as well as FTIR spectroscopy.

Synthesis of M_2PO_3N (M = Ca, Sr) under High Pressure

M_2PO_3N with M = Ca, Sr were synthesized under high-pressure high-temperature conditions in a modified Walker-type multianvil assembly using a 1000 t hydraulic press (Voggenreiter, Mainleus, Germany).[23] The starting materials PON and the respective alkaline earth metal oxide MO (M = Ca, Sr; SrO: 99.9%, Sigma Aldrich) were thoroughly ground in an agate mortar and tightly packed into a boron nitride crucible (Henze, Kempten, Germany). As pressure medium, Cr_2O_3-doped (6%) MgO octahedra (Ceramic Substrates & Components, Isle of Wight, UK) with an edge length of 18 mm (18/11 assembly) were employed. Eight tungsten carbide cubes (Hawedia, Marklkofen, Germany) with truncation edge lengths of 11 mm compressed the octahedron. Detailed information on the assembly can be found in literature.[23] The respective assembly was compressed up to 7 GPa at room temperature within 200 minutes, then heated to 1100 °C within 60 minutes and kept at this temperature for 60 minutes. The assembly was cooled to room temperature in 60 minutes and the pressure was subsequently released over a period of 600 minutes. The preparation of the respective starting mixture and the octahedron assembly was carried out in a glove box under purified argon atmosphere (Unilab, MBraun, Garching, O_2 < 1 ppm, H_2O < 0.1 ppm). In order to grow single crystals suitable for X-ray diffraction, small amounts ($\sim$2 mg NH_4Cl for 50 mg of starting mixture) of NH_4Cl were added to the starting mixture as mineralizer. This synthetic approach to grow single crystals of (oxo)nitridophosphates under high-pressure high-temperature conditions has previously proved to be successful.[15] For luminescence investigations 2 mol% $EuCl_2$ (99.99%, trace metals basis, Sigma

Aldrich) as dopand was added to the starting mixture.

Synthesis of M_2PO_3N (M = Ca, Sr) in the Silica Ampoule

The respective starting mixture from stoichiometric amounts of MO (M = Ca, Sr) and amorphous PON was thoroughly mixed and ground in a glove box (Unilab, MBraun, Garching, O_2 < 1 ppm, H_2O < 0.1 ppm) and pressed to a pellet. The latter was placed in a silica glass ampoule (wall thickness 1.5 mm, inner diameter 12 mm, length ca. 100 mm), which was filled with N_2 gas of 1 bar. After sealing, the N_2-filled ampoule was placed into a tube furnace and heated to 1000 °C (rate 1 °C / min), held for 2 h (Ca_2PO_3N) or 48 h (Sr_2PO_3N), respectively, and finally cooled (rate 3 °C / min) to room temperature. The resulting N_2-pressure in the ampoules during the heating phase was approximately 10 bar.

Spectroscopic Analysis

The chemical composition of the products was confirmed by energy-dispersive X-ray (EDX) spectroscopy using a JEOL JSM 6500F field emission scanning electron microscope with Oxford Instruments 7418 Si/Li EDX detector. In order to make the samples electrically conductive, they were coated with carbon using an electron beam evaporator (BAL-TEC MED 020, Bal Tex AG). FTIR spectra were collected with a IFS 66 v/S spectrometer (Bruker) using KBr pellets.

Single-Crystal X-Ray Diffraction

Single-crystal X-ray diffraction. Single-crystal diffraction data for both compounds were collected on a Bruker D8 Venture diffractometer with Mo-Kα radiation (λ = 0.71073 Å). The temperature-dependent single-crystal measurements of Sr_2PO_3N were recorded between 300 and 100 K using the Kryoflex low temperature attachment (Bruker AXS). Intensities were integrated with the Bruker SAINT software package using a narrow-frame algorithm and corrected for absorption effects with the semiempirical method (SADABS).[24,25] The structures were solved by direct methods and refined by full matrix least-squares calculation on F^2 with SHELXL-2014.[26] In the case of Ca_2PO_3N, the refinement of the modulated structure was performed with JANA2006 on F.[27] TLS analysis of Sr_2PO_3N was carried out using Schomaker's algorithm[28] as implemented in the Platon program package.[29,30] Details on the structure investigation may be obtained from the Fachinformationszentrum Karlsruhe, 76344 Eggenstein-Leopoldshafen, Germany (fax (+49)7247-808-666; E-Mail: crysdata@fiz-karlsruhe.de), on quoting the depository number CSD-430215 (Ca_2PO_3N modulated), CSD-430221 (Ca_2PO_3N

average structure), CSD-430220 (Sr_2PO_3N at 300 K), CSD-430219 (Sr_2PO_3N at 250 K), CSD-430218 (Sr_2PO_3N at 200 K), CSD-430217 (Sr_2PO_3N at 150 K), CSD-430216 (Sr_2PO_3N at 100 K).

Powder X-Ray Diffraction

Powder X-ray diffraction data were collected in parafocusing Debye-Scherer geometry on a Stadi P diffractometer (Stoe, Darmstadt, Germany), equipped with a Ge(111)-monochromator (Cu-Kα_1 radiation) and a MYTHEN 1K Si strip detector (Dectris, Baden, Switzerland, angular range 2θ = 12.5 °). The samples were sealed in glass capillaries (Hilgenberg, diameter 0.3 mm). Subsequent Rietveld refinements were carried out using TOPAS-Academic 4.[31] The peak shape was modeled with the fundamental parameters approach including direct convolution of source emission profiles, axial instrument contributions, crystallite-size and microstrain effects.[32,33] In order to describe preferred orientation, a spherical harmonics of fourth order was employed.[34]

Luminescence Spectroscopy

The measurements on $Ca_2PO_3N{:}Eu^{2+}$ were performed on a luminescence microscope consisting of a HORIBA Fluorimax4 spectrofluorimeter system attached to an Olympus BX51 microscope via fiber optical bundles. The excitation wavelength was chosen to 400 nm with a spectral width of 10 nm. The emission spectrum was collected in the wavelength range between 420 and 780 nm with 2 nm step size. For the luminescence measurements the samples were placed in silica glass capillaries in a glove box and sealed under Ar atmosphere.

3.3 Results and Discussion

3.3.1 Synthesis

Initially, samples of M_2PO_3N with M = Ca, Sr were obtained by high-pressure high-temperature reaction of stoichiometric amounts of MO (M = Ca, Sr) and amorphous PON at 7 GPa and 1100 °C. The synthesis under high-pressure condition is not a common synthetic route of oxonitridophosphates. So far, only three compounds, namely, $M^{II}P_6O_6N_8$ (M^{II} = Sr, Ba) and $CaMg_2P_6O_3N_{10}$, have been synthesized under high-pressure conditions.[35–37] All other oxonitridophopshates have been obtained by conventional solid-state reactions.[38] Due to this fact it appeared likely that the synthesis of M_2PO_3N would also be possible by conventional solid-state reaction in silica ampoules. The according syntheses were accomplished by heating mixtures of MO (M = Ca, Sr) and amorphous PON in N_2-

filled sealed silica glass ampoules to 1000 °C. Upon prolonged heating (> 2 h), Ca_2PO_3N decomposes to CaO and an amorphous phase. In the case of Sr_2PO_3N, no such decomposition was observed under the same conditions.

Both compounds were obtained as colorless and air-stable crystalline solids. However, if directly exposed to water, they decompose rapidly to the respective hydroxylapatite $M_5(PO_4)_3(OH)$,[39,40] $M(OH)_2$, M = Ca, Sr and NH_3.

3.3.2 Crystal Structure Determination

The single crystals of both compounds were grown under high-pressure high-temperature conditions by adding NH_4Cl as a mineralizer. The crystal structure of Sr_2PO_3N was solved and refined from single-crystal X-ray diffraction data in the orthorhombic space group *Pnma* (no. 62) with a = 7.1519(5), b = 5.5778(3) and c = 9.8132(7) Å. In the case of Ca_2PO_3N, an analogous refinement (a = 6.7942(7), b = 5.4392(6) and c = 9.4158(11) Å) was possible; however, reconstructed reciprocal lattice sections (Figure 3.1) revealed satellite reflections $hklm$ (m = 1) that indicate a modulation vector q = (0.287(5), 0, 0).

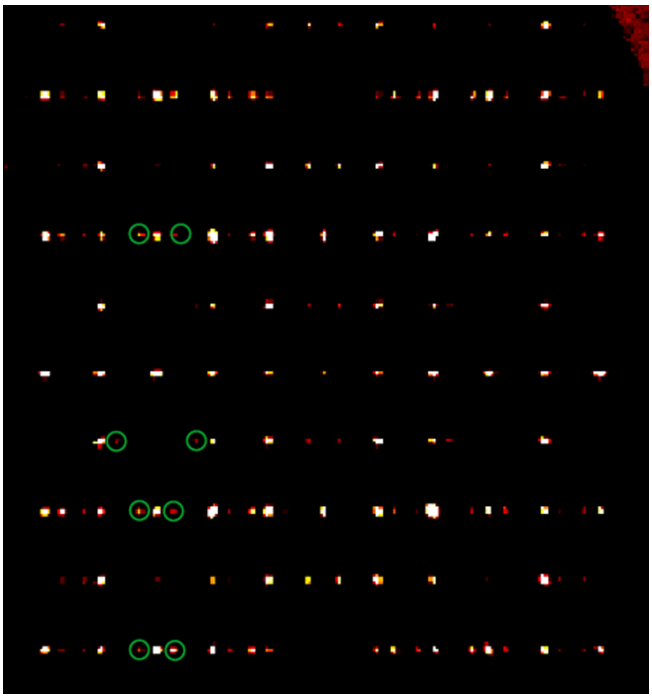

Figure 3.1: Reciprocal $hk2$ lattice plane reconstructed from the single-crystal data of Ca_2PO_3N; some satellite reflections are marked with green circles.

The observed reflection conditions are $h + m = 2n$ for $hk0m$, m = 2n for $h0lm$ and $k + l = 2n$ for $0kl0$. Although, in principle, the three-dimensional space groups $Pna2_1$ and *Pnma* are possible, only

the latter centro-symmetric one has a corresponding (3+1)D superspace group, *Pnma*(α00)0*ss*, that agrees with the observed reflection conditions. Hence this superspace group was used for the structure refinement. As only the first order satellites showed significant intensity, one harmonic wave of each atom was applied.

In contrast to Ca_2PO_3N, the reconstructed reciprocal lattice sections for Sr_2PO_3N did not show any satellite peaks (for a comparison, see Figures B.1 and B.2 in Supporting Information). No constraints or restraints were applied during structure refinements. All atoms were refined with anisotropic treatment of the thermal displacement. In both compounds, the assignment of O and N to the anion positions was possible in an ordered way. The models with the ordered occupancies of the anion sites were additionally supported by calculations of the lattice energy (MAPLE) as well as bond-valence sums (see Table B.1-B.4 in the Supporting Information). However, in the case of Ca_2PO_3N, the average structure model was used for both calculations. Thus, the calculations on Ca_2PO_3N offer merely approximate values and can only be used for rough estimations. Nevertheless, the calculated values for both compounds follow the trend quite well, thus giving a good hint on the ordered occupancy of the anion sites. Crystallographic data and refinement details of both compounds are summarized in Tables 3.2 and 3.3; atomic coordinates and displacement parameters are listed in Tables 3.4 and 3.5. All coefficients of the modulation functions are given in Table 3.1; anisotropic displacement parameters are listed in Tables B.5 and B.6 in the Supporting Information.

Table 3.1: Coefficients of the modulation functions for Ca_2PO_3N.

atom	**xsin1**	**ysin1**	**zsin1**	**xcos1**	**ycos1**	**zcos1**
Ca1	0	0.01960(12)	0	0	-0.00406(11)	0
Ca2	0	0.01697(13)	0	0	0.01344(13)	0
P1	0	-0.01032(14)	0	0	0.00561(13)	0
O1	0	0.0428(5)	0	0	-0.0014(4)	0
O2	-0.0161(3)	-0.0067(3)	-0.00129(17)	-0.0168(2)	-0.0122(3)	-0.0181(2)
N1	0	-0.0028(6)	0	0	0.0508(6)	0

Table 3.2: Crystallographic data and details of the structure refinement for Ca_2PO_3N.

formula	Ca_2PO_3N
molar mass / g·mol^{-1}	173.1
crystal system	orthorhombic
space group	*Pnma*(α00)0*ss*,* q = (0.287(5), 0, 0)
lattice parameters / Å	a = 6.7942(7), b = 5.4392(6), c = 9.4158(11)
cell volume / Å^3	347.9(1)
formula units per cell	4
temperature / K	293(2)
radiation	Mo-Kα (λ = 0.71073 Å)
calculated X-ray density / g·cm^{-1}	3.305
absorption coefficient / mm^{-1}	3.572
absorption correction	semiempirical[27]
min/max transmission	0.780 / 0.833
measured reflections	38916
independent reflections (main/satellite)	726 / 1202
observed reflections (main/satellite)	639 / 507
refined parameters	56
R_{int}; R_σ (overall)	0.0949; 0.0496
Goodness of fit	1.470
R values (main/satellite)	$R1$(obs) = 0.0328/0.0791; wR(all) = 0.0483 / 0.1043[a]
R values (overall)	$R1$(obs) = 0.0413; wR(all) = 0.0673

*symmetry operators: x, y, z, t, -x+1/2, -y, z+1/2, -t+1/2; -x, y+1/2, -z, -t+1/2; x+1/2, -y+1/2, -z+1/2, t; -x, -y, -z, -t; x+1/2, y, -z+1/2, t+1/2; x, -y+1/2, z, t+1/2, -x+1/2, y+1/2, z+1/2, -t;
[a] $w = 1 / [\sigma^2 (F_0) + 0.000625\ F_0{}^2]$

Table 3.3: Crystallographic data and details of the structure refinement for Sr_2PO_3N.

formula	Sr_2PO_3N
molar mass / g·mol^{-1}	268.22
crystal system	orthorhombic
space group	*Pnma* (no. 62)
lattice parameters / Å	a = 7.1519(5), b = 5.5778(3), c = 9.8132(7)
cell volume / Å^3	391.47(4)
formula units per cell	4
temperature / K	300
radiation	Mo-Kα (λ = 0.71073 Å)
calculated X-ray density / g·cm^{-1}	4.551
absorption coefficient / mm^{-1}	27.514
absorption correction	semiempirical[25]
min/max transmission	0.543 / 0.746
measured reflections	6650
independent reflections	533
observed reflections	495
refined parameters	40
R_{int}; R_σ (overall)	0.0790; 0.0264
Goodness of fit	1.180
R values [I > 2σ(I)]	$R1$(obs) = 0.0203; $wR2$ = 0.0468[a]
R values (all data)	$R1$(obs) = 0.0226; $wR2$ = 0.0476

[a] $w = 1 / [\sigma^2 (F_0^2) + (0.0.0198\ P)^2 + 0.5680\ P]$, with $P = (F_0^2 + 2\ F_c{}^2) / 3$

Table 3.4: Atomic coordinates and isotropic equivalent displacement parameters for Ca_2PO_3N.

atom	Wyckoff site	x	y	z	U_{eq} / Å^2
Ca1	4*c*	0.33897(8)	1/4	0.07227(6)	0.01749(17)
Ca2	4*c*	0.48248(8)	1/4	0.70319(5)	0.01110(14)
P1	4*c*	0.28261(10)	1/4	0.41595(6)	0.00771(17)
N1	4*c*	0.1619(3)	1/4	0.5566(2)	0.0171(7)
O1	8*d*	0.2358(2)	0.0212(3)	0.32014(18)	0.0234(5)
O2	4*c*	0.0075(3)	1/4	0.0582(2)	0.0181(6)

Table 3.5: Atomic coordinates and isotropic equivalent displacement parameters for Sr_2PO_3N.

atom	Wyckoff site	x	y	z	U_{eq} / Å^2
Sr1	4*c*	0.34092(5)	1/4	0.07825(4)	0.01371(14)
Sr2	4*c*	0.49361(5)	1/4	0.69815(4)	0.00925(13)
P1	4*c*	0.27521(15)	1/4	0.41894(10)	0.0085(2)
N1	4*c*	0.1781(5)	1/4	0.5629(3)	0.0129(7)
O1	8*d*	0.2162(4)	0.0239(4)	0.3340(2)	0.0238(5)
O2	4*c*	-0.0055(5)	1/4	0.0729(3)	0.0212(7)

3.3.3 Structure Description

The average crystal structure of modulated Ca_2PO_3N as well as the non-modulated crystal structure of Sr_2PO_3N are isotypic to that of β-K_2SO_4. Both feature discrete PO_3N tetrahedra as shown in Figure 3.2. As a consequence of the neglected modulation in the average structure of Ca_2PO_3N, its displacement ellipsoids are significantly larger than those in Sr_2PO_3N.

Coordination environments and bond lengths in Sr_2PO_3N are displayed in Figure 3.3. The P−O (1.569(2)−1.571(4) Å) and P−N (1.574(3) Å) bond lengths are are comparable to the P−O bond lengths found in *ortho*-oxophosphates $Sr_3(PO_4)_2$[40] (1.555 Å) and $Sr_5(PO_4)_3OH$[39] (1.555−1.586 Å) but are significantly shorter than those found in other *ortho*-(oxo)nitridophosphates, e.g. Li_7PN_4 (P−N: 1.687(12)−1.733(9) Å) and $Li_{14}P_2N_6O_3$ (P−O: 1.700(9) Å, P−N: 1.728(7) Å),[20,21] which can be explained by the lower charge of the $[PO_3N]^{4-}$ ion compared to $[PN_4]^{7-}$ and $[PON_3]^{6-}$. Additionally the bond lengths lie in the same range as those in SrP_3N_5O (P−(O,N): 1.565(13)−1.625(20)).[41] With values between 107.2(1) and 113.3(2)°, angles O/N−P−O/N differ only slightly from the regular tetrahedral angle. The crystal structure contains two crystallographically independent Sr positions. The Sr1 site is coordinated by seven O atoms and three N atoms with overall coordination number CN = 10. The Sr2 site is coordinated by seven O atoms and two N atoms, resulting in CN = 9. The distances Sr−O (2.478(4)−3.088(3) Å) and Sr−N (2.618(4)−2.7963(3) Å) correspond to typical values observed in other strontium-(oxo)nitridophosphates[17,41,42] as well as to the sum of the ionic radii.[43]

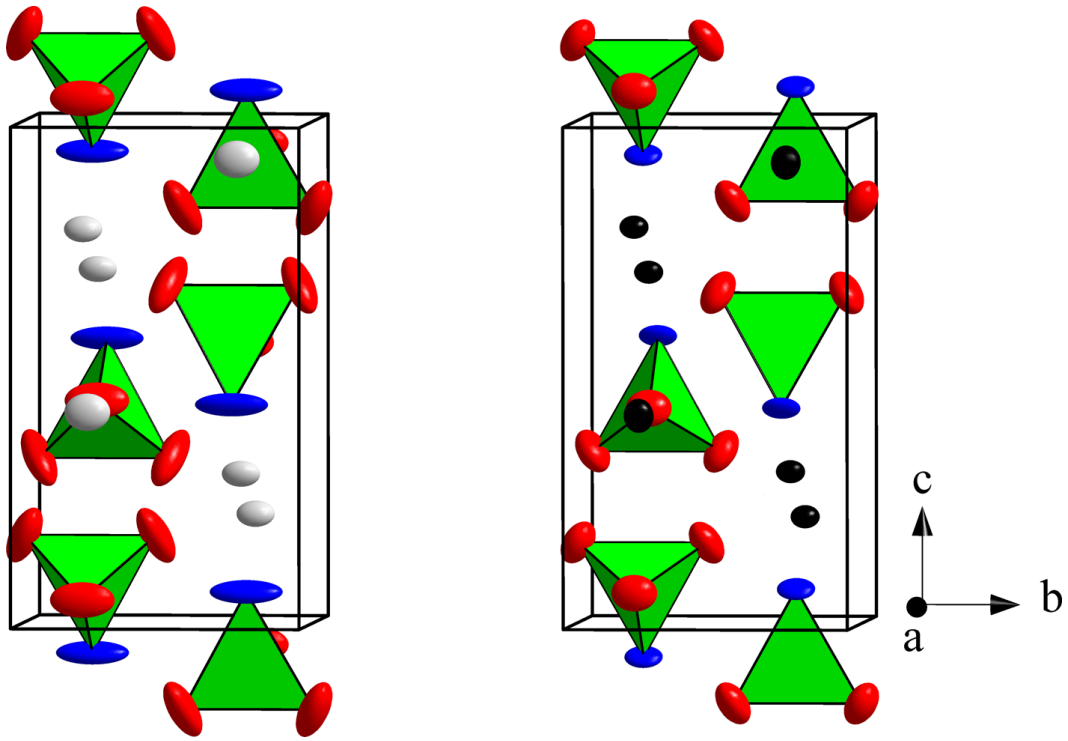

Figure 3.2: Unit cells of the average structure of modulated Ca_2PO_3N (left) and non-modulated Sr_2PO_3N (right), approximately along [001]; Ca atoms are gray, Sr atoms are black, O atoms are red, N atoms are blue and PO_3N tetrahedra are green; displacement ellipsoids are displayed at the 90% probability level.

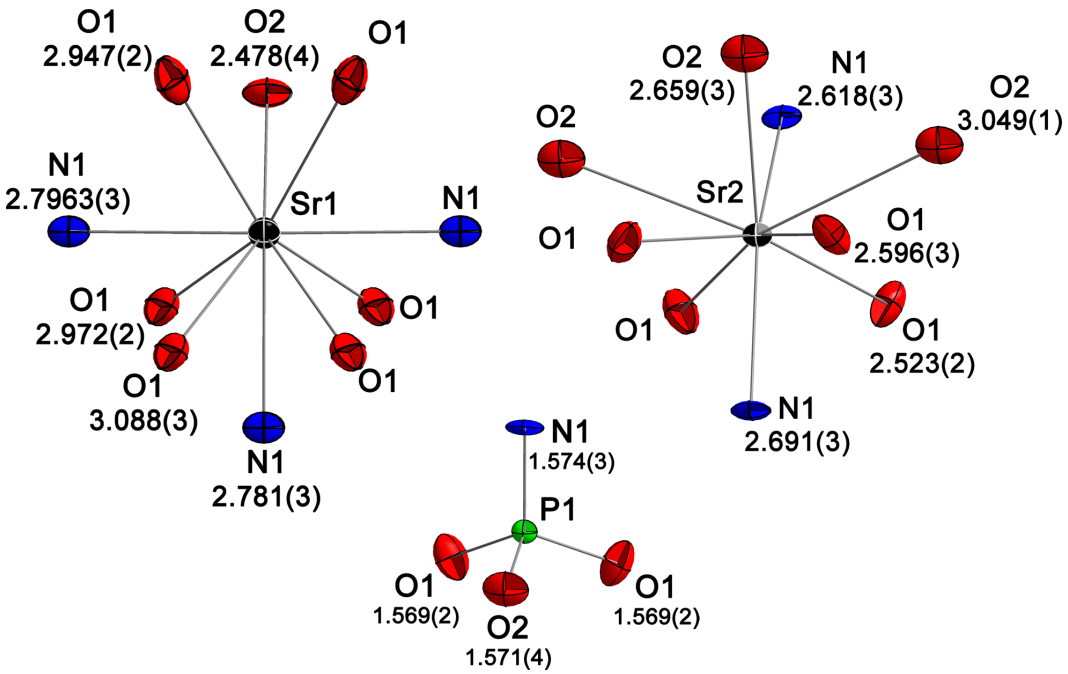

Figure 3.3: Coordination environment of Sr1 (top left), Sr2 (top right), and P1 (bottom) with interatomic distances in Å for Sr_2PO_3N; displacement ellipsoids are displayed at the 70% probability level.

Although the elements of the anisotropic displacement tensors of O and N atoms in Sr_2PO_3N are significantly smaller than those in the average structure of Ca_2PO_3N, the ellipsoids are still rather elongated perpendicular to the respective P−(O,N) bonds. This elongation may be caused by dynamical libration and / or static displacement of the discrete PO_3N tetrahedra. In order to yield information about the motional behavior of the PO_3N tetrahedron with decreasing temperature a study on the anisotropic displacement parameters by TLS analysis was carried out.[28] A PO_3N tetrahedron is defined as a rigid body, whereby translational, librational and vibrational modes are separated. The mean-square displacements of the PO_3N tetrahedron can be described in terms of a translation matrix **T**, a libration matrix **L**, and a correlation matrix **S**. By plotting the libration angle components L_x, L_y, and L_z obtained from temperature-dependent single crystal structure refinement versus temperature and extrapolation to 0 K significant residual values for all three librational angle components L_x, L_y, and L_z can be determined (see Figure 3.4). Accordingly, the PO_3N tetrahedra in Sr_2PO_3N exhibit marked static disorder. The lattice parameters and thus the cell volume determined at 300, 250, 200, 150 and 100 K show normal thermal contraction with decreasing temperature (see Figure B.3 in the Supporting Information). However, a closer look on the development of the libration angle components reveals that the values for L_y and L_z deviate slightly from linear behavior at 200 K. The same trend can be seen in the behavior of the lattice parameter *a*, whereas *b* and *c* do not appear to be affected. (see Figure B.3, Supporting Information). The examination of the reconstructed reciprocal lattice sections for Sr_2PO_3N at 200 K, however, did not show any structural changes, compared to the lattice sections at other temperatures. So the reason for this anomaly remains unknown.

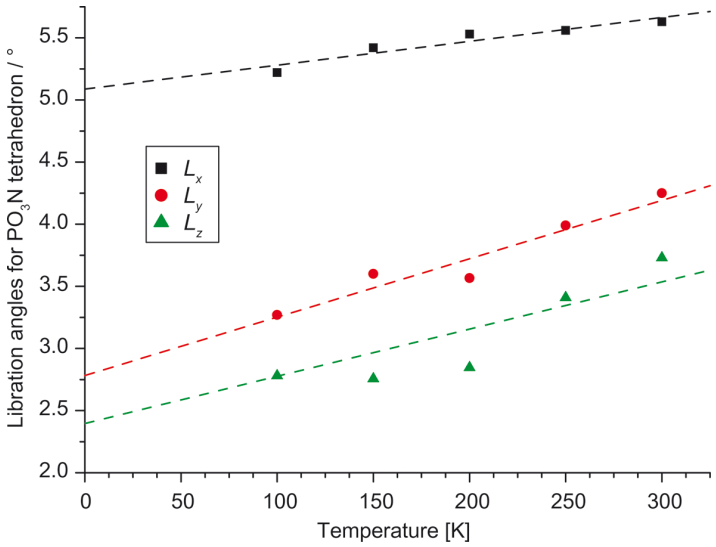

Figure 3.4: Results of the TLS analysis for the $[PO_3N]^{4-}$ anion in Sr_2PO_3N; the librational angle components L_x, L_y and L_z are shown as a function of temperature.

Ca_2PO_3N reveals an incommensurate modulation along [100]. Comparable modulations have also been reported for some of the numerous isostructural compounds, e.g. α-Sr_2SiO_4, $Ba_{2-x}Ca_2SiO_4$, Ca_xSiO_4 and $LaSrSiO_3N$.[10,44,45] The interatomic distances of the PO_3N tetrahedra in Ca_2PO_3N are little affected by the modulation and thus may be considered as almost rigid bodies in the following discussion. The P−O and P−N distances as a function of the superspace coordinate t are shown in Figure 3.5 a.

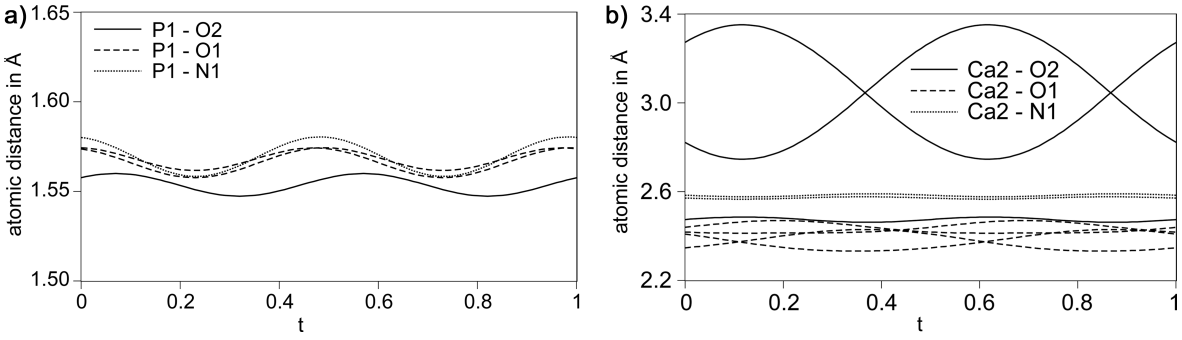

Figure 3.5: P−O and P−N distances (a) as well as Ca2−O and Ca2−N distances (b) as a function of the superspace coordinate t (one period) in the modulated structure of Ca_2PO_3N.

The displacive modulation of the tetrahedra strongly affects the coordination of Ca1. Figure 3.6 shows how the actual coordination spheres significantly deviate from those in the average structure (CN = 10). Distances Ca1−O1 and Ca1−N1 equal in the average structure due to the m mirror plane are significantly different in the modulated structure, while the Ca1−O2 and one Ca1−N1 distance (without a mirror equivalent in the average structure) are little affected by the modulation. The O1 atoms farther away from Ca1 (see Figure 3.6, a and e, purple bonds) are more strongly bonded to Ca2 (see Figure 3.5, b), but follow the same pattern of bond length variation as those closer to Ca1 (green and red bonds in Figure 3.6). The coordination variation of Ca1 is associated with corresponding displacements of the PO_3N tetrahedra. The major component is a rotation of the tetrahedra around [100] (see Figure 3.6, g) which amounts $\approx \pm 8^\circ$ with respect to an axis through the P atoms. Figure 3.6 shows the modulation visualized as an approximant structure. Fourier maps and refined atomic displacement waves are visualized in Figure B.4 in the Supporting Information.

The coordination environment of Ca2 (Figure 3.5, b) is much less affected by the modulation, only the distant O atoms in the 7+2 coordination show a strong fluctuation of the distance Ca2−O2. Minor variations of the shorter distanced Ca2−O1 compensate each other similar to those around Ca1 as discussed above.

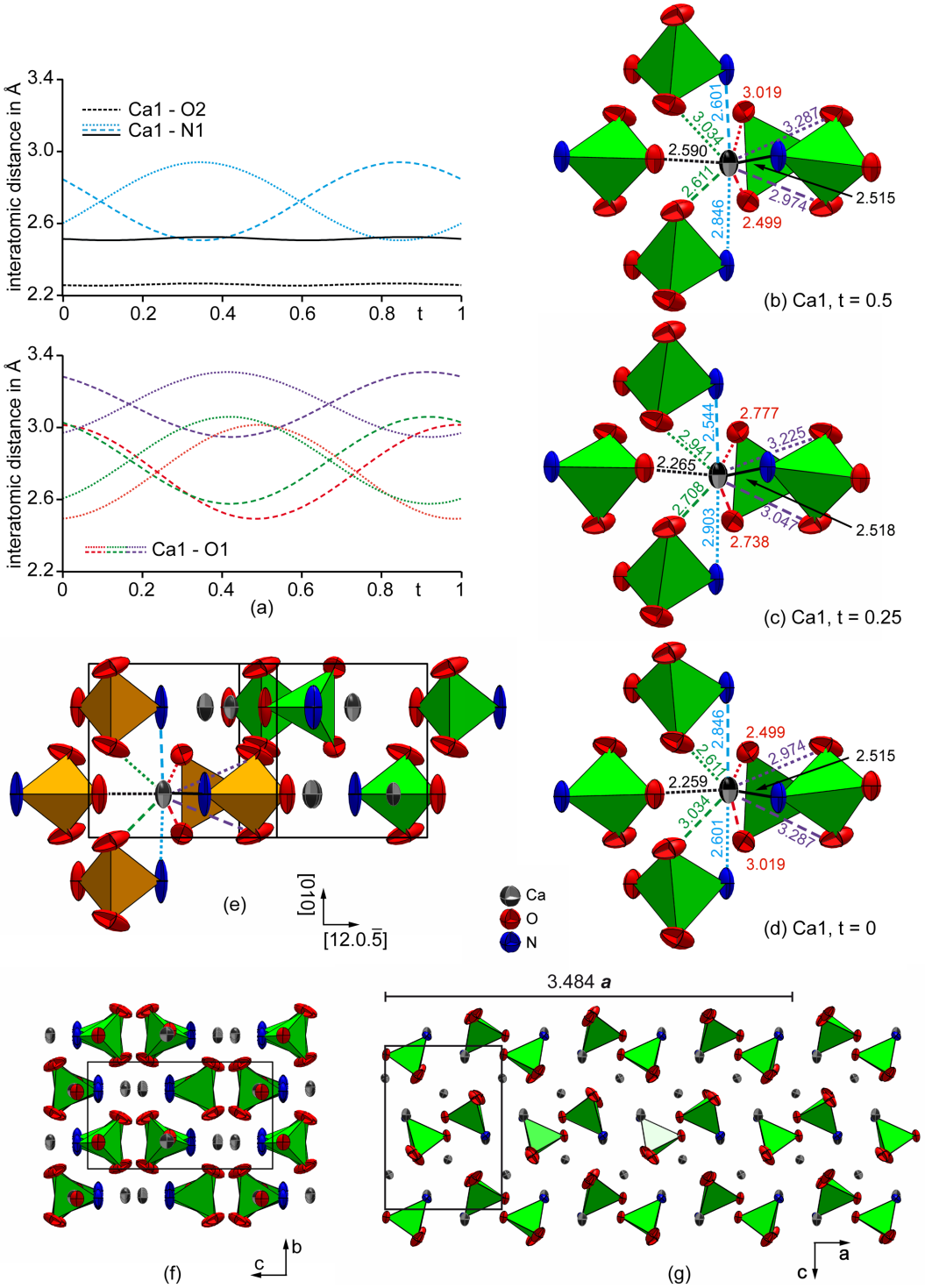

Figure 3.6: Interatomic distances and their variation in the modulated crystal structure of $Ca2PO_3N$ (displacement ellipsoids drawn at 90% probability level): (a) Coordination environment of the site as a function of the coordinate t for the distances Ca1−O1, Ca1−O2 and Ca1−N1; (b)–(d) coordination environments of Ca1 for different t values in projections along ∼[405]; (e) view of the average structure along [405], with the coordination environment of Ca1 highlighted in orange color; (f) view of the modulated structure along [100], projection of an approximate superstructure model with 10 unit cells of the average structure along the modulation direction [100]; (g) view of the same approximate structure along [010], 4 unit cells along [100], $1/q$ = 3.484 a is shown.

3.3.4 Powder X-Ray Diffraction and Rietveld Refinement

In order to confirm the structure model from single-crystal X-ray diffraction and to evaluate the possible presence of side phases, Rietveld refinement using X-ray powder diffraction data has been carried out starting from the average structure model of Ca_2PO_3N (Figure 3.7).

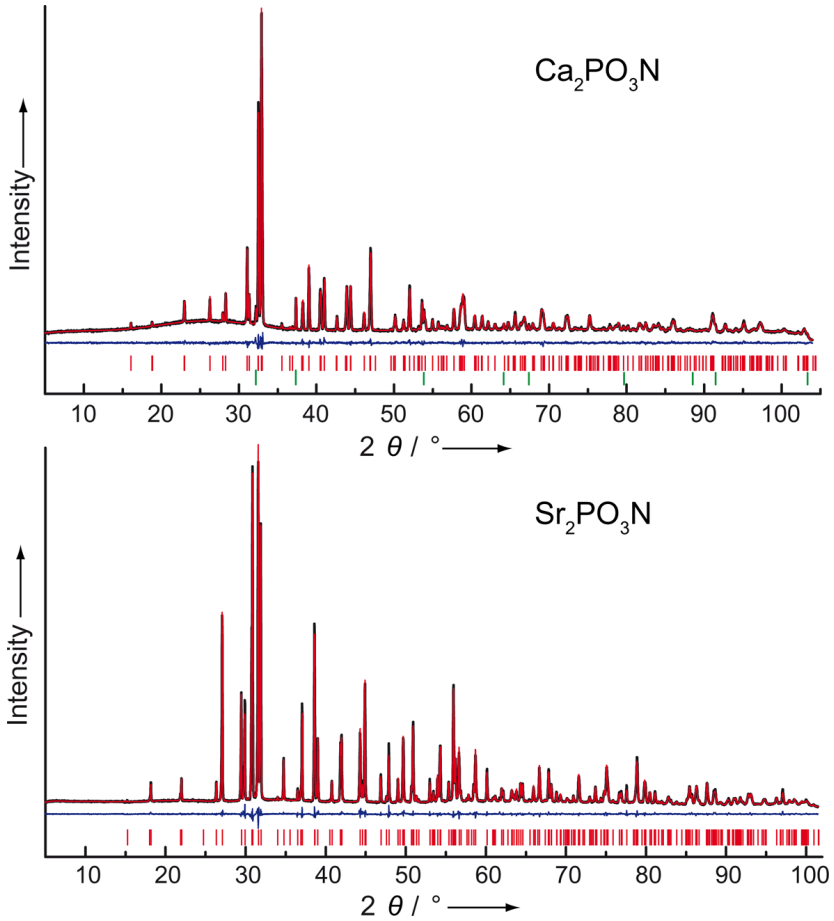

Figure 3.7: Observed (black line) and calculated (red line) X-ray powder diffraction patterns, positions of Bragg reflections (vertical red (M_2PO_3N) and green bars (CaO)) and difference profile (blue line) for the Rietveld refinement of Ca_2PO_3N (top) and Sr_2PO_3N (bottom).

The refinement revealed traces of CaO (3%) and probably an amorphous side phase due to the partial decomposition of Ca_2PO_3N during the heating phase. The satellite reflections are almost invisible in the powder X-ray diffraction pattern. For clarification, Figure B.5 in the Supporting Information shows the simulated PXRD pattern of the modulated structure of Ca_2PO_3N in comparison with the experimental one. In the case of Sr_2PO_3N, Rietveld refinement confirms presence of a single-phase product. Due to the fact that the single crystals of both samples were doped with Eu^{2+} and Rietveld refinements were performed on undoped samples, the lattice parameters determined from the Rietveld refinement are slightly smaller than those determined from single-crystal diffraction data. Further

details on the Rietveld refinements can be found in Tables B.7−B.9 in the Supporting Information. Under high-pressure conditions, we were not able to synthesize phase pure samples. Both samples exhibit an unknown side phase. For clarification, Figure 3.6 in the Supporting Information illustrates the Rietveld plots of the samples obtained from high-pressure experiments.

3.3.5 Spectroscopic Methods

The chemical composition of both products was confirmed by energy-dispersive X-ray (EDX) spectroscopy. No elements other than Ca/Sr, P, O and N were detected. The determined atomic ratio Ca/P and Sr/P, respectively, is in good agreement with the results from the crystal structure analysis (see. Tables B.10 and B.11 in Supporting Information). The determination of O and N is less reliable, however, in relation to each other much more O than N was detected.

In order to confirm the absence of NH groups, FTIR spectroscopy has been carried out. The spectra show very weak absorption bands in the characteristic region of the N-H vibration modes around 3000 cm^{-1} (see Figure 3.8). These can be explained by the partial surface hydrolysis of the samples. In the case of stoichiometric amounts of hydrogen in the structure, the characteristic N−H absorption bands are usually much more intensive, like in $MH_4P_6N_{12}$ (M = Mg, Ca).[46] Furthermore, the spectra of Ca_2PO_3N and Sr_2PO_3N are very similar, indicating the structural similarity.

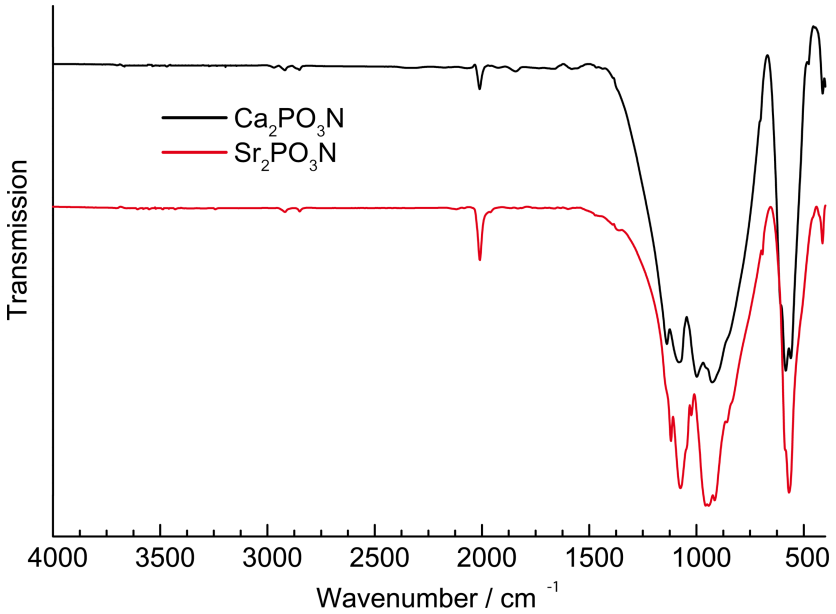

Figure 3.8: FTIR spectra of Ca_2PO_3N (black line) and Sr_2PO_3N (red line), measured using KBr pellets.

3.3.6 Luminescence

As many representatives of β-K_2SO_4 structure type exhibit luminescence properties (see above), samples of M_2PO_3N (M = Ca, Sr) were doped with 2 mol% Eu^{2+}. These show light green (M = Ca) and light brown (M = Sr) body colors, respectively. However, in contrast to $Ca_2PO_3N:Eu^{2+}$, $Sr_2PO_3N:Eu^{2+}$ did not show any luminescence under the given circumstances. The luminescence investigations were performed on single crystals in sealed glass capillaries.

Upon excitation of Eu^{2+}-doped Ca_2PO_3N with near-UV light (λ_{exc} = 400 nm), light green (LER = 418 lm/W) luminescence was detected (Figure 3.9). The excitation spectrum reveals a maximum at 397 nm. Thus, this compound can be efficiently excited by near-UV light. The excitation at 400 nm results in a broad emission band in the green spectral region with a maximum at 528 nm. The rather broad emission (FWHM ∼4025 cm^{-1}) consists most likely of two emission bands of Eu^{2+} ions substituting the Ca1 and Ca2 sites, which are not resolved due to the small difference between crystal fields of these two sites.

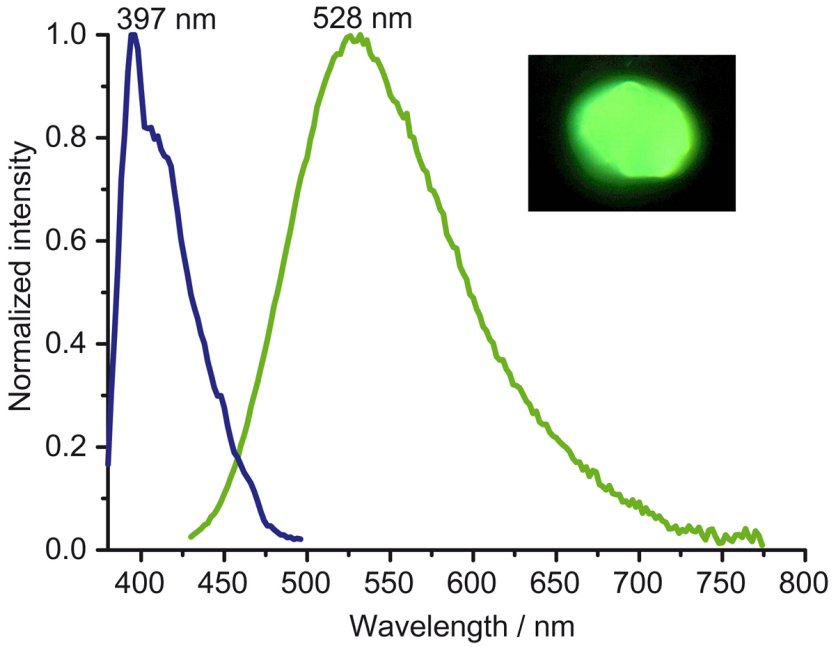

Figure 3.9: Excitation spectrum (blue curve, monitoring range 525 nm) and emission spectrum (green curve, λ_{exc} = 400 nm) of $Ca_2PO_3N:Eu^{2+}$; CIE color coordinates: x = 0.338, y = 0.512.

A similar situation is observed for isotypic oxosilicates M_2SiO_4 (M = Ca, Sr, Ba), where the emission bands also appear as single bands, although they originate from different Eu^{2+} sites in the materials. The FWHM values for the *ortho*-silicates $M_2SiO_4:Eu^{2+}$ (M = Ca: 3160 cm^{-1}; M = Sr: 3200 cm^{-1}; M = Ba: 2360 cm^{-1})[47] are, however, significantly smaller than that of $Ca_2PO_3N:Eu^{2+}$. Due to the

presence of impurities, luminescence measurements were not carried out on bulk samples. Further optimization of the synthesis of Ca_2PO_3N may deliver more insight into its luminescence properties, e.g. reliable values for the quantum efficiency which are rather sensitive towards light-absorbing side phases.

3.4 Conclusion

The novel oxonitridophosphates M_2PO_3N (M = Ca, Sr) were obtained from stoichiometric amounts of the respective alkaline earth metal oxide and amorphous PON at a temperature of 1000°C. Interestingly, the pressure range for the synthesis of the title compounds lies between 20 bar in the case of the synthesis in the silica ampoule and 7 GPa in the case of the synthesis by means of multianvil technique. The synthesis of oxonitridophosphates under high pressures usually leads to compounds with denser structures, exhibiting a degree of condensation $\kappa > 1/4$. However, in this case, the title compounds appear to be stable under high pressure and do not transform into higher condensed structures. It can however not be excluded that a reversible transition between the denser high-pressure phase and the ambient-pressure phase exists. Both compounds crystallize in β-K_2SO_4 structure type, containing discrete PO_3N tetrahedra. So far, only one representative of *ortho*-oxonitridophosphates, $Li_{14}(PON_3)_2O$ is known, with however isolated PON_3 tetrahedra instead.[21] While PO_3N tetrahedra in Sr_2PO_3N exhibit marked static disorder, the crystal structure of Ca_2PO_3N reveals an incommensurate modulation. Taking into account the fact that many compounds, which crystallize in the β-K_2SO_4 structure type, exhibit intriguing luminescence properties, the title compounds were doped with Eu^{2+}. While $Sr_2PO_3N:Eu^{2+}$ does not show luminescence, $Ca_2PO_3N:Eu^{2+}$ exhibits green luminescence upon excitation by near-UV light. This feature makes $Ca_2PO_3N:Eu^{2+}$ an interesting candidate for possible use as a luminescent material in pc-LEDs. Consequently, an important future research target is the optimization of the synthesis of this compound in order to get more insight into the luminescence properties and to investigate the quantum efficiency. Furthermore, the synthesis of isotypic compounds M_2PO_3N alkaline earth metal ion exchange or preparation of solid state solution series with mixed alkaline earth metal ions may lead to further compounds with possible intriguing luminescence properties.

3.5 References

[1] P. Villars, K. Cenzual, *Pearson's crystal data: Crystal structure database for inorganic compounds*; Release 2009/10; ASM International: Materials Park, Ohio, U.S.A.

[2] C. C. Lin, Z. R. Xiao, G. Y. Guo, T. S. Chan, R. S. Liu, *J. Am. Chem. Soc.* **2010**, *132*, 3020.

[3] Y. S. Tang, S. F. Hu, C. C. Lin, N. C. Bagkar, R. S. Liu, *Appl. Phys. Lett.* **2007**, *90*, 151108.

[4] C. C. Lin, Y. S. Tang, S. F. Hu, R. S. Liu, *J. Lumin.* **2009**, *129*, 1682.

[5] S. H. M. Poort, W. Janssen, G. Blasse, *J. Alloys Compd.* **1997**, *260*, 93.

[6] T. L. Barry, *J. Electrochem. Soc.* **1968**, *115*, 1181.

[7] G. Blasse, W. L. Wanmaker, J. W. ter Vrugt, A. Bril, *Philips Res. Rep.* **1968**, *23*, 189.

[8] L. M. Levinson, A. M. Srivastava, U.S. Patent 6,429,583, **2002**.

[9] R. Marchand, *Compt. Rend. Hebd. Seances Acad. Sci. C*, **1976**, *283*, 281.

[10] A. P. Black, K. A. Denault, J. Oró-Solé, A. R. Goñi, A. Fuertes, *Chem. Commun.* **2015**, *51*, 2166.

[11] A. Le Sauze, J. Haines, C. Chateac, J. M. Léger, R. Marchand, *Mater. Sci. Forum* **2000**, *325–326*, 77.

[12] J. M. Léger, J. Haines, L. S. de Oliveira, C. Chateau, A. Le Sauze, R. Marchand, S. Hull, *J. Phys. Chem. Solids* **1999**, *60*, 145.

[13] J. M. Léger, J. Haines, C. Chateau, G. Bocquillon, M. W. Schmidt, S. Hull, F. Gorelli, A. Lesauze, R. Marchand, *Phys. Chem. Miner.* **2001**, *28*, 388.

[14] W. Schnick, J. Lücke, *Z. Anorg. Allg. Chem.* **1992**, *610*, 121.

[15] A. Marchuk, F. J. Pucher, F. W. Karau, W. Schnick, *Angew. Chem. Int. Ed.* **2014**, *53*, 2469; *Angew. Chem.* **2014**, *126*, 2501.

[16] D. Baumann, R. Niklaus, W. Schnick, *Angew. Chem. Int. Ed.* **2015**, *54*, 4388; *Angew. Chem.* **2015**, *127*, 4463.

[17] S. J. Sedlmaier, J. Schmedt auf der Günne, W. Schnick, *Dalton Trans.* **2009**, 4081.

[18] A. Marchuk, W. Schnick, *Angew. Chem. Int. Ed.* **2015**, *54*, 2383; *Angew. Chem.* **2015**, *127*, 2413.

[19] A. Marchuk, S. Wendl, N. Imamovic, F. Tambornino, D. Wiechert, P. J. Schmidt, W. Schnick, *Chem. Mater.* **2015**, *27*, 6432.

[20] W. Schnick, J. Lücke, *J. Solid State Chem.* **1990**, *87*, 101.

[21] D. Baumann, W. Schnick, *Eur. J. Inorg. Chem.* **2015**, 617.

[22] R. Klement, O. Koch, *Chem. Ber.* **1954**, *87*, 333.

[23] a) N. Kawai, S. Endo, *Rev. Sci. Instrum.* **1970**, *41*, 1178; b) D. Walker, M. A. Carpenter, C. M. Hitch, *Am. Mineral.* **1990**, *75*, 1020; c) D. Walker, *Am. Mineral.* **1991**, *76*, 1092; d) D. C. Rubie, *Phase Transitions* **1999**, *68*, 431; e) H. Huppertz, *Z. Kristallogr.* **2004**, *219*, 330.

[24] *SAINT*, Bruker AXS Inc., Madison, Wisconsin (USA) **2007**.

[25] G. M. Sheldrick, *SADABS*, Multi-Scan Absorption Correction, v.2, Bruker-AXS, **2012**.

[26] G. M. Sheldrick, *Acta Crystallogr., Sect. A: Found. Crystallogr.* **2008**, *64*, 112.

[27] V. Petříček, M. Dušek, L. Z. Palatinus, *Kristallogr.* **2014**, *229*, 345.

[28] V. Schomaker, K. N. Trueblood, *Acta Crystallogr. Sect. B: Struct. Crystallogr. Cryst. Chem.* **1968**, *24*, 63.

[29] A. L. Spek, A. *Platon, A Multipurpose Crystallographic Tool*, Utrecht University, Utrecht (The Netherlands) **2000**.

[30] A. L. Spek, *J. Appl. Crystallogr.* **2003**, *36*, 7.

[31] A. A. Coelho, *TOPAS-Academic*, Version 4.1; Coelho Software: Brisbane, **2007**.

[32] J. Bergmann, R. Kleeberg, A. Haase, B. Breidenstein, *Mater. Sci. Forum* **2000**, *347–349*, 303.

[33] R. W. Cheary, A. A. Coelho, J. P. Cline, *J. Res. Natl. Inst. Stan.* **2004**, *109*, 1.

[34] J. M. Järvinen, *Appl. Crystallogr.* **1993**, *26*, 525.

[35] S. J. Sedlmaier, D. Weber, W. Schnick, *Z. Kristallogr. New Cryst. Struct.* **2012**, *227*, 1.

[36] A. Marchuk, L. Neudert, O. Oeckler, W. Schnick, *Eur. J. Inorg. Chem.* **2014**, 3427.

[37] R. Marchand, W. Schnick, N. Stock, *Adv. Inorg. Chem.* **2000**, *50*, 193.

[38] K. Sudarsanan, R. A. Young, *Acta Crystallogr. Sect. B: Struct. Crystallogr. Cryst. Chem.* **1972**, *28*, 3668.

[39] A. S. Posner, A. Perloff, A. F. Diorio, *Acta Crystallogr.* **1958**, *11*, 308.

[40] W. H. Zachariasen, *Acta Crystallogr.* **1948**, *1*, 263.

[41] S. J. Sedlmaier, E. Mugnaioli, O. Oeckler, U. Kolb, W. Schnick, *Chem. Eur. J.* **2011**, *17*, 11258.

[42] F. J. Pucher, W. Schnick, *Z. Anorg. Allg. Chem.* **2014**, *640*, 2708.

[43] R. D. Shannon, *Acta Crystallogr. Sect. A: Cryst. Phys., Diffr., Theor. Gen. Crystallogr.* **1976**, *32*, 751.

[44] L. Stenberg, J. R. Sellar, B. G. Hyde, *Nature* **1986**, *320*, 428.

[45] R. L. Withers, J. G. Thompson, B. G. Hyde, *Crystallogr. Rev.* **1989**, *2*, 27.

[46] A. Marchuk, V. R. Celinski, J. Schmedt auf der Günne, W. Schnick, *Chem. Eur. J.* **2015**, *21*, 5836.

[47] T. Q. Khanh, P. Bodrogi, Q. T. Vinh, H. Winkler, *LED Lighting*, Wiley-VCH, Weinheim, **2015**.

4 $MH_4P_6N_{12}$ (M = Mg, Ca): New Imidonitridophosphates with an Unprecedented Layered Network Structure Type

Alexey Marchuk,[a] Vinicius R. Celinski,[b] Jörn Schmedt auf der Günne,*[b] and Wolfgang Schnick*[a]

[a] *Department of Chemistry, University of Munich (LMU), Butenandtstraße 5–13, 81377 Munich, Germany*

[b] *Inorganic Materials Chemistry, University of Siegen, Adolf-Reichwein-Strasse 2, 57076 Siegen, Germany*

published in: *Chem. Eur. J.* **2015**, *21*, 5836-5842. DOI:10.1002/chem.201406240

Abstract

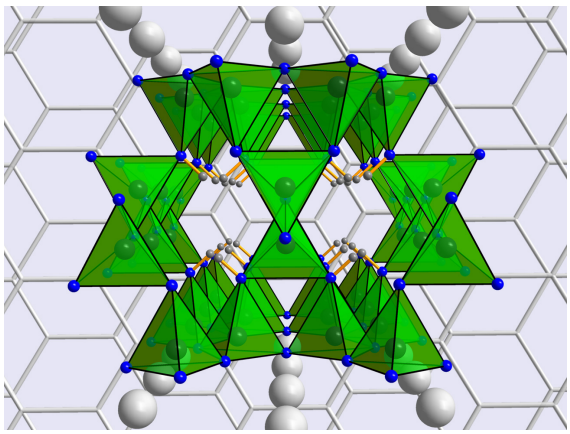

Isotypic imidonitridophosphates $MH_4P_6N_{12}$ (M = Mg, Ca) have been synthesized by high-pressure high-temperature reactions at 8 GPa and 1000 °C starting from stoichiometric amounts of the respective alkaline-earth metal nitrides, P_3N_5, and amorphous HPN_2. Both compounds form colorless transparent platelet crystals. The crystal structures have been solved and refined from single-crystal X-ray diffraction data. Rietveld refinement confirmed the accuracy of the structure determination. In order to quantify the amounts of H atoms in the respective compounds, quantitative solid-state ^{1}H NMR measurements were carried out. EDX spectroscopy confirmed the chemical compositions. FTIR spectra confirmed the presence of NH groups

in both structures. The crystal structures reveal an unprecedented layered tetrahedral arrangement, built up from all-side vertex-sharing PN_4 tetrahedra with condensed *dreier* and *sechser* rings. The resulting layers are separated by metal atoms.

4.1 Introduction

Nitridophosphates represent a silicate-analogous class of compounds since the element combination P/N is isoelectronic with Si/O. Consequently, the structural variety of this compound class is expected to be similar to that of silicates. Nitridophosphates can also form anionic tetrahedral network structures made up of condensed PN_4 tetrahedra. Analogously to nitridosilicates, both corner-sharing and edge-sharing PN_4 tetrahedra can occur.[1] Moreover, whereas oxosilicates can only form terminal or singly bridging O^{2-} ions, N atoms in the tetrahedral network structures of nitridophosphates can hypothetically connect up to four tetrahedral centers, as in the nitridosilicates MYbSi$_4$N$_7$ (M = Sr, Ba).[2] This feature opens up a wide range of new possible crystal structures in the nitridophosphate class of compounds, as well as higher degrees of condensation. With the successful synthesis of the nitridic clathrate $P_4N_4(NH)_4(NH_3)$, we were able to show that the structural diversity of nitridophosphates can even surpass that of oxosilicates.[3] The network structure of this clathrate had been predicted for silica, but has hitherto only been observed in this nitridic compound. The structure of the high-pressure poly-morph of silica-analogous phosphorus oxonitride PON has also been predicted for SiO_2, but has yet to be observed as a silica polymorph.[4] The first nitridic zeolites NPO and NPT are further unique representatives in this system.[5–7]

The structural diversity of nitridophosphates is combined with their interesting properties. As an example, phosphorus(V) nitride P_3N_5, which is the binary parent compound of nitridophosphates, can be mentioned. It is used industrially as a flame retardant, as a “getter” material for the elimination of oxygen during the production of incandescent and tungsten halogen lamps, and as a gate insulator material in metal insulator semiconductor field-effect transistors (MISFETs).[8–10] Vitreous compounds in the system Li-Ca-P-N exhibit remarkable refractive indices and hardness values.[11,12] Pseudo-binary phosphorus nitrides PON and HPN_2 are mainly used in the field of flame retardation.[13,14] The nitridic clathrate $P_4N_4(NH)_4(NH_3)$ has been discussed as a possible gas storage or membrane reactor material, due to the encapsulated ammonia within its $4^2 8^4$ cages and its high thermal and chemical stability.[15] Furthermore, $LiPN_2$ and Li_7PN_4 should be mentioned, which exhibit lithium ion conductivity.[16]

Considering all of the aspects mentioned above, it is apparent that the remarkable structural variety of nitridophosphates as well as the resulting diversity of their interesting properties makes a systematic search for new compounds of this type an important research target.

In this contribution, we report on the high-pressure high-temperature synthesis and structure elucidation of new isotypic imidonitridophosphates MH$_4$P$_6$N$_{12}$ (M = Mg, Ca), with an unprecedented layered structure type built up from all-side vertex-sharing PN_4 tetrahedra. In contrast to common

nitridophosphates, singly-bridging imide groups NH occur in the network structure. In our preceding publications, we have reported on several pseudo-binary phosphorus imide nitrides. Besides α-HPN_2 and its high-pressure polymorph β-HPN_2,[17,18] phosphorus imide nitride α-HP_4N_7 as well as its high-pressure polymorphs β-HP_4N_7 and γ-HP_4N_7 have been described.[19–21] The latter polymorph is the first example of trigonal-bipyramidal coordinated phosphorus being observed in an inorganic network structure. Furthermore, two important representatives of the imidonitridophosphate class of compounds, namely $Na_{10}[P_4(NH)_6N_4](NH_2)_6(NH_3)_{0.5}$ and $Rb_8[P_4N_6(NH)_4](NH_2)_2$, have been mentioned in the literature, both consisting of adamantane-like molecular anions $[P_4N_6(NH)_4]^{6-}$.[22,23] However, to the best of our knowledge no layered (imido)nitridophosphates have hitherto been discussed in the literature.

4.2 Results and Discussion

4.2.1 Synthesis

MH$_4$P$_6$N$_{12}$ (M = Mg, Ca) were synthesized by high-pressure high-temperature reaction at 8 GPa and 1000 °C using a Walker-type multianvil assembly.[24] Stoichiometric amounts of the respective alkaline-earth metal nitrides, amorphous HPN_2, and P_3N_5 were used as starting materials (Eq. 4.1).

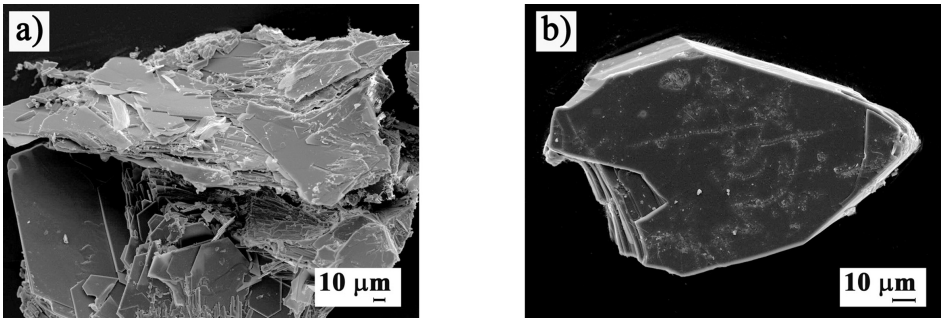

Figure 4.1: SEM images of crystals of MH$_4$P$_6$N$_{12}$, M = Ca (a), Mg (b).

$$M_3N_2 + 12\,HPN_2 + 2\,P_3N_5 \longrightarrow 3\,MH_3P_6N_{12};\ M = \text{Mg, Ca} \tag{4.1}$$

The products were obtained as air- and moisture-stable colorless crystalline solids. In order to grow single crystals of the respective products, small amounts of NH_4Cl as a mineralizer were added to the starting mixtures. In this way, colorless transparent platelet single crystals of MH$_4$P$_6$N$_{12}$ (M = Mg, Ca) were obtained and isolated (Figure 4.1). As mentioned in a preceding publication, intermediately formed HCl presumably enables reversible cleavage and reformation of P−N bonds and thus facilitates

the growth of single crystals.[18] NH_4Cl was removed from the product by washing with de-ionized water and ethanol. Detailed information on the synthesis of the title compounds is given in the Experimental Section.

4.2.2 Crystal Structure Determination

The crystal structures of $MH_4P_6N_{12}$ (M = Mg, Ca) were solved and refined in the orthorhombic space group *Cmce* (no. 64) from single-crystal X-ray diffraction data using direct methods. For single-crystal structure refinement, the respective lattice parameters from Rietveld refinement were used. The H atom positions were unequivocally determined from difference Fourier syntheses and were refined isotropically using restraints for N−H distances. All non-hydrogen atoms were refined anisotropically. The crystallographic data for $MH_4P_6N_{12}$ are summarized in Table 4.1; the atomic parameters are given in Tables 4.2 and 4.3.

Rietveld refinement based on powder X-ray data corroborated the accuracy of the structure determination of $MH_4P_6N_{12}$ from single-crystal data and confirmed the presence of a crystalline single-phase product (see Figure 4.2). The crystallographic data as well as atomic parameters of the Rietveld refinement of $MH_4P_6N_{12}$ are summarized in Tables C.1, C.2 and C.3.

The chemical compositions of the title compounds were determined by energy-dispersive X-ray (EDX) spectroscopy. No elements other than Mg/Ca, P, and N were detected. Trace amounts of oxygen were most probably attributable to surface hydrolysis of the sample. The atomic ratio (Ca/Mg):P:N was in good agreement with the predicted composition of the products. In calculating the chemical composition, it was kept in mind that hydrogen atoms cannot be detected by EDX. The results of the EDX analysis are summarized in Tables C.6 and C.7 (Supporting Information). The FTIR spectra of $MgH_4P_6N_{12}$ and $CaH_4P_6N_{12}$ are very similar, reflecting the structural similarity of these compounds (see Figure C.1). Both spectra feature a significantly wide multiple absorption band between 2538 and 3250 cm^{-1}. This can be attributed to the N−H valence modes of the NH groups of the layers. Additionally, absorption bands between 400 and 1500 cm^{-1} can be observed, which are characteristic of nitridophosphates. The latter can be assigned to symmetric and asymmetric P−N−P stretching modes.

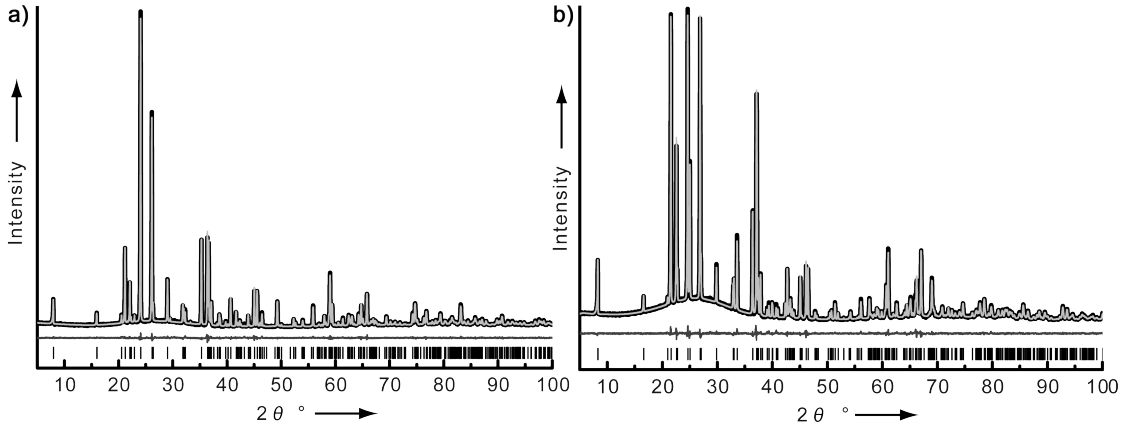

Figure 4.2: Rietveld refinements of MH$_4$P$_6$N$_{12}$, M = Mg (a), Ca (b); observed (black line) and calculated (light-gray line) X-ray powder diffraction patterns, positions of Bragg reflections (vertical black bars), and difference profile (dark-gray line).

Table 4.1: Selected crystallographic data of the single-crystal structure determination of MH$_4$P$_6$N$_{12}$ (M = Mg, Ca); standard deviations in parentheses.

formula	$MgH_4P_6N_{12}$	$CaH_4P_6N_{12}$
crystal system	orthorhombic	
space group	*Cmce* (no. 64)	
lattice parameters / Å	a = 8.4568(16)	a = 8.6289(17)
	b = 4.8270(10)	b = 4.9010(10)
	c = 21.309(4)	c = 22.153(4)
cell volume / Å^3	869.8(3)	936.9(3)
formula units per cell	4	4
calculated X-ray density / g·cm^{-1}	2.919	2.822
radiation	Mo-Kα (λ = 0.71073 Å)	
temperature / K	293(2)	293(2)
F(000)	760.0	792.0
θ-range / °	$3.68 \leq \theta \leq 27.48$	$3.82 \leq \theta \leq 29.99$
total number of reflections	4176	3376
independent relfections	671 [R(int) = 0.0344]	576 [R(int) = 0.0558]
refined parameters	54	54
goodness of fit	1.152	1.119
$R1$ (all data); $R1$ ($F^2 > 2\ \sigma(F^2)$)	0.0284; 0.0323	0.0354; 0.0397
$wR2$ (all data), $wR2$ ($F^2 > 2\ \sigma(F^2)$)	0.0805; 0.0825	0.0920; 0.0945
$\Delta\rho_{max}$; $\Delta\rho_{min}$ (e·Å^{-3})	0.570; -0.486	0.869; -0.466

Table 4.2: Fractional atomic coordinates, isotropic displacement parameters, and occupation of crystallographic positions of $MgH_4P_6N_{12}$; standard deviations in parentheses.

atom	Wyckoff site	*x*	*y*	*z*	U_{eq} / Å^2	occupancy
Mg1	4*a*	0	0	0	0.0094(3)	1.0
P1	16*g*	0.33547(6)	-0.00404(10)	0.08754(2)	0.00648(17)	1.0
P2	8*f*	0	0.40462(15)	0.21131(3)	0.00779(19)	1.0
N1	16*g*	0.1523(2)	0.4808(4)	0.16633(8)	0.0085(3)	1.0
N2	16*g*	0.3154(2)	0.3150(4)	0.06601(8)	0.0079(3)	1.0
N3	8*f*	0	0.0778(5)	0.22543(12)	0.0117(5)	1.0
N4	8*f*	0	0.3694(5)	0.06269(11)	0.0074(4)	1.0
H1	16*g*	0.241(3)	0.492(8)	0.1862(18)	0.048(11)	1.0

Table 4.3: Fractional atomic coordinates, isotropic displacement parameters, and occupation of crystallographic positions of $CaH_4P_6N_{12}$; standard deviations in parentheses.

atom	Wyckoff site	*x*	*y*	*z*	U_{eq} / Å^2	occupancy
Ca1	4*a*	0	0	0	0.0064(3)	1.0
P1	16*g*	0.33608(9)	0.00519(15)	0.09419(4)	0.0073(3)	1.0
P2	8*f*	0	0.4215(2)	0.21316(5)	0.0100(3)	1.0
N1	16*g*	0.1505(3)	0.4948(5)	0.17004(12)	0.0094(5)	1.0
N2	16*g*	0.3052(3)	0.3158(5)	0.07270(12)	0.0103(6)	1.0
N3	8*f*	0	0.0986(8)	0.22686(18)	0.0148(8)	1.0
N4	8*f*	0	0.4003(7)	0.06900(17)	0.0100(7)	1.0
H1	16*g*	0.225(7)	0.522(15)	0.197(3)	0.10(3)	1.0

4.2.3 Solid-state NMR study

The aim of the solid-state NMR study was to corroborate the models obtained from single-crystal X-ray diffraction analysis, mainly with respect to the H atoms, since these possess a lowscattering power in diffraction experiments. In the following, we identify the expected ^{31}P and ^{31}H NMR signals, quantify the latter, and finally demonstrate ^{31}P-^{1}H spatial proximity.

The unit cells of the title compounds both feature two P sites with an atomic ratio P1 : P2 = 2 : 1 (see Tables 4.2 and 4.2). The ^{31}P MAS NMR spectra of $MgH_4P_6N_{12}$ and $CaH_4P_6N_{12}$ are consistent with this model, showing two main peaks with the expected area ratio (see Figure C.3). These two signals correlate with one another, showing double-quantum filtered peaks (see Figures 4.3 and C.2), and thus confirm that the peaks assigned to P1 and P2 arise from the same phase.

Each of the solid-state ^{1}H NMR spectra (see Figure 4.4) features one peak attributable to the respective title compounds ($\delta \approx 6.5$ ppm). The other peak is assigned to an unknown side phase, which may contain NH_4^+ from the mineralizer NH_4Cl (δ = 7.3 ppm). For comparison, the solid-state ^{1}H NMR

spectrum of pure NH_4Cl is shown in Figure C.4 (Supporting Information). Moreover, the hydrogen contents were quantified as 3.8 $\pm$ 0.4 and 3.9 $\pm$ 0.4 hydrogen atoms per chemical formula unit of the magnesium and calcium compounds, respectively. These numbers support the models obtained from single-crystal structure solution and FTIR spectroscopy, confirming the chemical compositions $MgH_4P_6N_{12}$ and $CaH_4P_6N_{12}$.

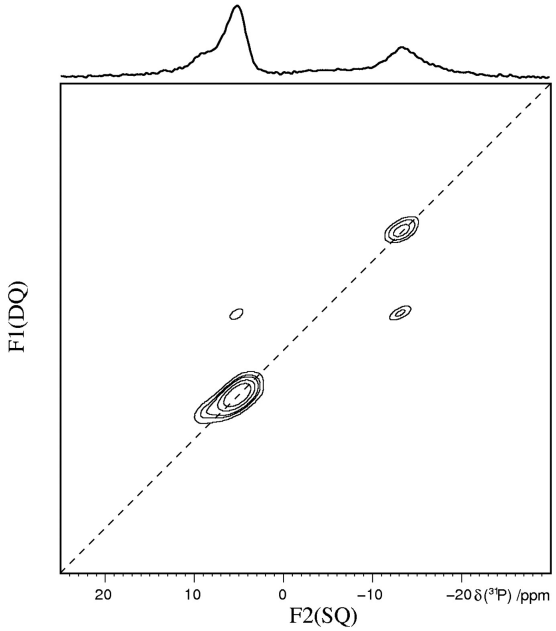

Figure 4.3: ^{31}P–^{31}P 2D double-quantum (DQ) single-quantum (SQ) correlation MAS NMR spectrum of $MgH_4P_6N_{12}$ obtained at a sample spinning frequency of 20 kHz. The dashed diagonal line denotes the peak position of isochronous spins (autocorrelation peaks).

Finally, the question remains as to whether the P atoms belong to the same phase as the quantified hydrogen atoms. The proximity of P1 and P2 to hydrogen was confirmed by $^{31}P\{^1H\}$ heteronuclear correlation NMR (see Figures 4.5 a and 4.5 b), with each spectrum showing two ^{31}P-^1H correlation peaks.

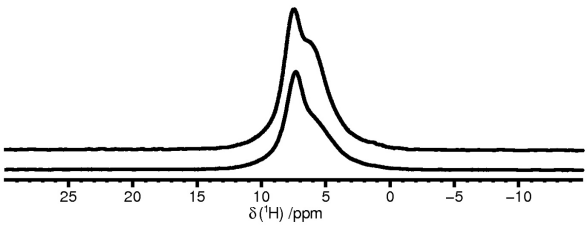

Figure 4.4: ^1H MAS NMR spectra of $MgH_4P_6N_{12}$ (bottom) and $CaH_4P_6N_{12}$ (top), measured at a sample spinning frequency of 40 kHz. The sharp peak at around 7.4 ppm in each spectrum is due to NH_4Cl, which was used as a mineralizer, while the other peak at around 6 ppm is assigned to the respective title compounds.

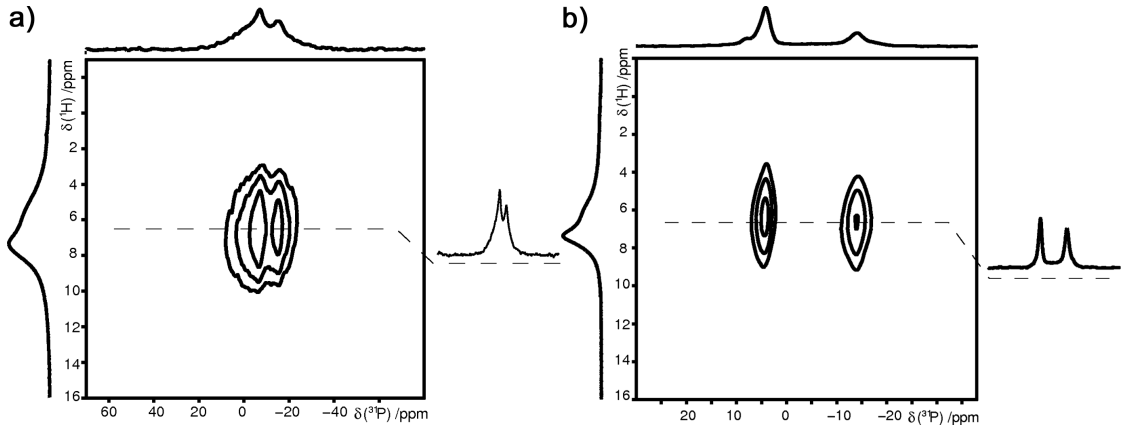

Figure 4.5: $^{31}P\{^{1}H\}$ heteronuclear correlation spectrum of $CaH_4P_6N_{12}$ (a) and $MgH_4P_6N_{12}$ (b) measured at a sample spinning frequency of 20 kHz. Correlation peaks are shown as a contour plot.

4.2.4 Structure Description

The crystal structure of $MH_4P_6N_{12}$ (M = Mg, Ca) consists of a layered network of all-side vertex-sharing Q^4-type PN_4 tetrahedra, leading to a degree of condensation $\kappa = n(P):n(N) = 0.5$ for the $^{3}_{\infty}[P_6^{[4]}N_8^{[2]}(NH)_4^{[2]}]^{6-}$ substructure (see Figure 4.6). The PN_4 tetrahedra form double layers, which are oriented parallel to the *ab* plane. These layers are separated by Mg and Ca, respectively.

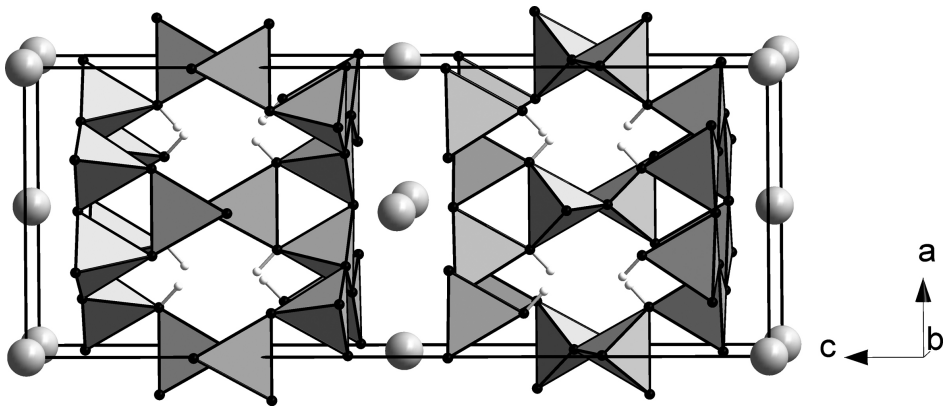

Figure 4.6: Crystal structure of $MH_4P_6N_{12}$ (M = Mg, Ca) viewed approximately along [010]. Light-gray alkaline-earth atoms Mg or Ca; dark-gray PN_4 tetrahedra, white H atoms.

The topology of these layers is represented by the point symbol 3.6^5 (determined by TOPOS software) and has not been found in any other known compound so far.[25] Condensation of PN_4 tetrahedra results in *dreier* and *sechser* rings, according to the nomenclature introduced by Liebau.[26] These form rhombic channels, in which H atoms are covalently bound to N1 atoms (see Figure 4.6). Each double layer can be subdivided into two opposing planar *sechser* ring single layers, which are mutually

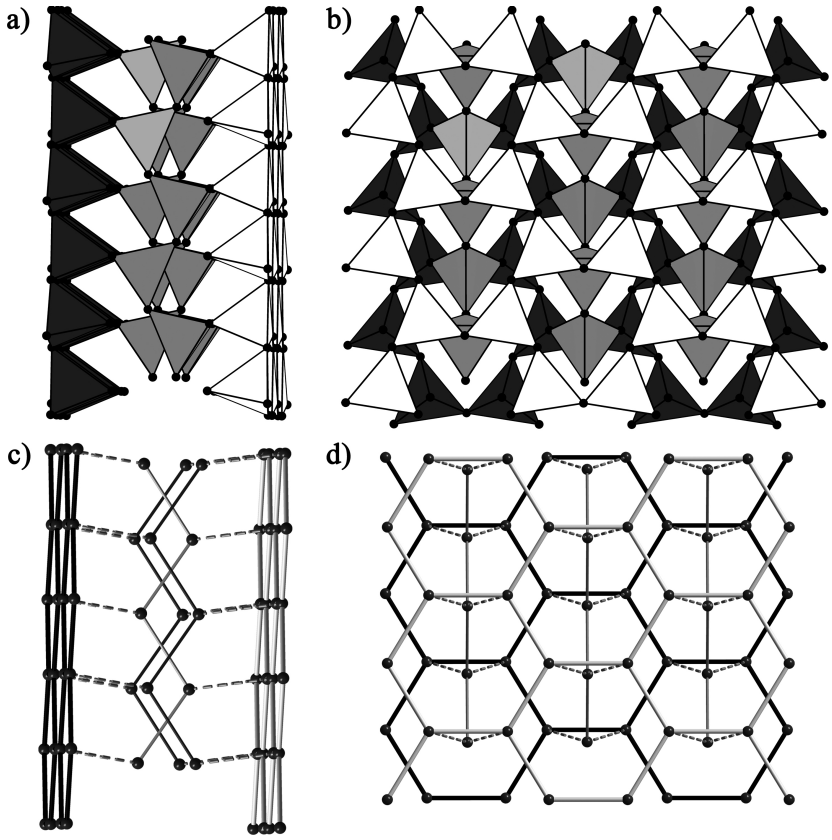

Figure 4.7: A *sechser* ring double layer in MH$_4$P$_6$N$_{12}$, viewed along [100] (a) and [001] (b), with the respective topological representations (c, d). White and black PN$_4$ tetrahedra belong to different *sechser* ring single layers, dark-gray PN$_4$ tetrahedra represent *zweier* single chains. Each connecting line in the topological representation represents a P−N−P bond. The dotted lines represent P−N−P bonds between a zigzag chain and a *sechser* ring layer.

staggered (see Figure 4.7 b). These single layers are interconnected by *zweier* zigzag single chains parallel to the b-axis (see Figure 4.7 a). According to the nomenclature introduced by Liebau,[26] the terms "*zweier*", "*dreier*", and "*sechser*" derive from the German words "zwei", "drei", and "sechs", meaning two, three, and six, respectively. Accordingly, a *zweier* single chain includes two PN$_4$ tetrahedra within one repeating unit of the linear part of the chain. Topological representation of the *sechser* ring double layers illustrates the arrangement of these condensed rings in a honeycomb-like pattern (see Figure 4.7 c, d).

The P−N bond lengths and P−N−P angles in both samples vary in similar ranges [Mg: 1.586(3)−1.684(2) Å, 119.7(2)−132.6(2) °; Ca: 1.587(4)−1.685(3) Å, 123.6(2)−134.0(3) °]. This can be rationalized by the fact that the layers contain no Mg or Ca atoms and thus are not affected by their size. The P−N bond lengths and P−N−P angles correspond to those usually observed in other imidonitridophosphates.[22,23] As expected, the P−(NH)[2] bond lengths [Mg: 1.684(2) Å; Ca:

Table 4.4: Selected bond lengths / Å and bond angles / ° in the crystal structures of MH$_4$P$_6$N$_{12}$, M = Mg, Ca; standard deviations in parentheses.

	Mg	Ca		Mg	Ca
P1−N2	1.613(2)	1.604(3)	P1−N1−P2	129.6(1)	129.6(2)
P1−N4	1.610(1)	1.605(2)	P1−N2−P1	121.3(1)	125.6(2)
P1−N2	1.616(2)	1.617(3)	P2−N3−P2	132.6(2)	134.0(3)
P1−N1	1.684(2)	1.685(3)	P1−N4−P1	119.7(2)	123.6(2)
P2−N3	1.586(3)	1.587(4)			
P2−N3	1.606(3)	1.611(4)			
P2−N1	1.647(2)	1.652(3)			

1.685(3) Å] are significantly longer than the P−N[2] bond lengths [Mg: 1.586(3)−1.616(2) Å; Ca: 1.587(4)−1.617(3) Å], in good agreement with the localization of the H atoms in the structure model. Detailed information on the bond lengths and angles is given in Table 4.4.

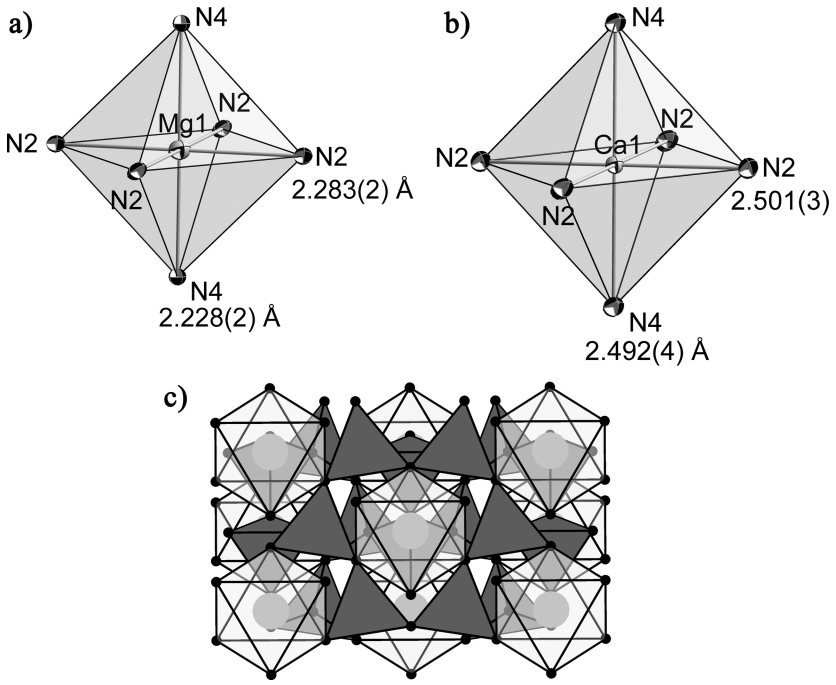

Figure 4.8: Coordination polyhedra and corresponding bond lengths / Å of the Ca1 position in CaH$_4$P$_6$N$_{12}$ (a) and the Mg1 position in MgH$_4$P$_6$N$_{12}$ (b); ellipsoids are drawn with a probability factor of 70%; the arrangement of the MN$_6$ (M = Mg, Ca) octahedra in the *sechser* ring layers (c).

A similar structural motif of double layers can be found in LiSrGaN$_2$.[23] However, the *sechser* ring single layers in the structure of this compound are not planar and are interconnected by edge-sharing pairs of GaN$_4$ tetrahedra, rather than *zweier* single chains. Furthermore, the structural motif of the almost planar *sechser* ring single layers can be found in layered silica compounds, such as muscovite

and pyrophyllite, in which two opposing layers $^2_\infty[Si_2O_5]^{2-}$ are interconnected by the edgesharing Al-centered octahedral units of oxyhydroxides.[26–29]

The metal atoms occupy only one crystallographic site in the crystal structure. They are coordinated by six N atoms at distances of 2.228(2)−2.283(2) Å (M = Mg) and 2.492(4)−2.501(4) Å (M = Ca), respectively, in a slightly distorted octahedral arrangement (see Figure 4.8). These M−N distances are in good agreement with those in other known Mg (2.056−2.248 Å, CN(Mg) = 6)[30–33] and Ca compounds (2.419−2.598 Å, CN(Ca) = 6),[34,35] as well as with the sums of the ionic radii.[36] The MN$_6$ octahedra are not interconnected with each other (see Figure 4.8 c). As only the N2 and N4 atoms belong to the coordination spheres of the respective metal atoms, it is reasonable that the P1−N2−P1 and P1−N4−P1 bond angles are larger in CaH$_4$P$_6$N$_{12}$ than in MgH$_4$P$_6$N$_{12}$, whereas the P1−N1−P2 and P2−N3−P2 bond angles remain almost identical.

4.3 Conclusion

MH$_4$P$_6$N$_{12}$ (M = Mg, Ca) represent new imidonitridophosphates with an unprecedented layered structure type. By adding small amounts of NH$_4$Cl, single crystals of the title compounds could be obtained and isolated. The hydrogen contents of the samples have been determined by quantitative solid-state ^{1}H NMR and support the models obtained from single-crystal structure solution. The layered structures of these compounds consist of condensed *sechser* rings arranged in a honeycomb-like pattern, alternating with metal ion layers. Both compounds are air- and moisture-stable. According to their structural features and material properties, MH$_4$P$_6$N$_{12}$ (M = Mg, Ca) appear to be promising candidates for liquid exfoliation of the single layers in order to obtain two-dimensional single nanomaterials. Additionally, the unusual layered structure of these compounds may lead to their use as gas absorbers or as ionic conductors. However, further investigations on the ion-exchange or intercalation properties of these compounds need to be carried out. Furthermore, considering the sandwich-type structure of the obtained materials, the synthesis of isotypic compounds by exchange of the alkaline-earth cations may lead to interesting new properties. Finally, it should be noted that the high-pressure high-temperature synthesis proved to be a very promising route for the synthesis of new nitridophosphates with interesting structural properties.

4.4 Experimental Section

4.4.1 Preparation of Starting Materials

Ca_3N_2 and Mg_3N_2 were synthesized by heating Ca (dendritic pieces, 99.99% trace metals basis, Sigma - Aldrich) or Mg (chips, 99%, *reinst*, Grüssing), respectively, in a ceramic corundum boat at 950°C (8 h) in a continuous flow of dried N_2. Ca_3N_2 was obtained as a darkviolet solid, and Mg_3N_2 was obtained as a dark-yellow solid. Detailed information is available in the literature.[37] The phase purities of the respective products were confirmed by powder X-ray diffraction analysis and FTIR spectroscopy.

P_3N_5 and amorphous HPN_2 were synthesized by heating $(PNCl_2)_3$ (Merck, p.s.) in a ceramic corundum boat at 100°C (10 h), 130°C (5 h), 190°C (3 h), and 300°C (4 h) in a continuous flow of dried NH_3 (Air Liquide, 5.0), followed by vacuum heat treatment of the mixture at 600°C (2 h) to obtain P_3N_5 or at 450°C (2 h) to obtain amorphous HPN_2. In the case of P_3N_5, the mixture was additionally heated at 950°C (2 h). This step was essential for complete condensation of the product. Detailed information is available in the literature.[38–41] The phase purities of the respective products were confirmed by powder X-ray diffraction analysis and FTIR spectroscopy.

4.4.2 Synthesis

$MH_4P_6N_{12}$ (M = Mg, Ca) were synthesized from stoichiometric amounts of the respective alkaline-earth metal nitrides and amorphous HPN_2 and P_3N_5 using a Walker-type multianvil apparatus.[6] A small amount of NH_4Cl was used as a mineralizer. Because of the high air-sensitivity of Mg_3N_2 and Ca_3N_2, all manipulations were carried out under exclusion of oxygen and moisture in an argon-filled glove box (Unilab, MBraun, Garching, $O_2 < 1$ ppm, $H_2O < 0.1$ ppm). The respective starting mixture was thoroughly ground and tightly packed into a cylindrical capsule of hexagonal boron nitride (Henze, Kempten). The filled capsule was sealed with a hexagonal boron nitride cap and placed in the center of a Cr_2O_3-doped MgO octahedron (edge length 18 mm, Ceramic Substrates & Components Ltd., Isle of Wight, U.K.). The MgO octahedron was equipped with a ZrO_2 tube (Cesima Ceramics, Wust-Fischbach, Germany), which served as a thermal insulator. Furthermore, two graphite tubes (one long tube and one short tube) were used as electrical resistance furnaces. In order to ensure that the short graphite tube was positioned in the center of the long tube, two MgO spacers (one on each side) were used. Finally, a Mo plate was placed on each side of the ZrO_2 tube in order to achieve electrical contact between the graphite tubes and the anvils of the multianvil press. The MgO octahedron was then

placed in the center of an assembly of eight truncated tungsten carbide cubes (truncation edge lengths 11 mm, Hawedia, Marklkofen, Germany), which were separated with pyrophyllite gaskets. Detailed information on the construction of the described multianvil assembly can be found in the literature.[19] The sample was compressed to 8 GPa at room temperature. It was then heated to 1000 °C over a period of 60 min, and the temperature was held at this level for 120 min. Subsequently, the sample was cooled to room temperature over a period of 60 min. After slow decompression (10 h), both products were recovered as colorless crystalline solids, which were not sensitive to air or moisture. NH_4Cl was removed from the products by washing with water and ethanol. However, for the solid-state NMR experiments, the washing step was omitted.

4.4.3 Single-Crystal X-Ray Diffraction Analysis

Single-crystal X-ray diffraction data were collected on a Nonius Kappa CCD diffractometer (MoK_α radiation, graphite monochromator, Bruker, Karlsruhe). A semi-empirical absorption correction was applied using the program XPREP.[42] The crystal structures were solved by direct methods using SHELXS,[42] and refined by full-matrix least-squares methods using SHELXL.[43] Further details of the crystal structure determinations can be obtained from the Fachinformationszentrum Karlsruhe, 76344 Eggenstein-Leopoldshafen, Germany (Fax: +49–7247–808–666; e-mail: crysdata@fiz-karlsruhe.de) on quoting the depository numbers CSD-427952 (M = Mg) and CSD-427953 (M = Ca).

4.4.4 Powder X-Ray Diffraction Analysis

Powder X-ray diffraction data for both compounds were collected on a STOE StadiP powder diffractometer ($CuK_{\alpha1}$ radiation, Ge(111) monochromator, MYTHEN 1 K Si strip detector) in parafocusing Debye–Scherer geometry. Rietveld refinements were carried out using the TOPAS Academic 4.1 package.[44] The preferred orientation of the crystallites was described using a fourth-order spherical harmonic. Peak shapes were modeled by the fundamental parameters approach (direct convolution of source emission profiles, axial instrument contributions, and crystallite size and microstrain effects).

4.4.5 Solid-State NMR Spectroscopy

For all measurements, the ^{1}H resonance of 1% $Si(CH_3)_4$ in $CDCl_3$ served as an external secondary reference, using the Ξ value for ^{31}P relative to 85% H_3PO_4 as reported by the IUPAC.[45] Solid-state NMR spectra were measured on a Bruker Avance III spectrometer with an 11.7 T magnet, operating at a ^{1}H frequency of 500.25 MHz, equipped with commercial 1.3 mm and 2.5 mm double-resonance MAS

probes. ^{31}P-^{31}P 2D double-quantum (DQ) single-quantum (SQ) correlation MAS NMR spectra were obtained at a sample spinning frequency of 20 kHz with a transient-adapted POSTC7 sequence.[46,47] The conversion period was set at 1.2 ms. Rotor synchronized data sampling of the indirect dimension accumulated 16 transients per FID. Proton decoupling was implemented by CW decoupling with a nutation frequency of 110 kHz. Repetition delays were set at 60 s and 42 s for $MgH_4P_6N_{12}$ and $CaH_4P_6N_{12}$, respectively. ^{31}P{^{1}H} heteronuclear correlation MAS NMR spectra were obtained through a 2D correlation experiment based on the PRESTO II pulse sequence[48] as described in the literature.[49] Here, proton decoupling was implemented by TPPM decoupling[50] with a nutation frequency of 115 kHz. The ^{1}H nutation frequency for the $R18_2^5$ recoupling sequence was 90 kHz for the R-elements, which consisted of simple p-pulses. All other hard pulses applied in both channels were implemented with a nutation frequency of 100 kHz. Both experiments were performed at a sample spinning frequency of 20 kHz with a repetition delay of 1.5 s. The numbers of accumulated transients per FID were 256 and 512 for $MgH_4P_6N_{12}$ and $CaH_4P_6N_{12}$, respectively.

4.4.6 FTIR Spectroscopy

The FTIR spectra of $MH_4P_6N_{12}$ (M = Mg, Ca) were measured using the KBr pellet method on a Spectrum BX II spectrometer (Perkin- Elmer, Waltham MA, USA).

4.4.7 Scanning Electron Microscopy and Energy-Dispersive X-Ray Spectroscopy

SEM imaging and EDX analysis were performed using a JEOL JSM-6500F field-emission scanning electron microscope (SEM), equipped with a Si/Li EDX detector 7418 (Oxford Instruments). In order to impart electrical conductivity to the sample surfaces, they were coated with carbon using an electron beam evaporator (BAL-TEC MED 020, Bal Tec AG).

4.5 References

[1] M. Zeuner, S. Pagano, W. Schnick, *Angew. Chem. Int. Ed.* **2011**, *50*, 7754; *Angew. Chem.* **2011**, *123*, 7898.

[2] H. Huppertz, W. Schnick, *Z. Anorg. Allg. Chem.* **1997**, *623*, 212.

[3] F. Karau, W. Schnick, *Angew. Chem. Int. Ed.* **2006**, *45*, 4505; *Angew. Chem.* **2006**, *118*, 4617.

[4] D. Baumann, S. J. Sedlmaier, W. Schnick, *Angew. Chem. Int. Ed.* **2012**, *51*, 4707; *Angew. Chem.* **2012**, *124*, 4785.

[5] S. Correll, O. Oeckler, N. Stock, W. Schnick, *Angew. Chem. Int. Ed.* **2003**, *42*, 3549; *Angew. Chem.* **2003**, *115*, 3674.

[6] S. Correll, N. Stock, O. Oeckler, J. Senker, T. Nilges, W. Schnick, *Z. Anorg. Allg. Chem.* **2004**, *630*, 2205.

[7] S. J. Sedlmaier, M. Döblinger, O. Oeckler, J. Weber, J. Schmedt auf der Günne, W. Schnick, *J. Am. Chem. Soc.* **2011**, *133*, 12069.

[8] M. S. Choudhary, J. K. Fink, K. Lederer, H. A. Krässig, *J. Appl. Polym. Sci.* **1987**, *34*, 863.

[9] a) Y. H. Jeong, J. H. Lee, Y. T. Hong, *Appl. Phys. Lett.* **1990**, *57*, 2680; b) Y. H. Jeong, G. T. Kim, K. I. Kim, U. J. Jeong, *J. Appl. Phys.* **1991**, *69*, 6699; c) Y. Hirota, T. Hisaki, O. Mikami, *Electron. Lett.* **1985**, *21*, 690.

[10] J. A. Graves, U.S. Patent 3475072, **1969**.

[11] T. Grande, J. R. Holloway, P. F. McMillan, C. A. Angell, *Nature* **1994**, *369*, 43.

[12] T. Grande, S. Jacob, J. R. Holloway, P. F. McMillan, C. A. Angell, *J. Non-Cryst. Solids* **1995**, *184*, 151.

[13] S. V. Levchik, G. F. Levchik, A. I. Balabanovich, E. D. Weil, M. Klatt, *Angew. Makromol. Chem.* **1999**, *264*, 48.

[14] E. D. Weil, N. G. Patel, *Fire Mater.* **1994**, *18*, 1.

[15] M. Pouchard, *Nature* **2006**, *442*, 878.

[16] W. Schnick, J. Lücke, *Solid State Ionics* **1990**, *38*, 271.

[17] W. Schnick, J. Lücke, *Z. Anorg. Allg. Chem.* **1992**, *610*, 121.

[18] A. Marchuk, F. J. Pucher, F. W. Karau, W. Schnick, *Angew. Chem. Int. Ed.* **2014**, *53*, 2469; *Angew. Chem.* **2014**, *126*, 2501.

[19] S. Horstmann, E. Irran, W. Schnick, *Z. Anorg. Allg. Chem.* **1998**, *624*, 221.

[20] D. Baumann, W. Schnick, *Inorg. Chem.* **2014**, *53*, 7977.

[21] D. Baumann, W. Schnick, *Angew. Chem. Int. Ed.* **2014**, *53*, 14490; *Angew. Chem.* **2014**, *126*, 14718.

[22] H. Jacobs, S. Pollok, F. Golinski, *Z. Allg. Anorg. Chem.* **1994**, *620*, 1213.

[23] F. Golinski, H. Jacobs, *Z. Allg. Anorg. Chem.* **1995**, *621*, 29.

[24] a) N. Kawai, S. Endo, *Rev. Sci. Instrum.* **1970**, *41*, 1178; b) D. Walker, M. A. Carpenter, C. M. Hitch, *Am. Mineral.* **1990**, *75*, 1020; c) D. Walker, *Am.Mineral.* **1991**, *76*, 1092; d) D. C. Rubie, *Phase Transitions* **1999**, *68*, 431; e) H. Huppertz, *Z. Kristallogr.* **2004**, *219*, 330.

[25] V. A. Blatov, A. P. Shevchenko, D. M. Proserpio, *Cryst. Growth Des.* **2014**, *14*, 3576.

[26] F. Liebau, *Structural Chemistry of Silicates*, Springer, Berlin, **1985**.

[27] D. G. Park, Z. A. Gal, F. J. DiSalvo, *J. Alloys Compd.* **2003**, *353*, 107.

[28] R. Wardle, G. W. Brindley, *Am. Mineral.* **1972**, *57*, 732.

[29] E. W. Radoslovich, *Acta. Crystallogr.* **1960**, *13*, 919.

[30] F. Karau, W. Schnick, *Z. Allg. Anorg. Chem.* **2006**, *632*, 49.

[31] B. Jürgens, E. Irran, W. Schnick, *J. Solid State Chem.* **2001**, *157*, 241.

[32] H. Hiraguchi, H. Hashizume, S. Sasaki, S. Nakano, O. Fukunaga, *Acta Crystallogr. Sect. B: Struct. Sci.* **1993**, *49*, 478.

[33] A. Marchuk, L. Neudert, O. Oeckler, W. Schnick, *Eur. J. Inorg. Chem.* **2014**, 3427.

[34] S. J. Clarke, F. J. DiSalvo, *Inorg. Chem.* **1997**, *36*, 1143.

[35] M. S. Bailey, F. J. DiSalvo, *J. Alloys Compd.* **2006**, *417*, 50.

[36] W. H. Baur, *Crystallogr. Rev.* **1987**, *1*, 59.

[37] O. Reckeweg, F. J. DiSalvo, *Z. Anorg Allg. Chem.* **2001**, *627*, 371.

[38] F. W. Karau, *Dissertation*, Ludwig-Maximilians-Universität München (Germany) **2007**.

[39] J. Lücke, *Dissertation*, Rheinische Friedrich-Wilhelms-Universität Bonn (Germany) **1994**.

[40] W. Schnick, J. Lücke, F. Krumeich, *Chem. Mater.* **1996**, *8*, 281.

[41] S. Horstmann, E. Irran, W. Schnick, *Angew. Chem. Int. Ed. Engl.* **1997**, *36*, 1873; *Angew. Chem.* **1997**, *109*, 1938.

[42] G. M. Sheldrick, *XPREP*, Data Preparation & Reciprocal Space Exploration, **1996**, v6.12, Siemens Analytical X-ray Instruments.

[43] G. M. Sheldrick, *Acta Crystallogr. Sect. A: Found. Crystallogr.* **2008**, *64*, 112.

[44] A. A. Coelho, *TOPAS-Academic*, Version 4.1, Coelho Software, Brisbane (Australia), **2007**.

[45] R. K. Harris, E. D. Becker, S. M. Cabral de Menezes, P. Granger, R. E. Hoffman, K. W. Zilm, *Pure Appl. Chem.* **2008**, *80*, 59.

[46] M. Hohwy, H. J. Jakobsen, M. Edén, M. H. Levitt, N. C. Nielsen, *J. Chem. Phys.* **1998**, *108*, 2686.

[47] J. Weber, M. Seemann, J. Schmedt auf der Günne, *Solid State Nucl. Magn. Reson.* **2012**, *43–44*, 42.

[48] X. Zhao, W. Hoffbauer, J. Schmedt auf der Günne, M. H. Levitt, *Solid State Nucl. Magn. Reson.* **2004**, *26*, 57.

[49] Y. S. Avadhut, J. Weber, E. Hammarberg, C. Feldmann, J. Schmedt auf der Günne, *Phys. Chem. Chem. Phys.* **2012**, *14*, 11610.

[50] A. E. Bennett, C. M. Rienstra, M. Auger, K. V. Lakshmi, R. G. Griffin, *J. Chem. Phys.* **1995**, *103*, 6951.

5 $CaMg_2P_6O_3N_{10}$ – A Quinary Oxonitridophosphate with an Unprecedented Tetrahedra Network Structure Type

Alexey Marchuk,[a] Lukas Neudert,[a] Oliver Oeckler,*[b] and Wolfgang Schnick*[b]

[a] *Department of Chemistry, University of Munich (LMU), Butenandtstraße 5–13, 81377 Munich, Germany*

[b] *Institute of Mineralogy, Crystallography and Materials Science, Faculty of Chemistry and Mineralogy, Leipzig University, Scharnhorststraße 20, 04275 Leipzig, Germany*

published in: *Eur. J. Inorg. Chem.* **2014**, 3427-3434. DOI: 10.1002/ejic.201402302

Abstract

$CaMg_2P_6O_3N_{10}$ has been synthesized starting from stoichiometric amounts of $Ca(N_3)_2$, Mg_3N_2, P_3N_5, and PON in a high- pressure/high-temperature reaction at 8 GPa and 1100°C. Adding small amounts of NH_4Cl to the starting mixture afforded single crystals of $CaMg_2P_6O_3N_{10}$, which form transparent, colorless truncated octahedra. The crystal structure [space group $I4_1/acd$ (no. 142), a = 12.494(1), c = 23.797(2) Å, Z = 16] was solved and refined by single-crystal X-ray diffraction analysis and confirmed by electron diffraction and transmission electron microscopy, including HRTEM image simulations. Rietveld refinement proved the phase purity of the product. FTIR analysis confirmed the absence N–H groups in the structure. Bond-valence and

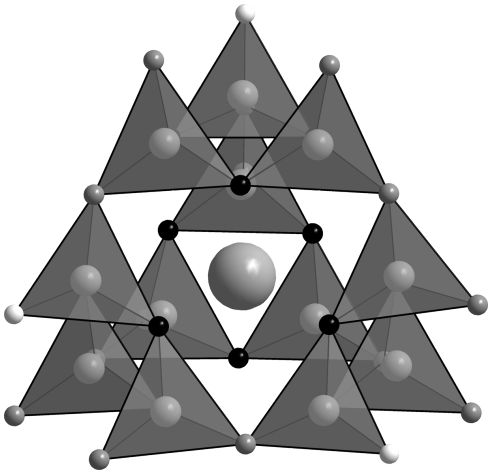

lattice energy calculations (MAPLE) of the title compound are discussed. The crystal structure consists of polyhedral building units constructed from vertex-sharing $P(O,N)_4$ tetrahedra with condensed *dreier* and *sechser* rings.

5.1 Introduction

Silicates form one of the most abundant, varied, and important classes of minerals, with more than 1000 representatives. More than 90% of the earth's crust consists of silicates.[1] Their wide range of applications in the ceramics and glass industries as well as their great potential as functional materials in catalysis, microelectronics, and optical fibers make silicates nearly indispensable for everyday life.[2,3] Their important role as luminescent materials for phosphor-converted light-emitting diodes (pcLEDs) also emphasizes the significance of silicates in future technologies.[4] Accordingly, the great structural variety and associated properties make structures that are analogous to silicates an attractive research target. Because PON is isoelectronic with SiO_2, the silicate-analogous compound class of oxonitridophosphates is expected to exhibit a structural diversity similar to that of silicates. The formal partial substitution of O by N in a tetrahedral network implies significant new structural possibilities. N in oxonitridophosphates may occur as $N^{[1]}$, $N^{[2]}$, $N^{[3]}$, or even $N^{[4]}$ atoms connecting up to four neighboring tetrahedral centers.[5,6] Compared with oxonitridophosphates, the structural variety of silicates is limited to terminal $O^{[1]}$ or singly bridging $O^{[2]}$ atoms. An excellent example of the additional structural possibilities arising from the substitution of O by N in a network structure analogous to silicates is the nitridic clathrate $P_4N_4(NH)_4(NH_3)$, which has been discussed as a possible gas-storage material.[7,8] This clathrate network structure had been predicted for silicates but has been observed only in this nitride compound so far. However, compared with oxosilicates or nitridophosphates, only a few oxonitridophosphates have been synthesized so far. This is due to fundamental difficulties concerning their synthesis and the often poor crystallinity of the reaction products. Thus, the structure determination of these compounds requires a combination of different analytical methods such as X-ray diffraction, solid-state NMR spectroscopy, or electron microscopy. Nevertheless, several important representatives of the class of oxonitridophosphates have already been described. In addition to the layer compounds $M^{II}P_6O_6N_8$ (M^{II} = Sr, Ba),[9,10] $M^{I}_2M^{II}_2P_3O_9N$ (M^{I} = Na; M^{II} = Mg, Mn, Fe, Co),[11] $M^{I}_3M^{III}P_3O_9N$ (M^{I} = Na, K; M^{III} = Al, Ga, In, Ti, V, Cr, Mn, Fe),[12] $Cs_3M^{II}_2P_6O_{17}N$ (M^{II} = Mg, Fe, Co),[13] and SrP_3N_5O,[14] the compounds $Li_xH_{x-y+z}[P_{12}O_yN_{24-y}]X_z$ (X = Cl, Br)[15] $Ba_{19}P_{36}O_{6+x}N_{66-x}Cl_{8+x}$[16] exhibit uncommon frameworks and represent the first nitridic zeolite-like network types NPO and NPT, respectively. This suggests that the structural chemistry of oxonitridophosphates has immense potential. In this contribution, we report on the synthesis and structural elucidation of the novel quinary oxonitridophosphate $CaMg_2P_6O_3N_{10}$ with an unprecedented tetrahedral network structure constructed from vertex-sharing $P(O,N)_4$ tetrahedra.

5.2 Results and Discussion

5.2.1 Synthesis

Almost all known oxonitridophoshates have been synthesized by conventional solid-state reactions.[17] In contrast, the synthesis of $CaMg_2P_6O_3N_{10}$ requires high-pressure conditions. So far, only two oxonitridophosphates, namely $M^{II}P_6O_6N_8$ (M^{II} = Sr, Ba), have been synthesized under such high-pressure conditions.[9,10] $CaMg_2P_6O_3N_{10}$ was obtained by using a Walker-type multianvil assembly[18] at 8 GPa and 1100 °C starting from stoichiometric amounts of $Ca(N_3)_2$, Mg_3N_2, P_3N_5, and PON [Eq. 5.1].

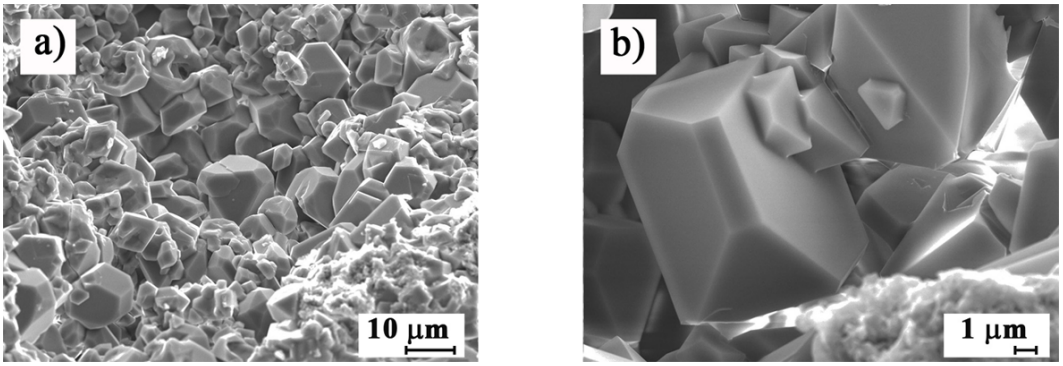

Figure 5.1: SEM images of crystals of $CaMg_2P_6O_3N_{10}$.

$$3Ca(N_3)_2 + 2Mg_3N_2 + 9PON + 3P_3N_5 \longrightarrow 3CaMg_2P_6O_3N_{10} + 8N_2 \qquad (5.1)$$

A high N_2 partial pressure, which is available by in situ thermolysis of $Ca(N_3)_2$, prevents P_3N_5 from dissociation into elements at reaction temperatures above 1000 °C;[19] under ambient pressure, P_3N_5 already dissociates into elements at temperatures above 850 °C. By adding small amounts of NH_4Cl to the mixture of starting materials, colorless crystals in the form of morphologically well-developed truncated octahedra were obtained and isolated (see Figure 5.1). Thus, the addition of NH_4Cl as a mineralizer helps to overcome the main problem of the poor crystallization of oxonitridophosphates mentioned above. As discussed previously, HCl, formed as an intermediate, presumably enables reversible bond cleavage and re-formation, and thus facilitates the growth of single crystals.[20] Detailed information on the synthesis of $CaMg_2P_6O_3N_{10}$ is given in the Experimental Section.

5.2.2 Crystal Structure Determination

The crystal structure of $CaMg_2P_6O_3N_{10}$ was solved and refined from the single-crystal X-ray diffraction data in the tetragonal space group $I4_1/acd$. For crystal structure refinement the values of the lattice parameters obtained from the Rietveld refinement were used. It was possible to refine significant site occupancies for the mixed O/N positions. All atoms were refined anisotropically. The crystallographic data of $CaMg_2P_6O_3N_{10}$ are summarized in the Experimental Section and the atomic parameters are given in Table 5.1.

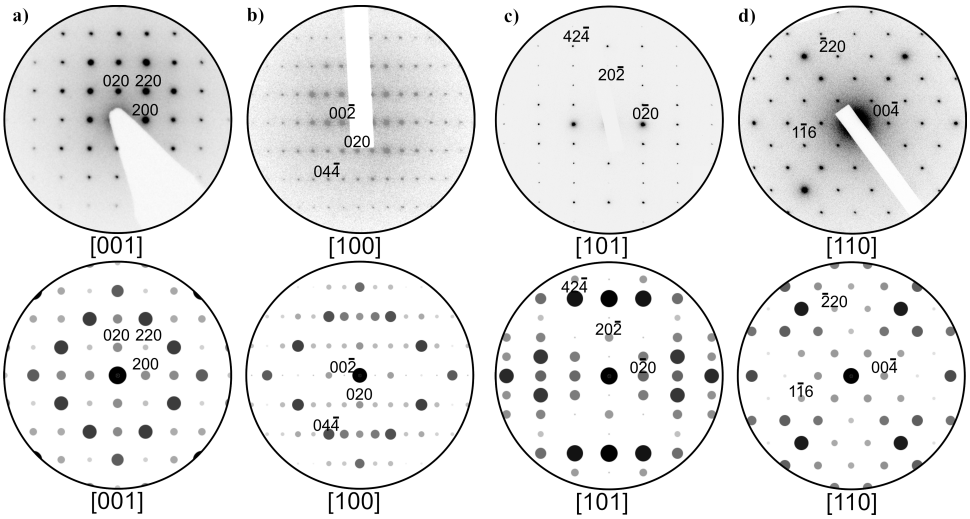

Figure 5.2: Experimental (top) SAED patterns with corresponding simulations (bottom, based on the single-crystal X-ray diffraction data) for $CaMg_2P_6O_3N_{10}$, obtained from different crystallites; exemplary reflections in the selected zero plains are labeled with indices.

Because some displacement parameters and interatomic distances appeared unusual (see below), TEM investigations were performed to verify the structure derived from the X-ray diffraction data. The reflection positions and intensities of the SAED (selected area electron diffraction) patterns (Figure 5.2) of different crystallites of $CaMg_2P_6O_3N_{10}$ matched the calculated ones, which proves the tetragonal metrics, the four-fold axis (Figure 5.2, a), and the reflection conditions ($h + k + l = 2n$) of the body-centered Bravais lattice. Systematic absences due to glide planes (a, c, d) are evident in the corresponding zone-axis patterns (Figure 5.2, a–d).

Significant features in the HRTEM image simulations match well the experimental data (Figure 5.3) and thus corroborate the structure model of $CaMg_2P_6O_3N_{10}$. In a structure projection along [713] the Ca atom positions appear as rows that strongly influence the image contrast. This is strongly affected by the Ca2 site (oblate displacement ellipsoid, see below). There are no indications of superstructures and there is no characteristic mismatch.

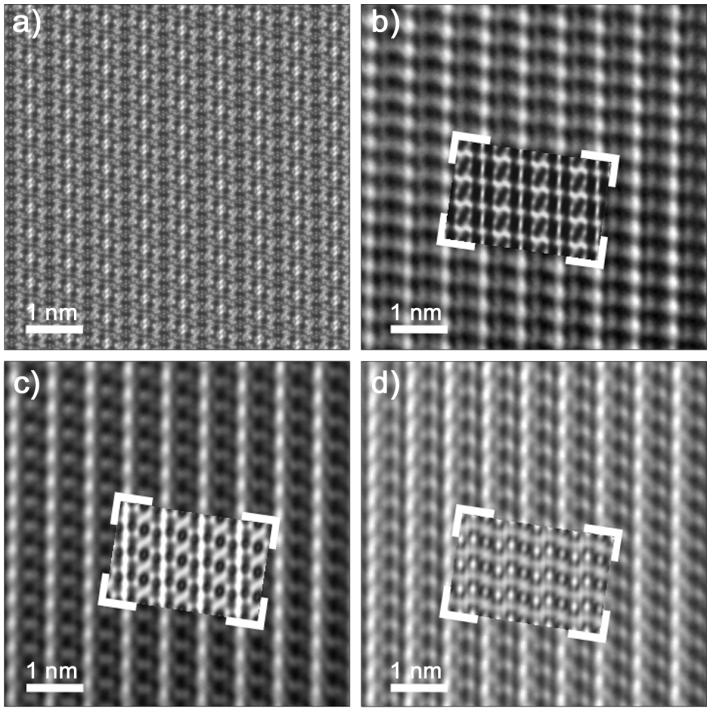

Figure 5.3: a) Projected potential and b-d) HRTEM images of $CaMg_2P_6O_3N_{10}$ along the <713> zone axis with image simulations (accelerating voltage: 300 keV, C_s = 0.6 mm, spread of focus: 3.6 nm, beam semiconvergence: 17 mrad, layer thickness two unit cells). Insets: defocus values: b) –70, c) –43, and d) –28 nm.

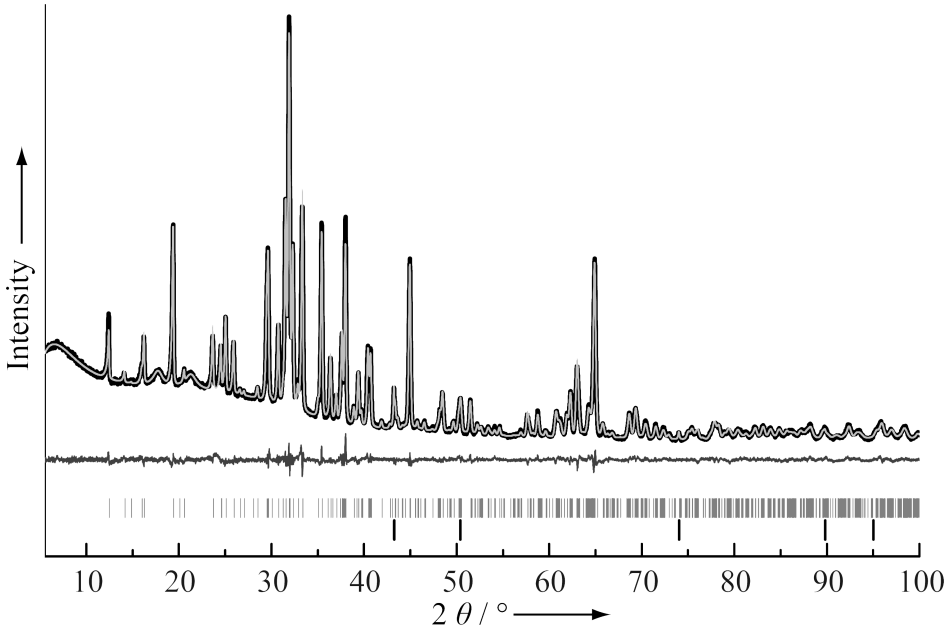

Figure 5.4: Observed (black line) and calculated (light-gray line) X-ray powder diffraction pattern, positions of Bragg reflections ($CaMg_2P_6O_3N_{10}$: vertical gray bars; c-BN: vertical bold bars), and difference profile for the Rietveld refinement of $CaMg_2P_6O_3N_{10}$ (dark-gray line).

Table 5.1: Fractional atomic coordinates, isotropic displacement parameters, and occupation of crystallographic positions of $CaMg_2P_6O_3N_{10}$; standard deviations in parentheses.

atom	Wyck.	*x*	*y*	*z*	U_{eq} / Å^2	occupancy
Ca1	8*a*	1/2	1/4	1/8	0.0086(3)	1.0
Ca2	8*b*	1	3/4	3/8	0.0590(9)	1.0
Mg1	32*g*	0.34412(11)	0.06404(12)	0.04286(7)	0.0128(3)	1.0
P1	32*g*	0.60101(8)	0.02018(8)	0.08042(5)	0.0052(2)	1.0
P2	32*g*	0.74435(8)	0.19018(8)	0.08350(4)	0.0053(2)	1.0
P3	32*g*	0.58898(7)	0.18157(8)	-0.00049(5)	0.0053(2)	1.0
N1	32*g*	0.6603(3)	0.2566(3)	0.04283(19)	0.0070(7)	1.0
N2/O2	32*g*	0.7981(3)	0.2733(2)	0.12829(16)	0.0072(8)	0.86(3)/0.14(3)
N3	32*g*	0.6724(3)	0.1035(3)	0.11819(15)	0.0069(7)	1.0
N4	32*g*	0.5260(3)	0.0931(3)	0.03859(18)	0.0061(7)	1.0
N5/O5	32*g*	0.8376(3)	0.1259(3)	0.04907(15)	0.0106(9)	0.76(4)/0.24(4)
N6/O6	16*d*	1/2	1/4	-0.0330(2)	0.0103(13)	0.76(7)/0.24(7)
O7	32*g*	0.6717(2)	-0.0534(2)	0.04400(14)	0.0106(6)	1.0

Significant contrast changes (in simulations and experiments) occur when the defocus values are altered by more than around 3 nm or when the thickness changes by more than around 5 nm, but also when the Ca atom positions are shifted by more than around 0.05 Å. The Rietveld refinement of the powder X-ray data confirmed the presence of a single-phase product corresponding to the crystal structure of $CaMg_2P_6O_3N_{10}$, as determined from the single-crystal data (see Figure 5.4); traces of cubic boron nitride (c-BN, 6%) correspond to residual amounts of the boron nitride capsule. Detailed information on the crystallographic data of the Rietveld refinement of $CaMg_2P_6O_3N_{10}$ can be found in Tables D.1 and D.1 in the Supporting Information. The absence of N–H groups in the title compound was confirmed by FTIR spectroscopy (see Figure D.1 in the Supporting Information). The chemical composition of the product was confirmed by energy-dispersive X-ray (EDX) spectroscopy; no elements other than Ca, Mg, P, O, and N were detected. The determined atomic ratio of Ca/O/P is in good agreement with the stoichiometric formula $CaMg_2P_6O_3N_{10}$ (see Table 5.3), and although the determination of N and P is less reliable, it is in the correct range.

5.2.3 Structure Description

The crystal structure of $CaMg_2P_6O_3N_{10}$ consists of a three-dimensional network of vertex-sharing Q^4- and Q^3-type $P(O,N)_4$ tetrahedra in the ratio Q^4 / Q^3 = 3:1, leading to a degree of condensation κ = n(P) / n(O,N) = 0.46 for the $[P_6O_3N_{10}]^{6-}$ substructure. The Q^3-type $P(O,N)_4$ tetrahedra are composed of two singly bridging $N^{[2]}$ atoms, one singly bridging $(O,N)^{[2]}$ atom, and one terminal $O^{[1]}$ atom. Figure 5.5 (a) shows the unit cell of $CaMg_2P_6O_3N_{10}$, one polyhedral building unit (PBU, light-gray

tetrahedra) is highlighted. It contains all the P, N, and O positions and is thus well suited to describing the whole structure. The interconnected PBUs form a three-dimensional network (Figure 5.5, b). As shown in Figure 5.7, the PBU consists of vertex-sharing $P(O,N)_4$ tetrahedra forming condensed *dreier* and *sechser* rings, each *dreier* ring unit containing one Q_3-type $P(O,N)_4$ tetrahedron with one terminal $O^{[1]}$ atom. This condensation results, in turn, in a truncated tetrahedron, with the centers of the $P(O,N)_4$ tetrahedra located at the vertices. The center of the PBU is occupied by a Ca1 atom. This PBU is connected to other PBUs through two singly bridging (N/O) atoms in each dreier ring to form a vierer ring (see Figure 5.7, c). Thus, a three-dimensional network structure containing channels filled with Ca and Mg atoms is formed (see Figure 5.5). The topology of this network, determined by the TOPOS software,[21] is represented by the point symbol $(3.4.5.6^2.8)_2(3.6^2)$ and has not been found in any other known compound so far. Furthermore, when taking a closer look at the structure, it becomes apparent that the interconnected PBUs in the structure of $CaMg_2P_6O_3N_{10}$ form two-fold interpenetrated network (see Figure 5.6).

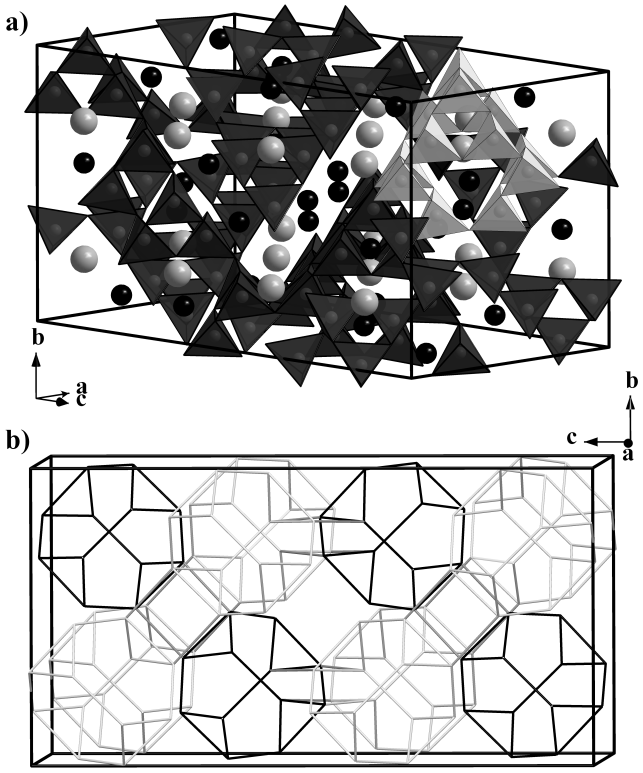

Figure 5.5: a) Crystal structure of $CaMg_2P_6O_3N_{10}$ viewed along [-9,2,17]. Ca atoms are gray, Mg atoms are black, the $P(O,N)_4$ tetrahedra are dark gray, and the characteristic building block is shown in light gray. b) Topological representation of the unit cell. Dark PBUs in unit cell, light gray PBUs partially outside unit cell along [100]. Each connecting line represents a P−N−P bond, cf. Figure 5.7.

The bond lengths P−(O,N) range between 1.541(3) and 1.652(4) Å, and are in the range of those usually observed in other oxonitridophosphates.[9–14] As expected, the P−$(O,N)^{[2]}$ bond lengths within a Q^4-type $P(O,N)_4$ tetrahedron [1.601(3)−1.631(4) Å] involving a singly bridging $O^{[2]}$ are significantly longer than the P−$O^{[1]}$ bond lengths [1.541(3) Å] in Q^3-type $P(O,N)_4$ tetrahedra. The angles (O,N)−P−(O,N) vary between 106.1(2) and 114.1(2) °, and thus differ slightly from the regular tetrahedral angle. The range of P−(O,N)−P angles [114.9(2)–124.0(2) °] is typical of oxonitridophosphate networks. Selected bond lengths and angles are given in Table 5.2.

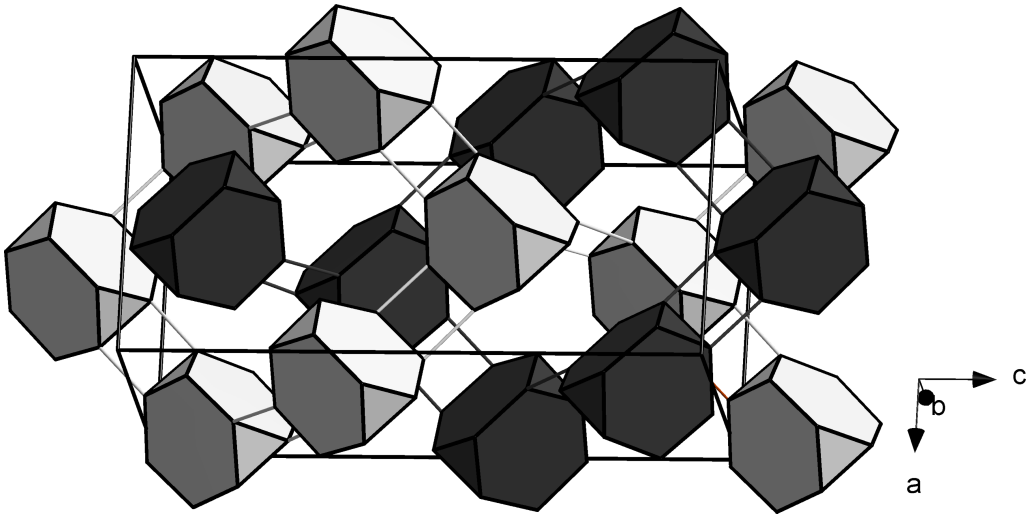

Figure 5.6: Two interrelated strands of PBUs (black and light gray) in the crystal structure of $CaMg_2P_6O_3N_{10}$ forming two-fold interpenetrated network.

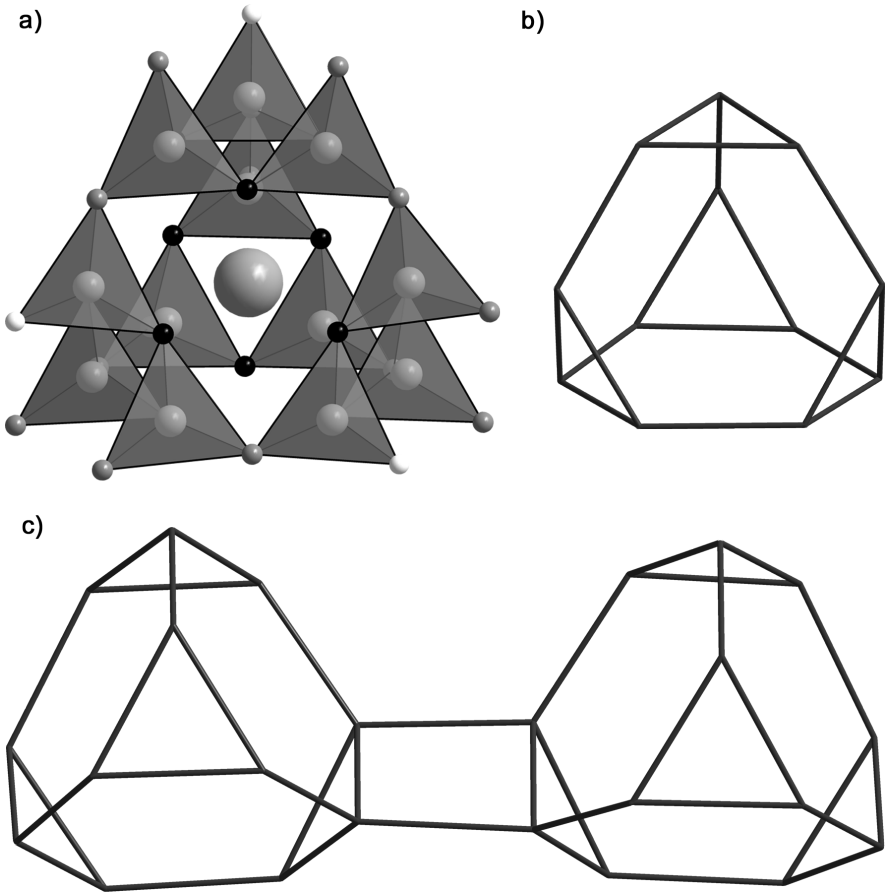

Figure 5.7: a) PBU of the structure of $CaMg_2P_6O_3N_{10}$ consisting of $P(O,N)_4$ tetrahedra (gray: Ca atom; black: N atoms; dark gray: N/O atoms; white: O atoms). b) Topological representation of the characteristic building unit. Each connecting line represents a P–N–P bond. c) Topological representation of two interconnected characteristic building blocks. Each connecting line represents a P–N–P bond.

The crystal structure contains two independent crystallographic Ca and one Mg position, the coordination spheres of which are shown in Figure 5.8. The two Ca positions exhibit remarkably different coordination polyhedra. The Ca1 position is coordinated by 12 N atoms that form a slightly distorted cuboctahedron (see Figure 5.8, left). Thus, $CaMg_2P_6O_3N_{10}$ is, to the best of our knowledge, the first compound with Ca atoms coordinated directly by such a large number of N atoms. The Ca−N distances in this cuboctahedron vary between 2.797(4) and 2.856(4) Å and are in good agreement with Ca−N distances in other known compounds as well as with the sum of the ionic radii.[22–24] The Ca2 position is coordinated by six O/N atoms at distances of 2.184(5)–2.541(4) Å in a distorted octahedral arrangement. These distorted $Ca(O,N)_6$ octahedra are not connected to any other metal-atom-centered polyhedra. Figure 5.8 (right) shows that the displacement ellipsoid Ca2 is rather oblate. This follows from significantly different Ca−(O/N) distances in the $Ca(O/N)_6$ octahedron. Although the Ca−(N6/O6) distances [2.184(5) Å] in the axial positions are very short, the Ca−(N2/O2) distances in the equatorial positions [2.541(3) Å] correspond to those in other known calcium compounds (2.365–3.001 Å).[22–25] Thus, the very short Ca2−N6/O6 distance [2.184(5) Å], based on the sum of the ionic radii (Ca−O: 2.35 Å; Ca−N: 2.46 Å),[22] is not real, but results from the average position of a disordered Ca2 atom that is randomly displaced from the center of the distorted octahedron.

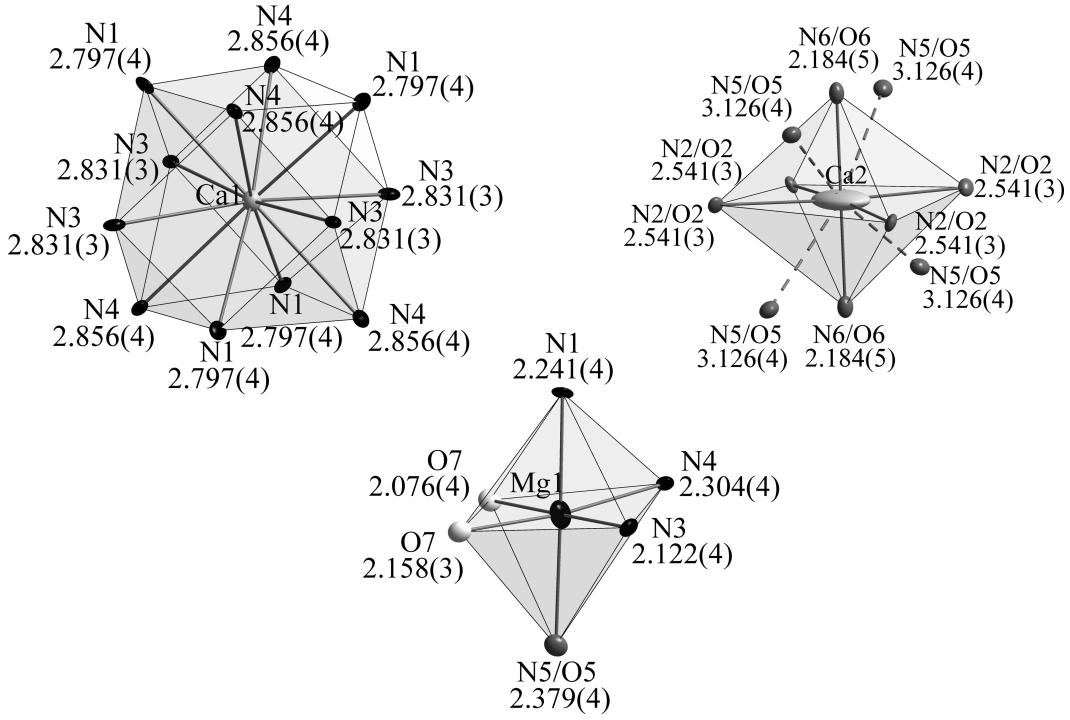

Figure 5.8: Coordination polyhedra and corresponding bond lengths / Å of the Ca1 position (left), the Ca2 position (right), and the Mg1 position (bottom); ellipsoids are drawn with a probability factor of 70%.

In the second coordination sphere, the Ca2 atom is coordinated by four N5/O5 atoms in a slightly distorted square-planar arrangement with a distance of 3.126(4) Å. The Mg1 position is hexacoordinated by one O5/N5 atom, two terminal $O^{[1]}$ atoms, and three N atoms in a slightly distorted octahedron (see Figure 5.8, bottom). The Mg−(O,N) distances range between 2.076(4) and 2.379(4) Å, and correspond to those in other magnesium compounds as well as to the sum of the ionic radii.[22,23,26,27] Two $Mg(O,N)_6$ octahedra are interconnected by two terminal $O^{[1]}$ atoms through a common edge to form $Mg_2(O,N)_{10}$ octahedron pairs. These pairs, in turn, interconnect with the CaN_{12} cuboctahedra through half of the latter's triangular faces (see Figure 5.9).

Table 5.2: Selected bond lengths / Å and bond angles / ° in the crystal structure of $CaMg_2P_6O_3N_{10}$; standard deviations in parentheses.

bond lengths / Å		bond angles / °	
P1−N2/O2	1.622(4)	O7−P1−N2/O2	111.7(2)
P1−N3	1.638(4)	O7−P1−N3	112.0(2)
P1−N4	1.642(4)	N2/O2−P1−N3	109.2(2)
P1−O7	1.541(3)	O7−P1−N4	108.6(2)
P2−N1	1.651(4)	N2/O2−P1−N4	108.4(2)
P2−N2/O2	1.631(4)	N3−P1−N4	106.8(2)
P2−N3	1.631(3)	N2/O2−P2−N3	108.9(2)
P2−N5/O5	1.634(4)	N2/O2−P2−N5/O5	110.3(2)
P3−N1	1.652(4)	N3−P2−N5/O5	108.6(2)
P3−N4	1.644(4)	N2/O2−P2−N1	108.8(2)
P3−N6/O6	1.601(3)	N3−P2−N1	106.2(2)
P3−N5/O5	1.630(4)	N5/O5−P2−N1	114.1(2)
		N6/O6−P3−N5/O5	106.1(2)
		N6/O6−P3−N4	107.4(2)
		N5/O5−P3−N4	112.5(2)
		N6/O6−P3−N1	111.8(2)
		N5/O5−P3−N1	112.3(2)
		N4−P3−N1	106.7(2)

5.2.4 Bond-Valence Sum Calculations

The structure model of $CaMg_2P_6O_3N_{10}$ and, in particular, the local displacements of Ca2 can be confirmed by bond-valence sum (BVS) calculations (see Table 5.3).[28] The deviations between the bond-valence sum and the oxidation state are in the range of 5%, with the exception of the average Ca2 position and N6/O6 (occupied by 86% N and 14% O), which is at a very short distance from it.

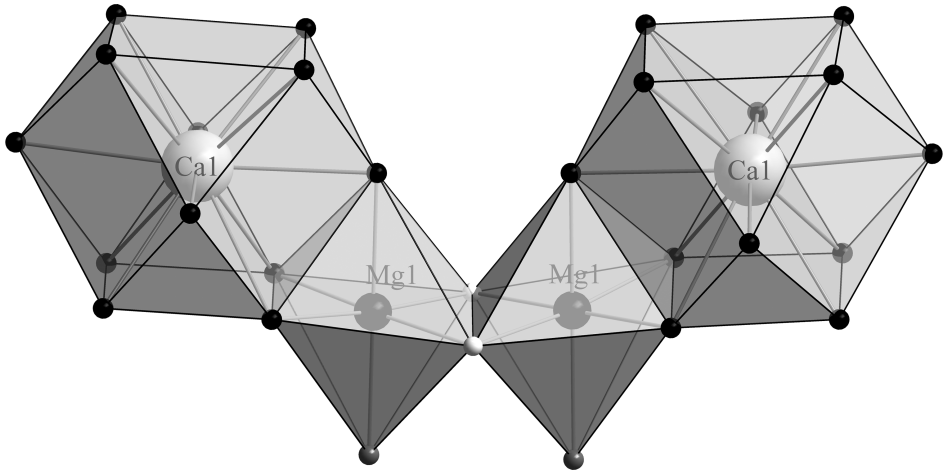

Figure 5.9: Representation of edge-sharing $Mg(O,N)_6$ octahedra sharing faces with CaN_{12} cuboctahedra.

At this distance, Ca2 would have a BVS of 3.1, and the values calulated for both N6 (3.54) and O6 (2.64) are also higher than their formal charge. This unfavorable situation is avoided by a displacement of Ca2 from the average position. This leads to longer interatomic distances and thus lower and more reasonable BVS values, and thus explains the oblate displacement ellipsoid (see Figure 5.8).

Table 5.3: Bond-valence sum values for $CaMg_2P_6O_3N_{10}$.

atom	Ca1	Ca2	Mg	P1	P2	P3	N1	N3
BVS	1.9	3.1	1.95	4.84	4.73	4.78	2.81	2.89
oxidation state	2	2	2	5	5	5	3	3
atom	N4	N2	O2	N5	O5	N6	O6	O1
BVS	2.83	2.83	2.18	2.74	2.12	3.54	2.64	1.86
oxidation state	3	3	2	3	2	3	2	2

5.2.5 Lattice Energy Calculations (MAPLE)

Taking into account exclusively electrostatic interactions in an ionic crystal, which depend on the charge, distance, and coordination spheres of the constituting ions, the Madelung part of the lattice energy (MAPLE) was calculated (Table 5.4).[22,29–31] The overall MAPLE value of $CaMg_2P_6O_3N_{10}$ (166621 $kJ \cdot mol^{-1}$) is in good agreement with the sum of those of the binary compounds that formally constitute the quinary compound (CaO[32] + $2MgO$[33] + $2P_3N_5$,[34] overall MAPLE value

166917 kJ·mol^{-1}). The negligible deviation of 0.2% confirms the electrostatic consistency of the refined crystal structure despite the expectedly rather different partial MAPLE values of the Ca1 and Ca2 positions. The difference between the partial MAPLE values of the Ca1 and Ca2 positions reflects the same discrepancy for Ca2 as its BVS value. The partial MAPLE values of the Mg, P, and O$^{[1]}$ atoms are congruent with reference values, whereas those of the N$^{[2]}$ atoms are slightly larger. As expected, the partial MAPLE values of the mixed O$^{[2]}$/N$^{[2]}$ positions range between those of the N$^{[2]}$ and O$^{[1]}$ sites.

Table 5.4: Partial MAPLE values and MAPLE sums / kJ·mol^{-1} of $CaMg_2P_6O_3N_{10}$.

$CaMg_2P_6O_3N_{10}$ [a]		model	
Ca1	1969	+1	CaO[32]
Ca2	2515	+2	MgO[33]
Mg1	2639	+2	P_3N_5[34]
P1	14708		
P2	14589		
P3	14571		
N1	6338		
N2/O2	5456		
N3	6339		
N4	6235		
N5/O5	5429		
N6/O6	5470		
O7	2572		
$\sum$ = 166621		$\sum$=166917	
		Δ=0.2%	

[a] Typical partial MAPLE values / kJ·mol^{-1}: Ca: 1700−2200[3,24]; Mg: 2263−2640,[23,35] P: 14422−15580; (N$^{[2]}$): 4600−6000; (O$^{[1]}$): 2000−2800.[3,19,36]

5.3 Conclusion

$CaMg_2P_6O_3N_{10}$ represents a novel oxonitridophosphate with an unprecedented network of tetrahedra. It is the first known compound with a twelve-fold N coordination of Ca atoms. Single crystals of $CaMg_2P_6O_3N_{10}$ were obtained and isolated by adding small amounts of NH_4Cl to the starting mixture. The high-pressure high-temperature synthesis appears to be a very promising route for the synthesis of new oxonitridophosphates with interesting structural properties. Moreover, single crystals of oxonitridophosphates, obtained by this route, may significantly accelerate structural investigations in the future.

5.4 Experimental Section

5.4.1 Preparation of Starting Materials

$Ca(N_3)_2$ was synthesized by stirring a suspension of ammonium azide with $Ca(OH)_2$ (Merck, p.a.). **Caution:** Special care is necessary when handling even dilute solutions of HN_3 because it is potentially explosive and the vapor is highly poisonous upon inhalation. Precautions have to be made that no volatile pure (boiling point 60 °C) or highly concentrated HN_3 can condense onto cool surfaces. After filtration, the solvent was evaporated under reduced pressure (90 mbar, 70 °C).[37] Finally, the colorless solid of $Ca(N_3)_2$ was recrystallized from acetone and dried in vacuo over P_4O_{10}.[38] The final product was stored under the exclusion of moisture and oxygen.

NH_4N_3 was synthesized by treating equimolar amounts of NH_4NO_3 (Grüssing, reinst) and NaN_3 (Acros Organics, 99%) in a Schlenk tube with one open end located outside the furnace and slowly heating (50 °C/h) the mixture to 200 °C.[39]

P_3N_5 was prepared starting from $(PNCl_2)_3$ (Merck, p.s.) in a corundum boat in a continuous flow of dried NH_3 (Messer, Griesheim, 3.8), as described in the literature.[40–42] PON was synthesized by heating a mixture of one part $PO(NH_2)_3$ and three parts NH_4Cl in a continuous flow of nitrogen at 680 °C. The process is detailed in the literature.[9]

5.4.2 Synthesis

$CaMg_2P_6O_3N_{10}$ was synthesized by using a modified Walker-type multianvil apparatus[18] starting from stoichiometric amounts of $Ca(N_3)_2$, Mg_3N_2, P_3N_5, and PON with small amounts of NH_4Cl (20.0 mg) as mineralizer. All manipulations were carried out under the exclusion of oxygen and moisture in an argon-filled glove-box (Unilab, Mbraun, Garching, $O_2 < 1$ ppm, $H_2O < 0.1$ ppm). The mixture of starting materials was thoroughly ground and tightly packed into a cylindrical capsule made of hexagonal boron nitride (Henze, Kempten) and sealed with a hexagonal boron nitride cap. By using two MgO spacers (TechniKer, Küps,Germany), the capsule was centered in the middle of a Cr_2O_3-doped MgO octahedron (edge length 18 mm, Ceramic Substrates & Components Ltd, Isle of Wight), which served as a pressure medium. This MgO octahedron was equipped with a ZrO_2 tube (Cesima Ceramics, Wust-Fischbach, Germany) as thermal insulator as well as graphite tubes, which were used as electrical resistance furnaces. To achieve good electrical contact between the graphite tubes and tungsten carbide cubes, two plates of molybdenum were used. The octahedron was then placed at the center of an assembly of eight truncated tungsten carbide cubes (truncation edge lengths

Table 5.5: Selected crystallographic data of the single-crystal structure determination of $CaMg_2P_6O_3N_{10}$; standard deviations in parentheses.

formula	$CaMg_2P_6O_3N_{10}$
crystal system	tetragonal
space group	$I4_1/acd$ (no. 142)
lattice parameters / Å	a = 12.494(1)
	c = 23.747(2)
cell volume / Å^3	3707.0(5)
formula units per cell	16
calculated X-ray density / g·cm^{-1}	3.316
linear absorption coefficient / mm^{-1}	1.888
radiation	Mo-Kα (λ = 0.71073 Å)
temperature / K	295
F(000)	3648.0
θ-range / °	$2.87 \leq \theta \leq 27.50$
total no. of reflections	9483
independent reflections	1068 [R_{int} = 0.0674]
refined parameters	104
goodness of fit	0.904
R_1 (all data); R_1 ($F^2 > 2\sigma(F^2)$)	0.0736; 0.0381
wR_2 (all data); wR_2 ($F^2 > 2\sigma(F^2)$)	0.0727; 0.0659
$\Delta\rho_{max}$, $\Delta\rho_{max}$ (e·Å^{-3})	1.463, -1.126

11 mm, Hawedia, Marklkofen, Germany), which were separated with pyrophyllite gaskets. Detailed information on the construction of the described multianvil assembly can be found in literature.[18] The sample was compressed up to 8 GPa at room temperature. Then it was heated up to 1100°C within 60 min. This temperature was held constant for 60 min and subsequently the sample was cooled to room temperature. After slow decompression (10 h), the sample was isolated as a light-gray solid, which was not sensitive to air and moisture. NH_4Cl was removed from the product by washing it with water and ethanol.

5.4.3 Single-Crystal X-Ray Diffraction

Single-crystal diffraction data were collected with a STOE IPDS I diffractometer (Mo-Kα radiation, graphite monochromator). A semi-empirical absorption correction was applied by using the XPREP program.[43] The crystal structure was solved by direct methods with SHELXS.[44] The structure was refined by the full-matrix least-squares method by using SHELXL.[44] Crystal data for $CaMg_2P_6O_3N_{10}$ are presented in Table 5.5. Further details on the crystal structure investigations may be obtained from the Fachinformationszentrum Karlsruhe, Germany, 76344 Eggenstein-Leopoldshafen,

Germany (fax: +49-7247-808-666; e-mail: crysdata@fiz-karlsruhe.de), on quoting the depository number CSD-427175.

5.4.4 Transmission Electron Microscopy

Ground samples were dispersed in absolute ethanol and drop-cast onto copper grids coated with a holey carbon film (S166–2, Plano GmbH, Germany). The grids were fixed on a double-tilt holder. SAED, HRTEM, and EDX measurements were taken with a Titan 80–300 (FEI, USA) with a field emission gun operated at 300 kV, equipped with a TEM TOPS 30 EDX spectrometer (EDAX, Germany). Images were recorded by using an UltraScan 1000 camera (Gatan, USA, resolution: 2k×2k). In addition, SAED and EDX measurements were taken with a JEOL 2010 instrument (JEOL, Germany) with a thermal emitter operated at 200 keV, equipped with a EDAX Apollo XLT EDX detector (EDAX Germany). Images were recorded by using a TemCam F216 camera (TVIPS, Germany, resolution. 2k×2k). HRTEM and SAED data were evaluated by using the Digital Micrograph,[45] Process Diffraction 7[46] and JEMS programs,[47] and EDX data were processed with ES Vision[48] and EDAX TEAM.[49]

5.4.5 Powder X-Ray Diffraction

Powder diffraction data were collected with a HUBER G670 diffractometer [Cu-Kα_1 radiation, monochromator: Ge(111)] in Guinier geometry. Simulations of Bragg data were performed by using the WINXPOW program package[50] on the basis of the single-crystal structural data. Rietveld refinement was carried out by using the TOPAS-Academic package.[51]

5.4.6 FTIR Spectroscopy

The FTIR spectrum of $CaMg_2P_6O_3N_{10}$ was recorded in a KBr pellet with a Spectrum BX II spectrometer (Perkin–Elmer, Waltham MA, USA).

5.4.7 Scanning Electron Microscopy and Energy-Dispersive X-Ray Spectroscopy

SEM images and EDX spectra were acquired by using a JEOL JSM-6500F field emission scanning electron microscope (SEM) operated at 15 kV, equipped with a Si/Li EDX detector 7418 (Oxford Instruments). To provide electrical conductivity on the sample surface, it was coated with carbon using an electron beam evaporator (BAL-TEC MED 020, Bal Tec AG).

5.5 References

[1] F. Liebau, *Structural Chemistry of Silicates: Structure, Bonding,and Classification*, Springer, Berlin, Germany, **1985**.

[2] A. K. Cheetham, G. Férey, T. Loiseau, *Angew. Chem. Int. Ed.* **1999**, *38*, 3268–3292; *Angew. Chem.* **1999**, *111*, 3466.

[3] M. Zeuner, S. Pagano, W. Schnick, *Angew. Chem. Int. Ed.* **2011**, *50*, 7754; *Angew. Chem.* **2011**, *123*, 7898.

[4] a) H. A. Höppe, *Angew. Chem. Int. Ed.* **2009**, *48*, 3572; *Angew. Chem.* **2009**, *121*, 3626–3636; b) W. Schnick, *Phys. Status Solidi RRL* **2009**, *3*, A113.

[5] W. Schnick, *Angew. Chem. Int. Ed. Engl.* **1993**, *32*, 806; *Angew. Chem.* **1993**, *105*, 846.

[6] H. Huppertz, W. Schnick, *Angew. Chem. Int. Ed. Engl.* **1996**, *35*, 1983–1984; *Angew. Chem.* **1996**, *108*, 2115.

[7] F. Karau, W. Schnick, *Angew. Chem. Int. Ed.* **2006**, *45*, 4505; *Angew. Chem.* **2006**, *118*, 4617.

[8] M. Pouchard, *Nature* **2006**, *442*, 878.

[9] S. J. Sedlmaier, J. Schmedt auf der Günne, W. Schnick, *Dalton Trans.* **2009**, 2081.

[10] S. J. Sedlmaier, D. Weber, W. Schnick, *Z. Kristallogr. New Cryst. Struct.* **2012**, *227*, 1.

[11] R. Conanec, W. Feldmann, R. Marchand, Y. Laurent, *J. Solid State Chem.* **1996**, *121*, 418.

[12] W. Feldmann, *Z. Chem.* **1987**, *27*, 100.

[13] W. Feldmann, P. L. Haridon, R. Marchand, *J. Solid State Chem.* **2000**, *153*, 185.

[14] S. J. Sedlmaier, E. Mugnaioli, O. Oeckler, U. Kolb, W. Schnick, *Chem. Eur. J.* **2011**, *17*, 11258.

[15] a) S. Correll, O. Oeckler, N. Stock, W. Schnick, *Angew. Chem. Int. Ed.* **2003**, *42*, 3549; *Angew. Chem.* **2003**, *115*, 3674; b) S. Correll, N. Stock, O. Oeckler, J. Senker, T. Nilges, W. Schnick, *Z. Anorg. Allg. Chem.* **2004**, *630*, 2205.

[16] S. J. Sedlmaier, M. Döblinger, O. Oeckler, J. Weber, J. Schmedt auf der Günne, W. Schnick, *J. Am. Chem. Soc.* **2011**, *133*, 12069.

[17] R. Marchand, W. Schnick, N. Stock, *Adv. Inorg. Chem.* **2000**, *50*, 193.

[18] a) N. Kawai, S. Endo, *Rev. Sci. Instrum.* **1970**, *41*, 1178; b) D. Walker, M. A. Carpenter, C. M. Hitch, *Am. Mineral.* **1990**, *75*, 1020; c) D. Walker, *Am. Mineral.* **1991**, *76*, 1092; d) D. C. Rubie, *Phase Transitions* **1999**, *68*, 431; e) H. Huppertz, *Z. Kristallogr.* **2004**, *219*, 330.

[19] F. W. Karau, L. Seyfarth, O. Oeckler, J. Senker, K. Landskron, W. Schnick, *Chem. Eur. J.* **2007**, *13*, 6841.

[20] A. Marchuk, F. J. Pucher, F. W. Karau, W. Schnick, *Angew. Chem. Int. Ed.* **2014**, *53*, 2469; *Angew. Chem.* **2014**, *126*, 2501.

[21] a) V. A. Blatov, M. O'Keeffe, D. M. Proserpio, *CrystEngComm* **2010**, *12*, 44; b) V. A. Blatov, *IUCr CompComm Newsletter* **2006**, *7*, 4.

[22] R. D. Shannon, *Acta Crystallogr. Sect. A: Found. Crystallogr.* **1976**, *32*, 751.

[23] V. Schultz-Coulon, W. Schnick, *Z. Anorg. Allg. Chem.* **1997**, *623*, 69.

[24] F. Karau, W. Schnick, *Z. Anorg. Allg. Chem.* **2006**, *632*, 231.

[25] M. Y. Chern, D. A. Vennos, F. J. DiSalvo, *J. Solid State Chem.* **1992**, *96*, 415.

[26] S. R. Römer, W. Schnick, *Z. Anorg. Allg. Chem.* **2005**, *631*, 31.

[27] F. Hinze, N. W. Johnson, M. Seibald, D. Muir, A. Moewes, W. Schnick, *Chem. Mater.* **2013**, *25*, 4044.

[28] A. S. Wills, *VaList*, v. 4.0.7, University College London, UK, **2010**.

[29] R. Hoppe, *Angew. Chem. Int. Ed. Engl.* **1970**, *9*, 25; *Angew. Chem.* **1970**, *82*, 7.

[30] R. Hoppe, R. Homann, *Z. Anorg. Allg. Chem.* **1970**, *379*, 193.

[31] R. Hübenthal, MAPLE, *Programm zur Berechnung des Madelunganteils der Gitterenergie*, v. 4, **1993**, University of Gießen,Germany.

[32] W. Primak, H. Kaufman, R. Ward, *J. Am. Chem. Soc.* **1948**, *70*, 2043.

[33] D. Sun, H. Enoki, F. Gingi, E. Akiba, *J. Alloys Compd.* **1999**, *285*, 279.

[34] P. Kroll, W. Schnick, *Chem. Eur. J.* **2002**, *8*, 3530.

[35] A. G. Petukhov, W. R. L. Lambrecht, B. Segall, *Phys. Rev. B* **1994**, *49*, 4549.

[36] L. Boukbir, R. Marchand, Y. Laurent, P. Bacher, *Ann. Chim.* **1989**, *14*, 475.

[37] F. Karau, *Dissertation*, Ludwig-Maximilians-Universität München, Germany, **1994**.

[38] H. D. Fair, R. F. Walker, *Energetic Materials, vol. 1: Physics and Chemistry of the Inorganic Azides*, Plenum Press, New York, **1977**.

[39] W. J. Frierson, *Inorg. Synth.* **1946**, *8*, 146.

[40] J. Lücke, *Dissertation*, Rheinische Friedrich-Wilhelm-Universität Bonn, Germany, **1994**.

[41] W. Schnick, J. Lücke, F. Kumeich, *Chem. Mater.* **1996**, *8*, 281.

[42] S. Horstmann, E. Irran, W. Schnick, *Angew. Chem. Int. Ed. Engl.* **1997**, *36*, 1873; *Angew. Chem.* **1997**, *109*, 1938.

[43] G. M. Sheldrick, *XPREP, Data Preperation & Reciprocal Space Exploration*, v. 6.12, Siemens Analytical X-ray Instruments, **1996**.

[44] G. M. Sheldrick, *Acta Crystallogr., Sect. A: Found. Crystallogr.* **2008**, *64*, 112.

[45] Gatan Software Team, *Digital Micrograph*, v. 3.6.1, Gatan Software, Pleasanton, CA, USA, **1999**.

[46] J. L. Lábár, *Ultramicroscopy* **2005**, *103*, 237.

[47] P. A. Stadelmann, *JEMS*, v. 3.3425U2008, CIME-EPFL, Switzerland, **1999**.

[48] *ES Vision*, v. 4.0.164, Emispec Systems Inc., Tempe, AZ, USA, **1994**.

[49] *TEAM*, v. 3.4.1, EDAX AMETEK, Wiesbaden, Germany, **2013**.

[50] *WINXPOW - Program for powder data handling*, v. 2.21, Stoe & Cie GmbH, Darmstadt, Germany, **2007**.

[51] A. Coelho, TOPAS - *Academic 2007*, Coelho Software, Brisbane, Australia, **2007**.

6 Luminescent Nitridophosphates $CaP_2N_4:Eu^{2+}$, $SrP_2N_4:Eu^{2+}$, $BaP_2N_4:Eu^{2+}$, and $BaSr_2P_6N_{12}:Eu^{2+}$

Florian J. Pucher,[a] Alexey Marchuk,[a] Peter J. Schmidt,[b] Detlef Wiechert,[b] and Wolfgang Schnick*[a]

[a] *Department of Chemistry, University of Munich (LMU), Butenandtstraße 5–13, 81377 Munich, Germany*
[b] *Lumileds Germany GmbH, Philipsstrasse 8, 52068 Aachen, Germany*

published in: *Chem. Eur. J.* **2015**, *21*, 6443-6448. DOI:10.1002/chem.201500047

Abstract

Nitridophosphates $MP_2N_4:Eu^{2+}$ (M = Ca, Sr, Ba) and $BaSr_2P_6N_{12}:Eu^{2+}$ have been synthesized at elevated pressures and 1100−1300 °C starting from the corresponding azides and P_3N_5 with $EuCl_2$ as dopant. Addition of NH_4Cl as mineralizer allowed for the growth of single crystals. This led to the successful structure elucidation of a highly condensed nitridophosphate from single-crystal X-ray diffraction data ($CaP_2N_4:Eu^{2+}$ ($P6_3$, no. 173), a = 16.847(2), c = 7.8592(16) Å, V = 1931.7(6) Å^3, Z = 24, 2033 observed reflections, 176 refined parameters, wR_2 = 0.096). Upon excitation by UV light, luminescence due to parity-allowed $4f^6(^7F)5d^1 \rightarrow$

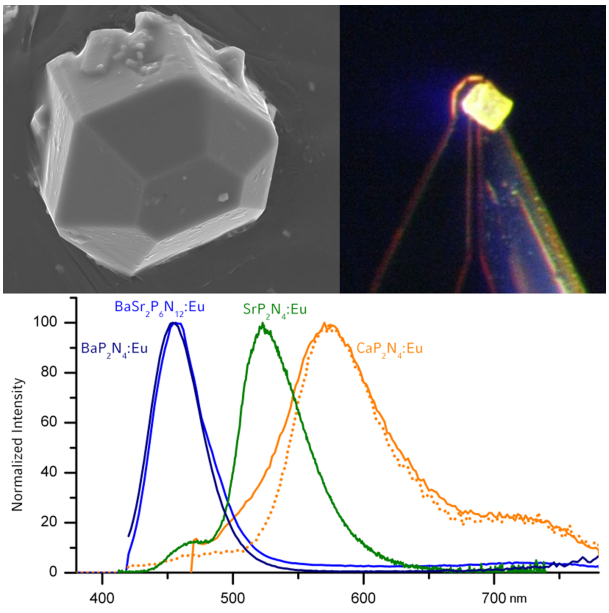

$4f^7(^8S_{7/2})$ transition was observed in the orange ($CaP_2N_4:Eu^{2+}$, λ_{max} = 575 nm), green ($SrP_2N_4:Eu^{2+}$, λ_{max} = 529 nm), and blue regions of the visible spectrum ($BaSr_2P_6N_{12}:Eu^{2+}$ and $BaP_2N_4:Eu^{2+}$, λ_{max} = 450 and 460 nm, respectively). Thus, the emission wavelength decreases with increasing ionic radius of the alkaline-earth ions. The corresponding full width at half maximum values ($2240-2460\ cm^{-1}$) are comparable to those of other known Eu^{2+}-doped (oxo)nitrides emitting in the same region of the visible spectrum. Following recently described quaternary $Ba_3P_5N_{10}Br:Eu^{2+}$, this investigation represents the first report on the luminescence of Eu^{2+}-doped ternary nitridophosphates. Similarly to nitridosilicates and related oxonitrides, Eu^{2+}-doped nitridophosphates may have the potential to be further developed into efficient light-emitting diode phosphors.

6.1 Introduction

Technologies based on luminescence gain more and more importance with increasing efforts to achieve an energy turnaround for sustainability.[1,2] In particular, phosphor-converted light-emitting diodes (pc-LEDs) are sources for lighting and illumination with a high potential to reduce the global energy consumption.[1–8] Accordingly, both improvement of known as well as development of new phosphor materials for pc-LEDs are of great importance.[9–11]

Due to parity-allowed $4f^6(^7F)5d^1 \rightarrow 4f^7(^8S_{7/2})$ transition, Eu^{2+} -doped materials exhibit intense broad band emission upon excitation with UV or blue light.[1,12] In nitridic host lattices, Eu^{2+} luminescence has been observed in the entire visible spectrum ranging from blue to red due to a strong nephelauxetic effect.[2,13] Especially, (oxo)nitrodosilicates and related compounds were identified as promising host lattices for Eu2+ doping.[14–16] These compounds have a high bandgap and are transparent in the entire visible spectrum. Furthermore, there is a manifold of representatives with a high degree of condensation κ (i.e., the atomic ratio Si:(O,N)). These compounds contain highly cross-linked nitridic network structures and thus exhibit remarkable chemical and thermal stability. Prominent examples of (oxo)nitridosilicate LED phosphors are $M\mathrm{Si_2O_2N_2}$:Eu^{2+} and $M_2\mathrm{Si_5N_8}$:Eu^{2+} (M = Ca, Sr, Ba).[5,14,15] General requirements for applicable materials are good chemical and thermal stability accompanied by a small Stokes shift, low thermal quenching, and last but not least high quantum efficiency.[1,5,12–18]

Synthesis of oxides is typically performed under oxidative conditions. In contrast, nitridosilicates can readily be prepared, for example, by condensation reactions of amides or imides and evolution of NH_3,[15] thus leading to advantageous reductive synthesis conditions that enable doping with Eu^{2+}. Condensed classical oxosilicates contain solely corner-sharing SiO_4 tetrahedra with O atoms being either terminally bound or simply bridging between two neighboring Si atoms. However, nitridosilicates and related compounds can exhibit a more varied connectivity with N being either terminally bound to Si or bridging two to four Si atoms.[15] Besides common vertices, even edge sharing of SiN_4 tetrahedra has been observed.[15,19] Consequently, the search for new and improved phosphors has been focused on alkaline-earth (oxo)nitridosilicates doped with Eu^{2+}.[15,17,20–37] However, research also has to be extended to related nitridic compounds such as nitridogallates,[38–40] nitridoaluminates,[40–42] and nitridophosphates.[43,44]

The element combination P/N is isoelectronic with Si/O. Nitridophosphates, which are typically made up of condensed PN_4 tetrahedra, exhibit structural analogies with oxosilicates. However, similarly to nitridosilicates, both corner sharing and edge sharing of $T\mathrm{N_4}$ tetrahedra (T = Si, P) can occur. Binary P_3N_5 as the parent compound of phosphorus nitrides has a high bandgap and has thus been applied in

electronic devices, for example, as gate insulator material in metal–insulator semiconductor field-effect transistors (MISFETs).[45–47] Accordingly, ternary and higher nitridophosphates are expected to exhibit high bandgap values as well. They have a remarkable chemical and thermal stability and are typically transparent and colorless. Analogously to nitridosilicates, they can be synthesized under reducing conditions by condensation reactions evolving NH_3. Thus, Eu^{2+}-doped nitridophosphates can be expected to represent promising new luminescent materials.

Usually, elevated pressures are applied during synthesis to enable reaction temperatures of 1000−1400 °C. Use of metal azides as starting materials besides phosphorus(V) nitride P_3N_5 also lowers the risk of thermal bond dissociation at these temperatures by increasing the nitrogen partial pressure.[48] In the past the obtained nitridophosphates were isolated in the form of crystalline powders, sometimes hampering detailed structure elucidation.[49]

Following our recent work on luminescent nitridophosphate zeolites emitting white light from a single compound,[44] we present herein the first all-nitride luminescent Eu^{2+}-doped nitridophosphates $MP_2N_4:Eu^{2+}$ (M = Ca, Sr, Ba) and $BaSr_2P_6N_{12}:Eu^{2+}$. Additionally, by applying our recently reported method of using NH_4Cl as mineralizer in high-pressure high-temperature synthesis of highly condensed nitridophosphates,[50] we present the first successful structure elucidation of a ternary member of this materials class from conventional single-crystal X-ray diffraction data.

6.2 Results and Discussion

$MP_2N_4:Eu^{2+}$ (M = Ca, Sr, Ba) and the mixed solid solution $BaSr_2P_6N_{12}:Eu^{2+}$ were synthesized from P_3N_5 and the binary metal azides by using a Walker-type multianvil press at 5−8 GPa and 1100−1300 °C, according to Equation (6.1) in which M = Ca, Sr, or Ba.[48,49,51,52] $EuCl_2$ (1−2 mol%) was added as dopant. Notably, employment of europium(II) azide $Eu(N_3)_2$ as dopant led to inhomogeneous samples.

$$3M(N_3)_2 + 2P_3N_5 \longrightarrow 3MP_2N_4 + 8N_2 \tag{6.1}$$

By adding small amounts of NH_4Cl to the starting materials as mineralizer, single crystals of CaP_2N_4 could be obtained and isolated. Structure elucidation confirmed the proposed megacalsilite structure type including the superstructure as described by Karau et al. (Table 6.1).[49,52]

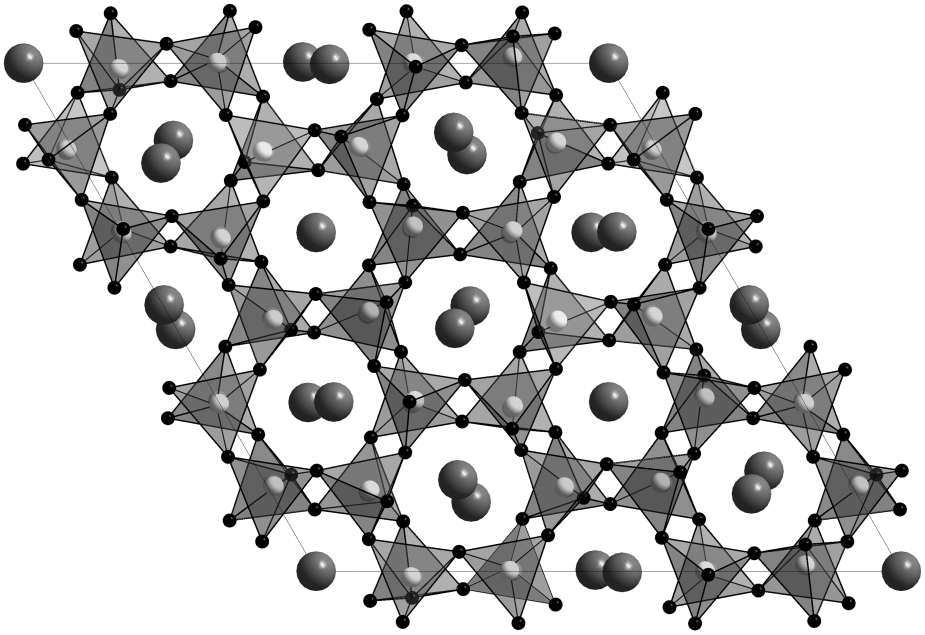

Figure 6.1: Crystal structure of CaP_2N_4, view along [001]. SrP_2N_4 is isostructural.

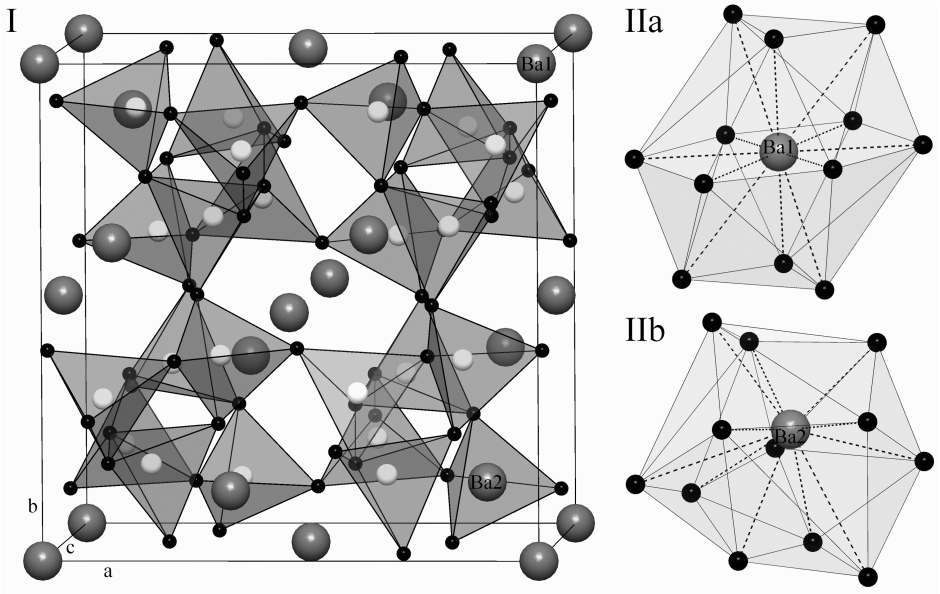

Figure 6.2: Crystal structure of BaP_2N_4, view along [001] (I). In $BaSr_2P_6N_{12}$ the Ba1 site (coordination depicted in IIa) is occupied by Ba, the Ba2 site (coordination depicted in IIb) by Sr.

This is the first known synthesis of single crystals of highly condensed ternary nitridophosphates. In the past, the crystal structure of SrP_2N_4 could only be solved by using a variety of different crystallographic and spectroscopic techniques. Due to the lack of sufficiently large single crystals, structure elucidation and proof of the complicated superstructure was not straightforward.[49] By adding NH_4Cl as a mineralizer, preparation of single-crystalline highly condensed nitridophosphates became possible

Table 6.1: Crystallographic data and details of the structure refinement of CaP_2N_4.

formula	CaP_2N_4
molar mass / g·mol^{-1}	156.06
crystal system	hexagonal
space group	$P6_3$ (no. 173)
lattice parameters / Å	$a = b$ = 16.847(2)
	c = 7.8592(16)
cell volume / Å^3	1931.7(6)
formula units per cell	24
diffractometer	Nonius Kappa CCD
temperature / K	293(2)
radiation	Mo-Kα (λ = 0.71073 Å)
radiation	Mo-Kα (λ = 0.71073 Å)
calculated X-ray density / g·cm^{-1}	1.766
crystal size / mm^3	0.04×0.03×0.03
linear correction / mm^{-1}	none
θ-range / °	$3.55 \leq \theta \leq 27.49$
index range	$-21 \leq h \leq 21$
	$-21 \leq k \leq 21$
	$-10 \leq l \leq 10$
refined parameters	176
twin law	010 100 001 -4
BASF	0.36400 0.15531 0.10043
observed reflections	14110
independent reflections	2085
observed reflections	2033
min./max. residual electron density [e Å^{-3}]	-0.48/0.76
final R indices [$I > 2\sigma I$]	R_1 = 0.0388, wR_2 = 0.0960[a]
final R indices (all data)	R_1 = 0.0470, wR_2 = 0.1010[a]
goodness of fit	1.059

[a] $w = 1 / [\sigma^2 (F_0^2)+(0.0477\ P)^2 + 0.8509P]$, with $P = (F_0^2 + 2\ F_c^2) / 3$

and was recently reported for pseudo-binary β-PN(NH).[50] This method significantly accelerates investigations of such compounds. Similarly to the synthesis of crystalline P_3N_5, intermediately formed HCl enables presumably reversible and reconstructive bond cleavage and re-formation and thus reversible conditions for the growth of larger crystals.[43]

CaP_2N_4 and isostructural SrP_2N_4 crystallize in the hexagonal megacalsilite structure type with six different Wyckoff sites for Ca or Sr, respectively,[49,52] whereas cubic BaP_2N_4 exhibits a high-pressure CaB_2O_4-(IV) type of structure with two different sites for the alkaline-earth atoms.[48] In $BaSr_2P_6N_{12}$ one of these positions is solely occupied by Sr, the other by Ba (Figures 6.1 and 6.2).[51]

The lattice parameters of CaP_2N_4 are slightly smaller than those of SrP_2N_4, thus shortening the

metal-nitrogen distances. Consequently, the coordination numbers of the alkaline-earth atoms vary between 5 (4+1) and 12 (9+3) with metal-nitrogen distances ranging from 2.50 to 3.38 Å in the case of $SrP_2N_4:Eu^{2+}$ (sum of ionic radii: 2.9 Å) and 2.36 to 3.21 Å (sum of ionic radii: 2.8 Å)[53] in the case of $CaP_2N_4:Eu^{2+}$ as calculated using the program MAPLE (Table 6.2).[54] The use of this algorithm not only provides an accurate tool for checking the electrostatic plausibility of a crystal structure, but also delivers information on the contribution of the different ligands to the effective coordination of a given central atom. Comparing BaP_2N_4 and $BaSr_2P_6N_{12}$, the lattice parameter a is slightly decreased (ca. 0.15 Å, Table 6.2). However, the range of the metal–nitrogen bond lengths is narrowed from 0.24 to 0.20 Å (Ba1−N) and from 0.70 (Ba2−N) to 0.60 Å (Sr−N). The Eu^{2+}-doped samples reveal a strong dependency of the luminescence properties on the metal−N distance. The latter are shortest in $CaP_2N_4:Eu^{2+}$, which exhibits orange luminescence (maximum at 570−574 nm), and longer in $SrP_2N_4:Eu^{2+}$ (green, 529 nm). $BaP_2N_4:Eu^{2+}$ and $BaSr_2P_6N_{12}:Eu^{2+}$ crystallize in a different structure type, yet the metal−N distances are longest here. These structural details lead to higher luminescence energies resulting in blue emission (454 and 456 nm, respectively) when UV irradiation is applied. In the series of nitridophosphates investigated, smaller cations lead to longer emission wavelengths (Table 6.2 and Figure 6.3). This is analogous with (oxo)nitridosilicates, namely, in the pure 2-5-8 ($M_2Si_5N_8:Eu^{2+}$) and the 1-2-2-2 ($MSi_2O_2N_2:Eu^{2+}$) systems.[15,17] Importantly, this effect can be deduced from the resulting different Eu−N distances. In the same structure type, the emission maximum shifts to longer wavelengths when the activator–host lattice distances decrease.[21–25]

Table 6.2: Lattice parameters, metal-nitrogen dostances, and luminescence properties[a] of $MP_2N_4:Eu^{2+}$ compounds.

compound:Eu^{2+}	CaP_2N_4[c]	CaP_2N_4	SrP_2N_4	BaP_2N_4	$BaSr_2P_6N_{12}$
lattice parameters / Å	a = 16.8470(20)	a = 16.8431(6)	a = 17.1113(1)	a = 10.2325(1)	a = 10.0874(5)
	c = 7.8592(16)	c = 7.8576(4)	c = 8.1066(1)		
metal−N distance / Å	2.38−3.21	2.36−3.21	2.50−3.38	2.78−3.48	2.80−3.40
coordination[b]	5−12	5−12	9−12	12	12
emission maximum / nm	574	570	529	454	456
FWHM / nm	76.2	92.3	70.3	46.6	47.4
FWHM / cm^{-1}	2275	2287	2432	2244	2240
color coordinates	x = 0.464	x = 0.490	x = 0.309	x = 0.142	x = 0.139
	y = 0.504	y = 0.495	y = 0.567	y = 0.057	y = 0.067
lumen equivalents / $lm \cdot W^{-1}$	373.7	374.5	508.0	64.8	74.1

[a] Excitation wavelengths: M = Sr: 365 nm; $CaP_2N_4:Eu^{2+}$ powder: 450 nm: $CaP_2N_4:Eu^{2+}$ single crystal, $BaP_2N_4:Eu^{2+}$, and $BaSr_2P_6N_{12}:Eu^{2+}$: 400 nm. [b] Determined with MAPLE[54]. [c] Single crystal.

Qualitatively, there is no marked difference between $BaP_2N_4:Eu^{2+}$ and $BaSr_2P_6N_{12}:Eu^{2+}$ concerning the position of the emission maximum (Figure 6.3. This can be explained by comparing the lattice

parameters, which do not differ substantially (Table 6.2). In both cases the coordination number for each metal site is 12 with distances to N ranging from 2.78 to 3.48 and 2.80 to 3.40 Å, respectively (Table 6.2 and Figure 6.2 IIa and IIb). The narrow full width at half maximum (FWHM $\approx$ 2240 cm^{-1}) of the emission bands can be explained by a high chemical similarity of both available activator sites.

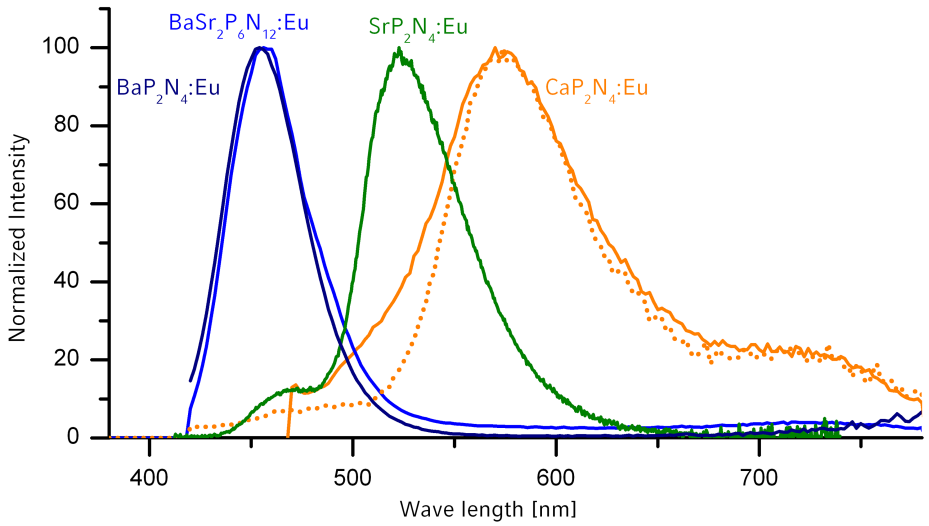

Figure 6.3: Emission spectra of $CaP_2N_4:Eu^{2+}$ (orange; solid line: powder sample, dotted line: single crystal), $SrP_2N_4:Eu^{2+}$ (green), $BaP_2N_4:Eu^{2+}$ (dark blue), and $BaSr_2P_6N_{12}:Eu^{2+}$ (blue).

With FWHM = 2432 cm^{-1} (70.3 nm) the emission peak of $SrP_2N_4:Eu^{2+}$ is moderately narrow (Table 6.2). UV excitation leads to additional emission in the blue spectral range (Figure 6.3) and is most likely caused by occupation of Eu^{2+} on a different Sr lattice site. Also, for isotypic $CaP_2N_4:Eu^{2+}$ superimposed emission bands with a peak at about 570 nm and shoulders in the blue and deep red spectral range can be observed. The strong intensity of the main emission band still leads to a rather narrow emission band (FWHM = 2275 cm^{-1}, 76.2 nm for single crystal). This work is the first report on single-band luminescent nitridophosphates, so these results cannot be compared to known values of the same materials class from the literature. Nevertheless, values for peak position and width are comparable to those for other nitridic and oxonitridic phosphors.[13,17] For example, $SrSi_2O_2N_2:Eu^{2+}$ has an emission maximum at 538 nm and a FWHM of 74 nm, $CaSi_2O_2N_2:Eu^{2+}$ at 563 nm with a FWHM of 98 nm.[33] It has to be pointed out that these compounds have long been studied and the synthesis has been optimized over years in most cases, whereas this contribution reports on the second investigation of luminescent nitridophosphates.

The narrow FWHM of $BaP_2N_4:Eu^{2+}$ (46.6 nm) and $BaSr_2P_6N_{12}:Eu^{2+}$ (47.4 nm) emission compares well with that of $BaSi_6N_8:Eu^{2+}$ (44 nm at an emission maximum of 450 nm).[55] In the future,

tuning of luminescence properties by solid- solution series experiments and further optimization of the syntheses could deliver more insight into this highly promising class of materials. With optimized synthesis, reliable values for quantum efficiencies will be obtainable. Although FWHM and color coordinates are hardly influenced by nonluminescent impurities, measured quantum efficiencies are highly sensitive towards light-absorbing side phases. The study of these values is an important future research target. However, even without optimization, FWHM values have been measured that are comparable with those of long-studied materials.

6.3 Conclusion

We have shown that CaP_2N_4, SrP_2N_4, BaP_2N_4, and $BaSr_2P_6N_{12}$ can be successfully doped with Eu^{2+} leading to novel luminescent materials. Synthesis of these compounds has been accomplished by means of high-pressure high-temperature methods ($5-8$ GPa and $1100-1300\,^{\circ}C$) employing a multianvil apparatus.

Although CaP_2N_4 and SrP_2N_4 crystallize in the megacalsilite structure type with coordination numbers of the alkaline-earth atoms varying between 5 and 12, BaP_2N_4 is isotypic to the high-pressure polymorph CaB_2O_4-(IV) with a coordination number of 12 for each cation position. In $BaSr_2P_6N_{12}$, one metal site of the BaP_2N_4 structure is occupied by Sr, the other by Ba.

By adding NH_4Cl as mineralizer as described recently for pseudo-binary β-PN(NH), single crystals of highly condensed ternary nitridophosphates were obtained for the first time. The proposed megacalsilite structure type for CaP_2N_4 was confirmed. This method may well present a breakthrough in the search for and the characterization of new highly condensed nitridophosphates.

Eu^{2+}-doped samples of CaP_2N_4, SrP_2N_4, BaP_2N_4, and $BaSr_2P_6N_{12}$ reveal luminescence properties depending on the length of the metal–N distances. With larger cations and thus longer distances, the emission maximum shifts to smaller wavelengths, thereby leading to orange ($CaP_2N_4:Eu^{2+}$) and green ($SrP_2N_4:Eu^{2+}$) emitting compounds. This is a similar effect to that observed for (oxo)nitridosilicates, namely, in the pure 2-5-8 ($M_2Si_5N_8:Eu^{2+}$) and the 1-2-2-2 ($MSi_2O_2N_2:Eu^{2+}$) systems. Although crystallizing in a different structure type and thus not comparable directly with the Ca and Sr compounds, blue-emitting $BaP_2N_4:Eu^{2+}$ and $BaSr_2P_6N_{12}:Eu^{2+}$ fit into this series as well.

In comparison with other well-known nitridic Eu^{2+}-doped materials emitting at roughly the same wavelength, the FWHM values of the nitridophosphates investigated herein are similar or even lower (Sr and Ca compounds). However, these materials have long been studied and optimized, whereas this new class of luminescent materials is just at the beginning of being systematically investigated and

optimized with regard to luminescence properties.

Consequently, nitridophosphates are promising candidates for the development of novel phosphor materials to be used in pc-LEDs. Our report is the first on luminescence properties in this materials class. Still, this system needs further optimization. However, we have demonstrated the high potential of nitridophosphates. Yet the diversity of already known and possible new structures of nitridophosphates is comparable to the situation of nitridosilicates, which underlines the high potential for identification of new host lattices for high-performance luminescence materials.

6.4 Experimental Section

6.4.1 Preparation of Starting Materials

$Ba(N_3)_2$ and $Sr(N_3)_2$ were synthesized by reacting the corresponding hydroxides or carbonates - (Merck, p.a.) with an aqueous solution of HN_3, prepared from NaN_3 (Merck, p.a.) and H_2SO_4 by distillation.[56,57] Special care is necessary when handling even dilute solutions of HN_3, since it is potentially explosive and the vapor is highly poisonous upon inhalation. Precautions have to be taken that no volatile pure (boiling point 60 °C) or highly concentrated HN_3 can condense onto cool surfaces.[52] $Ca(N_3)_2$ was prepared by stirring a suspension of $Ca(OH)_2$ (Merck, p.a.) with ammonium azide. After filtration of this solution the azide was precipitated by adding ethanol.[58] All alkaline-earth azides were dried in vacuum over P_4O_{10} and stored under exclusion of oxygen and moisture. Ammonium azide was prepared by mixing equimolar amounts of NH_4NO_3 (Grüssing, reinst) and NaN_3 (Acros Organics, 99%) and slowly heating (50 °C h^{-1}) the mixture (for safety reasons not more than 5 g) in a tube with one open end located outside the furnace to 180 °C.[59] P_3N_5 was prepared from $(PNCl_2)_3$ (Merck, p.s.) and dried gaseous ammonia (3.8, Messer Griesheim) as described in the literature.[60–63]

6.4.2 Synthesis

All syntheses were carried out using a modified Walker-type multianvil apparatus.[64,65] This method proved to be convenient for the synthesis of highly condensed nitridophosphates. However, pressures in the GPa range are not necessarily obligatory and no pressure ranges for the formation of the desired products have been investigated so far. Compared to syntheses carried out in standard autoclaves, less starting material is needed and in a rather short reaction time a well-defined product can be obtained. However, upscaling may well be possible by utilizing piston cylinder devices or even autoclaves and

will be part of future work.

The metal azides, P_3N_5, and $EuCl_2$ (1-2 mol%, Sigma–Aldrich, 99.99 %) were thoroughly mixed using a micro ball mill three times for 3 min. The mixture was then closely filled into a crucible of hexagonal boron nitride (HeBoSint S100, HENZE Boron Nitride Products, Kempten, Germany), which was placed in the middle of a graphite tube (SGL Carbon, Meitingen, Germany) used as furnace. To reduce the thermal gradient along the axis of the furnace, a second, longer graphite tube was placed over the first one, which was held in place by MgO spacers (TechnoKer, Küps, Germany). Samples prepared in that way were placed in the middle of a chromium oxide-doped (5 %) MgO octahedron (18 mm edge length, Ceramic Substrates and Components, Isle of Wight, UK) as pressure medium equipped with a ZrO_2 tube (Cesima Ceramics, Wust-Fischbach, Germany) as thermal insulator. Two plates of molybdenum secured the electrical contact to the tungsten carbide anvils (11 mm truncated edge length, Hawedia, Marklkofen, Germany). To prevent the pressure medium from being squeezed completely between the anvils, gaskets of pyrophyllite (Ceramic Substrates and Components, Isle of Wight, UK) were applied. The gaskets were held in place by sheets of cardboard (Bristol board, 369 $g \cdot m^{-2}$, Bähr, Kassel, Germany) and PTFE foil (Vitaflon, Bad Kreuznach, Germany), which served at the same time as electrical insulation between the tungsten carbide anvils.

The sample was compressed to $5-8$ GPa and heated subsequently to $1100-1300\,^{\circ}C$ within 20 min. The temperature was held for 10 min and was then quenched to room temperature by switching off the heater. After slow decompression the crucible was recovered and the product isolated.

6.4.3 Powder X-Ray Diffraction

X-ray diffraction experiments on powder samples were performed on a STOE Stadi P powder diffractometer in Debye–Scherrer geometry with Ge(111)-monochromatized CuKα1 (λ = 1.5406 Å) and MoKα1 (λ = 0.7093 Å) radiation. The registered diffractograms were compared with the known reflection patterns from the literature and the lattice parameters refined.

6.4.4 Single-Crystal X-Ray Diffraction

X-ray diffraction data of single crystals were recorded on a Nonius Kappa CCD diffractometer using MoKα radiation (λ = 0.71073 Å) and a graphite monochromator.

Further details of the structure investigations are available from the Fachinformationszentrum Karlsruhe, 76344 Eggenstein Leopoldshafen, Germany (fax: (+49)-7247-808-666; e-mail: crysdata@fiz-karlsruhe.de) on quoting the depository number CSD-425997.

6.4.5 Spectroscopic Measurements

For $SrP_2N_4:Eu^{2+}$, photoluminescence excitation, photoluminescence emission, and reflection spectra were recorded with an integrated setup based on a fiber spectrometer (Avantes 2000, 75 W xenon lamp) and an integrating sphere (Labsphere). To determine the spectral response function of the detection system, a calibration halogen lamp and different standard inorganic broad-band-emitting phosphors were used (spectral power distribution determined by the Physikalische Technische Bundesanstalt, Berlin, Germany).

For $CaP_2N_4:Eu^{2+}$, $BaP_2N_4:Eu^{2+}$, and $BaSr_2P_6N_{12}:Eu^{2+}$, the luminescence investigations were performed with the aid of a luminescence microscope consisting of a HORIBA Fluorimax4 spectrofluorimeter system attached to an Olympus BX51 microscope by fiber optics. The samples were measured inside a quartz capillary. The excitation wavelength was chosen as 400 or 450 nm with a spectral width of 10 nm. The emission spectra were measured in the wavelength range between 420 or 470 nm and 780 nm with a 2 nm step size. This range was also used for color point calculations.

6.5 References

[1] W. Schnick, *Phys. Status Solidi RRL* **2009**, *3*, A113.

[2] H. A. Höppe, *Angew. Chem. Int. Ed.* **2009**, *48*, 3572; *Angew. Chem.* **2009**, *121*, 3626.

[3] C. Feldmann, *Z. Anorg. Allg. Chem.* **2012**, *638*, 2169.

[4] S. Pimputkar, J. S. Speck, S. P. DenBaars, S. Nakamura, *Nat. Photonics* **2009**, *3*, 180.

[5] R. Mueller-Mach, G. Mueller, M. R. Krames, H. A. Höppe, F. Stadler, W. Schnick, T. Juestel, P. Schmidt, *Phys. Status Solidi A* **2005**, *202*, 1727.

[6] C. C. Lin, R.-S. Liu, *J. Phys. Chem. Lett.* **2011**, *2*, 1268.

[7] S. Ye, F. Xiao, Y. X. Pan, Y. Y. Ma, Q. Y. Zhang, *Mater. Sci. Eng. R* **2010**, *71*, 1.

[8] M. Mikami, H. Watanabe, K. Uheda, S. Shimooka, Y. Shimomura, T. Kurushima, N. Kijima, *IOP Conf. Ser. Mater. Sci. Eng.* **2009**, *1*, 012002.

[9] A. A. Setlur, *Electrochem. Soc. Interface* **2009**, *18*, 32.

[10] R.-J. Xie, N. Hirosaki, T. Takeda, T. Suehiro, *ECS J. Solid State Sci. Technol.* **2013**, *2*, R3031.

[11] M. R. Krames, O. B. Shchekin, R. Mueller-Mach, G. O. Mueller, L. Zhou, G. Harbers, M. G. Craford, *J. Disp. Technol.* **2007**, *3*, 160.

[12] R.-J. Xie, N. Hirosaki, *Sci. Technol. Adv. Mater.* **2007**, *8*, 588.

[13] R.-J. Xie, Y. Q. Li, N. Hirosaki, H. Yamamoto, *Nitride Phosphors and Solid State Lighting*, CRC Press, Taylor&Francis, New York, **2011**.

[14] H. A. Höppe, H. Lutz, P. Morys, W. Schnick, A. Seilmeier, *J. Phys. Chem. Solids* **2000**, *61*, 2001.

[15] M. Zeuner, S. Pagano, W. Schnick, *Angew. Chem. Int. Ed.* **2011**, *50*, 7754; *Angew. Chem.* **2011**, *123*, 7898.

[16] S. Schmiechen, P. Pust, P. J. Schmidt, W. Schnick, *Nachr. Chem.* **2014**, *62*, 847.

[17] R.-J. Xie, H. T. Hintzen, *J. Am. Ceram. Soc.* **2013**, *96*, 665.

[18] K. Uheda, N. Hirosaki, Y. Yamamoto, A. Naito, T. Nakajima, H. Yamamoto, *Electrochem. Solid-State Lett.* **2006**, *9*, H22.

[19] W. Schnick, H. Huppertz, *Chem. Eur. J.* **1997**, *3*, 679.

[20] K. Shioi, N. Hirosaki, R.-J. Xie, T. Takeda, Y. Q. Li, *J. Mater. Sci.* **2008**, *43*, 5659.

[21] M. Seibald, T. Rosenthal, O. Oeckler, W. Schnick, *Crit. Rev. Solid State Mater. Sci.* **2014**, *39*, 215.

[22] S. Schmiechen, H. Schneider, P. Wagatha, C. Hecht, P. J. Schmidt, W. Schnick, *Chem. Mater.* **2014**, *26*, 2712.

[23] M. Seibald, T. Rosenthal, O. Oeckler, C. Maak, A. Tücks, P. J. Schmidt, D. Wiechert, W. Schnick, *Chem. Mater.* **2013**, *25*, 1852.

[24] M. Seibald, O. Oeckler, V. R. Celinski, P. J. Schmidt, A. Tücks, W. Schnick, *Solid State Sci.* **2011**, *13*, 1769.

[25] M. Seibald, T. Rosenthal, O. Oeckler, F. Fahrnbauer, A. Tücks, P. J. Schmidt, W. Schnick, *Chem. Eur. J.* **2012**, *18*, 13446.

[26] H. L. Li, R.-J. Xie, G. H. Zhou, N. Hirosaki, Z. J. Sun, *J. Electrochem. Soc.* **2010**, *157*, J251.

[27] Y. Q. Li, A. C. Delsing, R. Metslaar, G. de With, H. T. Hintzen, *J. Alloys Compd.* **2009**, *487*, 28.

[28] Y. Q. Li, G. de With, H. T. Hintzen, *J. Solid State Chem.* **2008**, *181*, 515.

[29] X. Q. Piao, H. Horikawa, H. Hanzawa, K. Machida, *Appl. Phys. Lett.* **2006**, *88*, 161908.

[30] R.-J. Xie, N. Hirosaki, T. Suehiro, F.-F. Xu, M. Mitomo, *Chem. Mater.* **2006**, *18*, 5578.

[31] Y. Q. Li, N. Hirosaki, R.-J. Xie, T. Takeda, Y. Yamamoto, M. Mitomo, *Int. J. Appl. Ceram. Technol.* **2010**, *7*, 787.

[32] T. Horikawa, M. Fujitani, H. Hanzawa, K.Machida, *ECS J. Solid State Sci. Technol.* **2012**, *1*, R113.

[33] V. Bachmann, C. Ronda, O. Oeckler, W. Schnick, A. Meijerink, *Chem. Mater.* **2009**, *21*, 316.

[34] C. Braun, M. Seibald, S. L. Börger, O. Oeckler, T. D. Boyko, A. Moewes, G. Miehe, A. Tücks, W. Schnick, *Chem. Eur. J.* **2010**, *16*, 9646.

[35] Y. C. Chiu, C. H. Huang, T. J. Lee, W. R. Liu, Y. T. Yeh, S. M. Jang, R. S. Liu, *Opt. Express* **2011**, *19*, A331.

[36] X. M. Wang, C. H. Wang, X. J. Kuang, R. Q. Zou, Y. X. Wang, X. P. Jing, *Inorg. Chem.* **2012**, *51*, 3540.

[37] W. B. Park, S. P. Singh, C. Yoon, K. S. Sohn, *J. Mater. Chem.* **2012**, *22*, 14068.

[38] F. Hintze, F. Hummel, P. J. Schmidt, D. Wiechert, W. Schnick, *Chem. Mater.* **2012**, *24*, 402.

[39] F. Hintze, N. W. Johnson, M. Seibald, D. Muir, A. Moewes, W. Schnick, *Chem. Mater.* **2013**, *25*, 4044.

[40] P. Pust, F. Hintze, C. Hecht, V. Weiler, A. Locher, D. Zitnanska, S. Harm, D. Wiechert, P. J. Schmidt, W. Schnick, *Chem. Mater.* **2014**, *26*, 6113.

[41] P. Pust, A. Wochnik, E. Baumann, P. J. Schmidt, D. Wiechert, C. Scheu, W. Schnick, *Chem. Mater.* **2014**, *26*, 3544.

[42] P. Pust, V. Weiler, C. Hecht, A. Tücks, A. S. Wochnik, A.-K. Henß, D. Wiechert, C. Scheu, P. J. Schmidt, W. Schnick, *Nat. Mater.* **2014**, *13*, 891.

[43] W. Schnick, *Angew. Chem. Int. Ed. Engl.* **1993**, *32*, 806; *Angew. Chem.* **1993**, *105*, 846.

[44] A. Marchuk, W. Schnick, *Angew. Chem. Int. Ed.* **2015**, *54*, 2383; *Angew. Chem.* **2015**, *127*, 2413.

[45] Y. H. Jeong, Y. T. Lee, Y. T. Hong, *Appl. Phys. Lett.* **1990**, *57*, 2680.

[46] Y. H. Jeong, G. T. Kim, U. J. Jeong, *J. Appl. Phys.* **1991**, *69*, 6699.

[47] Y. Hirota, T. Hisaki, O. Mikami, *Electron. Lett.* **1985**, *21*, 690.

[48] F. W. Karau, W. Schnick, *J. Solid State Chem.* **2005**, *178*, 135.

[49] F. W. Karau, L. Seyfarth, O. Oeckler, J. Senker, K. Landskron, W. Schnick, *Chem. Eur. J.* **2007**, *13*, 6841.

[50] A. Marchuk, F. J. Pucher, F. W. Karau, W. Schnick, *Angew. Chem. Int. Ed.* **2014**, *53*, 2469; *Angew. Chem.* **2014**, *126*, 2501.

[51] F. Karau, W. Schnick, *Z. Anorg. Allg. Chem.* **2006**, *632*, 231.

[52] F. Karau, *Dissertation*, Ludwig-Maximilians-Universität München, Germany, **2007**.

[53] R. D. Shannon, *Acta Crystallogr. Sect. A: Found. Crystallogr.* **1976**, *32*, 751.

[54] R. Hübenthal, MAPLE, Version 4, Programm zur Berechnung des Madelunganteils der Gitterenergie, Universität Gießen, Germany, **1993**.

[55] H. Huppertz, W. Schnick, *Angew. Chem. Int. Ed. Engl.* **1996**, *35*, 1983; *Angew. Chem.* **1996**, *108*, 2115.

[56] P. Remy-Genneté, *Ann. Chim.* **1933**, *19*, 289.

[57] L. F. Audrieth , C. F. Gibbs, W. C. Johnson, H. C. Perrin in *Inorg. Synth. Vol. 1* (Ed.:H.S.Booth), John Wiley&Sons, Inc.,Hoboken, NJ, USA, **1939**,

[58] H. D. Fair, R. F. Walker, *Energetic Materials Vol. 1: Physics and Chemistry of the Inorganic Azides*, Plenum Press, New York, **1977**.

[59] W. J. Frierson, W. F. Filbert in *Inorg.Synth. Vol. 2* (Ed.:W.C.Fernelius), John Wiley&Sons, Inc., Hoboken, NJ, USA, **1946**, 136.

[60] J. Lücke, *Dissertation*, Rheinische Friedrich-Wilhelms-Universität Bonn, Germany, **1994**.

[61] W. Schnick, J. Lücke, F. Krumeich, *Chem. Mater.* **1996**, *8*, 281.

[62] S. Horstmann, E. Irran, W. Schnick, *Angew. Chem. Int. Ed. Engl.* **1997**, *36*, 1873; *Angew. Chem.* **1997**, *109*, 1938.

[63] S. Horstmann, E. Irran, W. Schnick, *Z. Anorg. Allg. Chem.* **1998**, *624*, 620.

[64] H. Huppertz, *Z. Kristallogr.* **2004**, *219*, 330.

[65] D. Walker, M. A. Carpenter, C. M. Hitch, *Am. Mineral.* **1990**, *75*, 1020.

7 $Ba_3P_5N_{10}Br:Eu^{2+}$: A Natural-White-Light Single Emitter with a Zeolite Structure Type

Alexey Marchuk[a] and Wolfgang Schnick*[a]

[a] *Department of Chemistry, University of Munich (LMU), Butenandtstraße 5–13, 81377 Munich, Germany*

published in: *Angew. Chem.* **2015**, *127*, 2413-2417. DOI: 10.1002/ange.201410528

published in: *Angew. Chem. Int. Ed.* **2015**, *54*, 2383-2387. DOI: 10.1002/anie.201410528

Abstract

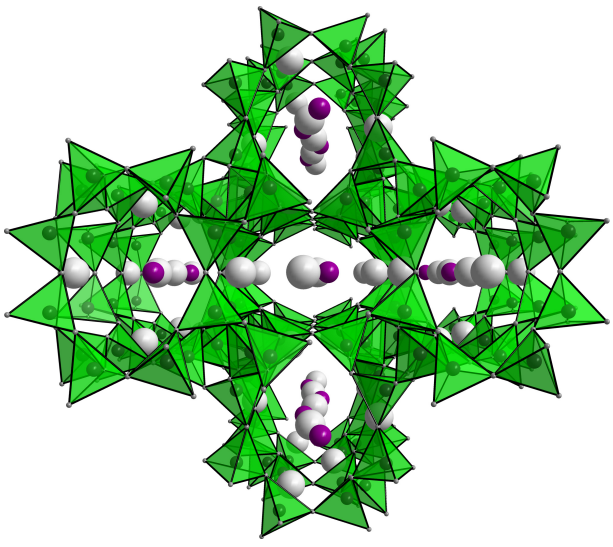

Illumination sources based on phosphor-converted light emitting diode (pcLED) technology are nowadays of great relevance. In particular, illumination-grade pcLEDs are attracting increasing attention. Regarding this, the application of a single warm-white-emitting phosphor could be of great advantage. Herein, we report the synthesis of a novel nitridophosphate zeolite $Ba_3P_5N_{10}Br:Eu^{2+}$. Upon excitation by near-UV light, natural-white-light luminescence was detected. The synthesis of $Ba_3P_5N_{10}Br:Eu^{2+}$ was carried out using the multianvil technique. The crystal structure of $Ba_3P_5N_{10}Br:Eu^{2+}$ was solved and refined by single-crystal X-ray diffraction analysis and confirmed by Rietveld refinement and FTIR spectroscopy. Furthermore, spectroscopic luminescence

measurements were performed. Through the synthesis of $Ba_3P_5N_{10}Br:Eu^{2+}$, we have shown the great potential of nitridophosphate zeolites to serve as high-performance luminescence materials.

7.1 Introduction with Results and Discussion

Zeolites find application in numerous technological areas worldwide and have become an irreplaceable materials class in modern industry. Classical zeolites, such as aluminosilicates and aluminophosphates, are widely used, for example in the fields of petroleum refining, in the petrochemical and fine chemical industry as adsorbents, and as ion exchangers or catalysts. Furthermore, this compound class also has the potential for further applications in future technologies, for example in sensors and electronic or optical systems.[1–6] Prominent examples of the commercially most important functional zeolites are $Na_x(H_2O)_{16}Al_xSi_{96-x}O_{192}$ ($x < 27$; ZSM-5) and $Na_{12}(H_2O)_{27}[Al_{12}Si_{12}O_{48}]_8$ (LTA), which exhibit excellent chemical and thermal stability.[7,8] Conventional oxidic zeolite structures are typically composed of a three-dimensional network of vertex-sharing SiO_4 and AlO_4 tetrahedra, in which a negative charge is associated with each AlO_4 tetrahedron.[9,10] Given that the element combination P/N is isoelectronic to Si/O, it is reasonable to expect that the resulting compound class of nitridophosphates exhibits a structural variety similar to or even more diverse than that of silicates. The formal substitution of O atoms by N atoms in a tetrahedral network implies significant new structural possibilities. The structural diversity of oxosilicates is limited to terminal or singly bridging O atoms, whereas N atoms in nitridophosphates may occur as $N^{[1]}$, $N^{[2]}$, $N^{[3]}$, or even $N^{[4]}$ atoms.[11] (The superscripted numbers in square brackets following element symbols define their coordination numbers.) Furthermore, nitridic zeolites promise useful chemical and physical properties (for example, adjustable acidity/basicity). A prominent example for these extended structural possibilities of nitridophosphates as well as their potential in the field of open-framework structures is the nitridic clathrate $P_4N_4(NH)_4(NH_3)$ that was discussed as a possible gas-storage material.[12,13] Its network structure has been predicted for silica but to date has only been found in this particular nitride compound. Furthermore, two nitridic zeolites in the compound class of nitridophosphates are known to date, namely $Li_xH_{12-x-y+z}[P_{12}O_yN_{24-y}]X_z$ (X = Cl, Br) and $Ba_{19}P_{36}O_{6+x}N_{66-x}Cl_{8+x}$ ($x \approx 4.54$). Both represent unusual network structure types, namely NPO (nitridophosphate one) and NPT (nitridophosphate two), respectively.[14–17]

As a result of their high thermal and chemical stability as well as highly cross-linked network structures, nitridic zeolites are basically well suited as host lattices for Eu^{2+} doping. Consequently, new interesting luminescent materials may be expected with possible application in phosphor-converted light-emitting diodes (pcLEDs). The constantly growing relevance of pcLEDs makes further investigation of luminescent materials an important research target. In particular, white light sources based on LED technology are gaining increasing attention. The Nobel Prize in Physics 2014 that was awarded to Akasaki, Amano, and Nakamura "*for the invention of efficient blue light-emitting diodes which has enabled*

bright and energy-saving white light sources" confirms this assessment.[18] Several strategies are available to obtain high quality pcLEDs for illumination. The strategy adopted in industry is based on the multiphosphors-conversion model.[19,20] In this case, for example, green (e.g. $Lu_3Al_5O_{12}:Ce^{3+}$),[21] red (e.g. $(Ba,Sr)_2Si_5N_8:Eu^{2+}$),[22,23] and yellow (e.g. Ca-α-SiAlON:Eu^{2+})[24,25] emitting phosphors are mixed and coated on an InGaN semiconductor LED chip to achieve white light. The main problem of this strategy, however, is the differing thermal stability of the individual phosphors, which often results in poor emission-color stability. Moreover, the particle sizes of individual phosphor materials have to be adapted to one another to avoid agglomeration. Finally, the individual phosphors have to be mixed very homogeneously in exact ratios. To alleviate these difficulties, application of a single white-emitting phosphor could be of great advantage. Several compounds, such as $Ba_{1.3}Ca_{0.7}SiO_4:Eu^{2+}$, Mn^{2+},[26] $Ba_3MgSi_2O_8:Eu^{2+}$, Mn^{2+},[27] and $CaAl_2Si_2O_8:Eu^{2+}$, Mn^{2+}[28] have been already investigated as promising single-phase phosphors for near-UV white LEDs. However, the co-doping with Eu^{2+} and Mn^{2+} ions may lead to poor emission-color stability because of the different emitting centers which exhibit different thermal-quenching behaviors.

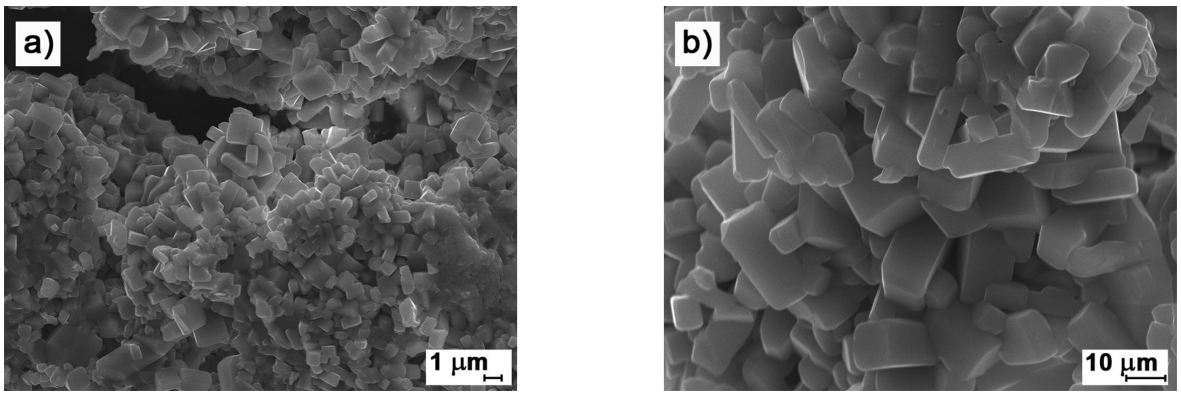

Figure 7.1: SEM images of crystals of $Ba_3P_5N_{10}Br:Eu^{2+}$ measured on a) 1 µm or b) 10 µm scale.

$$15\,Ba(N_3)_2 + 3\,BaBr_2 + 10\,P_3N_5 \longrightarrow 6\,Ba_3P_5N_{10}Br + 40\,N_2 \tag{7.1}$$

In this Communication, we report the synthesis and structural investigation of the novel nitridophosphate $Ba_3P_5N_{10}Br$ with a zeolite-type structure. Doped with Eu^{2+}, $Ba_3P_5N_{10}Br$ exhibits natural-white-light luminescence upon excitation by near-UV light, making this compound a promising candidate for use as a single white emitter in pcLEDs.

$Ba_3P_5N_{10}Br:Eu^{2+}$ was synthesized by the reaction of stoichiometric amounts of $Ba(N_3)_2$, $BaBr_2$, and P_3N_5 according to Equation (7.1). $EuCl_2$ (2 mol%) was used as the doping agent. The synthesis was carried out using a Walker-type multianvil assembly and a 1000 t hydraulic press at pressures

between 1 and 5 GPa and 1000 °C for 30 minutes.[29] Through the thermolysis of $Ba(N_3)_2$ a high N_2 partial pressure is available. It prevents P_3N_5 from dissociation into its composite elements under high pressure at reaction temperatures above 1000 °C.[30] At ambient pressure, P_3N_5 already decomposes at temperatures above 850 °C. The product was obtained as an air-stable colorless (light yellow when doped with Eu^{2+}) crystalline solid (see Figure 7.1). To grow single crystals of the compound which are large enough to be suitable for single-crystal X-ray diffraction, the heating time was increased up to 200 minutes.

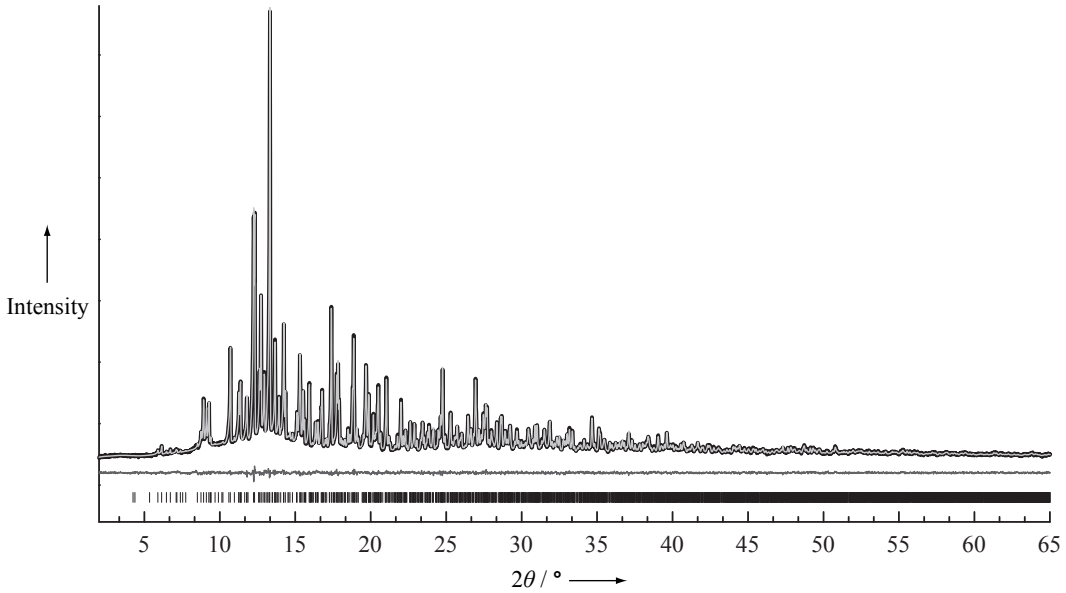

Figure 7.2: Experimentally observed (black line) and calculated (light gray line) X-ray powder diffraction pattern, positions of Bragg reflections (vertical bars) and difference profile (dark gray line) for the Rietveld refinement of $Ba_3P_5N_{10}Br:Eu^{2+}$.

At ambient pressure, the synthesis of $Ba_3P_5N_{10}Br$ was also accomplished by heating a mixture of $BaBr_2$, amorphous HPN_2, and NH_4Br as mineralizer in evacuated and sealed silica ampoules to 800 °C for 84 h. A similar approach has been already applied for the synthesis of various nitridophosphates exhibiting a sodalite-type structure.[16,31] However, by this procedure $Ba_3P_5N_{10}Br$ was only accessible as a minor side phase. To obtain a single-phase product, the reaction conditions as well as the starting materials have to be optimized. In addition to the starting materials named above, BaH_2 and $P(NH_2)_4Br$[32] may be used.

To clarify the chemical composition of the product, energy-dispersive X-ray (EDX) spectroscopy has been carried out. No elements other than Ba, P, N, and Br were detected. The determined atomic ratio Ba/P/N/Br is in good agreement with the predicted composition $Ba_3P_5N_{10}Br$ (see Table F.1 in the Supporting Information).

The crystal structure of $Ba_3P_5N_{10}Br:Eu^{2+}$ was solved and refined from single-crystal X-ray diffraction data in the orthorhombic space group Pnma (no. 62) using direct methods.[33] As a result of the elongated displacement ellipsoid of the N11 atom, it was possible to refine a split position for this atom with occupancy of approximately 0.5 each (Figure F.1). All atom positions were refined anisotropically. As a result of the small crystal size as well as significant differences in the X-ray scattering power of N atoms compared to Ba and Br atoms, a common anisotropic displacement parameter for the N atom positions was refined. The accuracy of the structure elucidation as well as phase purity of the product was confirmed by Rietveld refinement (Figure 7.2). The crystallographic details are summarized in the Supporting Information.

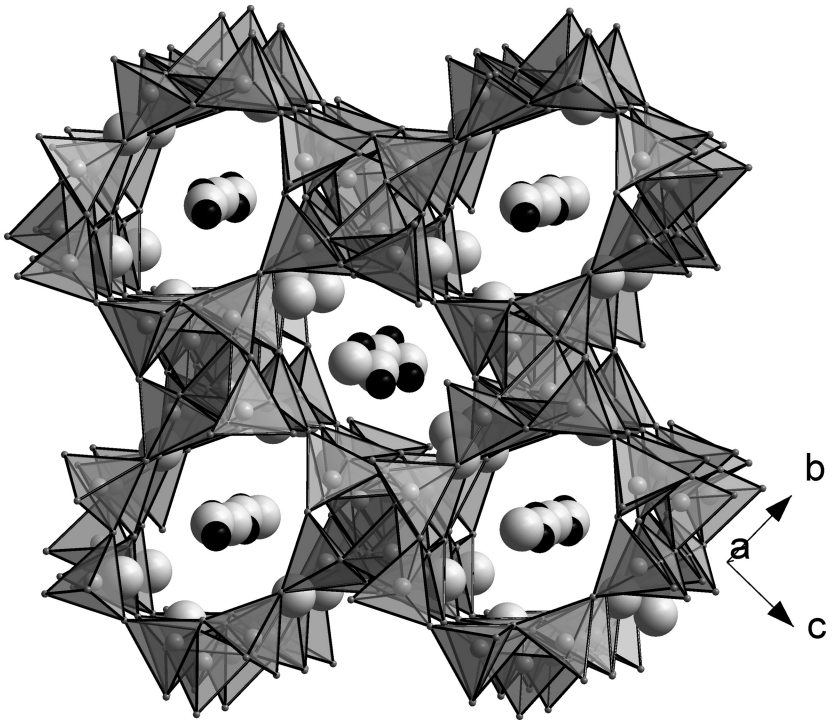

Figure 7.3: Crystal structure of $Ba_3P_5N_{10}Br$, viewed along [100]. Atom colors: Ba = light gray, Br = black, PN_4 tetrahedra = dark gray.

The crystal structure of $Ba_3P_5N_{10}Br$ consists of a network of all-side vertex-sharing PN_4 tetrahedra, leading to three-dimensional *achter*-ring channels, according to the nomenclature introduced by Liebau.[10] These channels contain alternately Ba and Br atoms (Figure 7.3). The PN_4 tetrahedra form condensed *dreier*, *vierer*, and *achter* rings. This condensation results in turn in two slightly distorted CBUs (composite building unit) both forming $3^4 4^2 8^6$ cages (Figure 7.4). Both cages exhibit the same basic atom arrangement but differ slightly in their degree of deformation.

The centers of the CBUs are occupied by Br atoms, which are coordinated by six Ba atoms in a

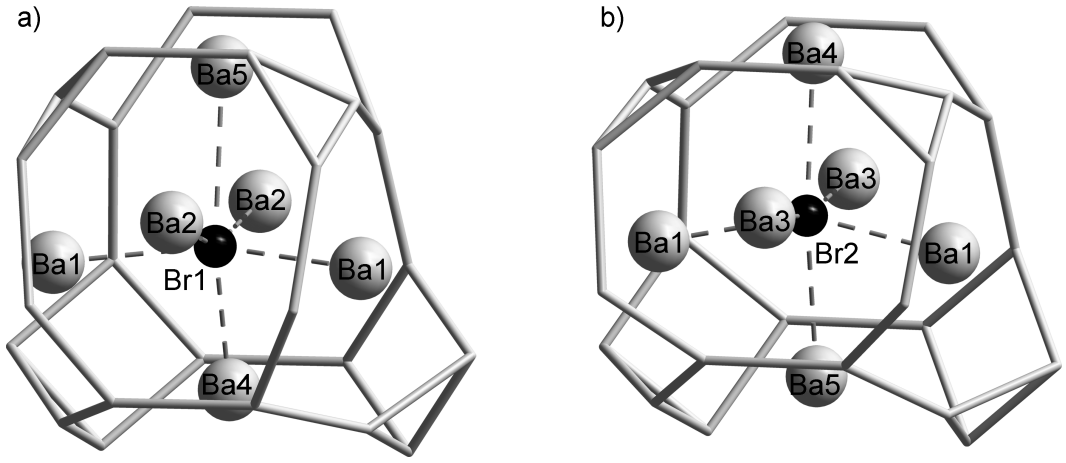

Figure 7.4: Topological representation of the two different $3^4 4^2 8^6$ cages with cage content in $Ba_3P_5N_{10}Br$ with each connecting line representing a P−N−P bond. Atom colors (spheres): Ba = light gray, Br = black.

distorted octahedral arrangement (Figure 7.4). These Ba_6Br octahedra are connected to each other via shared edges forming a three-dimensional network.

The framework topology of $Ba_3P_5N_{10}Br$ was determined by the TOPOS software.[34] It is represented by the point symbol $(3.4.5.8^3)_4(3^2.8^4)$ and is analogous to the topology of the JOZ zeolite framework type.[17,35] Despite this structural analogy $Ba_3P_5N_{10}Br$ is not porous and thus not prone to sorption of water and hydrolysis.

The P−N bond lengths range between 1.607 and 1.637 Å and lie in the range of those usually observed in similar nitridophosphates.[36,37] The N−P−N angles vary between 99.4 and 119.38° and thus differ slightly from the regular tetrahedral angle. However, the range is typical of other nitridophosphate zeolites.[15,16]

The crystal structure of $Ba_3P_5N_{10}Br$ contains five different crystallographic Ba positions, whose coordination spheres are shown in Figure 7.5. Ba1 is coordinated ninefold by seven N atoms (2.790−3.314 Å) and two Br atoms (3.341 and 3.391 Å). The Ba2 and Ba3 positions are coordinated by six N atoms (2.753−3.009 Å) and two Br atoms (3.174−3.241 Å), respectively, forming slightly distorted hexagonal bipyramids. In contrast, the coordination spheres of Ba4 and Ba5 centers represent irregular polyhedra consisting of eight N atoms (2.713−3.347 Å) and two Br atoms (3.360−3.668 Å). The N11a and N11b atoms represent one split position of the N11 position. All bond lengths Ba−N and Ba−Br correspond to those in other known compounds as well as to the sum of the ionic radii.[36–40]

The absence of N−H groups in $Ba_3P_5N_{10}Br:Eu^{2+}$ was confirmed by FTIR spectroscopy (Figure F.2). The FTIR spectrum shows several groups of bands below 1500 cm^{-1}. These can be attributed to

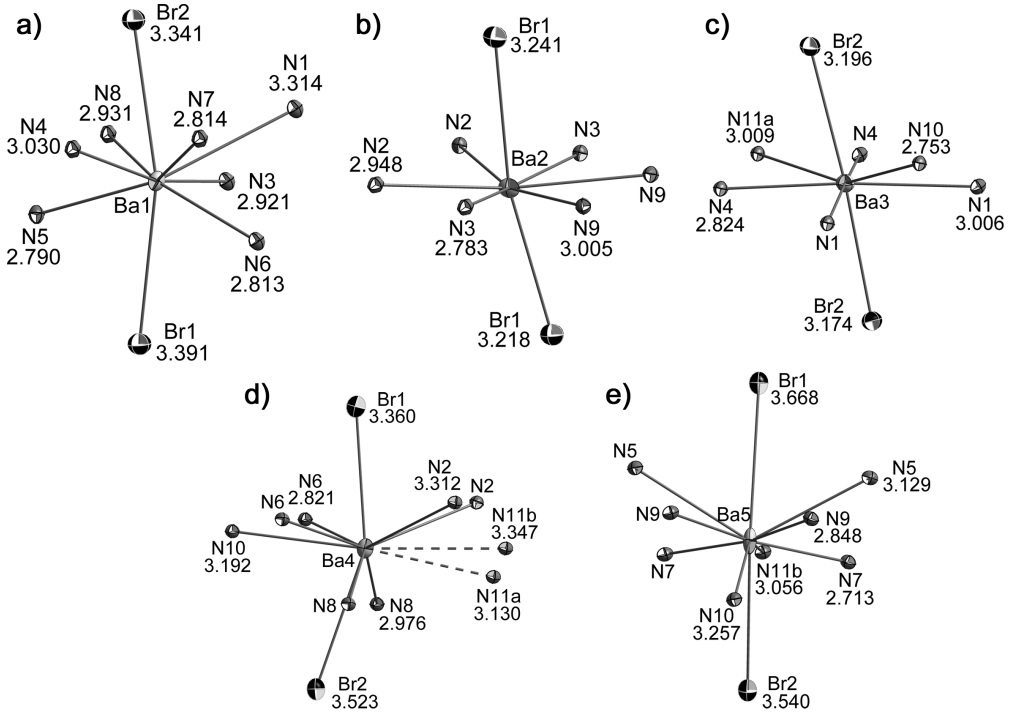

Figure 7.5: Coordination polyhedra and corresponding bond lengths / Å of the a) Ba1, b) Ba2, c) Ba3, d) Ba4, and e) Ba5 positions in the crystal structure of $Ba_3P_5N_{10}Br$. Thermal ellipsoids are set at 70% probability.

symmetric and asymmetric P−N−P stretching modes, respectively. However, there are no absorption bands around 3000 cm^{-1}, which would be typical for N−H valence vibrations.

By doping of $Ba_3P_5N_{10}Br$ with Eu^{2+} ions, natural-white-light luminescence was detected upon excitation by near-UV light (λ = 400 nm). Figure 7.6 displays the excitation and emission spectra of $Ba_3P_5N_{10}Br:Eu^{2+}$ crystallites. The excitation spectrum reveals a maximum at λ = 396 nm. Thus, this compound can be effectively excited by near-UV light. Excitation at λ = 400 nm results in an emission spectrum with two bands: one in the blue spectral region centered at λ = 472 nm, and the other in the yellow spectral region centered at λ = 582 nm. The values of the full width at half maximum (FWHM) are approximately 1502 cm^{-1} (for the band at λ = 472 nm) and 2374 cm^{-1} (for the band at λ = 582 nm). The presence of two emission bands can be explained by occupation of Eu^{2+} ions on different Ba lattice sites. The example of $Ba_3MgSi_2O_8:Eu^{2+}$, Mn^{2+} demonstrates that the differences in the coordination polyhedra of the different Ba lattice sites has a strong influence on the number of emission bands.[27] The combination of both emission bands generates the resulting natural-white-light luminescence of the title compound with a correlated color temperature (CCT) of 3384 K, lumen equivalent of 372 lm/W, and CIE color coordinates x = 0.415, y = 0.403. The quantum efficiency of a powder sample is close to 63% for λ = 390 nm excitation. In this context it should be noted that

the quantum efficiency was determined for a non-optimized sample. By optimizing the Eu^{2+} doping level in the sample the quantum efficiency could be certainly increased. Detailed information on the luminescent measurements is summarized in the Supporting Information.

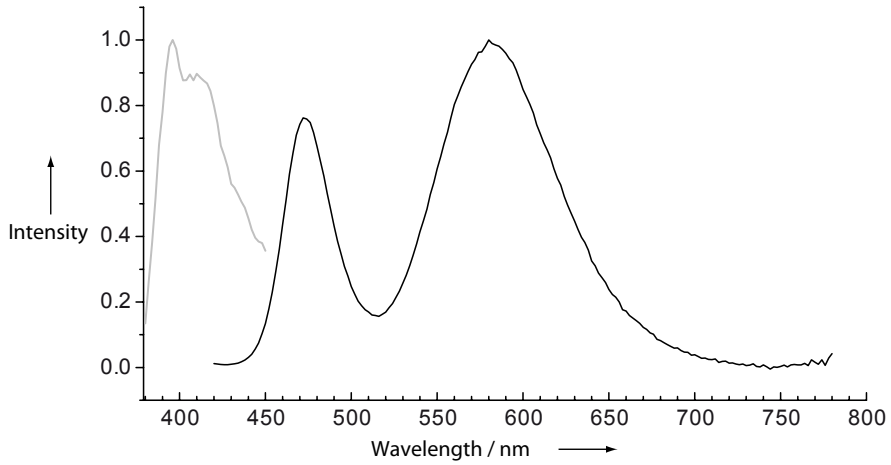

Figure 7.6: Excitation (gray) and emission (black) spectra of $Ba_3P_5N_{10}Br:Eu^{2+}$. Excitation spectrum: $\lambda_{exc,max}$ = 396 nm. Emission spectrum: λ_{exc} = 400 nm. CIE color coordinates: x = 0.415, y = 0.403.

To investigate the thermal stability of $Ba_3P_5N_{10}Br:Eu^{2+}$ temperature dependent powder X-ray diffraction up to 1000 °C was performed. The results (Figure F.3) show that the sample is stable in air up to at least 1000 °C. Furthermore, resistance against hydrolysis of $Ba_3P_5N_{10}Br:Eu^{2+}$ was checked by storing the sample under water for several days. However, neither a quenching of the luminescence nor the decomposition of the sample was observed.

7.2 Conclusion

In this Communication we presented a novel nitridophosphate $Ba_3P_5N_{10}Br$ with a zeolite-type structure. We were able to characterize this compound by single-crystal X-ray diffraction, powder X-ray diffraction, FTIR, and EDX spectroscopy. The topology of $Ba_3P_5N_{10}Br$ corresponds to that of the JOZ zeolite structure type. Doped with Eu^{2+}, the title compound exhibits natural-white-light luminescence upon excitation by near-UV light. This feature makes $Ba_3P_5N_{10}Br:Eu^{2+}$ a promising candidate for use as a single white emitter in pcLEDs. Moreover, using the example of $Ba_3P_5N_{10}Br:Eu^{2+}$, we have demonstrated that nitridic zeolites are well suited as host lattices for high-performance luminescence materials. Consequently, the synthesis of isotypic compounds $M_3P_5N_{10}X:Eu^{2+}$ by the exchange of halide ion X or alkaline-earth ion M may lead to further interesting luminescent properties.

7.3 References

[1] G. A. Ozin, *Angew. Chem. Int. Ed. Engl.* 1989, *28*, 359; *Angew. Chem.* **1989**, *101*, 373.

[2] M. E. Davis, *Nature* **2002**, *417*, 813.

[3] T. F. Degan, *Top. Catal.* **2000**, *13*, 349.

[4] A. Corma, *Chem. Rev.* **1997**, *97*, 2373.

[5] Y. Li, J. Yu, *Chem. Rev.* **2014**, *114*, 7268.

[6] M. Niwa, N. Katada, K. Okumura, *Characterization and Design of Zeolite Catalysis: Solid Acidity, Shape Selectivity, and Loading Properties*, Springer, Berlin, **2010**.

[7] G. T. Kokotailo, S. L. Lawton, D. H. Olson, W. M. Meier, *Nature* **1978**, *272*, 437.

[8] T. B. Reed, D. W. Breck, *J. Am. Chem. Soc.* **1956**, *78*, 5972.

[9] G. O. Brunner, W. M. Meier, *Nature* **1989**, *337*, 146.

[10] F. Liebau, *Structural Chemistry of Silicates*, Springer, Berlin, **1985**.

[11] W. Schnick, *Angew. Chem. Int. Ed. Engl.* **1993**, *32*, 806; *Angew. Chem.* **1993**, *105*, 846.

[12] F. Karau, W. Schnick, *Angew. Chem. Int. Ed.* **2006**, *45*, 4505; *Angew. Chem.* **2006**, *118*, 4617.

[13] M. Pouchard, *Nature* **2006**, *442*, 878.

[14] S. Correll, O. Oeckler, N. Stock, W. Schnick, *Angew. Chem. Int. Ed.* **2003**, *42*, 3549; *Angew. Chem.* **2003**, *115*, 3674.

[15] S. Correll, N. Stock, O. Oeckler, J. Senker, T. Nilges, W. Schnick, *Z. Anorg. Allg. Chem.* **2004**, *630*, 2205.

[16] S. J. Sedlmaier, M. Döblinger, O. Oeckler, J. Weber, J. Schmedt auf der Günne, W. Schnick, *J. Am. Chem. Soc.* **2011**, *133*, 12069.

[17] C. Baerlocher, L. B. McCusker, *Database of Zeolites Structures*: http://www.iza-structure.org/databases/, accessed October 2014.

[18] J. Heber, *Nat. Phys.* **2014**, *10*, 791.

[19] H. A. Höppe, *Angew. Chem. Int. Ed.* **2009**, *48*, 3572; *Angew. Chem.* **2009**, *121*, 3626.

[20] S. K. Panda, S. G. Hickey, H. V. Demir, A. Eychmüller, *Angew. Chem. Int. Ed.* **2011**, *50*, 4432; *Angew. Chem.* **2011**, *123*, 4524.

[21] H. L. Li, X. J. Liu, L. P. Huang, *Opt. Mater.* **2007**, *29*, 1138.

[22] T. Schlieper, W. Milius, W. Schnick, *Z. Anorg. Allg. Chem.* **1995**, *621*, 1380.

[23] M. Zeuner, S. Pagano, W. Schnick, *Angew. Chem. Int. Ed.* **2011**, *50*, 7754; *Angew. Chem.* **2011**, *123*, 7898.

[24] K. Sakuma, N. Hirosaki, R.-J. Xie, *J. Lumin.* **2007**, *126*, 843.

[25] K. Sakuma, K. Omichi, N. Kimura, M. Ohashi, D. Tanaka, N. Hirosaki, Y. Yamamoto, R.-J. Xie, T. Suehiro, *Opt. Lett.* **2004**, *29*, 2001.

[26] W. Lv, M. Jiao, Q. Zhao, B. Shao, W. Lü, H. You, *Inorg. Chem.* **2014**, *53*, 11007.

[27] J. S. Kim, P. E. Jeon, J. C. Choi, H. L. Park, S. I. Mho, G. C. Kim, *Appl. Phys. Lett.* **2004**, *84*, 2931.

[28] W. J. Yang, L. Luo, T. M. Chen, N. S. Wang, *Chem. Mater.* **2005**, *17*, 3883.

[29] a) N. Kawai, S. Endo, *Rev. Sci. Instrum.* **1970**, *41*, 1178; b) D. Walker, M. A. Carpenter, C. M. Hitch, *Am. Mineral.* **1990**, *75*, 1020; c) D. Walker, *Am. Mineral.* **1991**, *76*, 1092; d) D. C. Rubie, *Phase Transitions* **1999**, *68*, 431; e) H. Huppertz, *Z. Kristallogr.* **2004**, *219*, 330.

[30] F. W. Karau, L. Seyfarth, O. Oeckler, J. Senker, K. Landskron, W. Schnick, *Chem. Eur. J.* **2007**, *13*, 6841.

[31] W. Schnick, N. Stock, J. Lücke, M. Volkmann, M. Jansen, *Z. Anorg. Allg. Chem.* **1995**, *621*, 987.

[32] K. Landskron, S. Horstmann, W. Schnick, *Z. Naturforsch. B* **1999**, *54*, 1019.

[33] Crystal data for $Ba_3P_5N_{10}Br$: crystal size: 0.010×0.020×0.020 mm^3, space group *Pnma* (no. 62), a = 12.5660(13), b = 13.2240(13), c = 13.8030(14) Å, V = 2293.7(4) $Å^3$, Z = 8, ρ_{diff} = 4.557 gcm^{-1}, Bruker D8 Venture, Mo-Kα radiation (71.073 pm), multi-scan absorption correction, 31838 reflections, 2354 independent reflections, R_{int} = 0.0735, least-squares refinement on F^2, R values (all data /$F_0^2 \geq 2\sigma(F_0^2)$): R_1 = 0.0457/0.0339,wR_2 = 0.0658/0.0638, GooF = 1.216 for 1960 observed reflections ($F_0^2 \geq 2\sigma(F_0^2)$) and 132 parameters. Further details on the crystal structure investigations may be obtained from the Fachinformationszentrum Karlsruhe, 76344 Eggenstein-Leopoldshafen, Germany (fax: (+ 49)7247-808-666; e-mail: crysdata@fiz-karlsruhe.de), on quoting the depository number CSD-428381.

[34] V. A. Blatov, A. P. Shevchenko, D. M. Proserpio, *Cryst. Growth Des.* **2014**, *14*, 3576.

[35] J. A. Armstrong, M. T. Weller, *J. Am. Chem. Soc.* **2010**, *132*, 15679.

[36] F. W. Karau, W. Schnick, *J. Solid State Chem.* **2005**, *178*, 135.

[37] F. Karau, W. Schnick, *Z. Anorg. Allg. Chem.* **2006**, *632*, 238.

[38] A. Marchuk, F. J. Pucher, F. W. Karau, W. Schnick, *Angew. Chem. Int. Ed.* **2014**, *53*, 2469; *Angew. Chem.* **2014**, *126*, 2501.

[39] J. M. Linger, J. Haines, A. Atouf, *J. Appl. Crystallogr.* **1995**, *28*, 416.

[40] S. A. Hodorowicz, E. K. Hodorowicz, H. A. Eick, *J. Solid State Chem.* **1983**, *48*, 351.

8 Nontypical Luminescence Properties and Structural Relation of $Ba_3P_5N_{10}X:Eu^{2+}$ (X = Cl, I) – Nitridophosphate Halides with Zeolite-like Structure

Alexey Marchuk,[a] Sebastian Wendl,[a] Nedzada Imamovic,[a] Frank Tambornino,[a] Detlef Wiechert,[b] Peter J. Schmidt,[b] and Wolfgang Schnick*[a]

[a] *Department of Chemistry, University of Munich (LMU), Butenandtstraße 5–13, 81377 Munich, Germany*
[b] *Lumileds Germany GmbH, Philipsstrasse 8, 52068 Aachen, Germany*

published in: *Chem. Mater.* **2015**, *27*, 6432-6441. DOI: 10.1021/acs.chemmater.5b02668

Abstract

The isotypic nitridophosphates $Ba_3P_5N_{10}X$ (X = Cl, I) have been synthesized by high-temperature reaction under pressures between 1 and 5 GPa. The crystal structures of both compounds were solved and refined using single-crystal X-ray diffraction data. Accuracy of the structure determination as well as phase purity of the products were confirmed by Rietveld refinement and FTIR spectroscopy. The band gap values (4.0−4.3 eV) for the direct transitions were determined from UV-Vis data using the Kubelka-Munk function and were confirmed by DFT calculations. Both compounds crystallize in

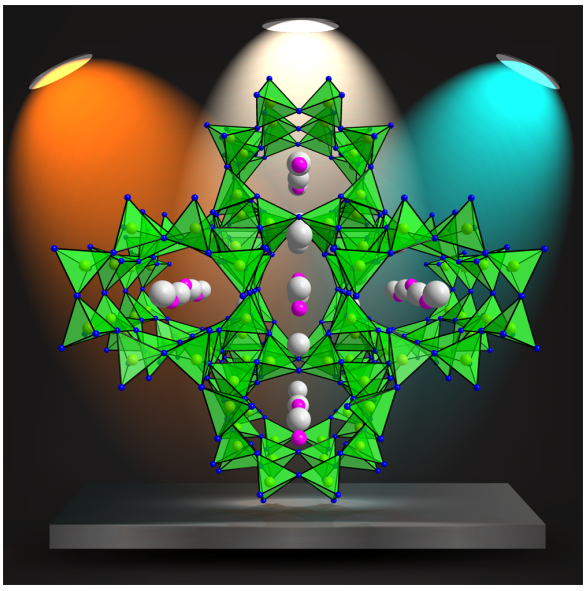

the $Ba_3P_5N_{10}Br$ structure type (space group *Pnma* (no. 62), Z =8, $Ba_3P_5N_{10}Cl$: a = 12.5182(5), b = 13.1798(5), c = 13.7676(6) Å, $R1$ = 0.0214, $wR2$ = 0.0526; $Ba_3P_5N_{10}I$: a = 12.6311(7), b = 13.2565(8), c = 13.8689(8) Å, $R1$ = 0.0257, $wR2$ = 0.0586) with a tetrahedra network being analogous to the topology of the JOZ zeolite structure type. The crystal structure is built up of all-side vertex-sharing PN_4 tetrahedra leading to a zeolite-like framework with three-dimensional *achter*-ring channels containing alternately Ba and respective halide atoms. The condensed *dreier*-, *vierer*- and *sechser*-rings form two different composite building units made up of $3^4 4^2 8^6$-cages. Upon doping with Eu^{2+} the title compounds exhibit intriguing luminescence properties, which were compared with that of $Ba_3P_5N_{10}Br:Eu^{2+}$. Upon excitation by near-UV light, non-saturated color luminescence from multiple emission centers was observed in the orange (X = Cl) and cyan to amber (X = I) spectral range of the visible spectrum.

8.1 Introduction

Illumination sources based on phosphor converted light emitting diodes (pc-LEDs) technology are increasingly gaining importance.[1] Due to their energy efficiency, pc-LEDs have been successfully established in the market and are about to replace inefficient and thus energy wasting common light sources, such as compact fluorescent lamps or incandescent light bulbs.[2–4] The constantly growing relevance of LEDs is reflected by the Nobel Prize in Physics 2014 that has been awarded to Akasaki, Amano and Nakamura "*for the invention of efficient blue light-emitting diodes which has enabled bright and energy-saving white light sources*".[5] Pc-LEDs are based on a blue light-emitting InGaN semiconductor LED, which is coated with phosphor materials in order to emit light covering the entire visible spectrum. Consequently, the explorative search for and investigation of new luminescent materials is an important research target. Besides already established garnet-type phosphors e.g. $Lu_3Al_5O_{12}$:Ce^{3+}[6] and $Y_{3-x}Gd_xAl_{5-y}Ga_yO_{12}$:$Ce^{3+}$ (YAG:Ce),[7,8] Eu^{2+}-doped nitridosilicates have proven to be excellent luminescent materials. In this context prominent examples such as $MSi_2O_2N_2:Eu^{2+}$ and $M_2Si_5N_8:Eu^{2+}$ (M = Ca, Sr, Ba) can be mentioned.[4,9,10] These compounds contain highly cross-linked nitridic network structures built up of solely corner-sharing $Si(O,N)_4$ tetrahedra, which is the reason for their chemical and thermal stability. These qualities combined with a small Stokes-shift, low thermal quenching and high quantum efficiency (QE) are general requirements for practical application of luminescent materials.[4,10–13] Furthermore, with nitridomagnesosilicate $Sr[Mg_3SiN_4]$:Eu^{2+}, we have identified a material with the most narrow band red emission for Eu^{2+}-doped phosphors to date, exhibiting a full width at half-maximum (FWHM) of only $\sim$1170 cm^{-1}.[14] However, the search for new and improved phosphors is not focused on alkaline-earth (oxo)nitridosilicates exclusively, but also on related nitride compounds such as nitridogallates,[15,16] nitridoaluminates[17] and nitridophosphates.[18] A prominent example is the nitrido-lithoaluminate $Sr[LiAl_3N_4]:Eu^{2+}$ that combines a very small FWHM of $\sim$1180 cm^{-1} with outstanding high QE values up to 500 K.[19]

Similarly to nitridosilicates, nitridophosphates are typically made up of condensed PN_4 tetrahedra, which may share common corners as well as common edges. Besides their remarkable thermal and chemical stability, they are typically colorless and transparent. The binary parent compound of nitridophosphates is P_3N_5. It exhibits a high band gap and has already been applied in electronic devices as insulator material.[20–22] Consequently, it can be expected that ternary or multinary nitridophosphates will show large band gap values as well. Furthermore, the structural diversity of already known nitridophosphates is comparable to that of nitridosilicates. Considering all these facts together, it is

likely that nitridophosphates, similarly to nitridosilicates, can be expected to represent promising host compounds for new luminescent materials as well.

In our preceding publication we have shown that nitridophosphates MP_2N_4 (M = Ca, Sr, Ba) and $BaSr_2P_6N_{12}$ can be successfully doped with Eu^{2+}, exhibiting orange, green and blue luminescence, respectively.[23] Quite recently, we reported on the synthesis of a novel natural-white light-emitting nitridophosphate, namely $Ba_3P_5N_{10}Br:Eu^{2+}$, with a zeolite analogous structure type.[24] With this compound we were able to demonstrate that nitridic zeolites are well suited as host lattices for Eu^{2+} in order to serve as high performance luminescence materials.

Following our recent work, we report now on synthesis and structural characterization of the novel nitridophosphates $Ba_3P_5N_{10}X$ with X = Cl, I. We place particular emphasis on luminescence properties of both compounds and put it into correlation to our recently reported $Ba_3P_5N_{10}Br:Eu^{2+}$.

8.2 Results and Discussion

8.2.1 Synthesis and Chemical Analysis

The elevated pressures by these reactions are required for the controlled decomposition of $Ba(N_3)_2$ generating a high N_2 partial pressure. The latter prevents P_3N_5 from decomposition into the elements at reaction temperatures above 850 °C. Due to the relatively low synthesis pressures (∼1 GPa) we are able to synthesize product amounts up to 250 mg per batch. However, the multianvil technique is not mandatory for synthesis of the title compounds. In order to obtain larger product amounts more common high-pressure techniques (e.g. piston cylinder, belt techniques or hot isostatic presses) may be useful. The non-doped samples were obtained as air-stable colorless crystalline solids, forming cuboid-shaped crystals (see Figure 8.1). Upon doping $Ba_3P_5N_{10}Cl:Eu^{2+}$ appears as light-orange and $Ba_3P_5N_{10}I:Eu^{2+}$ as yellow-green solids, respectively.

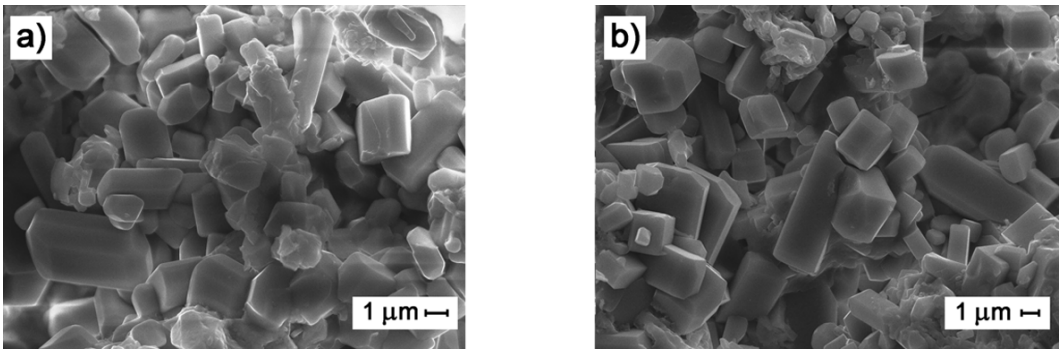

Figure 8.1: SEM images of crystals of $Ba_3P_5N_{10}Cl:Eu^{2+}$ (a) and $Ba_3P_5N_{10}I:Eu^{2+}$ (b).

The chemical composition of both products was clarified by energy-dispersive X-ray (EDX) spectroscopy. The determined atomic ratio Ba/P/N/Cl and Ba/P/N/I, respectively, is in good accordance with the predicted composition. Table 8.1 summarizes the average compositions obtained from EDX analysis. The absence of the N−H groups in the crystal structure of title compounds was confirmed by FTIR spectroscopy (see Figure G.1, Supporting Information). No characteristic absorption bands around 3000 cm^{-1} were observed, which would be typical for N−H valence vibration modes. Furthermore, the FTIR spectra of $Ba_3P_5N_{10}Cl$ and $Ba_3P_5N_{10}I$ are rather similar, indicating the structural similarity of both compounds. Both spectra exhibit several groups of bands below 1500 cm^{-1}, which can be attributed to symmetric and asymmetric P−N−P stretching modes, respectively.

Table 8.1: Results of the EDX measurements for $Ba_3P_5N_{10}X:Eu^{2+}$ (X = Cl, I).

EDX-analysis	chemical formula
$Ba_{3.0}P_{4.9}N_{11.3}Cl_{1.0}$	$Ba_3P_5N_{10}Cl$
$Ba_{3.3}P_{5.4}N_{14.2}I_{1.0}$	$Ba_3P_5N_{10}I$

In order to explore the thermal stability of the title compounds temperature dependent powder X-ray diffraction up to 900 °C was performed. The investigations showed that both compounds are stable in air up to at least 900 °C (see Figure G.2, Supporting Information). Moreover, the thermal stability indicates that both title compounds are most likely not high-pressure phases.

8.2.2 Crystal Structure Determination

The crystal structure of $Ba_3P_5N_{10}X$ (X = Cl, I) was solved and refined from single-crystal X-ray diffraction data in the orthorhombic space group *Pnma* (no. 62) using direct methods. In both cases a split position of the N11 atom was refined, similarly to $Ba_3P_5N_{10}Br$.[24] As a result of the small crystal size of $Ba_3P_5N_{10}I$ as well as significant differences in the X-ray scattering power of N atoms compared to Ba and I atoms, a common isotropic displacement parameter for the N1−N10 atom positions was refined. In case of $Ba_3P_5N_{10}Cl$, due to the better quality of the single crystal, it was possible to refine all atom positions freely. The crystallographic details are summarized in Table 8.2. Table 8.3 shows exemplarily the atomic parameters of $Ba_3P_5N_{10}Cl$. The relatively high residual electron density in the single crystal refinement for $Ba_3P_5N_{10}Cl$ is due to the elongated displacement ellipsoid of the Ba5 atom. However, it was not possible to refine this atom on a split position. The possible reasons for this appearance are discussed below. The atomic parameters of $Ba_3P_5N_{10}I$ are given in the Supporting

Information (see Tables G.1-G.2).

In order to confirm the accuracy of the structure elucidation from single-crystal X-ray diffraction as well as the phase purity of the synthesized products Rietveld refinement of X-ray powder diffraction data has been carried out (see Figure 8.2). For the N atom positions in both compounds a common isotropic displacement parameter was refined. The crystallographic details of the Rietveld refinements are summarized in the Supporting Information (see Table G.4). Figure 8.3 illustrates the dependency of lattice parameters *a*, *b* and *c*, determined from X-ray powder data refinements, on halide substitution in the compounds $Ba_3P_5N_{10}X$ (X = Cl, Br, I). The results show a linear increase of the lattice parameters and consequently of the cell volume with increasing ionic radius of the respective halide ion.

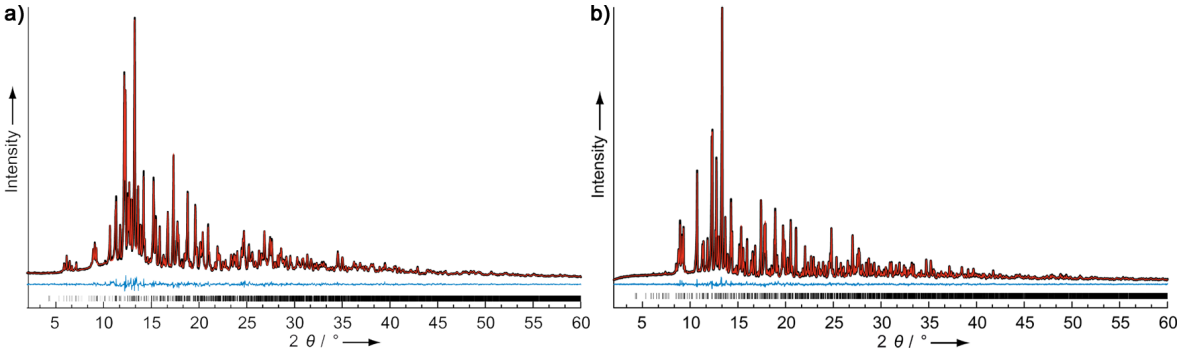

Figure 8.2: Observed (black line) and calculated (red line) X-ray powder diffraction pattern, positions of Bragg reflections (vertical bars) and difference profile (blue line) for the Rietveld refinement of $Ba_3P_5N_{10}Cl:Eu^{2+}$ (a) and $Ba_3P_5N_{10}I:Eu^{2+}$ (b).

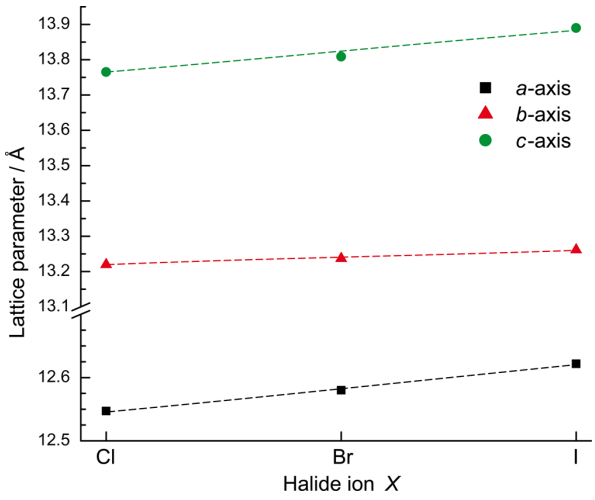

Figure 8.3: Lattice parameters of $Ba_3P_5N_{10}X$ (X = Cl, Br, I) obtained from Rietveld refinements.

8.2.3 Crystal Structure Description

$Ba_3P_5N_{10}X$ with X = Cl, I crystallize in the $Ba_3P_5N_{10}Br$-structure type.[24] The crystal structure is built up of all-side vertex-sharing PN_4 tetrahedra leading to a zeolite-like framework with three-dimensional *achter*-ring channels, according to the nomenclature introduced by Liebau[25] (see Figure 8.4). The framework topology is analogous to that of the JOZ zeolite structure type.[26,27] The *achter*-ring channels contain alternately Ba and halide atoms Cl and I, respectively.

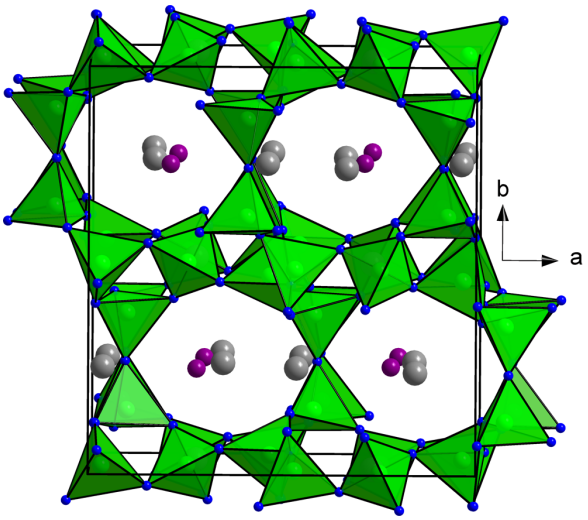

Figure 8.4: Crystal structure of $Ba_3P_5N_{10}X$ (X = Cl, I), viewing direction along [001]. PN_4-tetrahedra green, N atoms blue, Ba atoms gray and halide ions X magenta.

The structure can be subdivided into two CBUs (Composite Building Unit), which are made up of $3^4 4^2 8^6$-cages (see Figure 8.5). The center of each CBU is occupied by a respective halide atom X, which is coordinated by six Ba atoms in slightly distorted octahedral arrangement. The XBa_6 octahedra are interconnected via shared edges leading to a three-dimensional network.

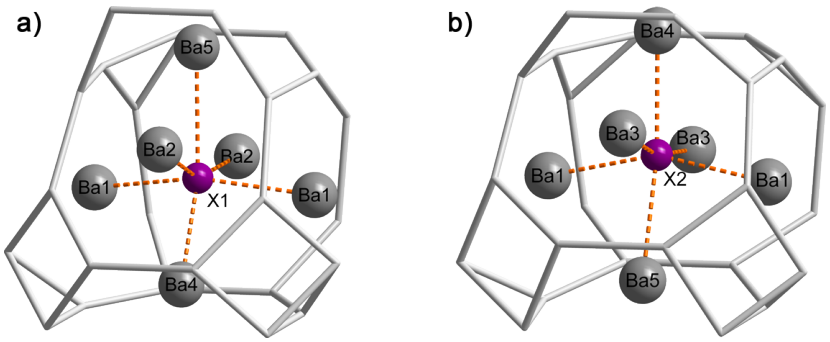

Figure 8.5: Topological representation of the two different $3^4 4^2 8^6$ cages with cage content in $Ba_3P_5N_{10}X$ (X = Cl, I). Each connecting line represents a P−N−P bond. Ba atoms are dark gray, halide atoms are magenta.

Table 8.2: Selected crystallographic data of the single-crystal structure determination of $Ba_3P_5N_{10}X$ (X = Cl, I).

formula	$Ba_3P_5N_{10}Cl$	$Ba_3P_5N_{10}I$
crystal system	orthorhombic	
space group	*Pnma* (no. 62)	
lattice parameters / Å	a = 12.5182(5)	a = 12.6311(7)
	b = 13.1798(5)	b = 13.2565(8)
	c = 13.7676(6)	c = 13.8689(8)
cell volume / Å^3	2271.5(2)	2322.3(2)
formula units per cell	8	8
calculated X-ray density / g·cm^{-1}	4.342	4.770
μ / mm^{-1}	11.226	13.410
temperature / K	289	289
F(000)	2640	2928
diffractometer	Bruker D8 Venture	
radiation / Å	Mo-Kα (λ = 0.71073 Å)	
monochromator	graphite	
absorption correction	semiempirical	
θ-range / °	2.119−27.493	2.181−25.999
index ranges	-16 ≤ h ≤ 16	-15 ≤ h ≤ 15
	-17 ≤ k ≤ 17	-16 ≤ k ≤ 14
	-17 ≤ l ≤ 17	-17 ≤ l ≤ 17
observed reflections	29059	38181
independent relfections (> 2σ)	2720(2399)	2383 (1883)
R_{int}; R_σ	0.0330; 0.0178	0.0596; 0.0241
refined parameters	184	132
goodness of fit	1.029	1.121
R_1 (all data); R_1 ($F^2 > 2\sigma(F^2)$)	0.0269; 0.0214	0.0441; 0.0257
wR_2 (all data), wR_2 ($F^2 > 2\sigma(F^2)$)	0.0552; 0.0526	0.0612; 0.0586
$\Delta\rho_{max}$; $\Delta\rho_{min}$ (e·Å^{-3})	3.436 / -1.942	1.487 / -0.807

Table 8.3: Fractional atomic coordinates, isotropic displacement parameters, and occupation of crystallographic positions of $Ba_3P_5N_{10}Cl$; standard deviations in parentheses.

atom	Wyckoff site	x	y	z	U_{eq} / Å^2	occupancy
Ba1	8*d*	0.27071(2)	0.00193(2)	0.32350(2)	0.01185(7)	1.0
Ba2	4*c*	0.03451(3)	1/4	0.73085(3)	0.01377(9)	1.0
Ba3	4*c*	0.04206(3)	1/4	0.24473(3)	0.01180(9)	1.0
Ba4	4*c*	0.33568(3)	1/4	0.03101(3)	0.01355(9)	1.0
Ba5	4*c*	0.34295(3)	1/4	0.53198(4)	0.02533(11)	1.0
Cl1	4*c*	0.27741(12)	1/4	0.80047(12)	0.0214(3)	1.0
Cl2	4*c*	0.29198(12)	1/4	0.28063(12)	0.0207(3)	1.0
P1	8*d*	0.02966(8)	0.00322(7)	0.63972(7)	0.00635(19)	1.0
P2	8*d*	0.03587(7)	0.53105(7)	0.14636(7)	0.00569(18)	1.0
P3	8*d*	0.07521(8)	0.13292(7)	0.01483(7)	0.00612(18)	1.0
P4	8*d*	0.09295(7)	0.13100(7)	0.48076(7)	0.00624(18)	1.0
P5	8*d*	0.24929(7)	0.50182(7)	0.07337(7)	0.00630(19)	1.0
N1	8*d*	0.0051(2)	0.0793(2)	0.1016(2)	0.0085(6)	1.0
N2	8*d*	0.0135(2)	0.1031(2)	0.5695(2)	0.0100(6)	1.0
N3	8*d*	0.0201(2)	0.0457(2)	0.7487(2)	0.0086(6)	1.0
N4	8*d*	0.0599(3)	0.0836(2)	0.3747(2)	0.0099(6)	1.0
N5	8*d*	0.1649(2)	0.5458(2)	0.1525(2)	0.0093(6)	1.0
N6	8*d*	0.1954(3)	0.0859(2)	0.0071(2)	0.0089(6)	1.0
N7	8*d*	0.2143(2)	0.0937(3)	0.5016(2)	0.0104(7)	1.0
N8	8*d*	0.3516(3)	0.0471(2)	0.1281(2)	0.0076(6)	1.0
N9	8*d*	0.5162(3)	0.1290(2)	0.5895(2)	0.0096(6)	1.0
N10	4*c*	0.0850(4)	1/4	0.0484(3)	0.0120(9)	1.0
N11a	4*c*	0.077(3)	1/4	0.453(2)	0.0105(14)	0.40(11)
N11b	4*c*	0.097(2)	1/4	0.4657(16)	0.0105(14)	0.60(11)

The P−N bond lengths and P−N−P bond angles [X = Cl: 1.606(3)−1.646(3) Å; 123.6(2)−148.1(5)°; X = I: 1.610(3)−1.647(5) Å; 123.8(3)−148.1(5)°] vary in a similar range and correspond to those usually observed in other nitridophosphates as well as in oxonitridophosphate zeolites.[28–32]

The crystal structures of both compounds contain five crystallographically independent Ba positions

(see Figure 8.6). These positions can be divided into two groups with regard to their coordination numbers (CN). The first group contains Ba2 and Ba3 positions with coordination number CN = 8 (six N and two X (X = Cl, Br, I)) forming slightly distorted hexagonal bipyramids. The second group contains Ba1, Ba4 and Ba5 positions (CN = 10),

which are coordinated by eight N atoms and two X atoms. The coordination number of the respective Ba position was determined using the MAPLE software.[33] The N11a and N11b atoms represent one split position of the N11 atom. The Ba−N and Ba−X distances of both compounds are summarized in Table 8.4. The Ba−N distances are in good agreement with those usually observed in other known barium nitridophosphates as well as with the sum of the ionic radii.[31,32,34] The Ba−X distances show, however, significant differences with respect to the CN of the Ba atoms. In both compounds, the Ba−X distances in the coordination sphere of Ba2 and Ba3 (CN = 8, Ba−Cl: 3.150−3.247 Å; Ba−I: 3.210−3.259 Å) are significantly shorter than those in the coordination sphere of Ba1, Ba4 and Ba5 (CN = 10, Ba−Cl: 3.257−3.386 Å; Ba−I: 3.353−3.640 Å). Moreover, while the Ba−Cl distances correspond to the sum of the ionic radii [Ba−Cl: 3.23 Å (CN = 8); 3.33 Å (CN = 10)], the Ba−I distances are notably shorter than the sum of the ionic radii [Ba−I: 3.62 Å (CN = 8), 3.72 Å (CN = 10)].[35] As already mentioned above, the displacement ellipsoid of the Ba5 atom in $Ba_3P_5N_{10}Cl$ is

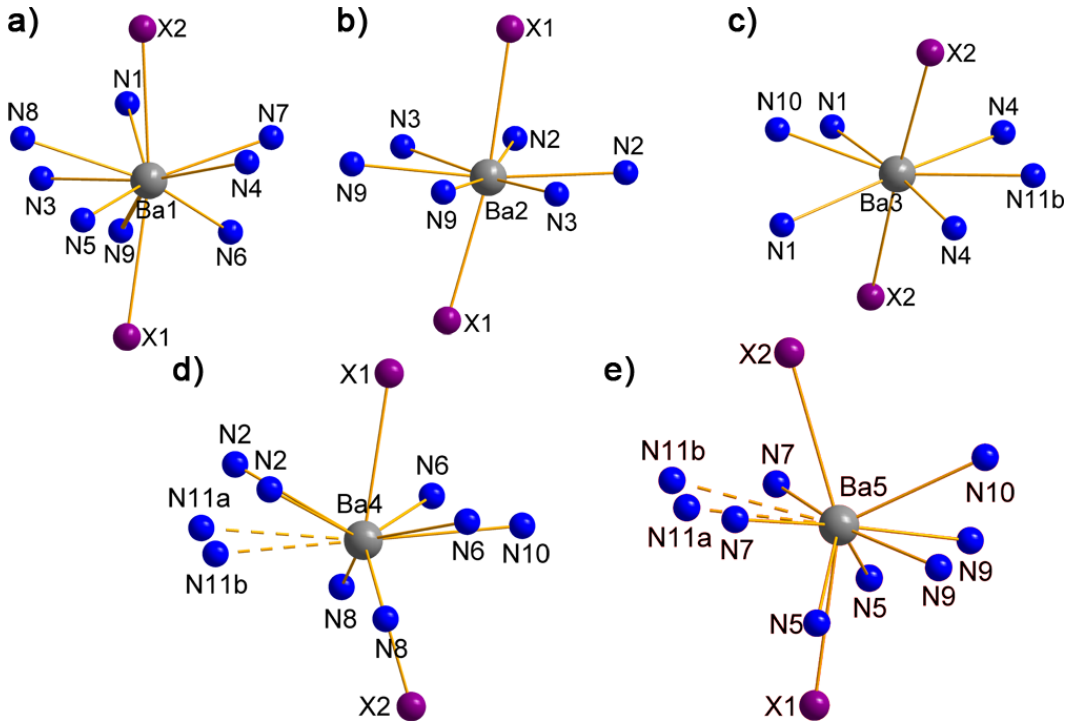

Figure 8.6: Coordination polyhedra of Ba1 position (a), Ba2 position (b), Ba3 position (c), Ba4 position (d) and Ba5 position (e); Ba atoms gray, N atoms blue and halide atoms magenta.

markedly elongated toward the halide atoms. This can be explained by the significantly longer Ba5−Cl distance compared to Ba1−Cl and Ba4−Cl distances. In $Ba_3P_5N_{10}I$ this large difference in the Ba−I distances is no longer given due to the larger halide ion, resulting in a regular displacement ellipsoid of the Ba5 atom.

Table 8.4: Coordination numbers (CN) of the respective Ba atoms as well as Ba−N and Ba−X distances / Å of $Ba_3P_5N_{10}X:Eu^{2+}$ (X = Cl, I); standard deviations in parentheses.

	CN		**$Ba_3P_5N_{10}Cl$**	**$Ba_3P_5N_{10}I$**
Ba1	10	Ba−N	2.774(3)−3.395(3)	2.803(5)−3.352(5)
		Ba−X	3.3330(4)−3.3894(4)	3.3529(5)−3.3860(5)
Ba2	8	Ba−N	2.710(3)−2.958(3)	2.853(5)−3.081(5)
		Ba−X	3.188(2)−3.247(2)	3.255(1)−3.259(1)
Ba3	8	Ba−N	2.756(4)−3.119(2)	2.697(7)−3.246(4)
		Ba−X	3.150(2)−3.167(2)	3.210(1)−3.224(1)
Ba4	10	Ba−N	2.805(3)−3.272(3)	2.840(5)−3.368(5)
		Ba−X	3.257(2)−3.480(2)	3.4435(9)−3.5581(9)
Ba5	10	Ba−N	2.648(4)−3.226(5)	2.750(5)−3.266(6)
		Ba−X	3.519(2)−3.786(2)	3.5523(9)−3.6402(9)

8.2.4 UV/Vis Spectroscopy

In order to determine experimental band gaps of the title compounds solid-state UV/Vis spectroscopy on undoped samples of $Ba_3P_5N_{10}X$ (X = Cl, Br, I) was performed. The reflectance spectra (see Figure 8.7, a) show broad absorption bands above 250 nm. No other absorption bands are visible, which corresponds well with the white body color of the non-doped compounds.

The band gaps, as determined using the Kubelka-Munk function, are approximately 4.3 and 4.0 eV for the chloride and iodide compound, respectively. For comparison the band gap of the bromide compound was also determined. With 4.2 eV this band gap falls in-between that of the iodide and chloride compound. Figure 8.7 (b) shows the Tauc plots for all three compounds. As expected, the band gap increases with decreasing ionic radius of the halide ion. For the calculations the value of the Kubelka-Munk function exponent n = 1/2 was chosen due to the direct allowed transition. The type of transition in the title compounds was determined by DFT calculations of the electronic band structures. Figure 8.8 illustrates the calculated band structures of $Ba_3P_5N_{10}X$ with X = Cl, Br, I showing a direct band gap in all three cases. With band gap decreasing with increasing ionic radii of the halide ion, the DFT calculations show the same trend as the Tauc plots.

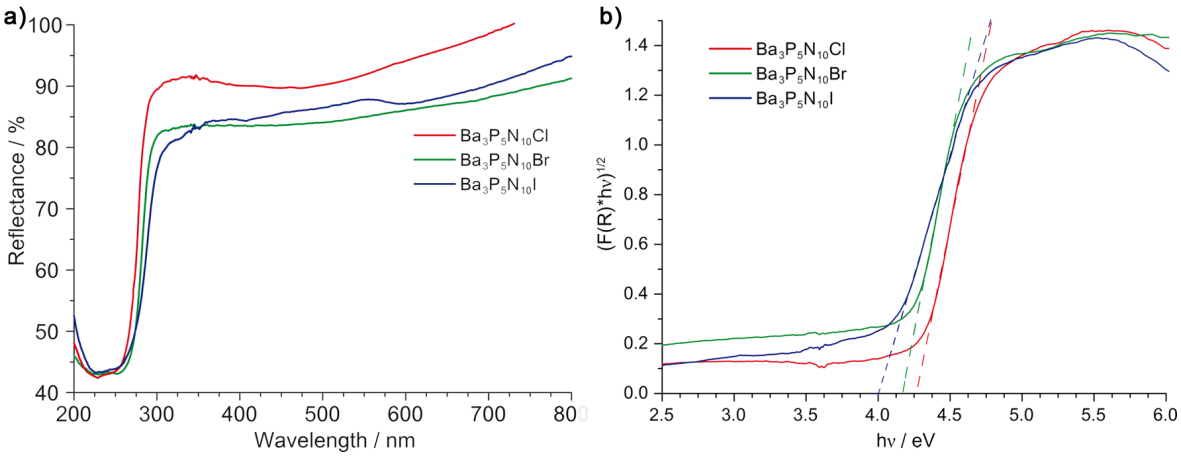

Figure 8.7: UV/Vis-reflection spectra (a) and Tauc Plots (n = 1/2) (b) for non-doped $Ba_3P_5N_{10}X$ with X = Cl (red line), Br (green line) and I (blue line).

8.2.5 Luminescence

Eu^{2+}-doped samples of $Ba_3P_5N_{10}X$ show light-orange (X = Cl) and yellow-green (X = I) body color, respectively. The luminescence investigations were performed on single crystals in sealed glass capillaries and for thick bed powder material.

Upon excitation of the Eu^{2+}-doped (nominal doping level of 2 mol%) products with near-UV light (λ = 390 nm), orange (X = Cl, LER = 376 lm/W) and cyan (X = I, LER = 383 lm/W) luminescence was detected. The quantum efficiency of the microcrystalline samples is 61% (X = Cl) and 33% (X = I) at λ = 410 nm excitation. Tuning of the dopant concentration and optimization of synthesis procedures may further increase QE of these materials. Figures 8.9 and 8.10 display the excitation and emission spectra of $Ba_3P_5N_{10}X:Eu^{2+}$ (X = Cl, I). Similarly to $Ba_3P_5N_{10}Br:Eu^{2+}$, each of the emission spectra exhibits several bands.

To analyze the observed composed emission spectra a least-squares fit of measured emission spectra with Pekarian-shaped functions was carried out.[36] The detailed information on the least-square fits of measured emission spectra can be found in the Supporting Information. The fit function has been found useful by the authors to describe Eu^{2+} emission band shapes for typical average phonon frequencies (> 200 cm^{-1}) and Huang-Rhys parameters (> 2). Figure 8.11 shows exemplarily a deconvolution fit of the emission spectrum of $Ba_3P_5N_{10}I:Eu^{2+}$ (2 mol%). It becomes obvious that all emission spectra consist of at least three bands if excited at λ = 390 nm. Analysis results of the other emission spectra can be found in the Supporting Information (Figure G.3).

For X = I, rather narrow emission bands in the 500−515 nm range (FWHM ∼1300−1360 cm^{-1}) are observed overlapped by at least one additional band at shorter wavelengths around 479−494 nm

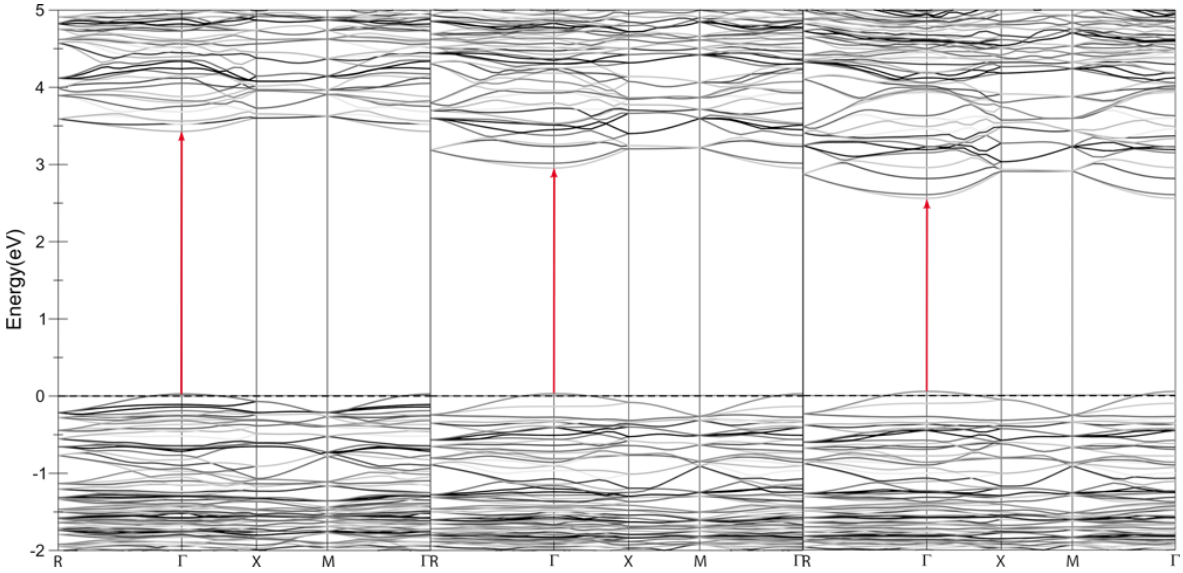

Figure 8.8: Calculated band structures of $Ba_3P_5N_{10}X$ with X = Cl (left), Br (center) and I (right), shown along the k-path R-Γ-X-M-Γ; the red arrows demonstrate the direct optical transitions.

(FWHM $\sim$2150$-$3260 cm^{-1}). In addition an emission band at 581 nm is observed (see Figure 8.11). For X = Cl, broadband emission around 435-465 nm, most likely also composed of at least two narrower emission bands, are observed besides a red-shifted emission band at $\sim$597 nm with FWHM in the 2300$-$2400 cm^{-1} range (see Figure G.3). The positions of the emission bands as well as their FWHMs are summarized in Table 8.5. Emission bands observed for X = Br fall in between the ranges of the iodine and chlorine compounds.

In order to approximate the position of the lowest lying absorption band and thus the zero-point energy, excitation spectra of the title compounds have been analyzed by the mirror-image relationship of absorption and emission bands on the energy scale.[37] It should be noted, however, that overlapping emission bands may lead to an overestimation of both spectral FWHMs and Stokes-shifts. The Stokes-shift for this lowest lying emission band in $Ba_3P_5N_{10}Cl{:}Eu^{2+}$, determined from the zero-point energy and the position of the emission maximum,[37] is approximated to $\sim$3100$-$3200 cm^{-1} for 2 and 5 mol% Eu^{2+}, respectively, indicating an average phonon frequency of this transition in the 400 cm^{-1} range.[38] Figure 8.12 shows exemplarily the mirror-image relationship between the low-energy excitation spectrum and the emission spectrum of $Ba_3P_5N_{10}Cl{:}Eu^{2+}$ (2 mol%). The excitation spectra fit the mirror-image of the respective emission band fairly well. The mirror-image fits of the other compounds can be found in the Supporting Information (Figure G.4).

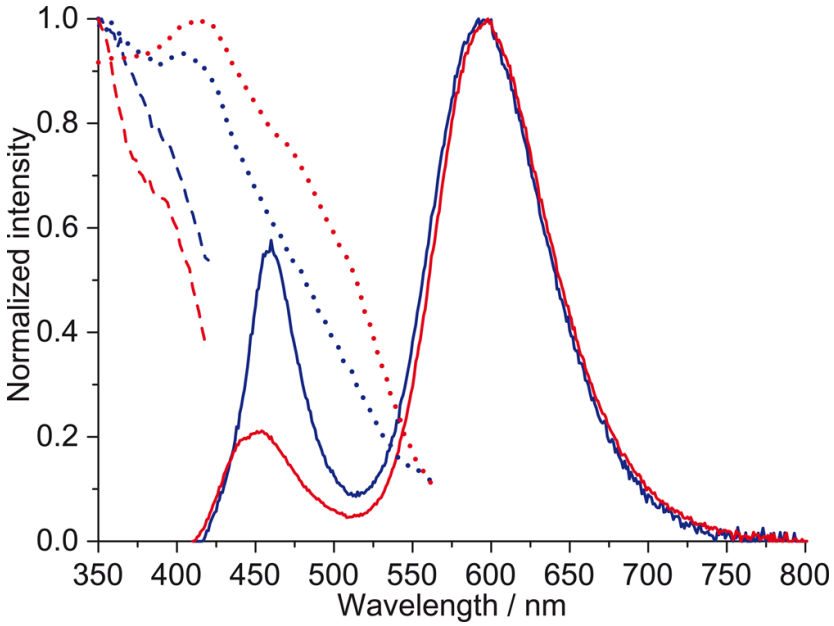

Figure 8.9: Excitation (dashed (dashed-dotted) line: monitoring range 435−490 (580−660) nm) and emission (solid lines) spectra of $Ba_3P_5N_{10}Cl:Eu^{2+}$ (2% Eu: blue curves, 5% Eu: red curves). CIE color coordinates: x = 0.442, y = 0.350 (2% Eu); x = 0.449, y = 0.381 (5% Eu).

Table 8.5: Determined emission band peak locations as well as their FWHMs for $Ba_3P_5N_{10}X:Eu^{2+}$ (2- and 5-mol%) with X = Cl, I.

$Ba_3P_5N_{10}X$		**wavelength / nm**	**energy / cm^{-1}**
X = Cl, 2% Eu^{2+}	emi1	450	1271
	emi2	461	2031
	emi3	597	2380
X = Cl, 5% Eu^{2+}	emi1	439	1650
	emi2	464	2310
	emi3	597	2310
X = I, 2% Eu^{2+}	emi1	479	2520
	emi2	509	1309
	emi3	581	3257
X = I, 5% Eu^{2+}	emi1	494	2400
	emi2	514	1360
	emi3	585	3150

In order to investigate the effect of the Eu doping level on the luminescence properties, the samples were also doped with 5-mol% Eu^{2+}. $Ba_3P_5N_{10}Cl:Eu^{2+}$ (5-mol%) shows pronounced orange luminescence,

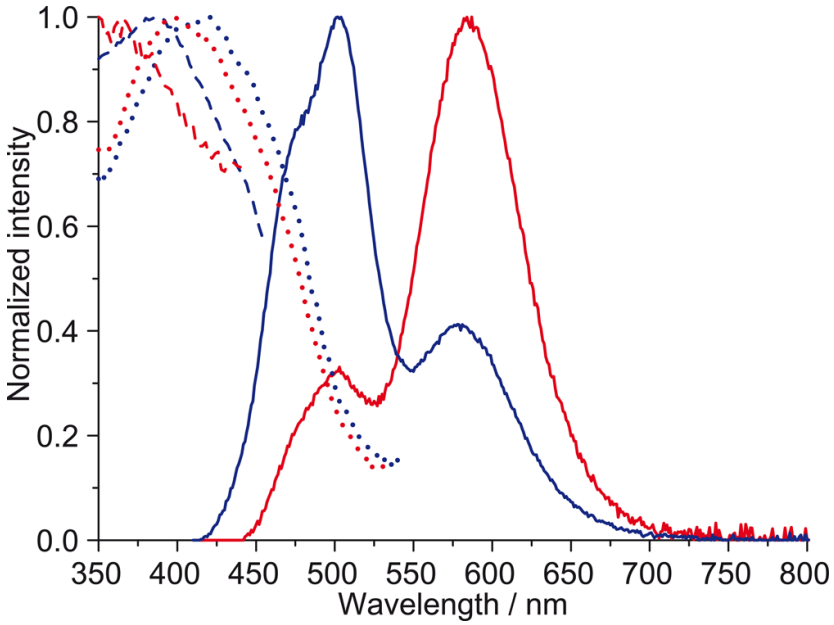

Figure 8.10: Excitation (dashed (dashed-dotted) line: monitoring range 460−510 (570−620) nm) and emission (solid lines) spectra of $Ba_3P_5N_{10}I:Eu^{2+}$ (2% Eu: blue curves, 5% Eu: red curves). CIE color coordinates: x = 0.265, y = 0.380 (2% Eu); x = 0.465, y = 0.463 (5% Eu).

$Ba_3P_5N_{10}I:Eu^{2+}$ (5-mol%) shows amber luminescence. Figure 8.13 illustrates the color coordinates of $Ba_3P_5N_{10}X:Eu^{2+}$ (X = Cl, I) revealing the shift of the respective color point depending on the doping level of Eu^{2+}. The change in color points with Eu concentration is similar to the change of correlated color temperatures of black body radiation with color points for X = Cl below and for X = I above Planckian, respectively (see Figure 8.12). As expected from these trends pure white on-Planckian emission is observed for X = Br.[24] For all samples investigated, an increase of the Eu concentration leads to a red-shift of the emission. The intensity of the higher energy bands decreases while the intensity of the low energy bands increases (see Figure 8.9 and 8.9). This shift of spectral power distribution to lower energies can be explained by increased reabsorption of the higher energy emission light by the centers with the lowest energy absorption bands and by increased quantum mechanical energy transfer between neighboring Eu centers due to decreased average Eu−Eu distances. A similar trend has been observed for $Ba_2Si_5N_8:Eu^{2+}$.[9]

The observation of multiple emission bands can be explained by the different crystal field strength and ligand charge density at the respective Eu^{2+} sites, occupying different Ba crystallographic sites. As discussed above, the five different Ba crystallographic sites can be divided into two groups depending on coordination numbers. Ba1, Ba4 and Ba5 (CN = 10) exhibit significantly longer Ba−N and Ba−X distances, causing a weaker crystal field on these sites. Consequently, Eu^{2+} ions occupying one of these three sites show the emission band in the high-energy part of the spectrum. The stronger crystal

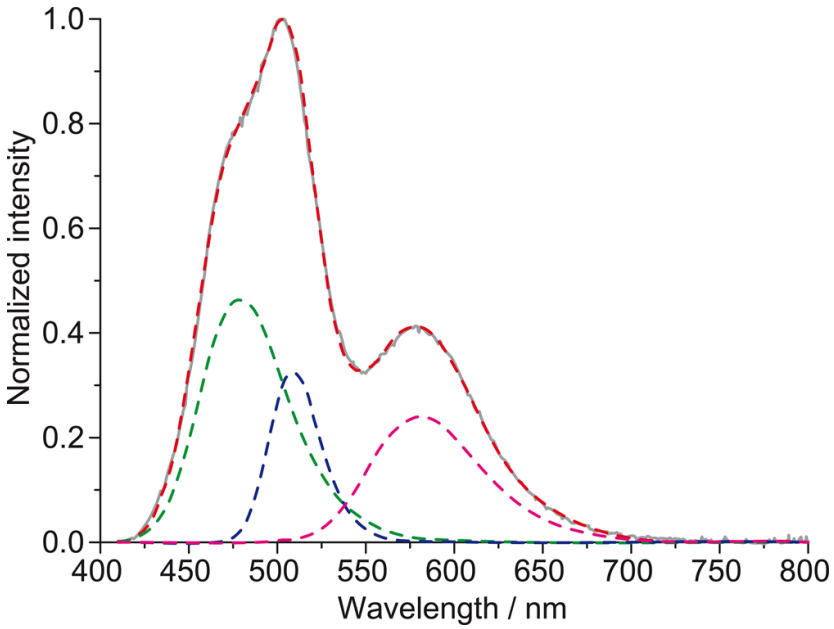

Figure 8.11: Least-square refinement of measured emission spectrum (gray solid line) of $Ba_3P_5N_{10}I:Eu^{2+}$ (2 mol%) with three individual curves (1: λ_{em} = 479 nm, FWHM = 2520 cm^{-1}, green dashed line; 2: λ_{em} = 509 nm, FWHM = 1309 cm^{-1}, blue dashed line; 3: λ_{em} = 581 nm, FWHM = 3257 cm^{-1}, magenta dashed line) and the resulting fit (red dashed line).

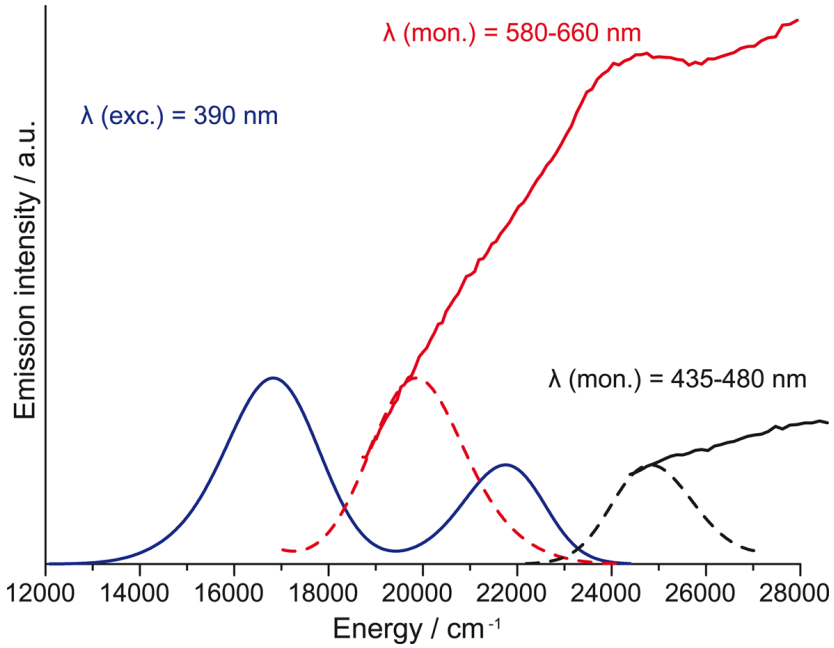

Figure 8.12: Estimation of absorption band position by mirror-image relationship between the excitation spectrum at λ_{mon} = 580−660 nm (red solid line) and λ_{mon} = 435-480 nm (black solid line) and the emission spectrum of $Ba_3P_5N_{10}Cl:Eu^{2+}$ (2 mol%), λ_{exc} = 390 nm (blue solid line). The red and black dashed lines are the mirror-images of the emission spectrum corresponding to zero phonon energies U_0 at ∼18320 and ∼23280 cm^{-1}, respectively.

field exerted on the Ba2 and Ba3 site (CN = 8) with shorter Ba−N and Ba−X bond lengths and resulting stronger crystal field strength leads to a red-shift of the emission band. A similar situation was observed in $Ba_3MgSi_2O_8:Eu^{2+}$, Mn^{2+}.[39] The absorption and emission bands of the Eu-centers with CN = 8 also show larger Stokes-shifts, most likely due to stronger relaxation of the Eu^{2+} ion on the smaller lattice sites.[40]

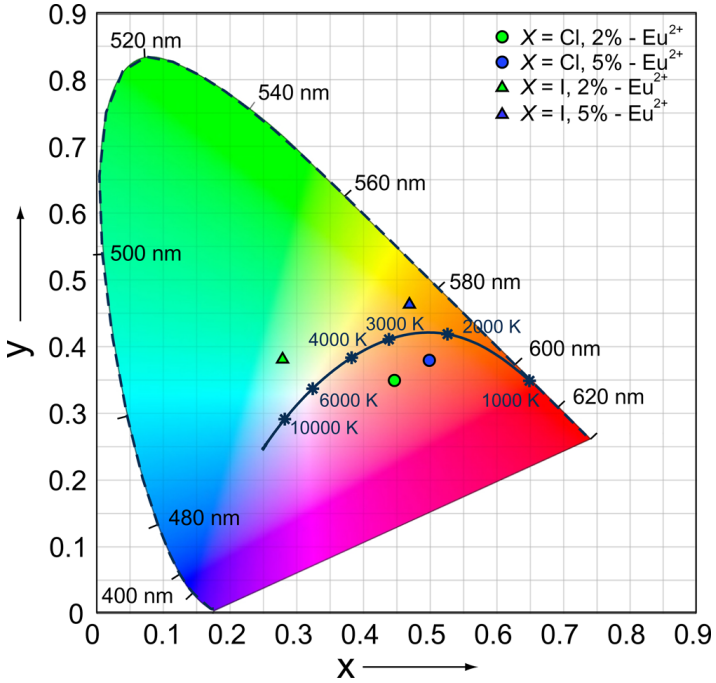

Figure 8.13: The CIE 1931 color space chromaticity diagram with color coordinates of $Ba_3P_5N_{10}X:Eu^{2+}$ (X = Cl, I) revealing the shift of the respective color point depending on variation of the doping level of Eu^{2+} from 2-mol% to 5-mol%.

Interestingly, the lower energy emission shows a red shift with decreasing size of halide ions while the higher energy emission bands show a respective blue shift. Since analysis of the excitation bands for the various transitions does not point towards significant Stokes-shift differences it is expected that this trend is due to changes of the local coordination of the Eu sites. A comparison of the bond lengths shows that the Ba−N distances are becoming significantly shorter for the CN = 8 sites while going from X = I to X = Cl, while the effect of the halide ion size on the Ba−N distances is less pronounced for the CN = 10 sites but the Ba−X distances may contribute more to the nephelauxetic effect for the CN = 10 sites. As a consequence, the CN = 10 sites lead to absorption and emission at lower energies for larger halide ion while for the CN = 8 sites leading to the long wavelength emission the impact of the Ba−N distances shortening on the crystal field splitting dominates and a shift of absorption and emission to higher energies for larger X is observed.

Due to the zeolite structure type of both nitridophosphates, possible hydrolysis sensibility as well as possible water intercalation, that could lead to luminescence quenching, was investigated. Therefore, the title compounds were stored under water for several days. However, neither decomposition nor luminescence quenching was observed. Thus, it can be noted that $Ba_3P_5N_{10}X$ (X = Cl, I), similarily to $Ba_3P_5N_{10}Br$, is only isotopological to the JOZ zeolite framework type[27] but is not porous at all. This feature is typical for other known oxonitridozeolites like NPO and NPT.[28–30] All these compounds are not porous thus preventing sorption of water and hydrolysis.

8.3 Conclusion

In this contribution we present novel nitridophosphates $Ba_3P_5N_{10}X$ (X = Cl, I) with a zeolite-like structure type. We were able to characterize these compounds by single-crystal and powder X-ray diffraction, FTIR and EDX spectroscopy. The title compounds are isotypic to the recently published $Ba_3P_5N_{10}Br$ and exhibit a topology which is analogous to the JOZ zeolite framework type. Furthermore the title compounds were successfully doped with Eu^{2+}, revealing intriguing luminescence properties. While $Ba_3P_5N_{10}Cl:Eu^{2+}$ shows orange luminescence, $Ba_3P_5N_{10}I:Eu^{2+}$ exhibits cyan to amber luminescence. Both compounds show several bands in the emission spectrum, which can be most likely explained by Eu^{2+} occupying different Ba lattice sites.

We are aware of the fact that the described system still needs further optimization in order to become competitive to currently used phosphors. However, we have underlined the high potential of nitridophosphates as high performance luminescence materials. Furthermore, $Ba_3P_5N_{10}X:Eu^{2+}$ represents an intriguing luminescence system with manifold tuning options. In this contribution we were able to show that by variation of halide ions X as well as variation of the Eu^{2+} doping level in $Ba_3P_5N_{10}X:Eu^{2+}$ the broad range of luminescence colors can be covered. It is therefore conceivable that the preparation of solid solution series with mixed halide ions on the one hand and varying Eu^{2+} doping level on the other hand, may lead even to higher variety on the possible luminescence colors. Moreover, taking into account the high thermal and chemical stability of nitridophosphates as well as the fact that its structural diversity is meanwhile similar to that of nitridosilicates, it is obvious, that particular attention should be paid to the luminescence properties of this compound class.

8.4 Experimental Section

8.4.1 Preparation of Starting Materials

Ba(N_3)$_2$ was synthesized by reaction of *in situ* formed diluted HN_3 with $BaCO_3$ (Grüssing, 99.8% trace metals basis) using a cation exchanger (Amberlyst 15). An aqueous solution of NaN_3 (Acros Organics, 99%, extra pure) was passed through the protonated cation exchanger, forming *in situ* diluted HN_3. The latter was dropped into a stirring aqueous suspension of $BaCO_3$, forming a solution of $Ba(N_3)_2$. The reaction is complete, when the suspension of $BaCO_3$ becomes entirely clear. In order to remove possible residues of $BaCO_3$, the product solution was filtered and the clear filtrate was then evaporated under reduced pressure (90 mbar, 80 °C). The product was formed as a colorless crystalline solid. Finally, $Ba(N_3)_2$ was recrystallized from acetone and dried *in vacuo* over P_4O_{10}. Phase purity of the product was confirmed by powder X-ray diffraction as well as FTIR spectroscopy. This synthesis procedure of $Ba(N_3)_2$ helps to overcome the problem of the potential danger of explosion of concentrated solutions of HN_3. However, special care is necessary when handling even dilute solutions of HN_3, since these are potentially explosive and the vapor is highly poisonous upon inhalation.

P_3N_5 was synthesized according to the procedure described by Stock and Grüneberg starting from P_4S_{10} (Sigma Aldrich, 99%) in a corundum boat in a continuous gas flow of dried NH_3 (Messer, Griesheim, 3.8).[41] The starting compound was heated to 900 °C at a rate of 3 °C/min and the temperature was held constant for 8 h. After cooling down to room temperature the product was washed with 1M HCl and ethanol to remove soluble byproducts. A yellow-brown product was finally dried at 100 °C. Phase purity of the product was confirmed by powder X-ray diffraction as well as FTIR spectroscopy.

8.4.2 Synthesis

$Ba_3P_5N_{10}X$ (X = Cl, I) were synthesized using a modified Walker-type multianvil apparatus by the reaction of stoichiometric amounts of $Ba(N_3)_2$, P_3N_5 and the respective barium halide (Sigma Aldrich, 99.999% trace metals basis) according to equation 8.1. Alternatively, the synthesis of both compounds can be carried out starting from other halide precursors, such as $P(NH_2)_4X$ (X = Cl, I)[42,43] or NH_4X (X = Cl, I) according to equations8.2 and 8.3. For luminescence investigations small amounts of the respective europium halide EuX_2 (X = Cl: Strem Chemicals, 99.9% trace metals basis; X = I: Sigma Aldrich, 99.9% trace metal basis) were added as dopand. All procedures were carried out under exclusion of oxygen and moisture in an argon filled glove box (Unilab, MBraun, Garching,

$O_2 < 1$ ppm, $H_2O < 0.1$ ppm).

The respective starting mixture was thoroughly ground, packed into a cylindrical crucible made up of hexagonal boron nitride (Henze, Kempten, Germany) and closed with a hexagonal boron nitride cap. The filled capsule was then centrally positioned in a Cr_2O_3-doped MgO octahedron (edge length 18 mm (18/11 assembly) and 25 mm (25/17 assembly), respectively, Ceramic Substrates & Components Ltd, Isle of Wight, UK). The MgO octahedron was equipped with a ZrO_2, sleeve (Cesima Ceramics, Wust-Fischbeck, Germany) which served as thermal insulator. Moreover, in order to heat the sample, the MgO octahedron also contained two concentric graphite tubes as electrical resistance furnaces. To center the sample capsule inside of the furnaces, two MgO-rods (Cesima Ceramics, Wust-Fischbach, Germany) were positioned on the bottom and top side. The furnace was contacted by two molybdenum plates (Mo007905, Goodfellow, Bad Nauheim, Germany) at the bottom and at the top of the ZrO_2 sleeve. The complete assembly was finally placed in the middle of a cube, which was built up of eight tungsten carbide cubes (Hawedia, Marklkofen, Germany) with a truncation edge length of 11 mm (18/11 assembly) and 17 mm (25/17 assembly), respectively. Detailed information on the assembly construction of the used multianvil assembly can be found in literature.[44] The starting mixture was pressed to the respective pressure (1-5 GPa) and then heated to approximately 1000 °C within 60 min. The temperature was held constant for 120 min. Subsequently, the sample was cooled down within 60 min and the pressure was slowly released.

$$15\,Ba(N_3)_2 + 3\,BaX_2 + 10\,P_3N_5 \longrightarrow 6\,Ba_3P_5N_{10}X + 40\,N_2 \tag{8.1}$$

$$9\,Ba(N_3)_2 + 4\,P_3N_5 + 3\,P(NH_2)_4X_2 \longrightarrow 3\,Ba_3P_5N_{10}X + 8\,NH_3 + 24\,N_2 \tag{8.2}$$

$$9\,Ba(N_3)_2 + 5\,P_3N_5 + 3\,NH_4X \longrightarrow 3\,Ba_3P_5N_{10}X + 4\,NH_3 + 24\,N_2 \tag{8.3}$$

8.4.3 Electron Microscopy

Electron microscopy as well as EDX analysis was carried out using a JEOL JSM 6500 F field emission scanning electron microscope (SEM) equipped with a field emission gun at a maximum acceleration voltage of 30 kV. The synthesized samples were prepared on adhesive conductive carbon pads. In order to make the surface of the samples conducting, they were sputtered with a conductive carbon film using an electron beam evaporator (BAL-TEC MED 020, Bal-Tec AG).

8.4.4 FTIR Spectroscopy

The FTIR spectra were recorded on a Spectrum BX II spectrometer (Perkin Elmer, Waltham MA, USA) using the KBr pellet method.

8.4.5 Single-Crystal X-Ray Diffraction

Single-crystal X-ray diffraction data of the synthesized samples were collected on a Bruker D8 Venture diffractometer with Mo-Kα-radiation (λ = 0.71073 Å). The frames were integrated with the Bruker SAINT software package using a narrow-frame algorithm and the data corrected for absorption effects using the semiempirical method (SADABS).[45,46] The structures were solved using direct methods implemented in SHELXS-97[47] and refined by full matrix least-squares calculation on F^2 using SHELXL-97.[47]

Details on the structure investigations may be obtained from the Fachinformationszentrum Karlsruhe, 76344 Eggenstein-Leopoldshafen, Germany (fax (+49)7247-808-666; E-Mail: crysdata@fiz-karlsruhe.de), on quoting the depository number CSD-429689 (X = Cl) and CSD-429688 (X = I).

8.4.6 Powder X-Ray Diffraction

Powder X-ray diffraction data was collected on a STOE StadiP powder diffractometer (Stoe & Cie, Darmstadt, Germany) in Debye-Scherer geometry using Mo-Kα_1-radiation (λ = 0.70930 Å) with a Ge(111)-monochromator and a linear position sensitive detector. Rietveld refinement was carried out using TOPAS Academics 4.1.[48] Background was handled using a shifted-Chebyshev function. Peak shapes were modeled by the fundamental parameters approach (direct convolution of source emission profiles, axial instrument contributions, crystallite size and microstrain effects).[49,50] In order to describe preferred orientation of the crystallites a spherical harmonics of fourth order was used.[51] Capillary absorption correction (inner diameter 0.08 mm) was carried out using the calculated absorption coefficient.

Temperature dependent X-ray powder diffraction measurements were performed on a Stoe StadiP diffractometer combined with a high-temperature furnace using Mo-Kα_1-radiation (λ = 0.70930 Å) with Ge(111)-monochromator and an image plate position sensitive detector. The samples were heated up to 900 °C with a rate of 1 °C/min between measurements. The temperature was held constant for each 15 min measurement.

8.4.7 UV/Vis Spectroscopy

Reflectance spectra were recorded on an Edinburgh Photonics FLS920 s spectrometer with a Xe900 450 W arclamp (Czerny Turner monochromator with three gratings, single photon photomultiplier detector). The measurements were carried out between 200 and 800 nm with step size of 5 nm.

8.4.8 Luminescence

Luminescence properties of single crystals were investigated using a luminescence microscope consisting of a HORIBA Fluorimax4 spectrofluorimeter-system attached to an Olympus BX51 microscope via fiber optics. Photoluminescence measurements on microcrystalline samples in PTFE sample holders were carried out using an in-house built system based on a 5.3" integrating sphere and a spectrofluorimeter equipped with a 150 W Xe lamp, two 500 mm Czerny–Turner monochromators, 1800 mm^{-1} lattices, and 250/500 nm lamps, with a spectral range from 230 to 820 nm. Low-temperature emission spectra of powder samples were recorded with an Ocean Optics HR2000 + ES spectrometer (2.048 pixels, grating UA (200-1.100 nm), slit 50) with the samples mounted in a closed-cycle He cryostat. The excitation wavelength was set to 390 nm with a spectral width of 10 nm. The emission spectra were collected in the wavelength interval between 410 and 820 nm with 1 nm step size. Excitation spectra were measured in the wavelength range between 350 and 570 nm with 1 nm step size.
Internal quantum efficiencies of samples were determined by comparing integrated emission intensities and absorption at excitation wavelength with standard materials ($BaSO_4$, Merck p.a.; commercial SCASN:Eu, Mitsubishi Chemical, and YAG:Ce, Philips).

8.4.9 DFT Calculations

DFT calculations of the electronic band structures were performed with the software Wien2000,[52] applying the full-potential linear augmented plane wave (FL-LAPW) method. The exchange and correlation functional of Perdew, Burke and Ernzerhof[53] with a generalized gradient approximation (GGA) was applied. The muffin-tin radii were set to 121.7 pm (2.5 a.u.) for Ba, Cl, Br and I atoms. Muffin-tin radii for N and P atoms were set to 75.45 pm and 71.56 pm, respectively (1.55 a.u. and 1.47 a.u.). The number of basis functions was determined by the value of $R_{mt} \cdot K_{max} = 8$ as the largest k vector. The separation energy was set to -8 Ry. 64 k points in the Brillouin zone (8 thereof in the irreducible Brillouin zone) were calculated in a $4 \times 4 \times 4$ Monkhorst-Pack grid.

8.5 References

[1] P. Pust, P. J. Schmidt, W. Schnick, *Nat. Mater.* **2015**, *14*, 454.

[2] M. Born, T. Jüstel, *Chem. unserer Zeit* **2006**, *40*, 294.

[3] C. Feldmann, *Z. Anorg. Allg. Chem.* **2012**, *638*, 2169.

[4] R. Mueller-Mach, G. Mueller, M. R. Krames, H. A. Höppe, F. Stadler, W. Schnick, T. Juestel, P. Schmidt, *Phys. Status Solidi A* **2005**, *202*, 1727.

[5] J. Heber, *Nat. Phys.* **2014**, *10*, 791.

[6] H. L. Li, X. J. Liu, L. P. Huang, *Opt. Mater.* **2007**, *29*, 1138.

[7] A. A. Setlur, *Electrochem. Soc. Interface* **2009**, *18*, 32.

[8] T. Moriguchi, Y. Noguchi, K. Sakano,Y. Shimizu, U.S. 5998925 A, July 29, **1997**.

[9] H. A. Höppe, H. Lutz, P. Morys, W. Schnick, A. Seilmeier, *J. Phys. Chem. Solids* **2000**, *61*, 2001.

[10] M. Zeuner, S. Pagano, W. Schnick, *Angew. Chem. Int. Ed.* **2011**, *50*, 7754; *Angew. Chem.* **2011**, *123*, 7898.

[11] W. Schnick, *Phys. Status Solidi RRL* **2009**, *3*, A113.

[12] R.-J. Xie, N. Hirosaki, *Sci. Technol. Adv. Mater.* **2007**, *8*, 588.

[13] R.-J. Xie, Y.Q. Li, N. Hirosaki, H. Yamamoto, *Nitride Phosphors and Solid State Lighting*, CRC Press (Taylor & Francis): New York **2011**.

[14] S. Schmiechen, H. Schneider, P. Wagatha, C. Hecht, P. J. Schmidt, W. Schnick, *Chem. Mater.* **2014**, *26*, 2712.

[15] F. Hintze, F. Hummel, P. J. Schmidt, D. Wiechert, W. Schnick, *Chem. Mater.* **2012**, *24*, 402.

[16] F. Hintze, N. W. Johnson, M. Seibald, D. Muir, A. Moewes, W. Schnick, *Chem. Mater.* **2013**, *25*, 4044.

[17] P. Pust, A. Wochnik, E. Baumann, P. J. Schmidt, D. Wiechert, C. Scheu, W. Schnick, *Chem. Mater.* **2014**, *26*, 3544.

[18] W. Schnick, *Angew. Chem. Int. Ed. Engl.* **1993**, *32*, 806; *Angew. Chem.* **1993**, *105*, 846.

[19] P. Pust, V. Weiler, C. Hecht, A. Tücks, A. S. Wochnik, A.-K. Henß, D. Wiechert, C. Scheu, P. J. Schmidt, W. Schnick, *Nat. Mater.* **2014**, *13*, 891.

[20] Y. Hirota, T. Hisaki, O. Mikami, *Electron. Lett.* **1985**, *21*, 690.

[21] Y. H. Jeong, G. T. Kim, U. J. Jeong, *J. Appl. Phys.* **1991**, *69*, 6699.

[22] Y. H. Jeong, Y. T. Lee, Y. T. Hong, *Appl. Phys. Lett.* **1990**, *57*, 2680.

[23] F. J. Pucher, A. Marchuk, P. J. Schmidt, D. Wiechert, W. Schnick, *Chem. Eur. J.* **2015**, *21*, 6443.

[24] A. Marchuk, W. Schnick, *Angew. Chem. Int. Ed.* **2015**, *54*, 2383; *Angew. Chem.* **2015**, *127*, 2413.

[25] F. Liebau, *Structural Chemistry of Silicates*, Springer, Berlin, **1985**.

[26] C. Bärlocher, L. B. McCusker, *Database of Zeolite Structures*: http://www.iza-structure.org/databases/, accessed April 2015.

[27] J. A. Armstrong, M. T. Weller, *J. Am. Chem. Soc.* **2010**, *132*, 15679.

[28] S. Correl, O. Oeckler, N. Stock, W. Schnick, *Angew. Chem. Int. Ed.* **2003**, *42*, 3549; *Angew. Chem.* **2003**, *115*, 3647.

[29] S. Correl, N. Stock, O. Oeckler, J. Senker, T. Nilges, W. Schnick, *Z. Anorg. Allg. Chem.* **2004**, *630*, 2205.

[30] S. J. Sedlmaier, M. Döblinger, O. Oeckler, J. Weber, J. Schmedt auf der Günne, W. Schnick, *J. Am. Chem. Soc.* **2011**, *133*, 12069.

[31] F. W. Karau, W. Schnick, *J. Solid State Chem.* **2005**, *178*, 135.

[32] F. Karau, W. Schnick, *Z. Anorg. Allg. Chem.* **2006**, *632*, 231.

[33] R. Hübenthal, *MAPLE, Version 4; Programm zur Berechnung des Madelunganteils der Gitterenergie*, Universität Gießen (Germany) **1993**.

[34] W. H. Baur, *Cryst. Rev.* **1987**, *1*, 59.

[35] R. D. Shannon, *Acta Crystallogr. Sect. A : Found. Crystallogr.* **1976**, *32*, 751.

[36] M. Seibald, T. Rosenthal, O. Oeckler, F. Fahrnbauer, A. Tücks, P. J. Schmidt, W. Schnick, *Chem. Eur. J.* **2012**, *18*, 13446.

[37] J. E. Van Haecke, P. F. Smet, D. Poelman, *J. Lumin.* **2007**, *126*, 508.

[38] B. Henderson, G. F. Imbusch, *Optical Spectroscopy of Inorganic Solids*, Clarendon Press, **1989**.

[39] J. S. Kim, P. E. Jeon, J. C. Choi, H. L. Parl, S. I. Mho, G. C. Kim, *Appl. Phys. Lett.* **2004**, *84*, 2931.

[40] A. Meijerink, G. Blasse, *J. Lumin.* **1989**, *43*, 283.

[41] A. Stock, H. Grüneberg, *Ber. Dtsch. Chem. Ges.* **1907**, *40*, 2573.

[42] S. Horstmann, W. Schnick, *Z. Naturforsch. B* **1996**, *51*, 127.

[43] W. Schnick, S. Horstmann, A. Schmidpeter, *Angew. Chem. Int. Ed. Engl.* **1994**, *33*, 785; *Angew. Chem.* **1994**, *106*, 818.

[44] a) N. Kawai, S. Endo, *Rev. Sci. Instrum.* **1970**, *41*, 1178; b) D. Walker, M. A. Carpenter, C. M. Hitch, *Am. Mineral.* **1990**, *75*, 1020; c) D. Walker, *Am. Mineral.* **1991**, *76*, 1092; d) D. C. Rubie, *Phase Transitions* **1999**, *68*, 431; e) H. Huppertz, *Z. Kristallogr.* **2004**, *219*, 330.

[45] Bruker, SAINT, Bruker AXS Inc., Madison, Wisconsin (USA) **2007**.

[46] Bruker, SADABS, Bruker AXS Inc., Madison, Wisconsin (USA) **2007**.

[47] G. M. Sheldrick, *Acta Crystallogr., Sect. A: Found. Crystallogr.* **2008**, *64*, 112.

[48] A. A. Coelho, *TOPAS-Academic*, Version 4.1, Coelho Software, Brisbane (Australia), **2007**.

[49] R. W. Cheary, A. Coelho, *J. Appl. Crystallogr.* **1992**, *25*, 109.

[50] R. W. Cheary, A. Coelho, J. P. Cline, *J. Res. Natl. Inst. Stand. Technol.* **2004**, *109*, 1.

[51] M. Järvinen, *J. Appl. Crystallogr.* **1993**, *26*, 525.

[52] P. Blaha, K. Schwarz, G. K. H. Madsen, D. Kvasnicka, J. Luitz, WIEN2k, Technische Universität Wien, Austria, **2006**.

[53] J. P. Perdew, K. Burke, M. Ernzerhof, *Phys. Rev. Lett.* **1996**, *77*, 3865.

9 Summary

Objectives of the Thesis

The main objectives of this thesis were the high-pressure high-temperature synthesis and characterization of new alkaline earth metal (oxo)nitridophosphates and phosphorus nitrides using the multianvil technique as well as investigation of possible luminescence properties of resulting compounds. Furthermore, a new synthetic strategy should be developed in order to grow single crystals of (oxo)nitridophosphates under high-pressure conditions. Prior to this work no single-crystals of this compound class could be obtained by using the synthesis under high-pressure conditions. Usually, the successful characterization of new (oxo)nitridophosphates requires the phase pure synthesis of the samples on the one hand and a combination of different analytical methods such as powder X-ray diffraction, solid-state NMR spectroscopy or electron microscopy on the other hand. Thus, the investigation of a new synthetic approach for the growth of single-crystals of (oxo)nitridophosphates should significantly accelerate the investigation of new compounds in the future.

Employment of NH_4Cl as a Mineralizer during High-Pressure High-Temperature Synthesis

The challenge of the poor crystallinity of (oxo)nitridohosphates has been mastered by adding NH_4Cl as mineralizer to the respective starting mixture. This compound decomposes at high temperatures to NH_3 and HCl. It is assumed that HCl enables reversible reconstructive P−N bond cleavage and reformation thus leading to the growth of single crystals. The advantage of NH_4Cl lies in the absence of any foreign metal ions, which could lead to undesirable side phases. Moreover, after successful synthesis, NH_4Cl may be easily removed from the sample by washing it with water and ethanol provided the products are stable against hydrolysis. Otherwise, should the samples be hydrolysis-sensitive, the mineralizer may be separated from the product by sublimation *in vacuo*.

A High-Pressure Polymorph of Phosphorus Nitride Imide (Chapter 2)

A first high-pressure polymorph of the phosphorus nitride imide HPN_2 has been synthesized in a Walker-type multianvil device at 6 GPa and 1000 °C. Amorphous HPN_2 was used as starting material. By adding small amounts of NH_4Cl as a mineralizer it was possible to grow single crystals of the product. This allowed complete structure elucidation of β-HPN_2 including unequivocal determination of the H atoms positions in the crystal structure. The crystal structure of the new polymorph β-HPN_2 (space group $P2/c$ (no. 13), a = 7.8853(16), b = 4.8278(10), c = 8.1456(16) Å, β = 108.19(3)°, V = 294.6(1) Å^3, Z = 8) was solved and refined from single-crystal X-ray diffraction data and confirmed by Rietveld refinement. Furthermore, the product was characterized by EDX, FTIR and solid-state NMR spectroscopy. The crystal structure can be described as a three-dimensional network of all-side vertex-sharing PN_4, in which the hydrogen atoms are covalently bound to half of the N atoms (see Figure 9.1). The condensation of the PN_4 tetrahedra leads to *sechser*-rings, P_6N_6. The topology of the structure network is identical with that of α-HPN_2, high- and low-cristobalite.

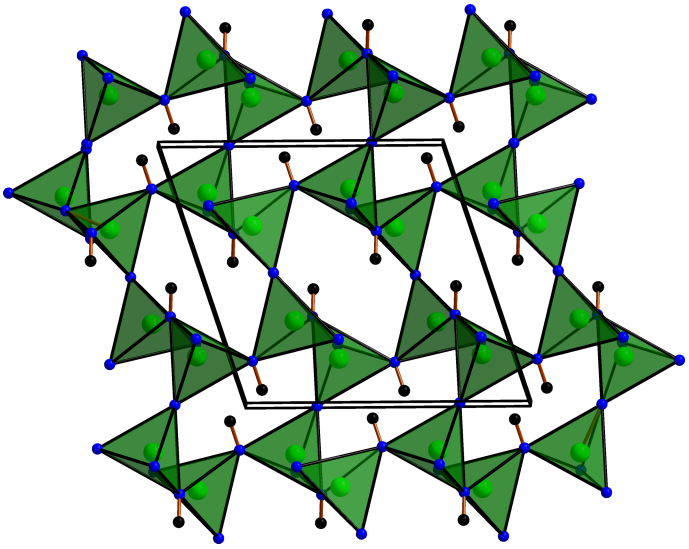

Figure 9.1: Crystal structure of β-HPN_2, view along [010]. PN_4 tetrahedra are drawn in green, H atoms in black.

The novel synthetic approach to grow single crystals of phosphorus nitrides under high-pressure high-temperature conditions allowed the first complete structural investigation of a highly condensed phosphorus nitride from single-crystal X-ray diffraction data.

M_2PO_3N (M = Ca, Sr) – *ortho*-Oxonitridophosphates with β-K_2SO_4 Structure Type (Chapter 3)

Two novel oxonitridophosphates M_2PO_3N with M = Ca, Sr were synthesized under high-pressure high-temperature conditions (7 GPa, 1100 °C) using the multianvil technique as well as by solid-state reactions in the silica ampoules (1100 °C) from amorphous phosphorus oxonitride PON and the respective alkaline earth oxides MO (M = Ca, Sr). It was possible to grow single crystals of both compounds under high-pressure condition by using NH_4Cl as a mineralizer allowing complete structure determination on the basis of single-crystal X-ray diffraction data. Both compounds crystallize in β-K_2SO_4 structure type, thus representing the first examples of alkaline earth *ortho*-oxonitridophosphates containing discrete $[PO_3N]^{4-}$ anions (see Figure 9.2). So far, only one *ortho*-oxonitridophosphate is known, namely $Li_{14}(PON_3)_2O$, however with isolated PON_3 tetrahedra instead. While PO_3N tetrahedra in Sr_2PO_3N (space group *Pnma*, no. 62, Z = 4, a = 7.1519(5), b = 5.5778(3), c = 9.8132(7) Å) exhibit marked static disorder, the crystal structure of Ca_2PO_3N reveals an incommensurate modulation along [100] ((3+1)D superspace group *Pnma*(α00)0*ss*, modulation vector q = (0.287(5), 0, 0), Z = 4, a = 6.7942(7), b = 5.4392(6), c = 9.4158(11) Å), as shown in Figure 9.3. Rietveld refinements support the structural models of the products. Furthermore, upon doping with Eu^{2+} Ca_2PO_3N exhibits green luminescence which can be excited by near-UV light (λ_{exc} = 400 nm). This feature makes Ca_2PO_3N:Eu^{2+} an interesting candidate for possible use as a luminescent material.

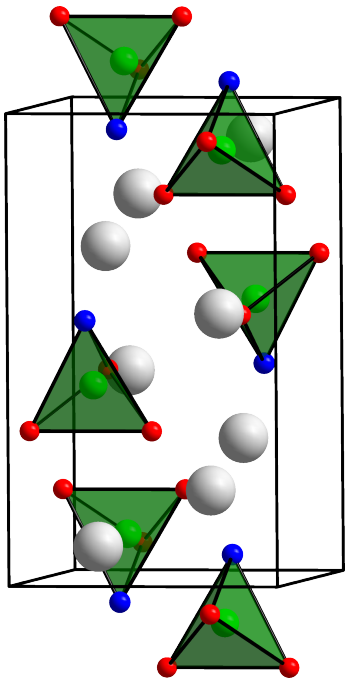

Figure 9.2: Crystal structure of M_2PO_3N (M =Mg, Ca), view along [100]. PO_3N tetrahedra are drawn in green., M in gray.

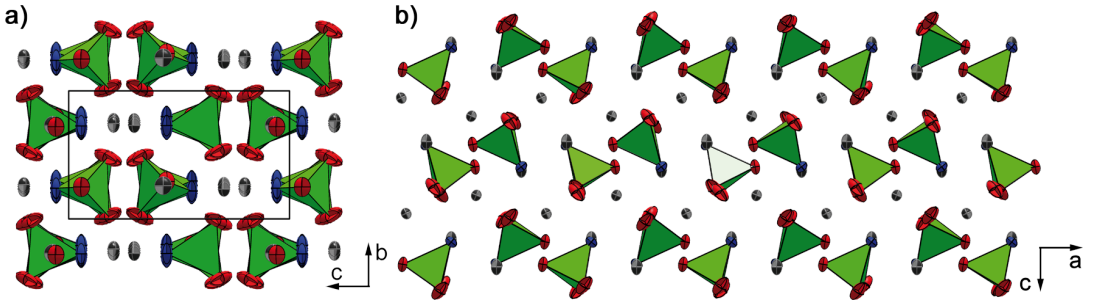

Figure 9.3: View of the modulated structure of Ca_2PO_3N along [100], approximate superstructure model with 10 unit cells along [100] (a). View of the same approximate structure along [010] (b), 4 unit cells along [100], 1/q = 3.484a.

MH$_4$P$_6$N$_{12}$ (M = Mg, Ca): New Imidonitridophosphates with an Unprecedented Layered Network Structure Type (Chapter 4)

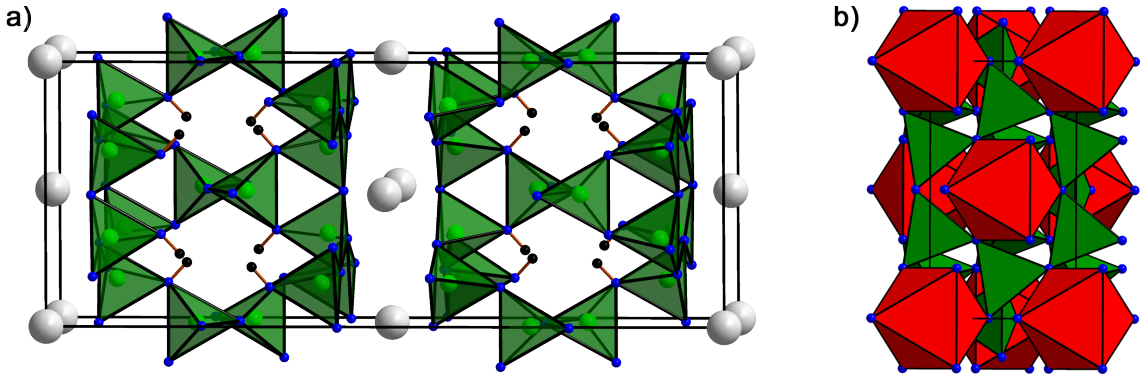

Figure 9.4: Crystal structure of MH$_4$P$_6$N$_{12}$ (M = Mg, Ca), view along [010] (left), and [001] (right). PN$_4$ tetrahedra are drawn in green, MN$_6$ octahedra in red, H atoms in black, M atoms in gray.

The first known layered nitridoimidophosphates MH$_4$P$_6$N$_{12}$ (M = Mg, Ca) were synthesized by high-pressure high-temperature reactions at 8 GPa and 1000°C starting from stoichiometric amounts of the respective alkaline earth metal nitrides M_3N$_2$, P$_3$N$_5$, and amorphous HPN$_2$. The addition of small amounts of NH$_4$Cl as mineralizer led to large transparent platelet single crystals of both compounds. The crystal structure elucidation of both isotypic compounds was carried out by the single-crystal X-ray diffraction data (space group *Cmce* (no. 64), ***M* = Mg**: a = 8.4568(16), b = 4.8270(10), c = 21.309(4) Å, V = 896.8(3) Å^3, Z = 4; ***M* = Ca**: a = 8.6289(17), b = 4.9010(10), c = 22.153(4) Å, V = 936.9(3) Å^3, Z = 4). Similar to β-HPN$_2$, the positions of H atoms could be clearly determined. The structural models were supported by Rietveld refinement and FTIR spectroscopy. Furthermore, the hydrogen contents of the samples have been successfully determined by quantitative solid-state ^{1}H NMR measurements.

The crystal structures of the products consist of all-side vertex-sharing PN$_4$ tetrahedra, forming parallel oriented double layers which alternate with respective metal ion layers (see Figure 9.4). The topology of these layers has not been found in any other known compound so far. The condensation of the PN$_4$ tetrahedra leads to the *dreier* and *sechser* rings forming rhombic channels, in which H atoms are covalently bound to N atoms. From a topologically point of view, the double layers represent parallel honeycomb-like pattern. With respect to this structural feature and the stability of the products against water, MH$_4$P$_6$N$_{12}$ appear to be promising candidates for liquid exfolation of the single layers, which may lead to two-dimensional single nanomaterials with intriguing properties.

$CaMg_2P_6O_3N_{10}$ – A Quinary Oxonitridophosphate with an Unprecedented Tetrahedra Network Structure Type (Chapter 5)

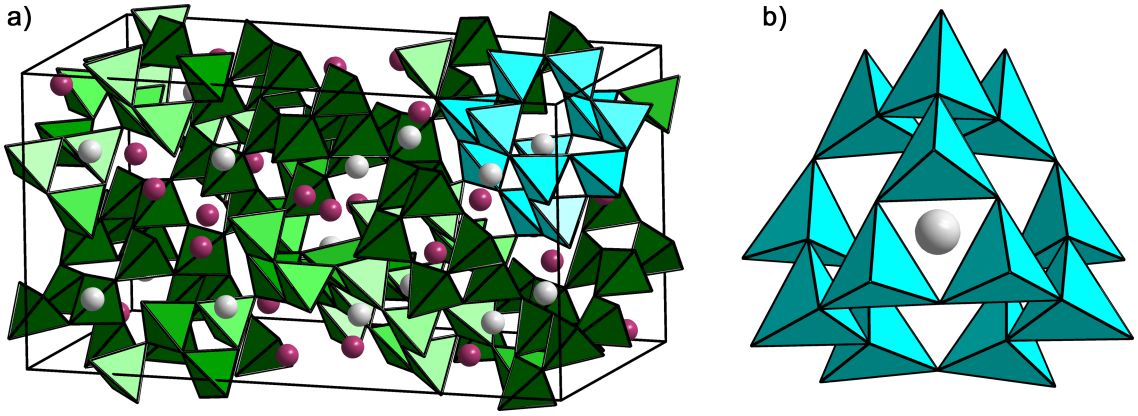

Figure 9.5: Crystal structure of $CaMg_2P_6O_3N_{10}$ with the characteristic polyhedral building unit (PBU), shwon in cyan (a) as well as the enlarged PBU (b). The $P(O,N)_4$ tetrahedra are shown in green, Ca atoms in gray, Mg atoms in dark-red, O atoms in light-red, N atoms in blue.

$CaMg_2P_6O_3N_{10}$ has been synthesized starting from stoichiometric amounts of $Ca(N_3)_2$, Mg_3N_2, P_3N_5, and PON in a high-pressure high-temperature reaction at 8 GPa and 1100 °C. By adding of NH_4Cl as a mineralizer, single crystals of the product were obtained, which form transparent, colorless truncated octahedra. Consequently, the crystal structure (space group $I4_1/acd$ (no. 142), a = 12.494(1), c = 23.797(2) Å, V = 3707.0(5) Å^3, Z = 16) could be solved and refined by single-crystal X-ray diffraction analysis. Phase purity was confirmed by Rietveld refinement. Furthermore, structure characterization includes a broad spectrum of analytical methods, such as transmission electron microscopy, including HRTEM image simulations, FTIR and EDX spectroscopy as well as bond valence and lattice energy calculations (MAPLE).

The crystal structure of $CaMg_2P_6O_3N_{10}$ consists of a three-dimensional interrupted network of vertex-sharing Q^4- and Q^3-type $P(O,N)_4$ tetrahedra exhibiting an unprecedented tetrahedra network structure type (see Figure 9.5, a). The structure can be subdivided in polyhedral building units (PBUs), built up from vertex-sharing $P(O,N)_4$ tetrahedra with condensed *dreier* and *sechser* rings (see Figure 9.5, b). The topological representation of the PBU corresponds to a slightly distorted Friauf polyhedron. When taking a closer look at the structure, it becomes apparent that the interconnected PBUs form two independent strands, resulting in two-fold interpenetrated network. Furthermore, $CaMg_2P_6O_3N_{10}$ is the first known compound with twelve-fold N coordination of Ca atoms.

Luminescent Nitridophosphates $CaP_2N_4:Eu^{2+}$, $SrP_2N_4:Eu^{2+}$, $BaP_2N_4:Eu^{2+}$, and $BaSr_2P_6N_{12}:Eu^{2+}$ (Chapter 6)

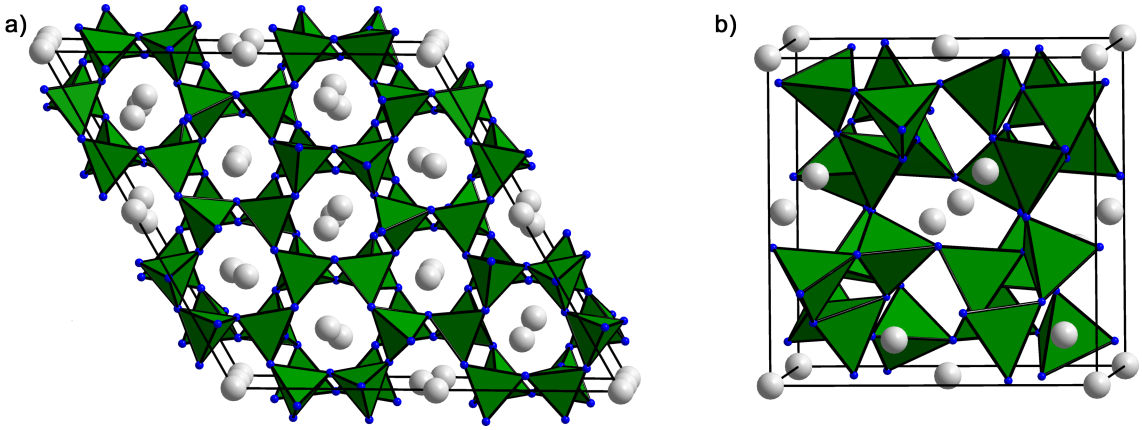

Figure 9.6: Crystal structure of MP_2N_4 with M = Ca, Sr (a) and BaP_2N_4 (b); both viewed along [001]. The PN_4 tetrahedra are shown in green, alkaline earth metal atoms in gray, nitrogen atoms in blue

The highly-condensed nitridophopshates $MP_2N_4:Eu^{2+}$ (M = Ca, Sr, Ba) and $BaSr_2P_6N_{12}:Eu^{2+}$ represent the first luminescent ternary nitridophosphates. The title compounds have been synthesized via high-pressure high-temperature reactions at 5−8 GPa and 1100− 1300 °C starting from the corresponding azides $M(N_3)_2$ and P_3N_5 using $EuCl_2$ as dopand. Addition of NH_4Cl as mineralizer allowed the growth of single crystals of $CaP_2N_4:Eu^{2+}$ (see Figure 9.7) and led to the first successful structure determination of a highly condensed ternary nitridophosphate from single-crystal X-ray diffraction data (space group $P6_3$ (no. 173), a = 16.847(2), c = 7.8592(16) Å, V = 1931.7(6) Å^3, Z = 24). The proposed megacalsilite structure type of CaP_2N_4 was confirmed (see Figure 9.6, a). SrP_2N_4 is isostructural to CaP_2N_4, whereas BaP_2N_4 and $BaSr_2P_6N_{12}$ exhibit a high-pressure CaB_2O_4-(IV) type of structure (see Figure 9.6, a). Eu^{2+}-doped samples of CaP_2N_4, SrP_2N_4, BaP_2N_4 and $BaSr_2P_6N_{12}$ reveal luminescence properties depending on the length of the metal-N-distances. With larger cations and thus longer distances, the emission maximum shifts to smaller wavelengths, leading to orange ($CaP_2N_4:Eu^{2+}$, λ_{max} = 575 nm) and green ($SrP_2N_4:Eu^{2+}$, λ_{max} = 529 nm) emitting compounds. In the case of $BaP_2N_4:Eu^{2+}$ and $BaSr_2P_6N_{12}:Eu^{2+}$ luminescence was observed in the blue region of the visible spectrum (λ_{max} = 450 nm and 460 nm, respectively).

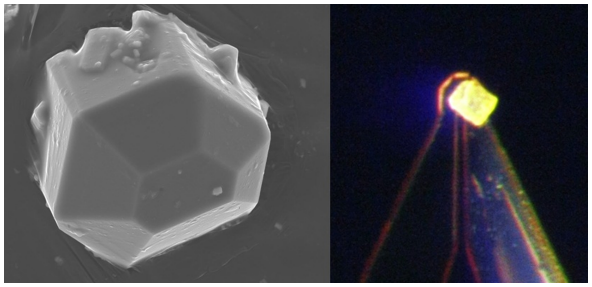

Figure 9.7: Single crystal of $CaP_2N_4:Eu^{2+}$; left: REM image, right: orange luminescence upon excitation by UV light.

Nontypical Luminescence Properties and Structural Relation of $Ba_3P_5N_{10}X:Eu^{2+}$ (X = Cl, Br, I) – Nitridophosphate Halides with Zeolite-like Structure (Chapter 7, 8)

The synthesis, structural characterization and luminescence properties of the novel nitridophosphates $Ba_3P_5N_{10}X$ (X = Cl, Br, I) are described. These isotypic compounds have been synthesized by the reaction of stoichiometric amounts of $Ba(N_3)_2$, BaX_2 (X = Cl, Br, I) and P_3N_5. 2 mol% $EuCl_2$ were used as doping agent. The synthesis was carried out in a Walker-type multianvil assembly at 1000 °C and pressures between 1 and 5 GPa.

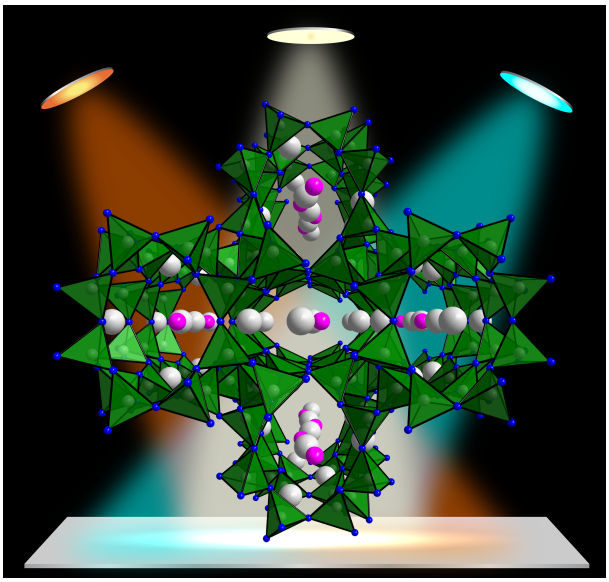

Figure 9.8: Crystal structure of $Ba_3P_5N_{10}X:Eu^{2+}$ with X = Cl, Br, I.

The crystal structures (space group *Pnma* (no. 62), Z = 8, **$Ba_3P_5N_{10}Cl$**: a = 12.5182(5), b = 13.1798(5), c = 13.7676(6) Å, V = 2271.5(2) Å^3; **$Ba_3P_5N_{10}Br$**: a = 12.5660(13), b = 13.2240(13), c = 13.8030(14) Å, V = 2293.7(4) Å^3; **$Ba_3P_5N_{10}I$**: a = 12.6311(7), b = 13.2565(8), c = 13.8689(8) Å, V = 2322.3(2) Å^3) were solved and refined on the basis of single-crystal X-ray diffraction data. Phase purity of the products as well as the accuracy of the structure elucidation was varified by Rietveld refinement. Further characterization by FTIR and energy-dispersive X-ray (EDX) spectroscopy supported the structural model.

The crystal structure is built up of all-side vertex-sharing PN_4 tetrahedra leading to a zeolite-like framework with three-dimensional *achter*-ring channels. These contain alternately Ba and halide atoms Cl, Br and I, respectively. The framework topology is analogous to that of the JOZ zeolite. The PN_4 tetrahedra form condensed *dreier*, *vierer* and *achter* rings. This condensation results in two slightly distorted composite building units made up of $3^4 4^2 8^6$-cages.

Upon excitation by near-UV light ($\lambda_{exc.}$ = 390 nm) orange (X = Cl), natural-white (X = Br) and cyan to amber (X = I) luminescence was observed. All three compounds exhibit several bands in the emission spectrum, which can be explained by Eu^{2+} occupying different Ba lattice sites.

10 Conclusion & Outlook

NH_4Cl as Mineralizer in High-Pressure High-Temperature Synthesis

Based on the results described in this thesis it becomes clear that the employment of NH_4Cl as mineralizer in high-pressure high-temperature synthesis using multianvil technique represents a breakthrough in the preparative P/O/N chemistry. This synthetic method opens up a completely new approach to search for new phosphorus nitrides and (oxo)nitridophosphates. By enabling single crystal growth it allows for the investigation of not only the main phase compounds but also minority phases, significantly accelerating the systematic study of the uncharted regions of (oxo)nitridophosphates with potentially unprecedented properties.

It should though be noted that NH_4Cl cannot be considered a universally applicable mineralizer, solving all kinds of problems concerning poor crystallization of (oxo)nitridophosphates. In some cases this compound provokes H^+- transfer reactions, thus acting not only as a mineralizer but also as a reaction partner. This irreversible protonation leads to the insertion of imide groups into the network structures of the target phosphorus nitrides and nitridophosphates, resulting in the formation of respective compound classes of phosphorus nitride imides and nitridoimidophosphates. However, this limitation can be turned into an advantage by making purposeful use of its features in order to synthesize deliberately nitridoimidophosphates and thus exploring these scarcely known compound classes. The suitability of this approach has been confirmed by the synthesis of β-HP_4N_7 and γ-HP_4N_7,[1,2] both representing unprecedented structure types. Nevertheless, it becomes clear that screening of other potential mineralizers should be carried out in order to employ them specifically for a given compound system.

Development of Further Synthetic Approaches

Additionally to the employment of a mineralizer, other potential synthetic approaches still remain, which may lead to the enhanced crystallinity of (oxo)nitridophosphates, such as high-pressure high-temperature synthesis via solid state metathesis reaction. Most recently, Kloß *et al.* reported on the synthesis of the rare earth metal nitridophosphate $LiNdP_4N_8$ via high-pressure high-temperature synthesis.[3] Lithium halide, formed *in situ* by the reaction of $LiPN_2$ with the respective rare earth

metal halide, here serves as flux and thus facilitates the formation of single crystals. However, as already mentioned in chapter 1, the sudden increase in sample volume of the pellet during liquefaction of the lithium halide often leads to technical problems (*blowouts*) when multianvil setup is used. Furthermore, due to the thermodynamic control of the metathesis reaction, the formation of exclusively thermodynamically stable phases can be expected, thus hindering access to metastable phases. The presented high-pressure metathesis approach is also limited by the use of $LiPN_2$ as a reaction partner, which increasingly leads to the formation of lithium-containing nitridophosphates. Mentioned problems may be avoided by applying phosphorus nitride imides, like HPN_2 instead of $LiPN_2$ as a starting material. This metathesis reaction then would lead to the *in situ* formation of HCl. Similar to NH_4Cl, it may enable reversible reconstructive P−N bond cleavage and reformation, thus facilitating single-crystal formation of (oxo)nitridophosphates. The degree of condensation in the network of the respective target compound could be adjusted by selection of anappropriate phosphorus nitride imide, e.g. HPN_2, HP_4N_7.

Novel Structural Varieties of (Oxo)Nitridophosphates and Nitridoimidophosphates

Appart from the above mentioned investigation of the novel synthetic approach, this work also presents investigations on numerous novel alkaline earth metal (oxo)nitridophosphates, exhibiting a degree of condensation κ ranging from 0.25 to 0.5. Most of the discovered compounds represent unprecedented structure types, thus significantly increasing the structural diversity of the compound class of (oxo)-nitridophosphates and in the same time revealing their structural potential being far from exhausted. Each of the discovered structure types is an ideal starting point for the research of further isotypic compounds which may exhibit intriguing properties. Not only the introduction of alkaline earth metal ions but also of transition or rare earth metal ions may possible in these compounds. Especially, the host lattices of $CaMg_2P_6O_3N_{10}$ and $MH_4P_6N_{12}$ (M = Mg, Ca) should be mentioned as promising candidates.

The interrupted tetrahedra network of the oxonitridophosphate $CaMg_2P_6O_3N_{10}$ offers a great possibility to vary the charge of the network structure by changing the O/N ratio. Kloß *et al.* could already confirm the feasibility by discovering of a novel rare earth metal nitridophosphate $Yb_5P_{12}O_3N_{23}$.[4] This compound crystallizes in the $CaMg_2P_6O_3N_{10}$ structure type with Yb atoms occupying the sites of Ca and Mg atoms, altering the network charge from $[P_6O_3N_{10}]^{6-}$ to $[P_{12}O_3N_{23}]^{15-}$ by adjusting the O/N ratio.

The possibilities for the network structures of $MH_4P_6N_{12}$ (M = Mg, Ca) are no less versatile. The

double layers in the crystal structure do not contain any metal atoms and thus are not affected by their size. Due to the sandwich type of this structure, the synthesis of isotypic compounds by exchanging of alkaline earth metal ions may lead to new interesting properties. An isotypic Sr compound should for example be accessible which, when doped with Eu^{2+}, may yield interesting luminescence properties. Considering all metal atoms occupying only one crystallographic site and being coordinated in highly symmetrical octahedral arrangement, a narrow-band emitter could be expected. According to the structural features and material properties, $MH_4P_6N_{12}$ (M = Mg, Ca) is furthermore predestined for liquid exfoliation of single layers in order to obtain two-dimensional nanomaterials. Future research also may focus on investigations of the ion-exchange or intercalation properties of these compounds with respect of application in gas absorbers or ionic conductors.

(Oxo)Nitridophosphates as Host Lattices for Novel Luminescent Materials

Not only the structural investigation of novel (oxo)nitridophosphates, but also the investigation of their remarkable luminescence properties represents an important advance in P/O/N chemistry. It was possible to synthesize numerous interesting luminescent materials by doping highly condensed nitridophosphates with Eu^{2+}, underlining their potential as high-performance luminescence materials. Especially, the Eu^{2+}-doped zeolite-like nitridophosphate halides $Ba_3P_5N_{10}X:Eu^{2+}$ with X = Cl, Br, I represent an intriguing luminescence system with manifold tuning options. By varying both the halide ions X and the Eu^{2+} doping level in $Ba_3P_5N_{10}X:Eu^{2+}$ it was possible to cover a broad range of luminescence colors. As a highlight of this system $Ba_3P_5N_{10}Br:Eu^{2+}$ should be mentioned, exhibiting natural-white-light as a single emitter and thus representing a promising candidate for application as single white emitter in warm-white pcLEDs. Consequently, preparing solid solutions by mixing halide ions in this system may lead to phosphors with luminescence colors covering the entire visible spectrum. Both systems $MP_2N_4:Eu^{2+}$ and $Ba_3P_5N_{10}X:Eu^{2+}$ furthermore demonstrate the necessity of the synthesis of homologous series in order to fully understand the nature of luminescence in the respective phosphors. Homologous series allow to set individual compounds and their luminescence properties into correlation in order to recognize trends. Without the synthesis of $Ba_3P_5N_{10}X:Eu^{2+}$ (X = Cl, I) in comparison $Ba_3P_5N_{10}Br:Eu^{2+}$ it would be impossible to understand the nontypical luminescence properties in these zeolite-like systems.

Due to the structural similarities of (oxo)nitridophosphates and (oxo)nitridosilicates, a screening of already existing high-performance luminescence materials should be carried out in order to synthesize the respective isotypic (oxo)nitridophosphates. The discovery of the luminescent *ortho*-oxonitrido-

phosphate $Ca_2PO_3N:Eu^{2+}$ isotypic to the already applied green phosphor $Ba_2SiO_4:Eu^{2+}$,[5–7] underlines the positive prospects for this method.

Considering this, the synthesis of novel garnet-type compounds such as $Ca_3Al_2P_3N_3O_9:Ce^{3+}$, $Ca_3P_5N_7O_5:Ce^{3+}$ or (oxo)nitridophosphates with UCr_4C_4 structure type, like $Sr[Li_3PO_2N_2]:Eu^{2+}$ could lead to highly promising phosphors. Preliminary experiments have already given hints on the existence of the latter.

Investigation of New Compound Classes

The discovery of silicon phosphorus nitride $SiPN_3$ by Lücke *et al.* has illustrated the possibility of mixing Si and P in tetrahedral centers of nitridophosphate network structures.[8] Although the synthesis of this compound was accomplished with a molecular approach, it is reasonable that the synthesis of mixed (oxo)nitridosilicatophosphates with both containing phosphorus and silicon occupying the tetrahedral centers is possible by means of high-pressure high-temperature reaction. The experiments in the course of this work already showed evidence for the existence of such a compound. The reaction of $Sr(N_3)_2$, P_3N_5, amorphous PON and amorphous Si_3N_4 under high-pressure high-temperature conditions led to a compound with composition $Sr_3P_3Si_5N_{11}O_4$, as determined by EDX spectroscopy. The single crystal X-ray diffraction data revealed an oxonitridosilicatophosphate $Sr_3P_{7-x}Si_{1+x}N_{15-x}O_x$, isotypic to the sialon $RE_3Si_{8-x}Al_xN_{11-x}O_{4+x}$ ($x \approx 1.75$ for RE = Ce; $x \approx 1.5$ for RE = La).[9]. Interestingly, the isotypic oxonitridosilicate $La_3Si_8O_4N_{11}$ is a blue phosphor when doped with Ce^{3+}.[10] This fact renders $Sr_3P_{7-x}Si_{1+x}N_{15-x}O_x$ a potential candidate for exhibiting luminescence properties if doped with Eu^{2+}. Furthermore, a broad spectrum of extremely promising compounds $M_3P_{7-x}Si_{1+x}N_{15-x}O_x$ with M = Ca, Sr, Ba and $x = 0-1$ results, including many potential phosphors, when doped with Eu^{2+}. The total crystal structure determination of $Sr_3P_{7-x}Si_{1+x}N_{15-x}O_x$ is strongly affected by difficulties resulting from the similarity of the electron density of Si/O and N/P, respectively, and building units with simultaneous Si/P and O/N disorder. Consequently, it is not impossible to clearly assign the Si, P, O and N atoms to the respective structure factors. A conceivable solution for this problem may be the synthesis of isotypic compounds with Ge instead of Si, free of O atoms, namely $Sr_3P_7GeN_{15}$. Due to the significantly higher electron density of Ge compared to Si as well as absence of O/N disorder it may be possible to determine the detailed crystal structure. Furthermore, solid-state ^{29}Si NMR spectroscopy would be a very helpful analytic method in this case in order to get hints on the number of crystallographic Si sites.

Final Remarks

The findings presented in this work underline the great significance of high-pressure high-temperature synthesis in P/O/N chemistry. Enhancing this more or less known synthesis technique led to a broad spectrum of novel interesting compounds, opening new horizons for the explorative research in this field.

This work could moreover show that Eu^{2+}-doped (oxo)nitridophosphates are generally well suited in order to serve as host lattices for novel luminescent materials. Still, it is obvious that the described systems need further optimization in order to compete with currently used nitridic phosphors. However, the latter have long been studied and optimized whereas this new class of luminescent materials is just at the beginning of systematic investigations and optimization with regard to luminescence properties.

10.1 References

[1] D. Baumann, W. Schnick, *Inorg. Chem.* **2014**, *53*, 7977.

[2] D. Baumann, W. Schnick, *Angew. Chem. Int. Ed.* **2014**, *53*, 14490; *Angew. Chem.* **2014**, *126*, 14718.

[3] S. D. Kloß, W. Schnick, *Angew. Chem. Int. Engl.* **2015**, *54*, 11250; *Angew. Chem.* **2015**, *127*, 11402.

[4] S. M. Wanninger, *bachelor thesis*, Ludwig-Maximilians-Universität München, **2015**.

[5] T. L. Barry, *J. Electrochem. Soc.* **1968**, *115*, 1181.

[6] G. Blasse, W.L. Wanmaker, J.W. Tervrugt, A. Bril, *Philips Res. Rep.* **1968**, *23*, 189.

[7] S. H. M. Poort, W. Janssen, G. Blasse, *J. Alloys Compd.* **1997**, *260*, 93.

[8] H.-P. Baldus, W. Schnick, J. Lücke, U. Wannagat, G. Bogedain, *Chem. Mater.* **1993**, *5*, 845.

[9] J. Grins, Z. Shen, S. Esmaeilzadeh, P. Berastegui, *J. Mater. Chem.* **2001**, *11*, 2358.

[10] B. Dierre, R. Xie, N. Hirosaki and T. Sekiguchi, *J. Mater. Res.* **2007**, *22*, 1933.

A Supporting Information for Chapter 2

A.1 Experimental Details of the HP/HT-Synthesis of β-HPN_2

Amorphous phosphorus nitride imide HPN_2 has been prepared in the similar way as outlined in the literature by heating of hexachlorotriphosphazene $(PNCl_2)_3$ in a ceramic corundum boat at 130 (5 h), 190 (3 h) an 300°C (4 h) in a continuous ammonia flow following by a vacuum heat treatment of the mixture at 450°C.[1] The high-pressure high-temperature synthesis of β-HPN_2 was carried out using a Walker-type multianvil assembly, starting from a mixture of amorphous HPN_2 and a small amount of ammonium chloride. The starting material was thoroughly ground and tightly packed into a cylindrical capsule of hexagonal boron nitride (Henze, Kempten). The capsule was sealed with a hexagonal boron nitride cap and centered within a specially prepared Cr_2O_3-doped MgO octahedron (Ceramic Substrated & Components Ltd, Isle of Wight) with an edge length of 18 mm, which served as pressure medium. Graphite tubes were used as electrical resistance furnaces. Subsequently, the octahedron was placed in the middle of eight truncated tungsten carbide cubes (Hawedia, Marklkofen, Germany) with the truncation edge length of 11 mm, separated by pyrophyllite gaskets. Detailed information regarding the construction of the described multianvil assembly can be found in the literature.[2] The assembly was compressed up to 6 GPa at room temperature. Sustaining this pressure the sample was heated up to 1000°C within 60 min and this temperature was held constant for 120 min. Finally, the sample was cooled down to room temperature within 60 min and the pressure was released within a period of 8 h. After the completed reaction β-HPN_2 was isolated as a colorless crystalline solid which was not sensitive to air or moisture.

A.2 Crystallographic Data for β-HPN_2 from Single-Crystal X-Ray Diffraction

Due to a pseudo-twofold screw axis along [010], the of β-PN(NH) structure can almost be described in space group $P2_1/c$ (Figure A.1).

Table A.1: Atomic coordinates, isotropic displacement parameters, and occupation of crystallographic positions of β-HPN_2; standard deviations in parentheses.

atom	Wyckoff site	x	y	z	U_{eq} / Å^2	occupancy
P1	4*g*	0.68210(8)	0.70431(14)	0.23211(8)	0.0116(2)	1.0
P2	4*g*	0.81747(8)	0.81123(13)	0.61716(8)	0.0113(2)	1.0
N1	2*f*	1/2	0.8080(6)	1/4	0.0140(6)	1.0
N2	4*g*	0.8345(3)	0.7152(5)	0.4268(3)	0.0136(5)	1.0
N3	4*g*	0.6602(3)	0.3777(5)	0.1609(3)	0.0145(5)	1.0
N4	2*e*	0	0.7213(7)	3/4	0.0152(6)	1.0
N5	4*g*	0.7571(3)	0.8719(5)	0.1018(3)	0.0144(5)	1.0
H1	4*g*	0.553(4)	0.305(9)	0.125(6)	0.050(13)	1.0
H2	4*g*	0.944(3)	0.684(8)	0.427(5)	0.030(10)	1.0

Table A.2: Selected bond lengths / pm in the crystal structure of β-HPN_2; standard deviations in parentheses.

P1−N1	1.5697(12)	P2−N2	1.663(2)
P1−N5	1.589(2)	P2−N3	1.665(2)
P1−N2	1.665(2)	N1−P1	1.5697(12)
P1−N3	1.670(2)	N3−P2	1.665(2)
P2−N4	1.5679(12)	N4−P2	1.5679(12)
P2−N5	1.596(2)	N5−P2	1.596(2)

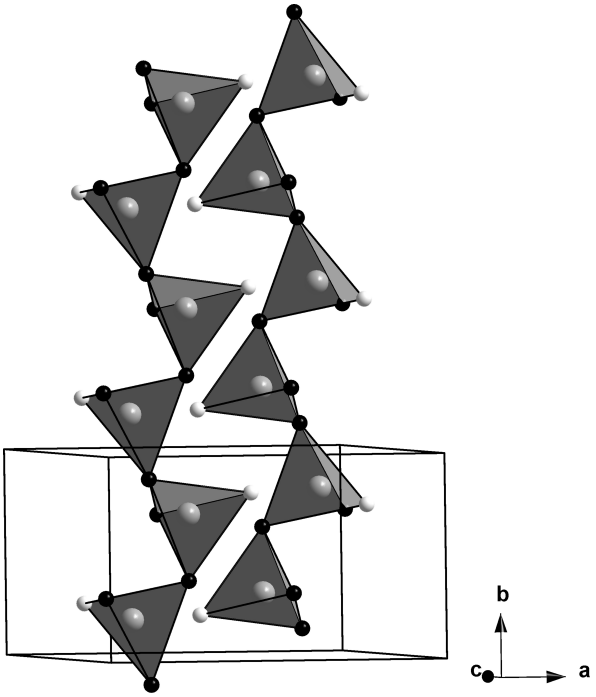

Figure A.1: Pseudo-twofold screw axis in the crystal structure of β-HPN_2 parallel to *b*-axis with white N atoms breaking the 2_1 symmetry.

Table A.3: Anisotropic displacement parameters of crystallographic positions of β-HPN_2; standard deviations in parentheses.

atom	U_{11}	U_{22}	U_{33}	U_{12}	U_{13}	U_{23}
P1	0.0114(3)	0.0117(4)	0.0115(3)	-0.0004(2)	0.0032(2)	-0.0003(2)
P2	0.0115(3)	0.0114(3)	0.0107(3)	-0.0002(2)	0.0029(2)	0.0003(2)
N1	0.0123(14)	0.0130(14)	0.0168(14)	0	0.0048(11)	0
N2	0.0121(10)	0.0168(11)	0.0117(10)	-0.0016(8)	0.0037(8)	0.0020(8)
N3	0.0110(9)	0.0148(11)	0.0176(11)	-0.0022(9)	0.0043(8)	-0.0003(8)
N4	0.0147(15)	0.0163(15)	0.0140(14)	0	0.0034(12)	0
N5	0.0156(10)	0.0133(11)	0.0143(9)	-0.0008(8)	0.0050(8)	-0.0029(8)
P1	0.0114(3)	0.0117(4)	0.0115(3)	-0.0004(2)	0.0032(2)	-0.0003(2)
P2	0.0115(3)	0.0114(3)	0.0107(3)	-0.0002(2)	0.0029(2)	0.0003(2)

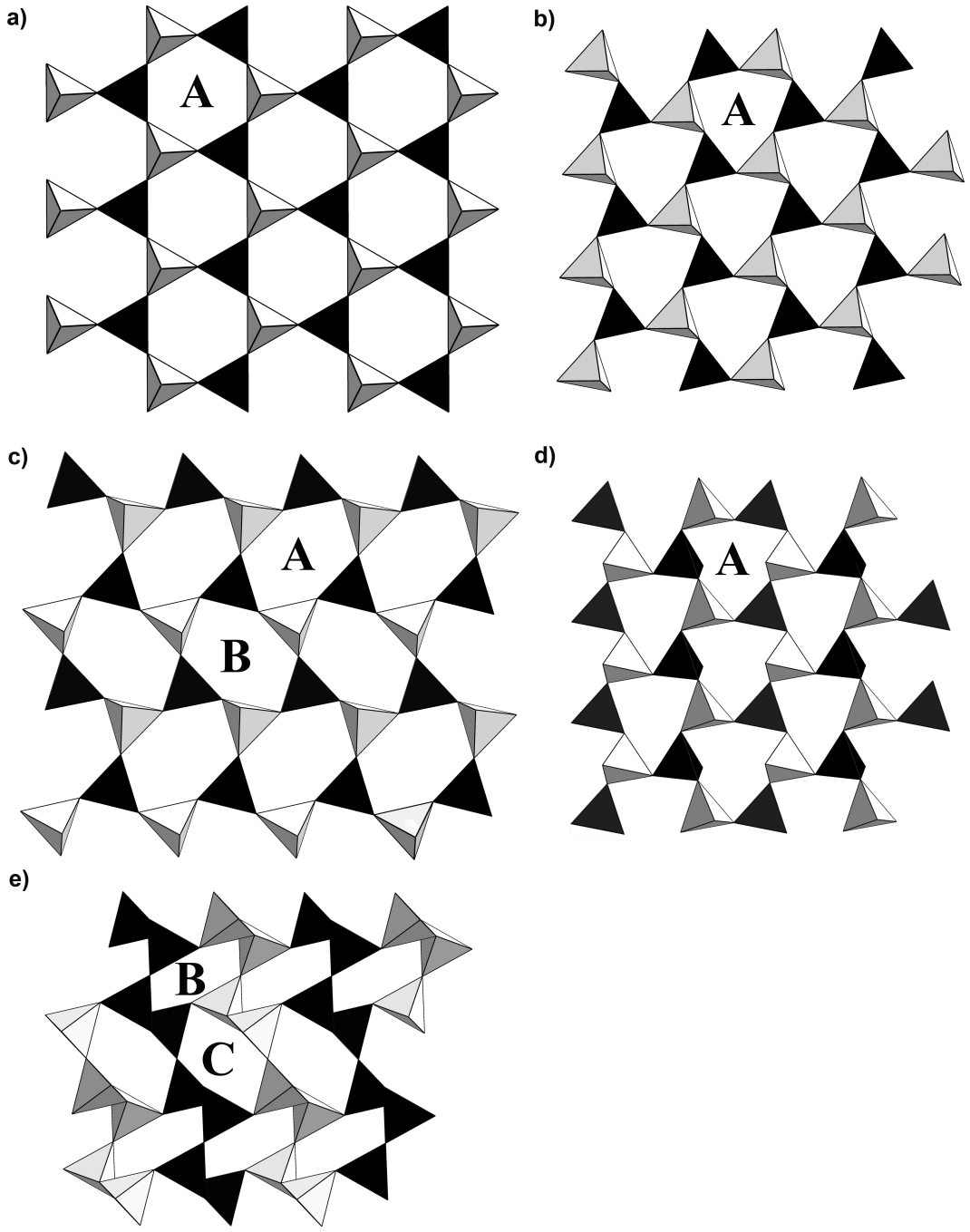

Figure A.2: Comparison of hexagonal layers in high cristobalite (**a**, view along [-111], one type of six-membered rings **A**), α-HPN_2(**b**, view along [-4-12], one type of six-membered rings **A**), low cristobalite (**c**, view along [0-1-1], two types of six-membered rings **A** and **B**) and β-HPN_2 (**d**, view along [00-1] and **e**, view diirection [010] with three types of six-membered rings **A**, **B** and **C**).

Table A.4: Bond angles / ° in the crystal structure of β-HPN_2; standard deviations in parentheses.

N1−P1−N5	116.23(12)	N4−P2−N3	106.56(11)
N1−P1−N2	108.10(9)	N5−P2−N3	108.57(12)
N5−P1−N2	108.17(12)	N2−P2−N3	109.21(12)
N1−P1−N3	109.56(13)	P1−N1−P1	142.8(2)
N5−P1−N3	105.56(12)	P2−N2−P1	130.73(14)
N2−P1−N3	109.04(11)	P2−N3−P1	126.05(14)
N4−P2−N5	120.45(14)	P2−N4−P2	147.9(2)
N4−P2−N2	104.03(9)	P1−N5−P2	126.86(15)
N5−P2−N2	107.62(12)		

A.3 Powder X-Ray Diffraction on β-HPN_2

Powder X-Ray diffraction data was collected on a STOE StadiP powder diffractometer in Debye Scherer geometry using Cu-Kα_1-radiation (λ = 154.06 pm), Ge(111)-monochromator and a position sensitive detector. Rietveld refinement was carried out using TOPAS Academics 4.1, employing the fundamental parameter approach (convolution of appropriate source emission profiles, axial instrument contributions and crystalline microstructure effects).[3,4] Preferred orientation of the crystallites in the powder was described using a spherical harmonics of fourth order.

Table A.5: Selected bond lengths / pm in the crystal structure of β-HPN_2; standard deviations in parentheses.

P1−N1	1.5818(16)	P2−N4	1.5369(18)
P1−N2	1.581(4)	P2−N3	1.646(4)
P1−N3	1.645(4)	P2−N5	1.612(3)
P1−N5	1.584(3)	N2−H2	0.94
P2−N2	1.712(3)	N3−H1	0.90

Table A.6: Selected crystallographic data of the Rietveld refinement of β-HPN_2; standard deviations in parentheses.

formula	HPN_2
crystal system / space group	monoclinic, *P*2/*c*
lattice parameters / Å, °	*a* = 7.89365(5)
	b = 4.81867(2)
	c = 8.11718(4)
	$\beta = 108.0548(4)$
cell volume / $Å^3$	293.549(3)
formula units per cell Z	4
calculated X-ray density / $g \cdot cm^{-1}$	2.7152
liear absorption coefficient / cm^{-1}	115.66
radiation	Cu-Kα_1 (λ = 154.056 pm)
monochromator	Ge(111)
diffractometer	Stoe StadiP
detector	linear PSD
2θ-range / °	5−70
temperature / K	298(2)
data points	6500
number of observed reflections	131
program used	TOPAS Academic
structure refinement	Rietveld-Method
profile function	fundamental parameters model
background function / parameters	shifted Chebychev / 36
R_{wp}	0.04297
R_p	0.03312
goodness of fit	1.528

Table A.7: Fractional coordinates, isotropic displacement parameters, and occupation of crystallographic positions of β-HPN_2; standard deviations in parentheses.

atom	x	y	z	U_{eq} / Å^2	occupancy
P1	0.6826(2)	0.7001(3)	0.23176(17)	0.0198(6)	1.0
P2	0.8203(2)	0.8070(3)	0.62093(14)	0.0201(6)	1.0
N1	1/2	0.808	$1/4$	0.0046(19)	1.0
N2	0.8231(5)	0.7080(6)	0.4192(4)	0.0032(12)	1.0
N3	0.6637(4)	0.3755(7)	0.1656(4)	0.0185(14)	1.0
N4	0	0.7205(9)	$3/4$	0.0066(18)	1.0
N5	0.7593(4)	0.8723(6)	0.1046(4)	0.0063(13)	1.0
H1	0.553	0.305	0.125	0.05	1.0
H2	0.944	0.684	0.427	0.03	1.0

Table A.8: Bond angles / ° in the crystal structure of β-HPN_2; standard deviations in parentheses.

N1−P1−N2	106.84(16)	N3−P2−N5	107.74(19)
N1−P1−N3	110.48(15)	P1−N1−P1	141.62(8)
N1−P1−N5	115.61(14)	P1−N2−P2	135.5(3)
N2−P1−N3	107.61(17)	P1−N3−P2	125.5(2)
N2−P1−N5	108.6(2)	P2−N4−P2	148.5(3)
N3−P1−N5	107.44(17)	P1−N5−P2	127.9(2)
N2−P2−N4	107.07(17)	P1−N2−H2	117
N2−P2−N3	107.15(18)	P2−N2−H2	106
N2−P2−N5	106.29(16)	P1−N3−H1	117
N3−P2−N4	107.60(17)	P2−N3−H1	115
N4−P2−N5	120.3(2)		

A.4 FTIR Spectroscopy of β-HPN_2

The FTIR spectrum of β-HPN_2 was measured using KBr tablet method on a Spectrum BX II spectrometer (Perkin Elmer, Waltham MA, USA).

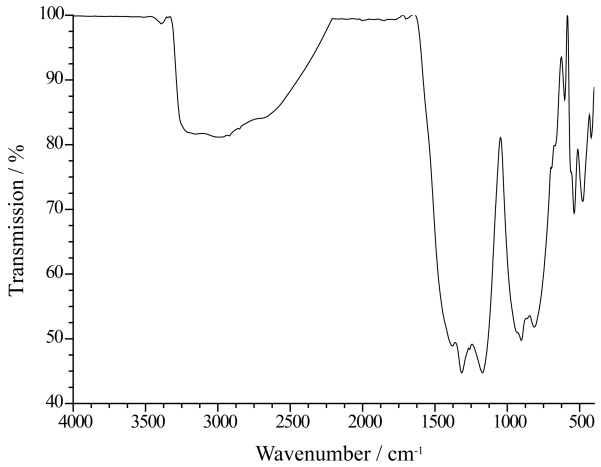

Figure A.3: FTIR spectrum of β-HPN_2.

A.5 Cycle Class Sequence of the β-HPN_2 Network

Table A.9: Cycle class sequence of the network of β-HPN_2 showing the prevalence of the P_nN_n-rings.

n	2	3	4	5	6	7	8	9	10
	0	0	0	0	16	0	24	0	192

A.6 Solid-State NMR Spectroscopy of β-HPN_2

Solid-state NMR spectroscopy was carried out in a Avance III Spectrometer (500 MHz, 4.7 T, Bruker, Bellerica, USA).

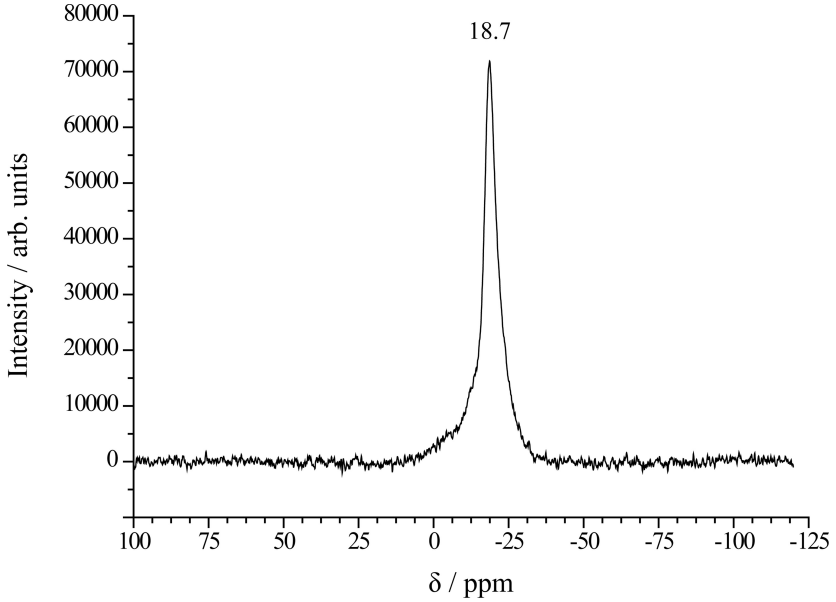

Figure A.4: ^{31}P-solid-state NMR spectrum of β-HPN_2.

A.7 Energy Dispersive X-Ray (EDX) Analysis of β-HPN_2

EDX analysis was carried out using a JEOL JSM-6500F field emission scanning electron microscope (SEM) operated at 12 kV. In order to make the surface of the sample conducting it was sputtered with carbon using an electron beam evaporator (BAL-TEC MED 020, Bal-Tec AG). During calculation of the chemical composition of the investigated sample it has to be considered that hydrogen atoms cannot be detected by SEM.

Table A.10: Results of the EDX measurements for β-HPN_2.

	P	N	chemical composition
EDX point 1 [atom%]	36	64	HPN_2
EDX point 2 [atom%]	32	68	HPN_2
EDX point 3 [atom%]	33	67	HPN_2

A.8 References

[1] F. Karau, *Dissertation*, Ludwig-Maximilians-Universität München, **2007**.

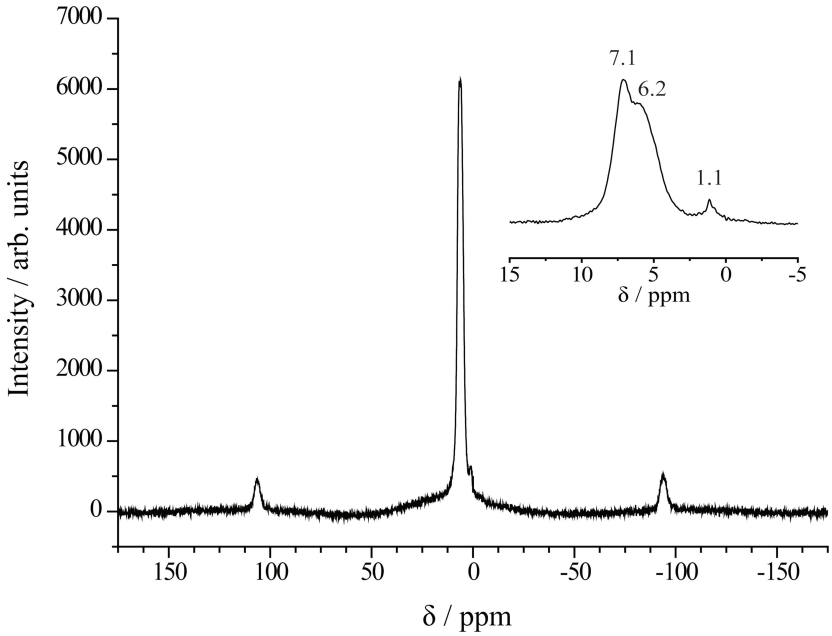

Figure A.5: ^{1}H-solid-state NMR spectrum of β-HPN_2. The small peak at δ = 1.1 ppm results from small amounts of hydrolysis products.

[2] a) N. Kawai, S. Endo, *Rev. Sci. Instrum.* **1970**, *41*, 1178; b) D.Walker, M. A. Carpenter, C. M. Hitch, *Am. Mineral.* **1990**, *75*, 1020; c) D. Walker, *Am. Mineral.* **1991**, *76*, 1092; d) D. C. Rubie, *Phase Transitions* **1999**, *68*, 431; e) H. Huppertz, *Z. Kristallogr.* **2004**, *219*, 330.

[3] A. A. Coehlo, *TOPAS-Academic*, Version 4.1, Coehlo Software, Brisbane (Australia), **2007**.

[4] J. Bergmann, R. Kleeberg, A. Haase, B. Breidenstein, *Mater. Sci. Forum* **2000**, *347*, 303.

B Supporting Information for Chapter 3

B.1 Crystallographic Details of the Single-Crystal Refinement of M_2PO_3N

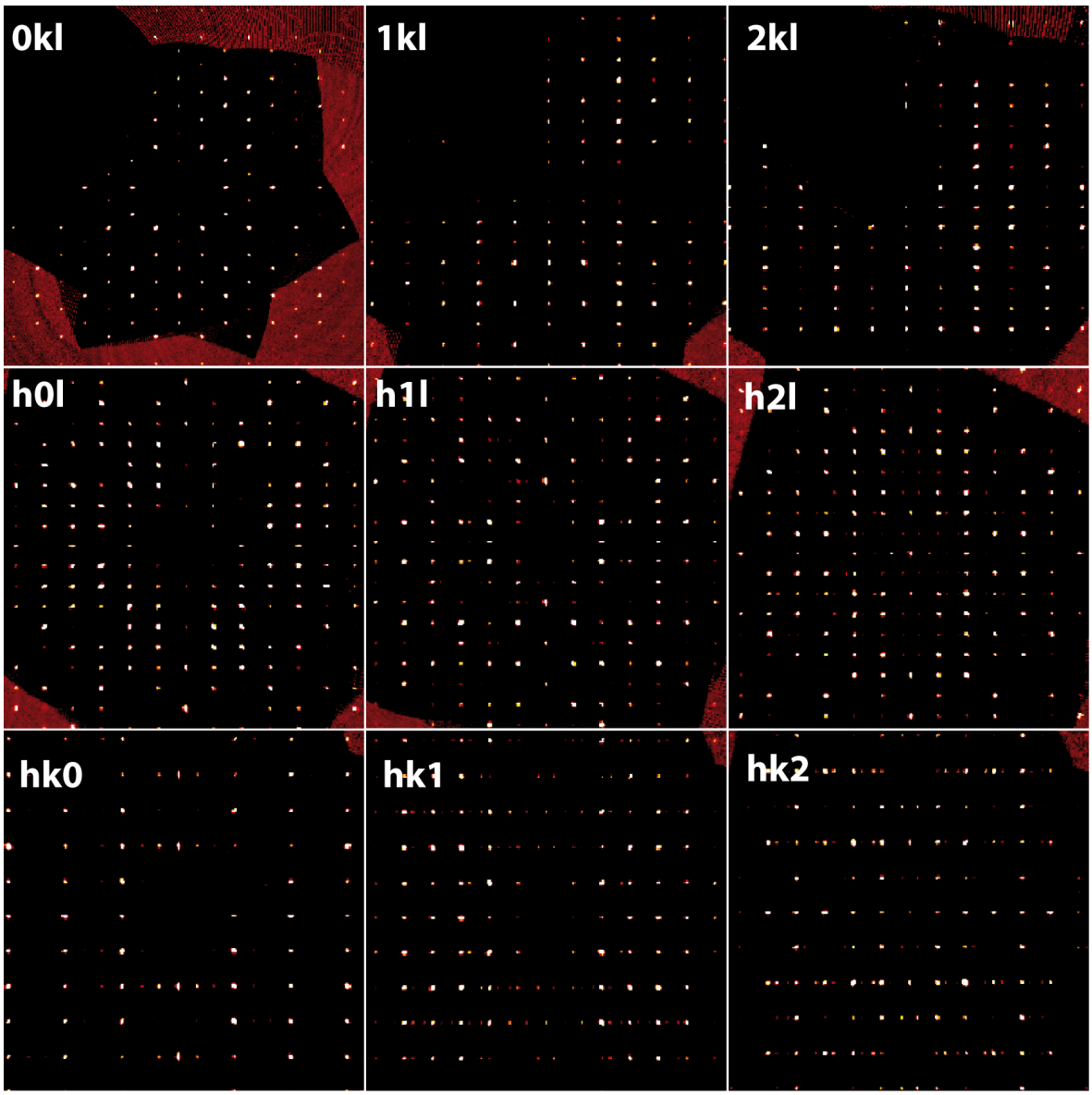

Figure B.1: Reconstructed reciprocal lattice sections from the single-crystal data of Ca_2PO_3N.

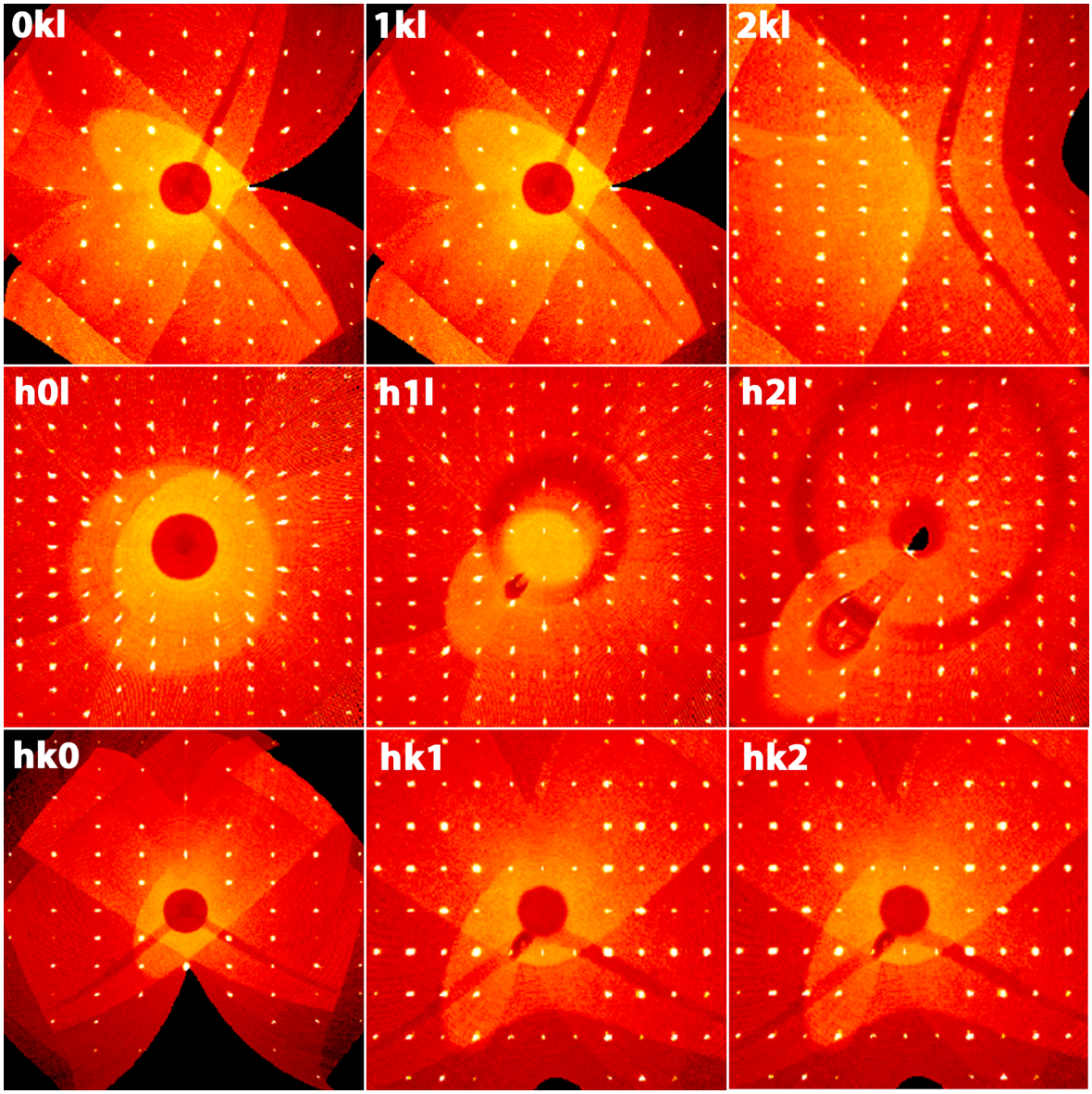

Figure B.2: Reconstructed reciprocal lattice sections from the single-crystal data of Sr_2PO_3N.

B.2 Lattice Energy (MAPLE) Calculations for M_2PO_3N

In order to support the crystal structure model of M_2PO_3N (M = Ca, Sr) with ordered anion occupancies the Madelung part of lattice energy (MAPLE) of each compound was calculated, whereby different mixed occupancies of N/O as well as ordered crystal structure models were considered. The theoretical MAPLE values for both compounds were calculated by taking a sum of the respective binary compounds (2 MO + PON, overall MAPLE value for Ca_2PO_3N: 32217 kJ·mol^{-1}; Sr_2PO-3N: 31667 kJ·mol^{-1}). As can be seen in Tables B.1 and B.2, the overall MAPLE values of M_2PO_3N are in good agreement when ordered crystal structure models are considered (Ca_2PO_3N: 32129 kJ·mol^{-1},

Δ = 0.2%; Sr_2PO_3N: 31518 kJ·mol^{-1}, Δ = 0.4%). Several types of mixed O/N occupancies in both cases lead to the significantly greater deviations from the theoretical calculated MAPLE values. Furthermore, negligible deviations in the ordered cases confirm the electrostatic consistency of the refined crystal structures.

Table B.1: Partial MAPLE values and MAPLE sums / kJ·mol^{-1} for average structure of Ca_2PO_3N.

Wyck.	atom	MAPLE	atom	MAPLE	atom	MAPLE	atom	MAPLE
8*d*	O1	2677	O1	2670	O1/N1	2707	O1	2673
4*c*	O2	2770	N1	4966	O1	2802	O2/N1	3802
4*c*	N1	5254	O2	2859	O2	3793	O2/N1	3975
4*c*	P1	14617	P1	14763	P1	14628	P1	14691
4*c*	Ca1	2200	Ca1	2219	Ca1	2259	Ca1	1872
4*c*	Ca2	1917	Ca2	1825	Ca2	1834	Ca2	2209
		$\sum$ = 32129		$\sum$ = 31988		$\sum$ 31831		$\sum$ 31912
		Δ = 0.2%		Δ = 0.7%		Δ = 1.2%		Δ = 0.9%

Table B.2: Partial MAPLE values and MAPLE sums / kJ·mol^{-1} for Sr_2PO_3N.

Wyck.	atom	MAPLE	atom	MAPLE	atom	MAPLE	atom	MAPLE
8*d*	O1	2634	O1	2643	O1/N1	3738	O1	2638
4*c*	O2	2699	N1	4865	O1	2652	O2/N1	3714
4*c*	N1	5132	O2	2778	O2	2722	O2/N1	3874
4*c*	P1	14545	P1	14662	P1	14556	P1	14603
4*c*	Sr1	1796	Sr1	1703	Sr1	1741	Sr1	1749
4*c*	Sr2	2065	Sr2	2082	Sr2	2096	Sr2	2074
		$\sum$ = 31518		$\sum$ = 31389		$\sum$ 31258		$\sum$ 31304
		Δ = 0.4%		Δ = 0.9%		Δ = 1.3%		Δ = 1.2%

B.3 Bond-Valence Sums (BVS) for M_2PO_3N

Table B.3: Bond-valence sums for average structure of Ca_2PO_3N.

T / K	Ca1	Ca2	O1	O2	N1	P1
293	1.775	2.246	2.006	2.021	2.883	4.989
oxidation state	2	2	2	2	3	5

Table B.4: Bond-valence sums for Sr_2PO_3N.

T / K	Sr1	Sr2	O1	O2	N1	P1
100	1.694	2.255	2.068	1.909	2.726	4.768
150	1.682	2.225	2.065	1.911	2.730	4.800
200	1.674	2.200	2.068	1.920	2.735	4.852
250	1.660	2.201	2.057	1.910	2.720	4.816
300	1.656	2.190	2.058	1.904	2.718	4.831
oxidation state	2	2	2	2	3	5

B.4 Crystallographic Data for M_2PO_3N (M = Ca, Sr) from the Single-Crystal Diffraction Data

Table B.5: Anisotropic displacement parameters of crystallographic positions of Ca_2PO_3N; standard deviations in parentheses.

atom	U_{11}	U_{22}	U_{33}	U_{12}	U_{13}	U_{23}
Ca1	0.0094(3)	0.0227(3)	0.0205(3)	0	-0.00001(19)	0
Ca2	0.0088(2)	0.0142(3)	0.0103(3)	0	-0.00081(17)	0
P1	0.0064(3)	0.0083(3)	0.0084(3)	0	0.0001(2)	0
N1	0.0110(11)	0.0304(14)	0.0099(10)	0	-0.0028(8)	0
O1	0.0250(8)	0.0164(7)	0.0288(8)	0.0026(6)	0.0116(8)	0.0090(6)
O2	0.0082(9)	0.0267(11)	0.0195(10)	0	-0.0020(7)	0

Table B.6: Anisotropic displacement parameters of crystallographic positions of Sr_2PO_3N; standard deviations in parentheses.

atom	U_{11}	U_{22}	U_{33}	U_{12}	U_{13}	U_{23}
Sr1	0.0093(2)	0.0139(2)	0.0179(2)	0	-0.00156(15)	0
Sr2	0.0065(2)	0.0130(2)	0.00819(19)	0	0.00017(13)	0
P1	0.0073(5)	0.0099(4)	0.0083(4)	0	-0.0005(4)	0
N1	0.0090(16)	0.0226(18)	0.0071(15)	0	0.0045(13)	0
O1	0.0248(13)	0.0193(11)	0.0273(12)	0.0017(10)	-0.0067(10)	-0.0088(9)
O2	0.0103(15)	0.0325(19)	0.0210(16)	0	0.0015(12)	0

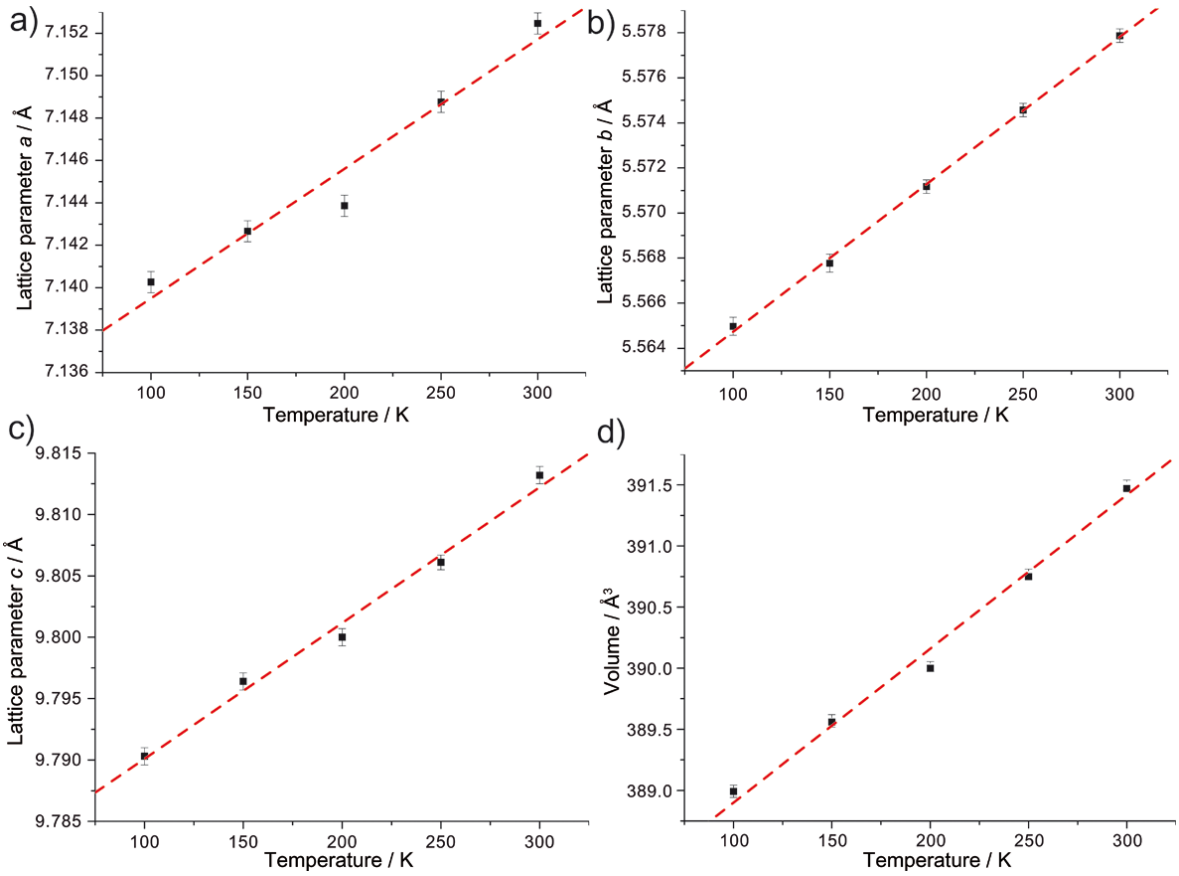

Figure B.3: Lattice parameters and volume of the unit cell of Sr_2PO_3N as a function of temperature as monitored by temperature-dependent single-crystal X-ray diffraction.

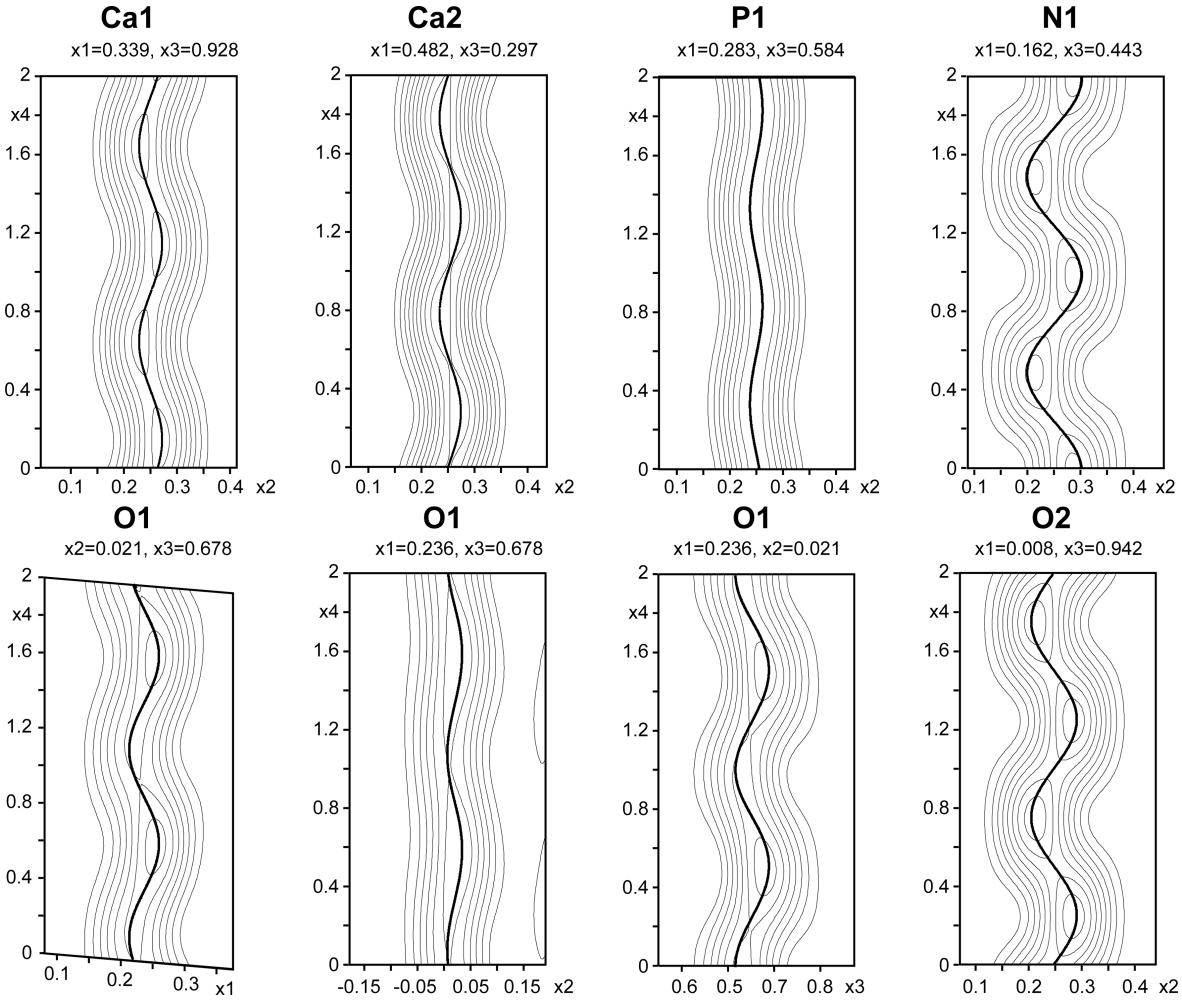

Figure B.4: Fourier sections calculated from the observed structure factors (F_{obs}) for all atoms, with the real-space coordinates on the abscissa and its variation along the modulation direction (x4, two periods) on the ordinate; the refined coordinates are represented by solid lines.

B.5 Crystallographic Details for M_2PO_3N (M = Ca, Sr) from Rietveld Refinement

Table B.7: Crystallographic details of the Rietveld refinement for M_2PO_3N (M = Ca, Sr); standard deviations in parentheses.

formula	Ca_2PO_3N	Sr_2PO_3N
crystal system	orthorhombic	
space group	*Pnma* (no. 62)	
lattice parameters / Å	a = 6.7847(1)	a = 7.1269(5)
	b = 5.4248(1)	b = 5.5768(4)
	c = 9.4325(2)	c = 9.8140(7)
cell volume / Å^3	347.1	390.1
formula units per cell	4	4
calculated X-ray density / g·cm^{-1}	3.3125(1)	4.56734(6)
linear absorption coefficient	319.23(1)	390.57(6)
diffractometer	Stoe StadiP	
detector	MYTHEN 1K	
monochromator	Ge(111)	
radiation	Cu-Kα_1 (λ = 1.54056 Å)	
2θ-range / °	5.0−104.0	5.0−101.5
data points	4221	4221
total number of reflections	6600	6432
refined parameters	69	61
program used	TOPAS Academics	
structure refinement	Rietveld refinement	
profile function	fundamental parameters	
background function	shifted Chebyshev	
number of background parameter	24	
goodness of fit	1.191	1.503
R_p, R_{wp}	0.0313, 0.0408	0.0364, 0.0500

Table B.8: Fractional atomic coordinates, isotropic displacement parameters, and occupation of crystallographic positions of Ca_2PO_3N; standard deviations in parentheses.

atom	Wyckoff site	x	y	z	U_{eq} / Å^2
Ca1	4*c*	0.3378(2)	1/4	0.0749(2)	0.0135(5)
Ca2	4*c*	0.4784(2)	1/4	0.7038(1)	0.0108(6)
P1	4*c*	0.2838(2)	1/4	0.4152(2)	0.0079(5)
N1	4*c*	0.1529(8)	1/4	0.5561(6)	0.0102(14)
O1	8*d*	0.2406(4)	0.0160(7)	0.3201(4)	0.0153(9)
O2	4*c*	0.0090(4)	1/4	0.0587(4)	0.0113(11)

Table B.9: Fractional atomic coordinates, isotropic displacement parameters, and occupation of crystallographic positions of Sr_2PO_3N; standard deviations in parentheses.

atom	Wyckoff site	x	y	z	U_{eq} / Å^2
Sr1	4*c*	0.3433(1)	1/4	0.0745(1)	0.0181(3)
Sr2	4*c*	0.4975(1)	1/4	0.69680(8)	0.0140(3)
P1	4*c*	0.2731(3)	1/4	0.4190(3)	0.0115(6)
N1	4*c*	0.1848(9)	1/4	0.5657(7)	0.0074(15)
O1	8*d*	0.2099(5)	0.0234(6)	0.3376(4)	0.0236(13)
O2	4*c*	-0.0037(7)	1/4	0.0778(5)	0.0286(16)

B.6 Energy Dispersive X-Ray (EDX) Analysis of M_2PO_3N (M = Ca, Sr)

Table B.10: Results of the EDX measurements for Ca_2PO_3N.

	Ca	P	O	N	composition
EDX point 1 [atom%]	25.3	13.0	38.4	23.3	$Ca_{2.0}PO_{3.0}N_{1.8}$
EDX point 2 [atom%]	19.6	10.6	47.2	22.6	$Ca_{1.9}PO_{4.5}N_{2.1}$
EDX point 3 [atom%]	18.5	9.9	45.7	26.8	$Ca_{1.9}PO_{4.6}N_{2.7}$

Table B.11: Results of the EDX measurements for Sr_2PO_3N.

	Sr	P	O	N	composition
EDX point 1 [atom%]	18.2	9.0	52.0	20.8	$Sr_{2.0}PO_{5.8}N_{2.3}$
EDX point 2 [atom%]	23.5	11.5	46.6	18.4	$Sr_{2.0}PO_{4.1}N_{1.6}$
EDX point 3 [atom%]	23.7	12.5	46.1	17.7	$Sr_{1.9}PO_{3.7}N_{1.4}$
EDX point 4 [atom%]	28.2	14.1	41.2	16.5	$Sr_{2.0}PO_{2.9}N_{1.2}$

B.7 Powder X-Ray Diffraction

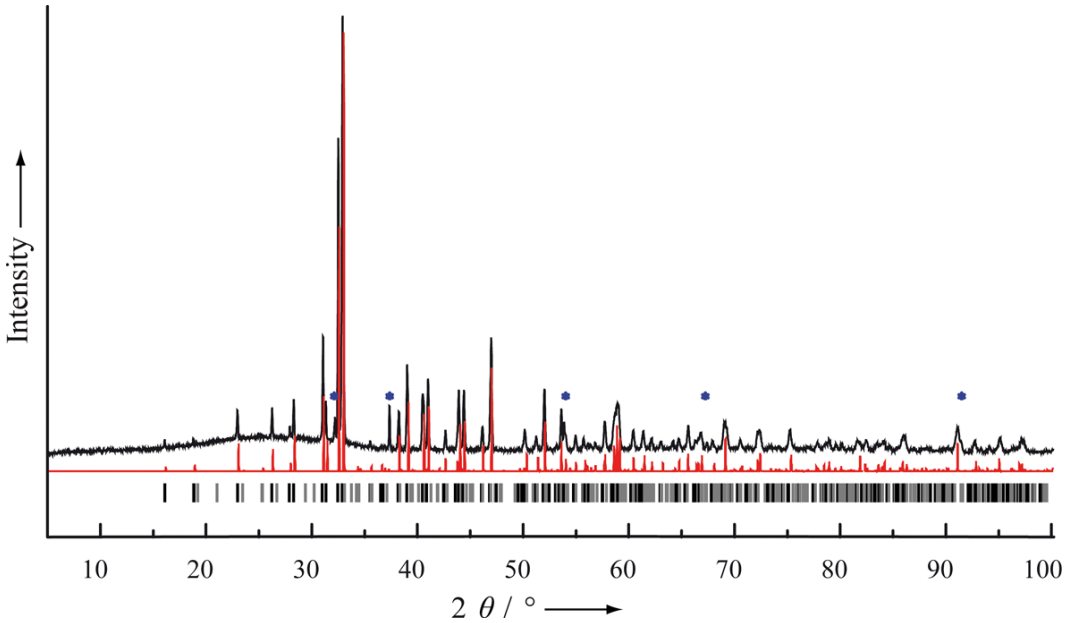

Figure B.5: Simulated powder X-ray diffraction pattern of the modulated structure of Ca_2PO_3N (red line) and experimental PXRD of Ca_2PO_3N (black line) as well as positions of Bragg reflections of the average structure of Ca_2PO_3N (vertical black bars) and satellites reflections (vertical gray bars). The CaO reflections are labelled with blue asterisks.

B.8 Rietveld Refinement of M_2PO_3N (M = Ca, Sr) Synthesized under High-Pressure High-Temperature Conditions

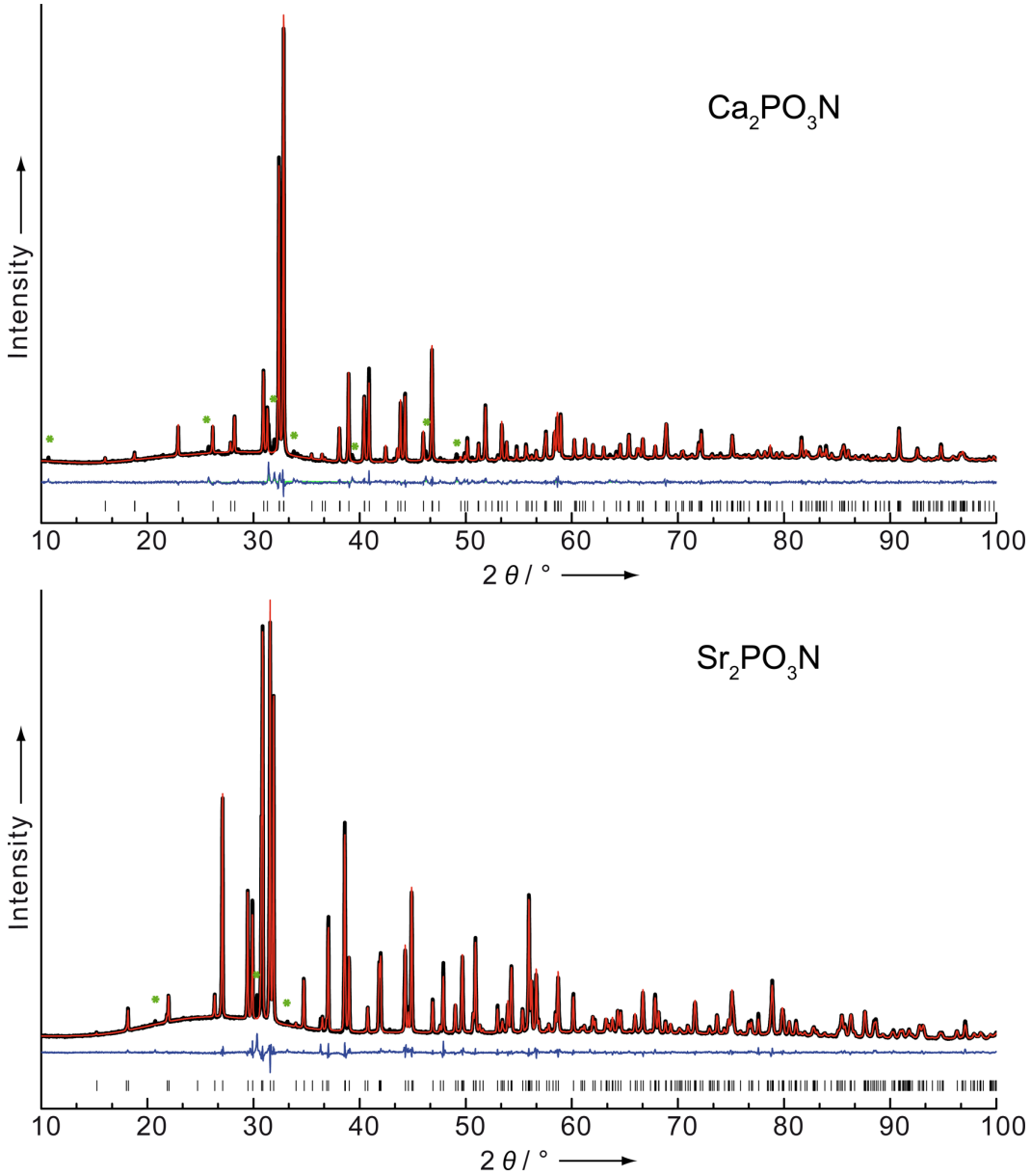

Figure B.6: Observed (black line) and calculated (red line) X-ray powder diffraction patterns, positions of Bragg reflections (vertical bars) and difference profile (blue line) for the Rietveld refinement of Ca_2PO_3N (top) and Sr_2PO_3N (bottom), synthesized under high-pressure high-temperature conditions using multianvil technique. Reflections from an unknown side phase are marked with green asterisks.

C Supporting Information for Chapter 4

C.1 Crystallographic Data of $M\mathrm{H_4P_6N_{12}}$ (M = Mg, Ca) from Single-Crystal X-Ray Diffraction Data

Table C.1: Anisotropic displacement parameters of crystallographic positions of $\mathrm{MgH_4P_6N_{12}}$; standard deviations in parentheses.

atom	U_{11}	U_{22}	U_{33}	U_{12}	U_{13}	U_{23}
Mg1	0.0098(7)	0.0077(7)	0.0108(7)	-0.0003(5)	0	0
P1	0.0060(3)	0.0049(3)	0.0086(3)	0.00011(15)	0.00019(16)	-0.0002(2)
P2	0.0090(3)	0.0063(4)	0.0080(3)	0.0000(2)	0	0
N1	0.0073(7)	0.0099(8)	0.0081(8)	0.0002(6)	-0.0003(6)	-0.0009(6)
N2	0.0072(7)	0.0049(7)	0.0115(7)	0.0003(6)	0.0011(6)	0.0006(6)
N3	0.0198(13)	0.0062(11)	0.0091(10)	0.0013(9)	0	0
N4	0.0055(10)	0.0068(10)	0.0097(10)	-0.0019(8)	0	0

Table C.2: Anisotropic displacement parameters of crystallographic positions of $\mathrm{CaH_4P_6N_{12}}$; standard deviations in parentheses.

atom	U_{11}	U_{22}	U_{33}	U_{12}	U_{13}	U_{23}
Ca1	0.0060(6)	0.0062(6)	0.0069(5)	0.0000(4)	0	0
P1	0.0064(4)	0.0053(4)	0.0101(4)	-0.0001(2)	0.0003(3)	0.0000(3)
P2	0.0116(6)	0.0082(5)	0.0101(5)	0.0000(4)	0	0
N1	0.0084(12)	0.0106(13)	0.0092(12)	0.0007(9)	-0.0013(10)	-0.0011(10)
N2	0.0086(12)	0.0068(11)	0.0156(12)	0.0012(10)	0.0020(10)	-0.0002(10)
N3	0.025(2)	0.0072(17)	0.0124(17)	-0.0002(15)	0	0
N4	0.0079(17)	0.0070(17)	0.0150(17)	-0.0004(14)	0	0

C.2 Rietveld Refinement of MH$_4$P$_6$N$_{12}$ (M = Mg, Ca)

Rietveld refinement was carried out using TOPAS Academic 4.1, employing the fundamental parameter approach (convolution of source emission profiles, axial instrument contributions and crystalline microstructure effects). Preferred orientation of the crystallites in the powder was described using a spherical harmonics function of fourth order. All atomic positions as well as isotropic thermal displacement parameters of P, Mg and Ca, respectively, atom positions were refined freely. A common isotropic displacement parameter for the N atom positions was refined.

Table C.3: Selected crystallographic data of Rietveld refinement of MH$_4$P$_6$N$_{12}$ (M = Mg, Ca); standard deviations in parentheses.

formula	$MgH_4P_6N_{12}$	$CaH_4P_6N_{12}$
crystal system	orthorhombic	
space group	*Cmce* (no. 64)	
lattice parameters / Å	a = 8.45680(6)	a = 8.62980(6)
	b = 4.82694(3)	b = 4.90097(4)
	c = 21.3088(2)	c = 22.1533(2)
cell volume / Å^3	869.83(1)	936.86(1)
formula units per cell	4	4
calculated X-ray density / g·cm^{-1}	2.918	2.822
diffractometer	Stoe StadiP	
detector	MYTHEN 1K	
monochromator	Ge(111)	
radiation	Cu-Kα_1 (λ = 1.54056 Å)	
2θ-range / °	5.0−101.5	3.0−100.0
data points	6432	6468
total number of reflections	252	264
refined parameters	60	60
background function	shifted Chebyshev	
number of background parameter	24	
goodness of fit	1.515	1.370
R_p, R_{wp}	0.0234, 0.0316	0.0312, 0.0411

Table C.4: Fractional atomic coordinates, isotropic displacement parameters, and occupation of crystallographic positions of $MgH_4P_6N_{12}$; standard deviations in parentheses.

atom	Wyckoff site	x	y	z	U_{eq} / Å^2	occupancy
Mg1	4*a*	0	0	0	0.0113(7)	1.0
P1	16*g*	0.3357(1)	-0.0050(2)	0.08789(4)	0.0084(3)	1.0
P2	8*f*	0	0.4101(3)	0.21109(7)	0.0168(5)	1.0
N1	16*g*	0.1512(3)	0.4825(5)	0.16723(9)	0.0060(5)	1.0
N2	16*g*	0.3147(3)	0.3146(6)	0.06577(9)	0.0060(5)	1.0
N3	8*f*	0	0.0734(8)	0.22525(15)	0.0060(5)	1.0
N4	8*f*	0	0.3698(7)	0.06273(16)	0.0060(5)	1.0
H1	16*g*	0.245	0.485	0.185	0.0510	1.0

Table C.5: Fractional atomic coordinates, isotropic displacement parameters, and occupation of crystallographic positions of $CaH_4P_6N_{12}$; standard deviations in parentheses.

atom	Wyckoff site	x	y	z	U_{eq} / Å^2	occupancy
Ca1	4*a*	0	0	0	0.0127(6)	1.0
P1	16*g*	0.3365(1)	0.0052(3)	0.09440(4)	0.0105(4)	1.0
P2	8*f*	0	0.4255(4)	0.21355(8)	0.0190(5)	1.0
N1	16*g*	0.1510(3)	0.4957(6)	0.16978(9)	0.0077(5)	1.0
N2	16*g*	0.3047(3)	0.3115(7)	0.0726(1)	0.0077(5)	1.0
N3	8*f*	0	0.0953(8)	0.2278(2)	0.0077(5)	1.0
N4	8*f*	0	0.4011(8)	0.0703(2)	0.0077(5)	1.0
H1	16*g*	0.225	0.522	0.197	0.1	1.0

C.3 FTIR Spectroscopy of $MH_4P_6N_{12}$ (M = Mg, Ca)

The FTIR spectra of $MH_4P_6N_{12}$ were measured using KBr tablet method on a Spectrum BX II spectrometer (Perkin Elmer, Waltham MA, USA).

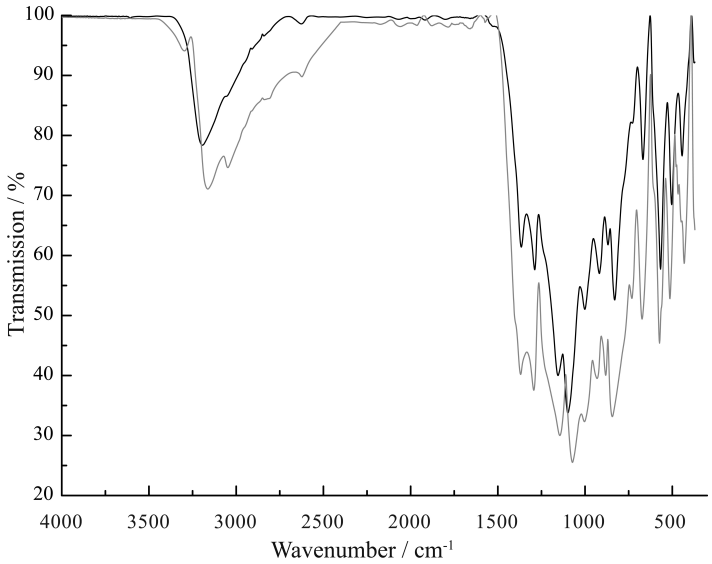

Figure C.1: FTIR spectra of $MgH_4P_6N_{12}$ (gray line) and $CaH_4P_6N_{12}$ (black line), measured using the KBr pellet method.

C.4 Energy Dispersive X-Ray (EDX) Analysis of $MH_4P_6N_{12}$ (M = Mg, Ca)

EDX analysis was carried out using a JEOL JSM-6500F field emission scanning electron microscope (SEM) operated at 12 kV. In order to make the surface of the sample conducting it was sputtered with carbon using an electron beam evaporator (BAL-TEC MED 020, Bal-Tec AG). During the calculation of the chemical composition of the investigated sample it has to be considered that hydrogen atoms cannot be detected by EDX.

Table C.6: Results of the EDX measurements for $MgH_4P_6N_{12}$.

	Mg	P	N	O
EDX point 1 [atom%]	5.3	31.9	59.9	2.9
EDX point 2 [atom%]	5.1	30.6	61.7	2.6
EDX point 3 [atom%]	5.3	32.4	58.2	4.0
calculated atom %	5.2	31.6	63.2	-

Table C.7: Results of the EDX measurements for $CaH_4P_6N_{12}$.

	Ca	P	N	O
EDX point 1 [atom%]	5.1	29.3	63.6	2.0
EDX point 2 [atom%]	4.4	27.0	63.5	4.0
EDX point 3 [atom%]	6.0	36.5	55.5	2.0
calculated atom %	5.2	31.6	63.2	-

C.5 Solid-State NMR Spectroscopy of MH$_4$P$_6$N$_{12}$ (M = Mg, Ca)

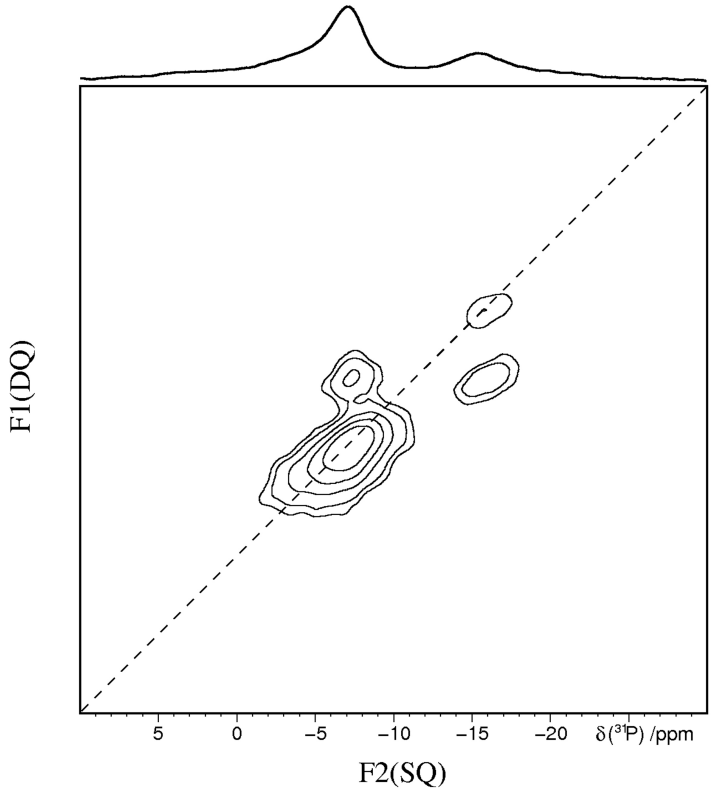

Figure C.2: ^{31}P-^{31}P 2D double-quantum (DQ) single-quantum (SQ) correlation MAS NMR spectra of $CaH_4P_6N_{12}$ obtained at a sample spinning frequency of 20 kHz with a repetition delay of 42 s. A transient adapted POSTC7 sequence[1,2] was used with a conversion period of 1.2 ms. Rotor-synchronized data sampling of the indirect dimension accumulated 16 transients/FID. Proton decoupling was implemented using CW decoupling with a nutation frequency of 110 kHz. The dashed diagonal line denotes the peak position of isochronous spins (autocorrelation peak).

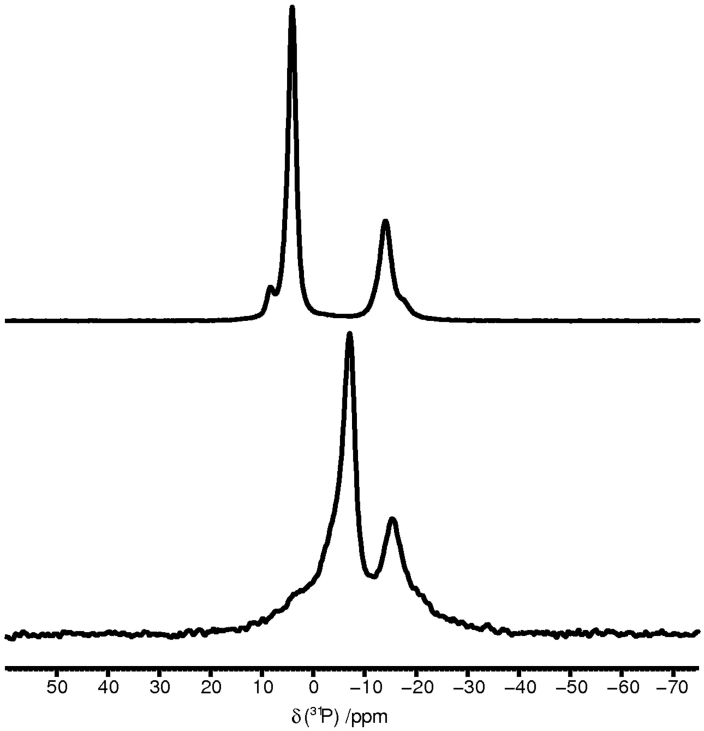

Figure C.3: ^{31}P MAS NMR spectra of $MgH_4P_6N_{12}$ (top) and $CaH_4P_6N_{12}$ (bottom), measured at a sample spinning frequency of 25 kHz, using ^{1}H CW decoupling with a nutation frequency of 110 kHz. The peak assignments of $MgH_4P_6N_{12}$ (top) are: P1 (4.1 ppm), P2 (-13.9 ppm), side phases (8.6 and -17.0 ppm). The peak assignments of $CaH_4P_6N_{12}$ (bottom) are: P1 (-7.1 ppm), P2 (-15.4 ppm), side phases (0.8 ppm, -4.3 ppm and -17.6 ppm).

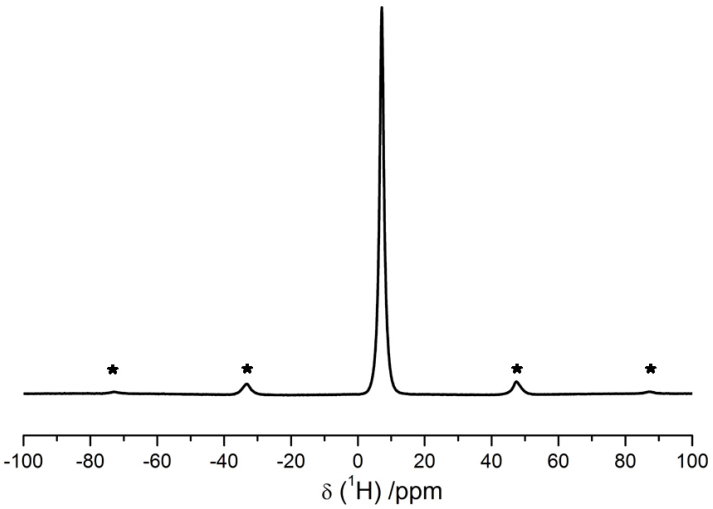

Figure C.4: ^{1}H MAS NMR spectrum of $^{15}NH_4Cl$ at 20 kHz with the sharp peak at around 7.2 ppm. Rotational sidebands are marked with asterisks.

D Supporting Information for Chapter 5

D.1 Rietveld Refinement of $CaMg_2P_6O_3N_{10}$

Rietveld refinement was carried out using TOPAS Academic 4.1, employing the fundamental parameter approach (convolution of source emission profiles, axial instrument contributions and crystalline microstructure effects). Preferred orientation of the crystallites in the powder was described using a spherical harmonics function of fourth order.

Table D.1: Selected crystallographic data of Rietveld refinement of $CaMg_2P_6O_3N_{10}$; standard deviations in parentheses.

formula	$CaMg_2P_6O_3N_{10}$
crystal system	tetragonal
space group	$I4_1/acd$ (no. 142)
lattice parameters / Å	a = 12.4939(1)
	c = 23.7468(3)
cell volume / Å^3	3706.84(9)
formula units per cell	16
calculated X-ray density / g·cm^{-1}	3.316
diffractometer	Huber G670
radiation	Cu-Kα_1 (λ = 1.54056 Å)
2θ-range / °	5.5−99.9
data points	9449
total number of reflections	487
refined parameters	86
background function	shifted Chebyshev (18 parameters)
goodness of fit	1.753
R_p, R_{wp}	0.0171, 0.0229

Table D.2: Fractional atomic coordinates, isotropic displacement parameters, and occupation of crystallographic positions of $CaMg_2P_6O_3N_{10}$; standard deviations in parentheses.

atom	Wyckoff	x	y	z	U_{eq} / Å^2	occupancy
Ca1	8*a*	1/2	1/4	1/8	0.0055(10)	1.0
Ca2	8*b*	1	3/4	3/8	0.0773(16)	1.0
Mg1	32*g*	0.3439(2)	0.0624(2)	0.0427(1)	0.0292(12)	1.0
P1	32*g*	0.6012(2)	0.0204(2)	0.0796(1)	0.0152(8)	1.0
P2	32*g*	0.7432(2)	0.1898(2)	0.0836(1)	0.0129(8)	1.0
P3	32*g*	0.5884(2)	0.1817(2)	0.0001(1)	0.0202(9)	1.0
N1	32*g*	0.6585(5)	0.2559(4)	0.0418(4)	0.0053(6)	1.0
N2/O2	32*g*	0.7976(4)	0.2745(3)	0.1267(3)	0.0053(6)	0.86/0.14
N3	32*g*	0.6736(4)	0.1021(5)	0.1188(2)	0.0053(6)	1.0
N4	32*g*	0.5223(4)	0.0921(5)	0.0391(3)	0.0053(6)	1.0
N5/O5	32*g*	0.8390(4)	0.1230(4)	0.0490(2)	0.0053(6)	0.76/0.24
N6/O6	16*d*	1/2	1/4	-0.0308(3)	0.0053(6)	0.76/0.24
O7	32*g*	0.6702(4)	-0.0548(4)	0.0440(2)	0.0053(6)	1.0

D.2 FTIR Spectrum of $CaMg_2P_6O_3N_{10}$

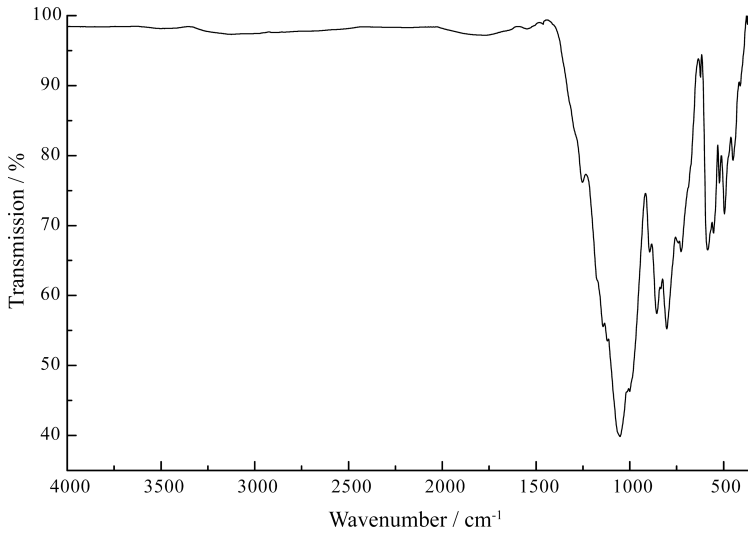

Figure D.1: FTIR spectrum of $CaMg_2P_6O_3N_{10}$, measured using the KBr pellet method.

D.3 Energy Dispersive X-Ray (EDX) Analysis of $CaMg_2P_6O_3N_{10}$

Table D.3: Results of EDX measurements (left part SEM, right part TEM) for various crystals of $CaMg_2P_6O_3N_{10}$ in atom-%; the absolute values for light atoms depend on the systematic errors associated with different experimental setups (electron microscope, EDX detector, software, see Experimental section) was used, the average composition agrees with the compound $CaMg_2P_6O_3N_{10}$.

Crystal	**1**	**2**	**3**	**∅SEM**	**1**	**2**	**3**	**∅TEM1**
N	57.6	51.9	55.8	**55.1(29)**	47.1	42.1	43.9	**44.4(21)**
O	14.5	14.5	11.4	**13.5(18)**	10.2	10.9	10.0	**10.4(4)**
Mg	7.0	7.5	7.8	**7.4(4)**	8.2	7.6	8.3	**8.0(3)**
P	18.4	22.6	21.8	**20.9(23)**	30.5	33.8	31.9	**32.1(14)**
Ca	2.5	3.5	3.2	**3.1(5)**	4.0	5.6	5.9	**5.2(8)**
Ca/P	0.14	0.15	0.15	**0.15**	0.13	0.17	0.18	**0.16**

Crystal	**1**	**2**	**3**	**4**	**5**	**6**	**∅TEM2**	**calc.**
N	37.0	47.0	39.5	37.9	36.8	41.1	**39.9(35)**	**45.5**
O	14.0	9.1	11.2	10.8	11.3	13.8	**11.7(17)**	**13.6**
Mg	13.5	13.9	15.0	15.6	16.6	14.8	**14.9(10)**	**9.1**
P	31.2	27.5	31.5	32.8	32.4	27.5	**30.5(21)**	**27.3**
Ca	4.2	2.5	2.9	2.9	2.9	2.8	**3.0(5)**	**4.5**
Ca/P	0.13	0.09	0.09	0.09	0.09	0.10	**0.10**	**0.16**

E Supporting Information for Chapter 6

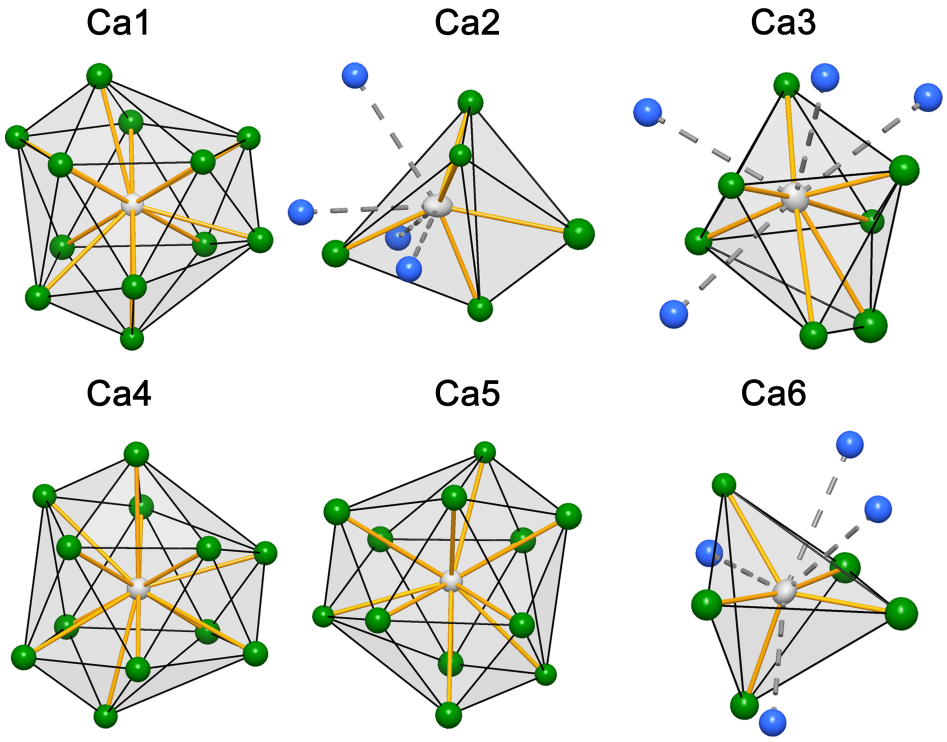

Figure E.1: Coordination of Ca^{2+} in $CaP_2N_4:Eu^{2+}$. Atoms are shown in ellipsoids with 95 % probability. Green atoms: Nitrogen atoms coordinating Ca. Blue atoms: Additional atoms coordinating Sr in $SrP_2N_4:Eu^{2+}$.

Table E.1: Anisotropic displacement parameters of crystallographic positions of CaP_2N_4; standard deviations in parentheses.

atom	U_{11}	U_{22}	U_{33}	U_{23}	U_{13}	U_{12}
Ca1	0.0083(5)	0.0083(5)	0.0043(8)	0	0	0.0042(3)
Ca2	0.0099(3)	0.0104(4)	0.0133(3)	0.0033(5)	0.0044(3)	0.0050(3)
Ca3	0.0090(3)	0.0111(4)	0.0095(3)	-0.0010(6)	0.0008(3)	0.0040(4)
Ca4	0.0087(3)	0.0087(3)	0.0098(7)	0	0	0.00433(16)
Ca5	0.0080(3)	0.0080(3)	0.0086(7)	0	0	0.00402(16)
Ca6	0.0146(4)	0.0081(5)	0.0095(5)	0.0004(5)	-0.0015(4)	0.0058(4)
P1	0.0060(6)	0.0052(7)	0.0106(8)	0.0003(5)	0.0029(6)	0.0035(5)
P2	0.0056(7)	0.0038(6)	0.0123(8)	0.0005(6)	0.0001(5)	0.0013(5)
P3	0.0060(8)	0.0070(8)	0.0071(6)	-0.0016(7)	-0.0008(5)	0.0037(6)
P4	0.0057(8)	0.0065(8)	0.0092(7)	-0.0013(7)	-0.0009(6)	0.0032(6)
P5	0.0061(6)	0.0061(6)	0.0059(6)	-0.0006(4)	-0.0008(5)	0.0040(4)
P6	0.0094(6)	0.0094(7)	0.0065(6)	0.0017(5)	0.0017(6)	0.0050(5)
P7	0.0058(7)	0.0093(6)	0.0055(6)	0.0006(6)	0.0002(4)	0.0044(5)
P8	0.0078(6)	0.0083(7)	0.0062(6)	-0.0006(5)	-0.0016(5)	0.0035(5)

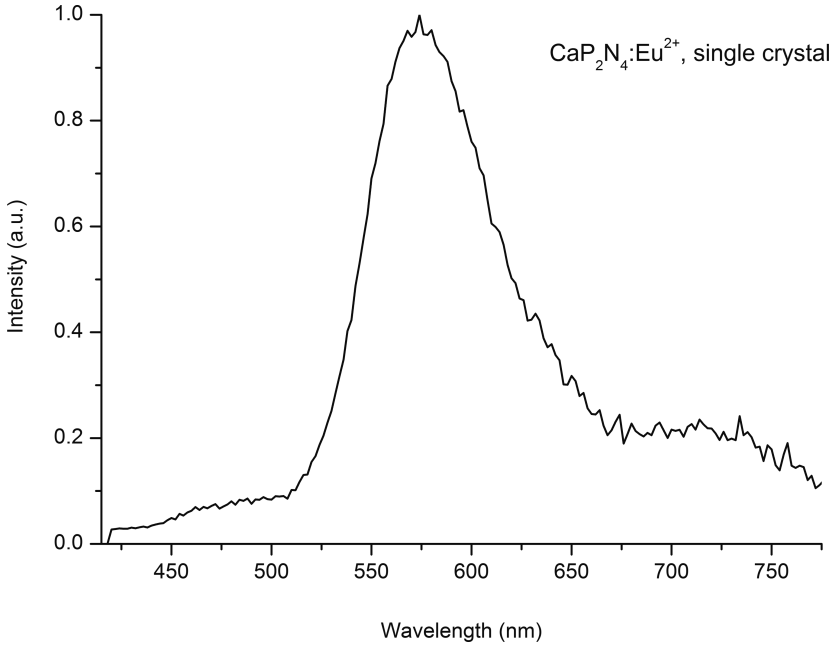

Figure E.2: Excitation and emission spectrum of $CaP_2N_4:Eu^{2+}$, single crystal.

Table E.2: Fractional coordinates, isotropic displacement parameters, and occupation of crystallographic positions of CaP_2N_4; standard deviations in parentheses.

atom	Wyckoff	x	y	z	U_{eq}/Å^2
Ca1	6*c*	0	0	0.00152(18)	0.0070(4)
Ca2	6*c*	0.33303(8)	0.13642(6)	0.48281(18)	0.01124(15)
Ca3	6*c*	0.33224(7)	0.17996(5)	-0.01640(17)	0.01034(14)
Ca4	2*b*	1/3	-1/3	-0.0303(2)	0.0090(3)
Ca5	2*b*	2/3	1/3	-0.0284(2)	0.0082(3)
Ca6	2*b*	0.52160(7)	-0.00229(4)	-0.00769(11)	0.0107(2)
P1	6*c*	-0.01141(11)	-0.16741(9)	0.28402(17)	0.0070(3)
P2	6*c*	0.15931(9)	-0.01174(11)	0.16994(18)	0.0077(4)
P3	6*c*	0.33552(9)	-0.00009(9)	0.18164(16)	0.0065(4)
P4	6*c*	0.33063(9)	0.00090(9)	-0.21490(16)	0.0071(4)
P5	6*c*	0.32108(10)	-0.17389(9)	-0.19912(16)	0.0056(3)
P6	6*c*	0.32495(10)	-0.17424(10)	0.18529(16)	0.0083(3)
P7	6*c*	0.16543(8)	-0.34102(9)	0.29982(16)	0.0066(3)
P8	6*c*	0.51005(11)	0.16457(8)	0.18632(15)	0.0077(3)
N1	6*c*	0.3980(2)	-0.2111(2)	0.1930(4)	0.0104(6)
N2	6*c*	0.1375(2)	-0.05264(19)	-0.0244(5)	0.0105(6)
N3	6*c*	0.0633(3)	-0.0589(3)	0.2723(5)	0.0101(6)
N4	6*c*	0.2335(2)	-0.0352(2)	0.2607(5)	0.0087(9)
N5	6*c*	0.2627(2)	0.0375(2)	-0.2806(5)	0.0087(9)
N6	6*c*	0.2735(2)	-0.2720(2)	-0.2986(4)	0.0101(6)
N7	6*c*	-0.0996(2)	-0.1979(2)	0.1595(4)	0.0090(7)
N8	6*c*	0.2945(3)	-0.1021(2)	-0.2934(5)	0.0088(8)
N9	6*c*	0.0710(2)	-0.3602(2)	0.2005(5)	0.0134(9)
N10	6*c*	0.3764(3)	-0.0656(2)	0.2425(4)	0.0128(9)
N11	6*c*	0.4312(2)	-0.1321(2)	-0.1950(4)	0.0110(6)
N12	6*c*	0.4036(2)	0.1030(2)	0.2529(5)	0.0084(8)
N13	6*c*	0.14454(19)	-0.38481(16)	0.4906(4)	0.0082(5)
N14	6*c*	0.2383(2)	-0.2318(2)	0.3138(4)	0.0116(7)
N15	6*c*	0.3328(3)	0.00703(10)	-0.0205(6)	0.0130(4)
N16	6*c*	0.28055(16)	-0.19463(19)	-0.0056(4)	0.0098(5)

Table E.3: Coordination of the M(II) ions in $CaP_2N_4:Eu^{2+}$ (single crystal) and $SrP_2N_4:Eu^{2+}$ (powder sample) according to MAPLE.

atom	CN	d_{min}	d_{max}	1-EFCON
Ca1	12	253.484	314.300	8.7240
Ca2	5	238.013	294.988	4.3673
Ca3	7	241.088	302.730	4.7540
Ca4	12	250.241	320.988	7.9302
Ca5	12	252.659	312.550	8.6288
Ca6	5	236.006	289.459	4.3634
Ca1	12	253.484	314.300	8.7240
Ca2	5	238.013	294.988	4.3673
Ca3	7	241.088	302.730	4.7540
Ca4	12	250.241	320.988	7.9302
Ca5	12	252.659	312.550	8.6288
Ca6	5	236.006	289.459	4.3634
Ca1	12	253.484	314.300	8.7240
Ca2	5	238.013	294.988	4.3673
Sr1	12	268.388	318.796	10.0410
Sr2	9	256.582	334.627	5.6710
Sr3	11	256.625	329.038	5.2977
Sr4	12	278.399	317.390	10.9278
Sr5	12	272.759	338.381	9.2458
Sr6	9	249.610	325.556	5.0621

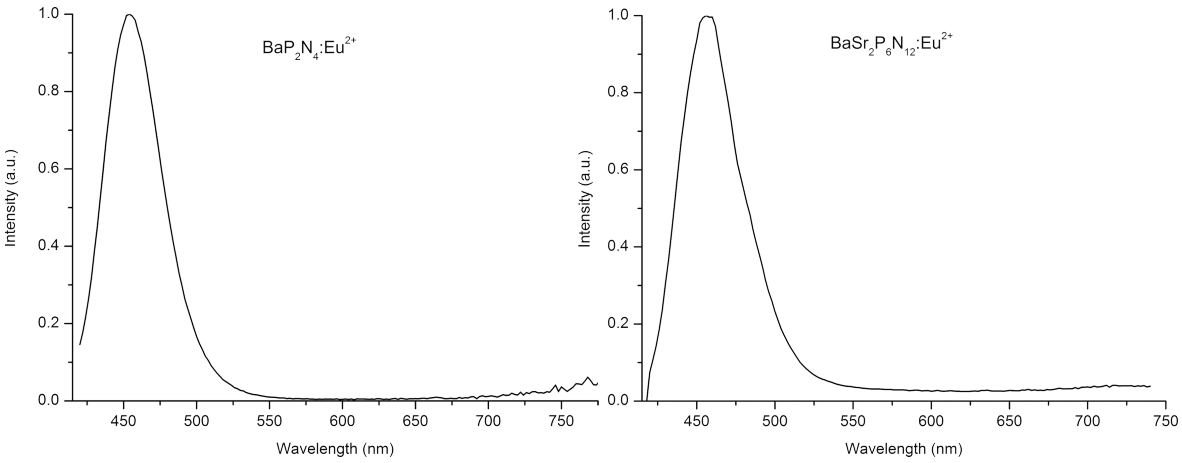

Figure E.3: Emission spectrum of $BaP_2N_4:Eu^{2+}$ (left) and $BaSr_2P_6N_{12}:Eu^{2+}$ (right).

Table E.4: Coordination of the M(II) ions in $BaP_2N_4:Eu^{2+}$ and $BaSr_2P_6N_{12}:Eu^{2+}$ according to MAPLE.

atom	CN	d_{min}	d_{max}	1-EFCON
Ba1	12	308.061	331.785	11.3824
Ba2	12	278.090	347.876	9.3917
Ba1	12	301.405	321.132	11.5363
Sr1	12	280.310	340.275	9.9636

Table E.5: Selected bond lengths / pm in the crystal structure of CaP_2N_4.

Ca1−N3	2.535(4)	Ca5−N1	2.825(3)	P4−N5	1.631(4)
Ca1−N3	2.776(4)	Ca5−N13	2.852(3)	P4−N9	1.645(4)
Ca1−N2	2.872(3)	Ca6−N9	2.360(4)	P4−N8	1.646(4)
Ca1−P2	3.0862(15)	Ca6−N13	2.411(3)	P5−N11	1.622(3)
Ca2−N5	2.380(4)	Ca6−N11	2.437(3)	P5−N6	1.631(4)
Ca2−N12	2.380(4)	Ca6−N10	2.480(4)	P5−N16	1.632(4)
Ca2−N16	2.413(3)	Ca6−N10	2.894(4)	P5−N8	1.659(4)
Ca2−N2	2.417(3)	Ca6−N11	3.162(3)	P6−N16	1.634(3)
Ca2−N9	2.950(4)	P1−N2	1.622(4)	P6−N1	1.634(4)
Ca2−N4	3.061(4)	P1−N3	1.623(4)	P6−N14	1.636(3)
Ca3−N7	2.411(3)	P1−N7	1.633(3)	P6−N10	1.648(4)
Ca3−N14	2.420(3)	P1−N5	1.639(4)	P7−N14	1.627(3)
Ca3−N8	2.425(4)	P2−N3	1.615(4)	P7−N1	1.627(4)
Ca3−N4	2.448(4)	P2−N7	1.631(4)	P7−N13	1.630(4)
Ca3−N15	2.919(2)	P2−N2	1.640(4)	P7−N9	1.653(4)
Ca3−N5	2.938(4)	P2−N4	1.649(4)	P8−N6	1.626(4)
Ca3−N12	3.027(4)	P3−N15	1.595(5)	P8−N11	1.640(3)
Ca4−N1	2.503(3)	P3−N12	1.629(4)	P8−N13	1.642(4)
Ca4−N6	2.752(4)	P3−N4	1.635(4)	P8−N12	1.645(4)
Ca4−N16	2.893(3)	P3−N10	1.638(4)		
Ca5−N6	2.527(4)	P4−N15	1.531(5)		

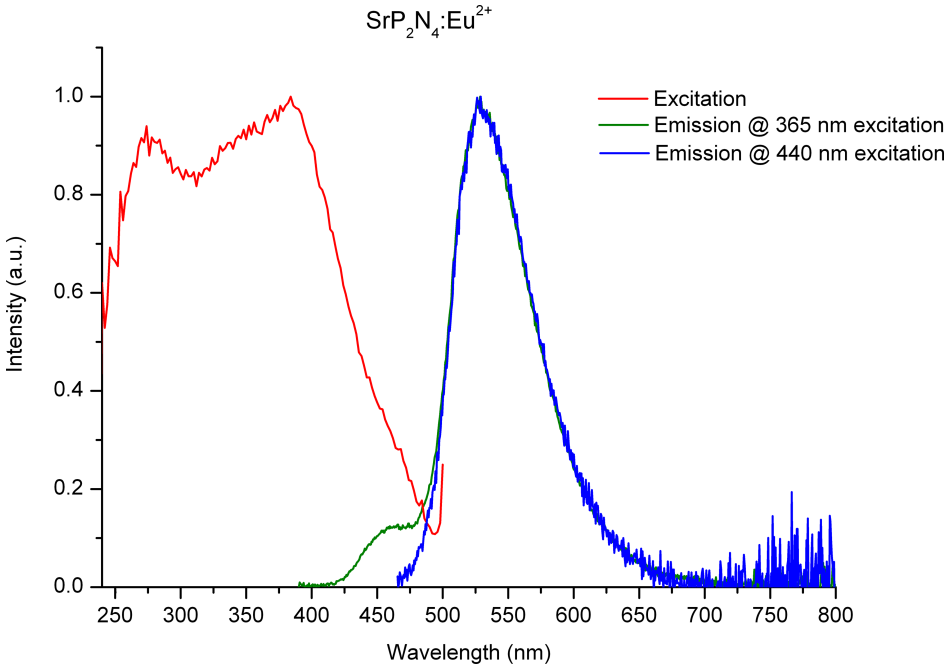

Figure E.4: Excitation and emission spectrum of $SrP_2N_4:Eu^{2+}$.

Table E.6: Selected bond angles / ° in the crystal structure of CaP_2N_4.

N2−P1−N3	108.55(19)	N12−P3−N10	108.0(2)	N1−P6−N14	111.76(17)
N2−P1−N7	105.49(17)	N4−P3−N10	111.45(19)	N16−P6−N10	114.53(18)
N3−P1−N7	113.05(18)	N15−P4−N5	106.8(2)	N1−P6−N10	109.5(2)
N2−P1−N5	115.5(2)	N15−P4−N9	111.9(2)	N14−P6−N10	107.93(19)
N3−P1−N5	108.3(2)	N5−P4−N9	105.4(2)	N14−P7−N1	109.55(16)
N7−P1−N5	106.0(2)	N15−P4−N8	115.41(18)	N14−P7−N13	108.66(16)
N3−P2−N7	108.44(18)	N5−P4−N8	108.7(2)	N1−P7−N13	106.96(17)
N3−P2−N2	107.3(2)	N9−P4−N8	108.1(2)	N14−P7−N9	111.16(18)
N7−P2−N2	108.00(18)	N11−P5−N6	108.95(17)	N1−P7−N9	108.2(2)
N3−P2−N4	111.0(2)	N11−P5−N16	109.85(16)	N13−P7−N9	112.15(17)
N7−P2−N4	112.01(19)	N6−P5−N16	106.81(17)	N6−P8−N11	113.12(18)
N2−P2−N4	109.85(19)	N11−P5−N8	111.04(19)	N6−P8−N13	107.54(17)
N15−P3−N12	107.06(17)	N6−P5−N8	110.45(19)	N11−P8−N13	104.45(15)
N15−P3−N4	109.9(2)	N16−P5−N8	109.65(18)	N6−P8−N12	111.0(2)
N12−P3−N4	107.9(2)	N16−P6−N1	107.88(17)	N11−P8−N12	104.98(19)
N15−P3−N10	112.25(19)	N16−P6−N14	105.25(16)	N13−P8−N12	115.71(18)

F Supporting Information for Chapter 7

F.1 Experimental Details of the HP/HT-Synthesis of $Ba_3P_5N_{10}Br:Eu^{2+}$

$Ba(N_3)_2$ was synthesized using a cation exchanger by reaction of *in situ* formed diluted HN_3 with $BaCO_3$. In the first step, the cation exchanger (Amberlyst 15) was protonated by concentrated HCl. Then the aqueous solution of NaN_3 was passed through the protonated cation exchanger. The thus *in situ* synthesized diluted HN_3 was dripped on the stirring aqueous suspension of $BaCO_3$ forming an aqueous solution of $Ba(N_3)_2$. The reaction is complete, when the suspension of $BaCO_3$ becomes entirely clear. The solvent was filtered to remove possible residues of $BaCO_3$ and then evaporated under reduced pressure (90 mbar, 80°C). The white solid of $Ba(N_3)_2$ was finally recrystallized from acetone, dried in vacuo over P_4O_{10} and stored under exclusion of oxygen and moisture. Phase purity of the product was confirmed by powder X-ray diffraction as well as FTIR spectroscopy.

This synthesis procedure of $Ba(N_3)_2$ helps to overcome the problem of the potential danger of explosion of concentrated solutions of HN_3. However, special care is necessary when handling even dilute solutions of HN_3, since it is potentially explosive and the vapor is highly poisonous upon inhalation. Precautions have to be made that no volatile pure (boiling point 60°C) or highly concentrated HN_3 can condensate onto cool surfaces.

P_3N_5 was synthesized according to the procedure described by Stock and Grüneberg starting from P_4S_{10} (Sigma Aldrich, 99 %) in a corundum boat in a continuous gas flow of dried NH_3 (Messer, Griesheim, 3.8).[1] The temperature was raised to 900°C at a rate of 3°C/min and held constant for 8 h. After the product was cooled it was ground and washed with 1M HCl and ethanol to remove soluble byproducts. A yellow-brown product was finally dried at 100°C. Phase purity of the product was confirmed by powder X-ray diffraction as well as FTIR spectroscopy.

$Ba_3P_5N_{10}Br:Eu^{2+}$ was synthesized using a modified Walker-type multianvil apparatus, starting from stoichiometric amounts of $Ba(N_3)_2$, P_3N_5 and $BaBr_2$ (Sigma Aldrich, 99.999 % trace metals basis). 2 mol% $EuCl_2$ (powder, Sigma Aldrich, 99.99 %, trace metal basis) were used as doping agent. All steps were carried out under exclusion of oxygen and moisture in an argon filled glove box (Unilab, MBraun, Garching, O_2 < 1 ppm, H_2O < 0.1 ppm). The starting mixture was thoroughly ground and packed into

a cylindrical capsule, made up of hexagonal boron nitride (Henze, Kempten). This capsule was sealed with a hexagonal boron nitride cap and placed in the middle of a Cr_2O_3-doped MgO octahedron (edge length 18 mm (18/11 assembly) and 25 mm (25/17 assembly), Ceramic Substrates & Components Ltd, Isle of Wight, UK), which served as pressure medium. The MgO octahedron was equipped with a ZrO_2 tube (Cesima Ceramics, Wust-Fischbach, Germany) as a thermal insulator and two concentric graphite tubes, which served as electrical resistance furnaces. The whole assembly was placed between eight tungsten carbide cubes (Hawedia, Marklkofen, Germany) with a truncation edge length of 11 mm (18/11 assembly) and 17 mm (25/17 assembly), respectively. Detailed information on the construction of the described multianvil assembly can be found in literature.[2] The mixture was compressed to the respective pressure ($1-5$ GPa). Then the temperature was raised to approximately 1000 °C within 30 min and was held for 30 min. Finally, the sample was cooled down within 30 min. After slow decompression, the sample was isolated as a light yellow crystalline solid.

F.2 Experimental Details of the Synthesis of $Ba_3P_5N_{10}Br:Eu^{2+}$ at Ambient Pressure

HPN_2 (amorphous) was synthesized by heating $(PNCl_2)_3$ (Merck, p.s.) in a ceramic corundum boat at 100 °C (10 h), 130 °C (5 h), 190 °C (3 h), 300 °C (4 h) in a continuous dried NH_3 (Messer, Griesheim, 3.8) flow, followed by vacuum heat treatment of the mixture at 450 °C (2 h). Details are described in the literature.[3] Phase purity of the product was confirmed by powder X-ray diffraction as well as FTIR spectroscopy. The title compound was synthesized starting from stoichiometric amounts of $BaBr_2$ (Sigma Aldrich, 99.999 % trace metals basis) and amorphous HPN_2. Furthermore, NH_4Br (Sigma Aldrich, $\geq$ 99.0 % trace metals basis) was added as mineralizer. The amounts of the starting materials are limited by the final pressure in the ampoule (max. 15 bar). The mixture was thoroughly mixed and ground in a glove box (Unilab, MBraun, Garching, $O_2 < 1$ ppm, $H_2O < 0.1$ ppm) and pressed to a tablet which was placed in an evacuated silica ampoule (wall thickness 1.5 mm, inner diameter 12 mm, length around 120 mm). After sealing the silica ampoule was placed into a tube furnace and heated to 850 °C (rate 1 °C/min) for 84 h. Finally, the sample was cooled down (rate 3 °C/min) to room temperature. The title compound was observed as minor component. In order to obtain a single phase product, the reaction conditions as well as the starting materials have to be optimized. Besides the starting materials mentioned above BaH_2 and $P(NH_2)_4Br$[4] may be used.

F.3 Energy Dispersive X-Ray (EDX) Analysis of $Ba_3P_5N_{10}Br:Eu^{2+}$

EDX analysis was carried out using a JEOL JSM-6500F field emission scanning electron microscope (SEM) operated at 16 kV. In order to make the surface of the sample conducting it was sputtered with carbon using an electron beam evaporator (BAL-TEC MED 020, Bal-Tec AG).

Table F.1: Results of the EDX measurements for $Ba_3P_5N_{10}Br:Eu^{2+}$.

	Ba	P	N	Br
EDX point 1 [atom %]	13.5	22.6	58.0	4.4
EDX point 2 [atom %]	13.9	22.9	56.6	4.4
EDX point 3 [atom %]	11.1	19.1	58.4	3.5
calculated atom %	14.0	23.3	46.7	4.7

F.4 Crystallographic Data for $Ba_3P_5N_{10}Br:Eu^{2+}$ from Single-Crystal Diffraction

Table F.2: Selected bond lengths Å in the crystal structure of $Ba_3P_5N_{10}Br:Eu^{2+}$; standard deviations in parentheses.

P1−N1	1.623(7)	P3−N11a	1.635(7)
P1−N3	1.608(7)	P3−N11b	1.608(5)
P1−N5	1.629(7)	P4−N5	1.635(7)
P1−N9	1.636(7)	P4−N6	1.637(7)
P2−N1	1.636(7)	P4−N7	1.618(7)
P2−N6	1.620(7)	P4−N8	1.620(7)
P2−N9	1.624(7)	P5−N4	1.635(7)
P2−N10	1.607(3)	P5−N2	1.636(7)
P3−N2	1.632(7)	P5−N3	1.614(7)
P3−N4	1.630(7)	P5−N8	1.634(7)
P3−N7	1.617(7)		

Table F.3: Selected bond angles / ° in the crystal structure of $Ba_3P_5N_{10}Br:Eu^{2+}$; standard deviations in parentheses.

N1−P1−N5	111.3(4)	N7−P3−N11a	113.8(8)
N1−P1−N9	114.8(4)	N11b−P3−N2	99.6(8)
N3−P1−N1	110.6(4)	N11b−P3−N4	119.3(9)
N3−P1−N5	111.0(4)	N11b−P3−N7	103.8(8)
N3−P1−N9	99.4(4)	N7−P4−N5	109.6(4)
N5−P1−N9	109.2(4)	N5−P4−N6	111.1(4)
N6−P2−N1	112.4(4)	N7−P4−N6	107.8(3)
N6−P2−N9	110.2(4)	N7−P4−N8	110.5(4)
N9−P2−N1	112.7(4)	N8−P4−N5	109.4(3)
N10−P2−N1	105.4(4)	N8−P4−N6	108.5(4)
N10−P2−N6	107.9(4)	N3−P5−N2	104.5(4)
N10−P2−N9	108.0(4)	N3−P5−N4	108.5(4)
N2−P3−N11a	114.8(8)	N3−P5−N8	107.5(4)
N4−P3−N2	114.5(4)	N4−P5−N2	114.6(3)
N4−P3−N11a	93.2(9)	N8−P5−N2	112.7(4)
N7−P3−N2	111.8(4)	N8−P5−N4	108.5(4)
N7−P3−N4	107.4(4)		

Table F.4: Selected crystallographic data of the single-crystal structure determination of $Ba_3P_5N_{10}Br:Eu^{2+}$; standard deviations in parentheses.

formula	$Ba_3P_5N_{10}Br$
formula mass / g·mol^{-1}	768.88
crystal system	orthorhombic
space group	*Pnma* (no. 62)
lattice parameters / Å	a = 12.5660(13)
	b = 13.2240(13)
	c = 13.8030(14)
cell volume / Å^3	2293.7(4)
formula units per cell	8
calculated X-ray density / g·cm^{-1}	4.557
linear absorption coefficient / mm^{-1}	14.369
radiation	Mo-Kα (λ = 0.71073 Å)
diffractometer	Bruker D8 Venture
θ-range / °	$2.13 \leq \theta \leq 26.0$
temperature / K	293(2)
F(000)	2784
observed reflections	31838
independent reflections ($> 2\sigma$)	2354(1960)
number of parameters	131
R_{int}; R_σ	0.0735; 0.0289
final R indices [I $> 2\sigma$(I)]	R_1 = 0.0339, wR_2 = 0.0638
final R indices (all data)	R_1 = 0.0457, wR_2 = 0.0657
goodness of fit	1.216

[a] = 1 / [$\sigma^2(F_0^2)$+(0.0042 P)^2 + 45.0789 P], with $P = (F_0^2 + 2\,F_c^2) / 3$

Table F.5: Fractional coordinates, isotropic displacement parameters, and occupation of crystallographic positions of $Ba_3P_5N_{10}Br:Eu^{2+}$; standard deviations in parentheses.

atom	Wyckoff	x	y	z	U_{eq} / Å^2	occupancy
Ba1	8*d*	0.26967(4)	0.00107(4)	0.32403(3)	0.00831(12)	1.0
Ba2	4*c*	0.03390(6)	1/4	0.72543(5)	0.01118(17)	1.0
Ba3	4*c*	0.04008(6)	1/4	0.23902(6)	0.01221(18)	1.0
Ba4	4*c*	0.33766(6)	1/4	0.03507(5)	0.01123(17)	1.0
Ba5	4*c*	0.34079(6)	1/4	0.53856(6)	0.01410(18)	1.0
Br1	4*c*	0.27725(11)	1/4	0.79794(9)	0.0150(3)	1.0
Br2	4*c*	0.28903(10)	1/4	0.28647(9)	0.0145(3)	1.0
P1	8*d*	0.03581(16)	0.52956(15)	0.14605(14)	0.0040(4)	1.0
P2	8*d*	0.07530(16)	0.13301(16)	0.01315(15)	0.0042(4)	1.0
P3	8*d*	0.09225(16)	0.13067(15)	0.48333(15)	0.0041(4)	1.0
P4	8*d*	0.24940(16)	0.5002(2)	0.07302(13)	0.0033(4)	1.0
P5	8*d*	0.46975(16)	0.00111(17)	0.13981(14)	0.0057(4)	1.0
N1	8*d*	0.0056(5)	0.0791(5)	0.0989(5)	0.0080(5)	1.0
N2	8*d*	0.0118(6)	0.0978(5)	0.5707(5)	0.0080(5)	1.0
N3	8*d*	0.0177(6)	0.0415(5)	0.7488(5)	0.0080(5)	1.0
N4	8*d*	0.0560(5)	0.0922(5)	0.3761(5)	0.0080(5)	1.0
N5	8*d*	0.1643(5)	0.5450(5)	0.1517(5)	0.0080(5)	1.0
N6	8*d*	0.1950(5)	0.0881(5)	0.0062(5)	0.0080(5)	1.0
N7	8*d*	0.2119(5)	0.0900(5)	0.5016(5)	0.0080(5)	1.0
N8	8*d*	0.3501(5)	0.0482(5)	0.1299(5)	0.0080(5)	1.0
N9	8*d*	0.5176(5)	0.1273(5)	0.5919(5)	0.0080(5)	1.0
N10	4*c*	0.0838(8)	1/4	0.0436(7)	0.0080(5)	1.0
N11a	4*c*	0.0864(16)	1/4	0.4529(18)	0.0080(5)	0.49(2)
N11b	4*c*	0.1005(16)	1/4	0.5044(17)	0.0080(5)	0.51(2)

Table F.6: Anisotropic displacement parameters of crystallographic positions of $Ba_3P_5N_{10}Br:Eu^{2+}$; standard deviations in parentheses.

atom	U_{11}	U_{22}	U_{33}	U_{12}	U_{13}	U_{23}
Ba1	0.0098(2)	0.0106(2)	0.0046(2)	-0.0003(2)	0.00105(18)	0.0016(2)
Ba2	0.0116(4)	0.0061(4)	0.0159(4)	0	-0.0004(3)	0
Ba3	0.0109(4)	0.0105(4)	0.0153(4)	0	0.0005(3)	0
Ba4	0.0100(4)	0.0089(4)	0.0148(4)	0	-0.0001(3)	0
Ba5	0.0124(4)	0.0062(4)	0.0238(4)	0	-0.0030(3)	0
Br1	0.0140(6)	0.0130(7)	0.0181(7)	0	-0.0004(5)	0
Br2	0.0128(7)	0.0127(7)	0.0179(6)	0	0.0010(5)	0
P1	0.0040(9)	0.0030(10)	0.0049(9)	0.0018(8)	-0.0002(8)	0.0000(8)
P2	0.0066(10)	0.0020(10)	0.0041(9)	-0.0002(8)	-0.0018(8)	-0.0006(8)
P3	0.0040(10)	0.0025(10)	0.0057(10)	-0.0002(8)	0.0009(8)	0.0000(8)
P4	0.0040(9)	0.0051(9)	0.0007(8)	-0.0004(9)	0.0007(6)	-0.0003(7)
P5	0.0055(9)	0.0092(10)	0.0025(9)	0.0011(8)	-0.0010(7)	-0.0026(9)
N1	0.0080(11)	0.0092(11)	0.0069(10)	0.0007(9)	-0.0003(9)	-0.0005(10)
N2	0.0080(11)	0.0092(11)	0.0069(10)	0.0007(9)	-0.0003(9)	-0.0005(10)
N3	0.0080(11)	0.0092(11)	0.0069(10)	0.0007(9)	-0.0003(9)	-0.0005(10)
N4	0.0080(11)	0.0092(11)	0.0069(10)	0.0007(9)	-0.0003(9)	-0.0005(10)
N5	0.0080(11)	0.0092(11)	0.0069(10)	0.0007(9)	-0.0003(9)	-0.0005(10)
N6	0.0080(11)	0.0092(11)	0.0069(10)	0.0007(9)	-0.0003(9)	-0.0005(10)
N7	0.0080(11)	0.0092(11)	0.0069(10)	0.0007(9)	-0.0003(9)	-0.0005(10)
N8	0.0080(11)	0.0092(11)	0.0069(10)	0.0007(9)	-0.0003(9)	-0.0005(10)
N9	0.0080(11)	0.0092(11)	0.0069(10)	0.0007(9)	-0.0003(9)	-0.0005(10)
N10	0.0080(11)	0.0092(11)	0.0069(10)	0.0007(9)	-0.0003(9)	-0.0005(10)
N11a	0.0080(11)	0.0092(11)	0.0069(10)	0.0007(9)	-0.0003(9)	-0.0005(10)
N11b	0.0080(11)	0.0092(11)	0.0069(10)	0.0007(9)	-0.0003(9)	-0.0005(10)

F.5 Split Position in $Ba_3P_5N_{10}Br:Eu^{2+}$

Due to the quite elongated displacement ellipsoid of the N11 atom (Figure F.1, left), it was possible to refine a split position for this atom with occupancy of ∼0.5 each (Figure F.1, right).

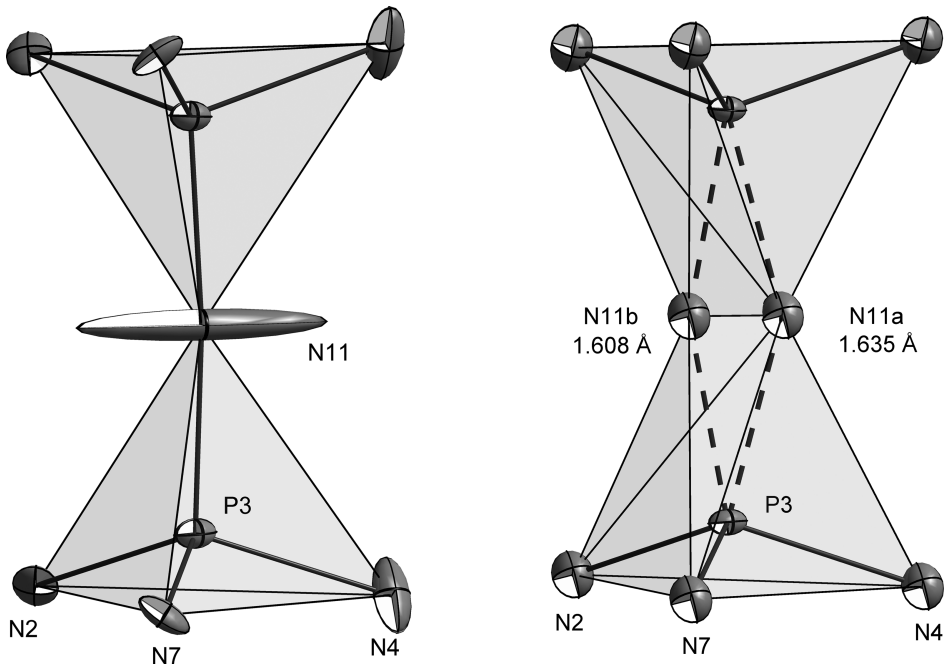

Figure F.1: Split position of the N11 atom; ellipsoids are drawn with a probability factor of 70 %.

F.6 Crystallographic Data for $Ba_3P_5N_{10}Br:Eu^{2+}$ from Rietveld Refinement

Powder X-ray diffraction data was collected on a STOE StadiP powder diffractometer in Debye Scherer geometry using Mo-Kα_1-radiation (λ = 0.71073 Å) with Ge(111)-monochromator and a position sensitive detector. Rietveld refinement was performed using TOPAS Academics 4.1,[5] employing the fundamental parameter approach. Preferred orientation of the crystallites was described using a spherical harmonics of fourth order.

Table F.7: Selected crystallographic data of Rietveld refinement of $Ba_3P_5N_{10}Br:Eu^{2+}$; standard deviations in parentheses.

formula	$Ba_3P_5N_{10}Br$
crystal system	orthorhombic
space group	*Pnma* (no. 62)
lattice parameters / Å	a = 12.57918(12)
	b = 13.23628(11)
	c = 13.80106(14)
cell volume / $Å^3$	2297.9
formula units per cell	8
calculated X-ray density / $g \cdot cm^{-1}$	5.54864(7)
linear absorption coefficient / cm^{-1}	157.74
radiation	Mo-Kα_1 (λ = 0.71073 Å)
monochromator	Ge(111)
diffractometer	Stoe StadiP
detector	linear PSD
2θ-range / °	2−65.300
temperature / K	298(2)
data points	4221
number of observed reflections	4485
number of parameters	116
program used	TOPAS-Academics
structure refinement	Rietveld method
profile function	fundamental parameters model
background function	shifted Chebyshev
R_p, R_{wp}	0.01630, 0.02077
goodness of fit	1.231

F.7 Luminescence Spectroscopy on $Ba_3P_5N_{10}Br:Eu^{2+}$

Investigations on luminescence properties of $Ba_3P_5N_{10}Br:Eu^{2+}$ were performed with a luminescence microscope consisting of a HORIBA Fluorimax4 spectrofluorimeter system attached to an Olympus BX51 microscope via fiber optical bundles. The excitation wavelength was chosen to 400 nm with a spectral width of 10 nm. The emission spectrum was collected in the wavelength range between 420 nm and 780 nm with 2 nm step size. For the measurements of the photoluminescence quantum efficiency of the powder sample, commercially available $CaAlSiN_3:Eu^{2+}$ with an internal quantum efficiency of 92 % at a 390 nm excitation wavelengths was used as reference phosphor.

F.8 FTIR Spectroscopy of $Ba_3P_5N_{10}Br:Eu^{2+}$

The FTIR spectrum of $Ba_3P_5N_{10}Br:Eu^{2+}$ was measured using KBr tablet method on a Spectrum BX II spectrometer (Perkin Elmer, Waltham MA, USA).

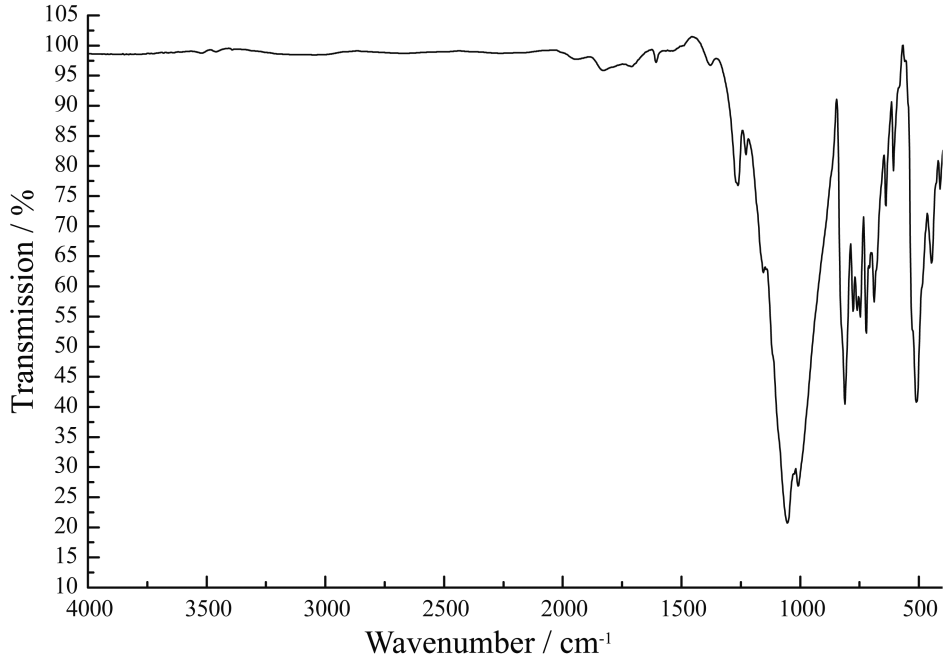

Figure F.2: FTIR spectrum of $Ba_3P_5N_{10}Br:Eu^{2+}$.

F.9 Temperature Dependent Powder X-Ray Diffraction for $Ba_3P_5N_{10}Br:Eu^{2+}$

Temperature dependent X-ray powder diffraction measurements were carried out on a Stoe StadiP diffractometer. It was equipped with a high-temperature graphite furnace using Ge(111) monochromated Mo-$K_{\alpha1}$ radiation (λ = 0.70930 Å) and an image plate position sensitive detector. The sample was heated with a rate of 1°C/min between measurements. The temperature was held constant for each 15 min measurement.

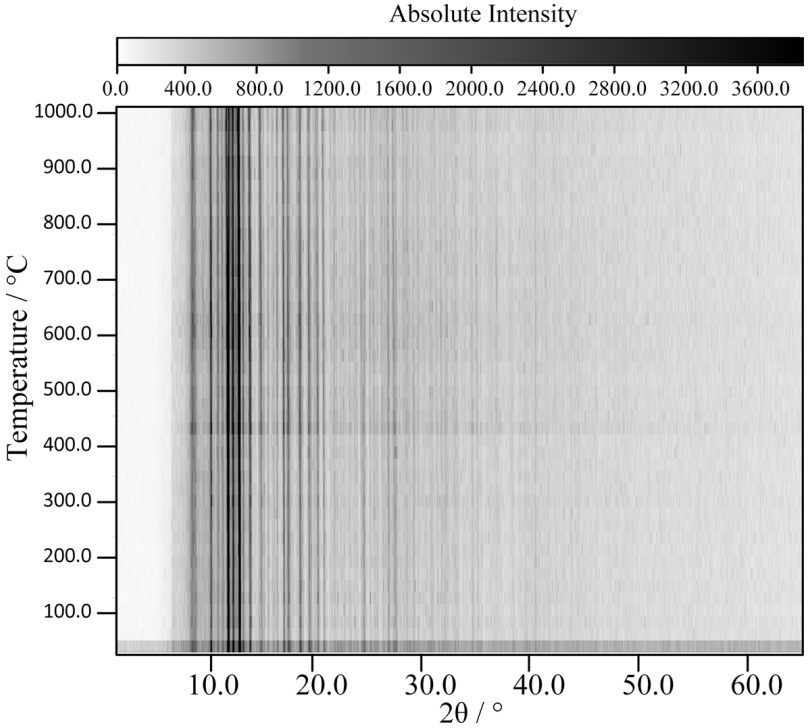

Figure F.3: Temperature dependent powder X-ray diffraction for $Ba_3P_5N_{10}Br:Eu^{2+}$.

F.10 References

[1] A. Stock, H. Grüneberg, *Ber. Dtsch. Chem. Ges.* **1907**, *40*, 2573.

[2] a) N. Kawai, S. Endo, *Rev. Sci. Instrum.* **1970**, *41*, 1178; b) D. Walker, M. A. Carpenter, C. M. Hitch, *Am. Mineral.* **1990**, *75*, 1020; c) D. Walker, *Am. Mineral.* **1991**, *76*, 1092; d) D. C. Rubie, *Phase Transitions* **1999**, *68*, 431; e) H. Huppertz, *Z. Kristallogr.* **2004**, *219*, 330.

[3] F. W. Karau, *Dissertation*, Ludwig-Maximilians-Universität München (Germany), **2007**.

[4] K. Landskron, S. Horstmann, W. Schnick, *Z. Naturforsch.* **1999**, *54*, 1019.

[5] A. A. Coelho, *TOPAS-Academic*, Version 4.1, Coelho Software, Brisbane (Australia), **2007**.

G Supporting Information for Chapter 8

G.1 FTIR Spectroscopy of $Ba_3P_5N_{10}X:Eu^{2+}$ (X = Cl, I)

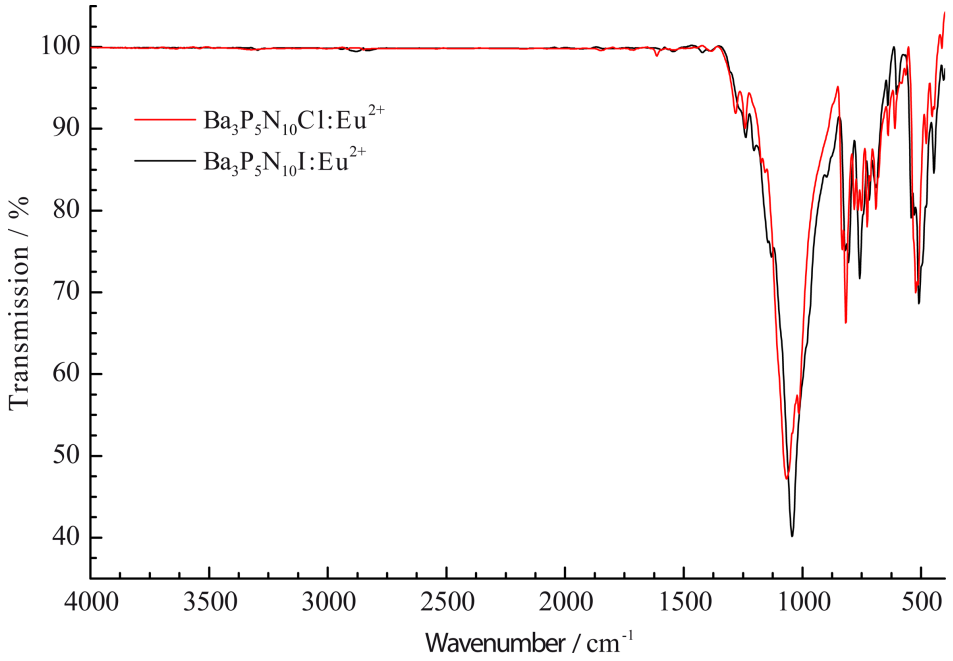

Figure G.1: FTIR spectra of $Ba_3P_5N_{10}X:Eu^{2+}$ (X = Cl, I).

G.2 Temperature Dependent Powder X-Ray Diffraction for $Ba_3P_5N_{10}X:Eu^{2+}$

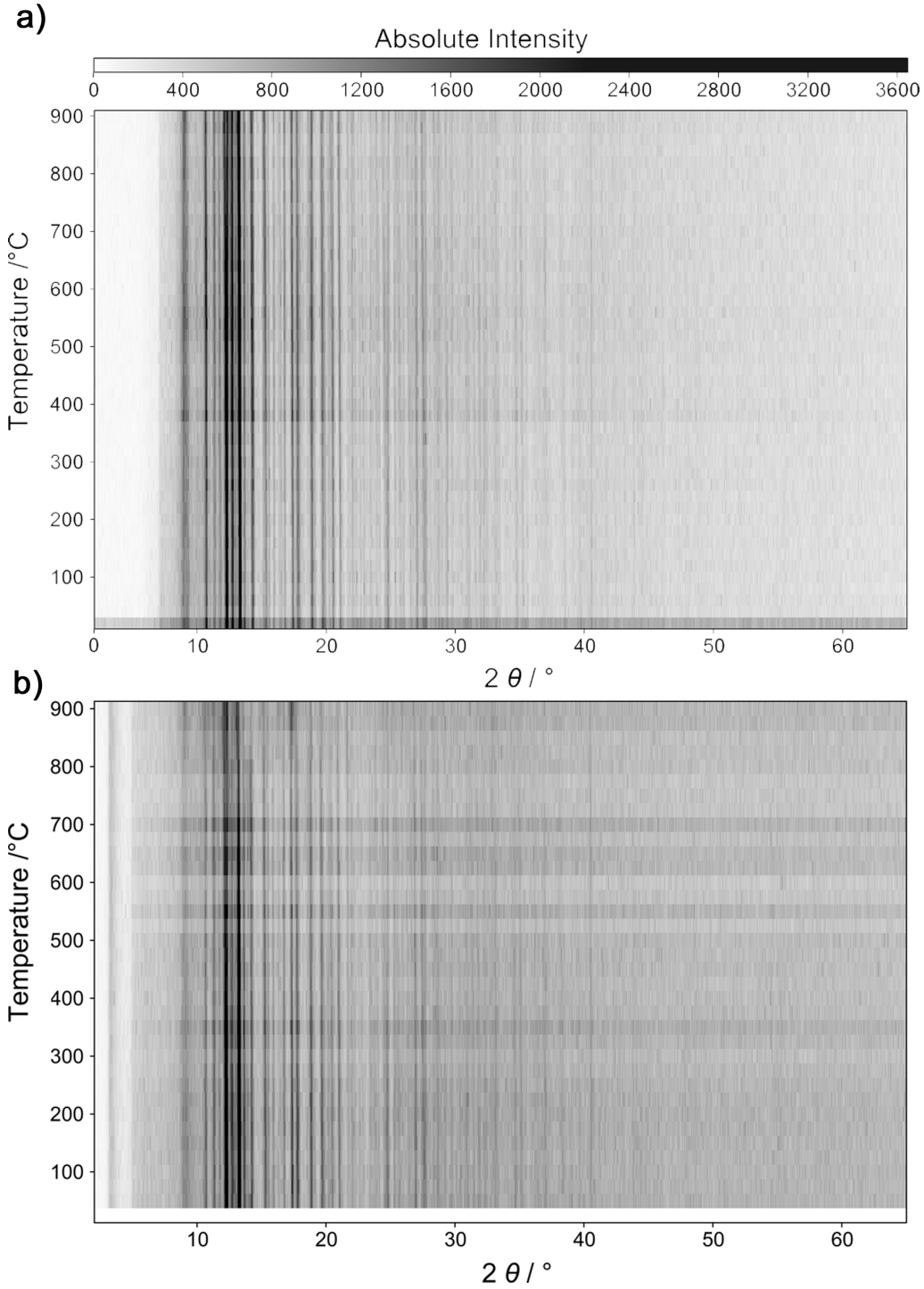

Figure G.2: Temperature dependent powder X-ray diffraction for $Ba_3P_5N_{10}Cl : Eu^{2+}$ (a) and $Ba_3P_5N_{10}I:Eu^{2+}$ (b).

G.3 Crystallographic Data for $Ba_3P_5N_{10}X$ from Single-Crystal Diffraction

Table G.1: Anisotropic displacement parameters of crystallographic positions of $Ba_3P_5N_{10}Cl:Eu^{2+}$; standard deviations in parentheses.

atom	U_{11}	U_{22}	U_{33}	U_{12}	U_{13}	U_{23}
Ba1	0.01239(13)	0.01483(13)	0.00832(13)	-0.00048(8)	0.00087(8)	0.00279(9)
Ba2	0.02073(19)	0.00550(16)	0.01509(18)	0	-0.00087(14)	0
Ba3	0.01484(17)	0.00937(16)	0.01120(17)	0	0.00029(13)	0
Ba4	0.01248(16)	0.00969(17)	0.01846(19)	0	-0.00116(13)	0
Ba5	0.01368(18)	0.00752(17)	0.0548(3)	0	-0.00934(18)	0
Cl1	0.0205(7)	0.0166(7)	0.0271(8)	0	0.0001(6)	0
Cl2	0.0177(7)	0.0150(7)	0.0293(8)	0	0.0024(6)	0
P1	0.0069(4)	0.0057(4)	0.0065(5)	-0.0001(3)	0.0006(3)	-0.0012(3)
P2	0.0066(4)	0.0039(4)	0.0066(4)	0.0001(3)	-0.0001(4)	0.0001(3)
P3	0.0075(4)	0.0039(4)	0.0070(4)	0.0003(3)	-0.0009(3)	0.0003(3)
P4	0.0074(4)	0.0045(4)	0.0069(4)	0.0003(3)	-0.0001(3)	-0.0005(3)
P5	0.0063(4)	0.0056(4)	0.0070(5)	-0.0003(3)	-0.0005(4)	-0.0007(3)
N1	0.0081(14)	0.0054(15)	0.0120(16)	0.0001(12)	0.0006(13)	0.0018(12)
N2	0.0105(15)	0.0087(16)	0.0108(16)	0.0005(12)	0.0011(13)	0.0019(12)
N3	0.0094(15)	0.0081(16)	0.0083(15)	-0.0007(12)	0.0022(12)	-0.0001(12)
N4	0.0120(15)	0.0118(16)	0.0060(15)	0.0000(12)	0.0005(12)	-0.0070(12)
N5	0.0085(15)	0.0122(16)	0.0073(15)	-0.0033(12)	0.0009(12)	-0.0013(12)
N6	0.0088(15)	0.0093(16)	0.0086(15)	0.0016(12)	0.0006(12)	0.0021(12)
N7	0.0078(15)	0.0125(16)	0.0110(16)	0.0031(13)	0.0008(12)	0.0010(12)
N8	0.0094(14)	0.0068(15)	0.0065(15)	-0.0031(12)	-0.0010(12)	0.0012(12)
N9	0.0132(15)	0.0062(15)	0.0093(15)	-0.0007(12)	0.0016(13)	0.0006(12)
N10	0.022(3)	0.006(2)	0.008(2)	0	-0.004(2)	0
N11a	0.01239(13)	0.01483(13)	0.00832(13)	-0.00048(8)	0.00087(8)	0.00279(9)
N11b	0.02073(19)	0.00550(16)	0.01509(18)	0	-0.00087(14)	0

Table G.2: Anisotropic displacement parameters of crystallographic positions of $Ba_3P_5N_{10}Cl$; standard deviations in parentheses.

atom	U_{11}	U_{22}	U_{33}	U_{12}	U_{13}	U_{23}
Ba1	0.0144(2)	0.0162(2)	0.0059(2)	-0.0005(2)	0.0013(1)	0.0033(2)
Ba2	0.0262(3)	0.0084(3)	0.0183(3)	0	0.0021(2)	0
Ba3	0.0327(4)	0.0122(3)	0.0157(3)	0	0.0071(3)	0
Ba4	0.0129(3)	0.0105(3)	0.0131(3)	0	-0.0004(2)	0
Ba5	0.0121(3)	0.0072(3)	0.0164(3)	0	-0.0025(2)	0
Cl1	0.0167(4)	0.0124(4)	0.0150(4)	0	0.0004(3)	0
Cl2	0.0203(5)	0.0116(4)	0.0155(4)	0	0.0014(3)	0
P1	0.0043(7)	0.0058(8)	0.0037(7)	0.0004(6)	0.0009(5)	0.0000(5)
P2	0.0044(7)	0.0033(7)	0.0061(7)	0.0000(6)	-0.0018(5)	0.0001(5)
P3	0.0037(7)	0.0025(7)	0.0078(7)	-0.0005(6)	-0.0005(6)	-0.0006(5)
P4	0.0026(6)	0.0065(7)	0.0037(6)	-0.0007(7)	-0.0001(4)	-0.0002(5)
P5	0.0051(6)	0.0091(7)	0.0027(7)	0.0008(6)	-0.0013(5)	-0.0015(6)
N1	0.0080(8)	0.0104(8)	0.0066(8)	0.0002(7)	0.0000(6)	-0.0013(7)
N2	0.0080(8)	0.0104(8)	0.0066(8)	0.0002(7)	0.0000(6)	-0.0013(7)
N3	0.0080(8)	0.0104(8)	0.0066(8)	0.0002(7)	0.0000(6)	-0.0013(7)
N4	0.0080(8)	0.0104(8)	0.0066(8)	0.0002(7)	0.0000(6)	-0.0013(7)
N5	0.0080(8)	0.0104(8)	0.0066(8)	0.0002(7)	0.0000(6)	-0.0013(7)
N6	0.0080(8)	0.0104(8)	0.0066(8)	0.0002(7)	0.0000(6)	-0.0013(7)
N7	0.0080(8)	0.0104(8)	0.0066(8)	0.0002(7)	0.0000(6)	-0.0013(7)
N8	0.0080(8)	0.0104(8)	0.0066(8)	0.0002(7)	0.0000(6)	-0.0013(7)
N9	0.0080(8)	0.0104(8)	0.0066(8)	0.0002(7)	0.0000(6)	-0.0013(7)
N10	0.0080(8)	0.0104(8)	0.0066(8)	0.0002(7)	0.0000(6)	-0.0013(7)
N11a	0.0144(2)	0.0162(2)	0.0059(2)	-0.0005(2)	0.0013(1)	0.0033(2)
N11b	0.0262(3)	0.0084(3)	0.0183(3)	0	0.0021(2)	0

Table G.3: Fractional atomic coordinates, isotropic displacement parameters, and occupation of crystallographic positions of $Ba_3P_5N_{10}I$; standard deviations in parentheses.

atom	Wyckoff site	x	y	z	U_{eq} / Å^2	occupancy
Ba1	8*d*	0.26952(3)	0.00014(3)	0.32538(2)	0.01218(9)	1.0
Ba2	4*c*	0.03304(5)	1/4	0.71915(4)	0.0176(1)	1.0
Ba3	4*c*	0.03854(5)	1/4	0.23334(4)	0.0202(2)	1.0
Ba4	4*c*	0.34051(4)	1/4	0.03925(4)	0.0122(1)	1.0
Ba5	4*c*	0.34006(4)	1/4	0.54224(4)	0.0119(1)	1.0
I1	4*c*	0.27570(6)	1/4	0.79808(5)	0.0147(3)	1.0
I2	4*c*	0.28581(6)	1/4	0.29092(5)	0.0158(3)	1.0
P1	8*d*	0.0360(1)	0.5283(1)	0.1460(1)	0.0046(3)	1.0
P2	8*d*	0.0754(1)	0.1330(1)	0.0113(1)	0.0046(3)	1.0
P3	8*d*	0.0917(1)	0.1304(1)	0.4864(1)	0.0047(3)	1.0
P4	8*d*	0.2493(1)	0.4986(2)	0.0730(1)	0.0043(3)	1.0
P5	8*d*	0.4691(1)	0.0052(1)	0.1401(1)	0.0056(3)	1.0
N1	8*d*	0.0056(4)	0.0791(4)	0.0973(3)	0.0083(3)	1.0
N2	8*d*	0.0117(4)	0.0932(4)	0.5712(3)	0.0083(3)	1.0
N3	8*d*	0.0164(4)	0.0375(4)	0.7481(3)	0.0083(3)	1.0
N4	8*d*	0.0519(4)	0.0980(4)	0.3783(3)	0.0083(3)	1.0
N5	8*d*	0.1642(4)	0.5441(4)	0.1505(3)	0.0083(3)	1.0
N6	8*d*	0.1966(4)	0.0890(4)	0.0065(3)	0.0083(3)	1.0
N7	8*d*	0.2115(4)	0.0881(4)	0.5014(3)	0.0083(3)	1.0
N8	8*d*	0.3488(3)	0.0497(4)	0.1312(3)	0.0083(3)	1.0
N9	8*d*	0.5188(4)	0.1264(4)	0.5932(3)	0.0083(3)	1.0
N10	4*c*	0.0812(5)	1/4	0.0428(5)	0.0083(3)	1.0
N11a	4*c*	0.101(1)	1/4	0.504(1)	0.013(2)	0.71(3)
N11b	4*c*	0.082(2)	1/4	0.464(3)	0.013(2)	0.29(3)

G.4 Crystallographic Data for $Ba_3P_5N_{10}X$ from Rietveld Refinement

Table G.4: Selected crystallographic data of Rietveld refinement of $Ba_3P_5N_{10}X$:Eu^{2+} (X = Cl, I); standard deviations in parentheses.

formula	$Ba_3P_5N_{10}Cl$	$Ba_3P_5N_{10}I$
crystal system	orthorhombic	
space group	*Pnma* (no. 62)	
lattice parameters / Å	a = 12.54722(11)	a = 12.62148(20)
	b = 13.21986(10)	b = 13.26115(19)
	c = 13.77620(12)	c = 13.89433(23)
cell volume / $Å^3$	2285.1	2325.6
formula units per cell	8	8
calculated X-ray density / $g \cdot cm^{-1}$	4.256(8)	4.550(11)
linear absorption coefficient / cm^{-1}	120.13(28)	138.50(37)
radiation	Mo-Kα_1 (λ = 0.71073 Å)	
monochromator	Ge(111)	
diffractometer	Stoe StadiP	
detector	MYTHEN 1K	
2θ-range / °	$2 - 65.300$	$2-65.300$
data points	4221	4221
number of observed reflections	4459	4533
number of parameters	111	141
program used	TOPAS Academics	
structure refinement	Rietveld refinement	
profile function	fundamental parameters model	
background function	shifted Chebyshev	
goodness of fit	1.251	1.429
R_p, R_{wp}	0.0299, 0.0391	0.0270, 0.0350

G.5 Luminescence Spectroscopy of $Ba_3P_5N_{10}X$ (X = Cl, I)

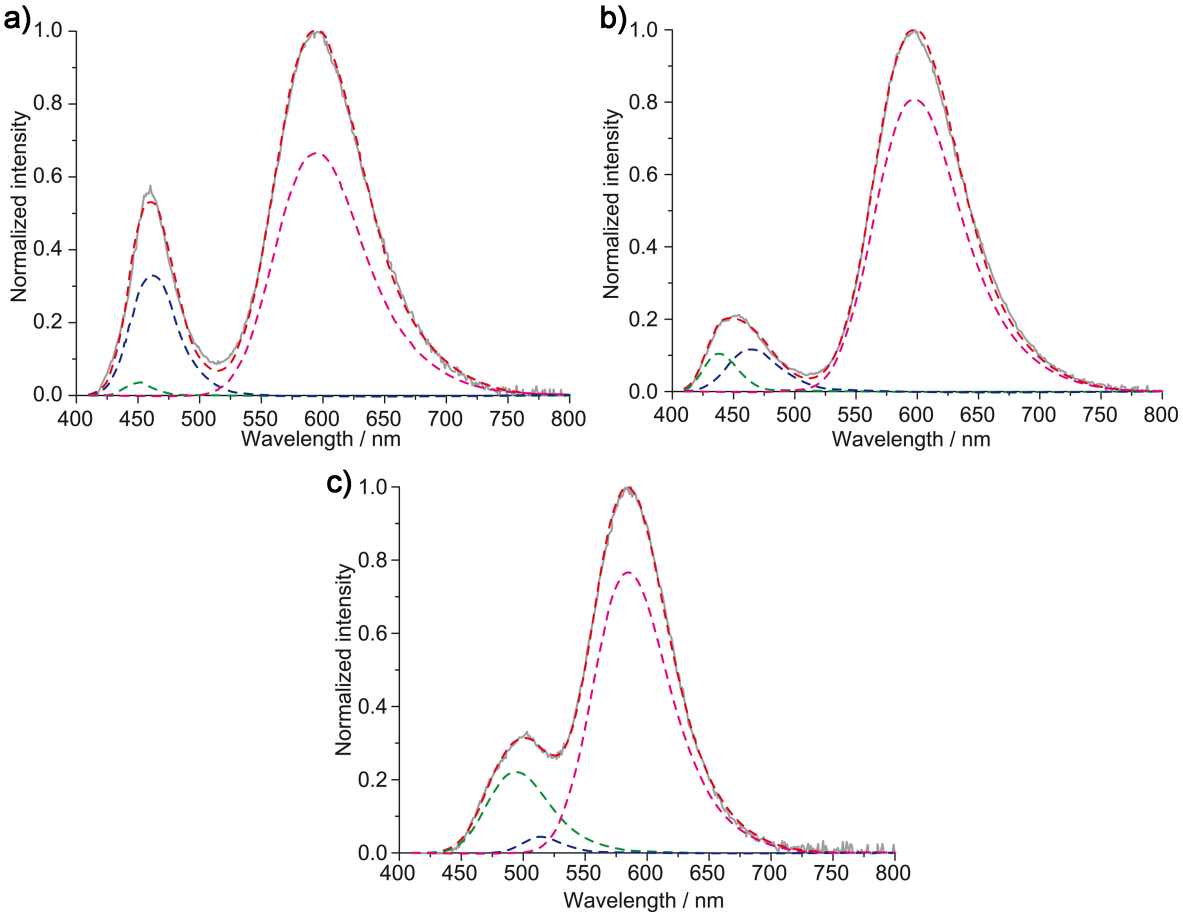

Figure G.3: Least square refinement of measured emission spectrum (gray solid line) of $Ba_3P_5N_{10}X{:}Eu^{2+}$, X = Cl with 2 mol% Eu (a) and 5 mol% Eu (b) and X = I with 5 mol% Eu (c) as well as respective three individual Pekarian-shaped functions.

To analyze the observed composed emission spectra a least-squares fit of measured emission spectra with Pekarian-shaped functions was carried out (see Figure G.3). Each component of the composed emission bands has been fitted numerically by means of a sum of two Gaussian peaks, generated from the peak position P_0 and the FWHM given in nm according to the following equations, with P_0 being the position of the emission peak and σ being the standard deviation of the Gaussian peaks (Gaussian RMS width).

$$I(E) = H\left(e^{\frac{-(E-E_0)^2}{2\sigma^2}} + 0.12e^{\frac{-(E-E_0+1.7\sigma)^2}{2\sigma^2}}\right) \tag{G.1}$$

$$E_0 = \frac{10^7}{P_0};\ \sigma = \frac{1}{\sqrt{2\pi}}10^7\left(P_0 - \frac{FWHM}{2}\right)^{-1} - \left(P_0 + \frac{FWHM}{2}\right)^{-1}$$

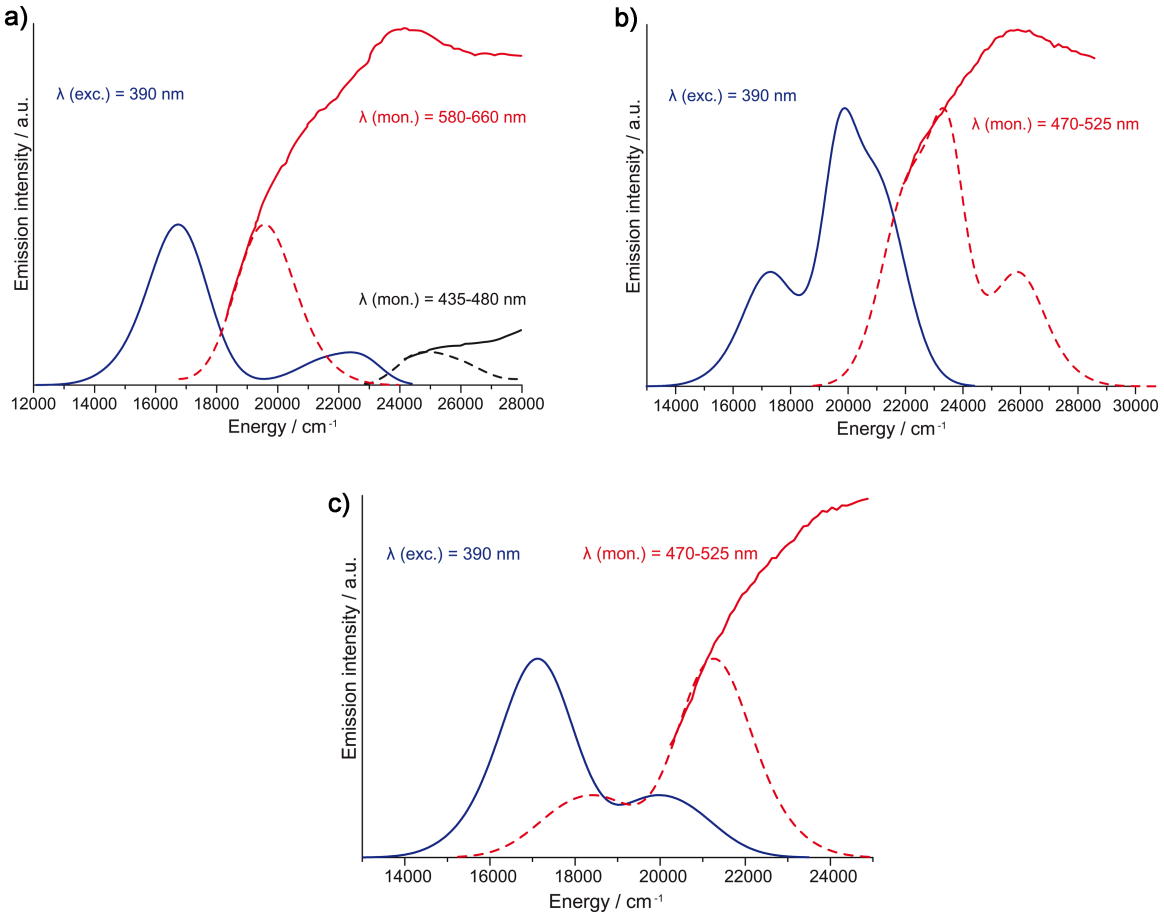

Figure G.4: Estimation of absorption band position by mirror-image relationship between the excitation spectra (red and black solid lines) and the emission spectra of $Ba_3P_5N_{10}Cl:Eu^{2+}$ (5 mol%, a), $Ba_3P_5N_{10}I:Eu^{2+}$ (2 mol%, b) and $Ba_3P_5N_{10}I:Eu^{2+}$ (5 mol%, c) at excitation at 390 nm (blue solid line). The red and black dashed lines are the mirror-images of the respective emission spectrum.

H Miscellaneous

H.1 List of Publications

The results compiled in this thesis were published in scientific journals as detailed in the following list.

Publications Within this Thesis

1. **A High-Pressure Polymorph of Phosphorus Nitride Imide**

   A. Marchuk, F. J. Pucher, F. W. Karau, and W. Schnick

   published in: *Angew. Chem.* **2014**, *126*, 2501-2504. DOI: 10.1002/ange.201309020

   published in: *Angew. Chem. Int. Ed.* **2014**, *53*, 2469-2472. DOI: 10.1002/anie.201309020

   Writing the manuscript, synthesis of the samples, structure elucidation from single-crystal X-ray diffraction data, evaluation of analytical data, Rietveld refinement and MAPLE calculations were done by A. Marchuk. ^{31}P *and* ^{1}H *solid-state NMR spectroscopy was carried out by C. Minke and evaluated by A. Marchuk. Literature and database research and topological analysis were made by A. Marchuk, F. J. Pucher, and F. W. Karau in close collaboration. W. Schnick directed and supervised the work. All authors revised the manuscript.*

2. M_2PO_3N **(*M* = Ca, Sr) – *ortho*-Oxonitridophosphates with β-K_2SO_4 Structure Type**

   A. Marchuk, P. Schultz, C. Hoch, O. Oeckler, and W. Schnick

   published in: *Chem. Eur. J.* **2015**, *21*, 6443-6448. DOI: 10.1021/acs.inorgchem.5b02647

   Writing the main part of the manuscript and creation of graphical material was accomplished by A. Marchuk and P. Schultz. Synthesis of the samples, structure elucidation of average

structures from single-crystal X-ray diffraction data, Rietveld refinements, topological analysis, evaluation of the spectroscopic details and literature research were performed by A. Marchuk. Reconstruction of reciprocal lattice sections was performed by C. Hoch. TLS analysis of Sr_2PO_3N was carried out by C. Hoch and A. Marchuk. Elucidation of the modulated structure of Ca_2PO_3N was done by P. Schmidt, O. Oeckler, A. Marchuk and C. Hoch in strong collaboration. W. Schnick directed and supervised the work. All authors revised the manuscript.

3. **$CaMg_2P_6O_3N_{10}$ – A Quinary Oxonitridophosphate with an Unprecedented Tetrahedra Network Structure Type**

A. Marchuk, L. Neudert, O. Oeckler, and W. Schnick

published in: *Eur. J. Inorg. Chem.* **2014**, 3427-3434. DOI: 10.1002/ejic.201402302

Writing the main part of the mansucript, synthesis of the sample, Rietveld refinement, creation of graphical material, topological analysis, evaluation of the spectroscopic details and literature research were performed by A. Marchuk. Structure elucidation from single crystal data was made by A. Marchuk and O. Oeckler. Electron diffraction and transmission microscopy including HRTEM image simulations and their evaluation were done by L. Neudert and O. Oeckler. W. Schnick directed and supervised the work. All authors revised the manuscript.

4. ***M*$H_4P_6N_{12}$ (*M* = Mg, Ca): New Imidonitridophosphates with an Unprecedented Layered Network Structure Type**

A. Marchuk, V. R. Celinski, J. Schmedt auf der Günne, and W. Schnick

published in: *Chem. Eur. J.* **2015**, *21*, 5836-5842. DOI:10.1002/chem.201406240

For this publication, writing the main part of the manuscript, synthesis of the samples, structure elucidation from single-crystal X-ray data, Rietveld refinements, creation of the graphical materials, evaluation of spectroscopic data and topological analysis were carried out by A. Marchuk. The qualitative and quantitative solid-state NMR measurements and the evaluation

thereof were carried out by V. R. Celinski and J. Schmedt auf der Günne. W. Schnick directed and supervised the work. All authors revised the manuscript.

5. **Luminescent Nitridophosphates CaP_2N_4:Eu^{2+}, SrP_2N_4:Eu^{2+}, BaP_2N_4:Eu^{2+}, and $BaSr_2P_6N_{12}$**

   F. J. Pucher, A. Marchuk, P. J. Schmidt, D. Wiechert, and W. Schnick

   published in: *Chem. Eur. J.* **2015**, *21*, 6443-6448. DOI: 10.1002/chem.201500047

   Writing the main part of the manuscript, structure elucidation of the powder samples, Rietveld refinements, literature research and creation of graphical material were carried out by F. J. Pucher. Synthesis of the single crystals and structure elucidation of CaP_2N_4:Eu^{2+} was performed by A. Marchuk. Luminescence investigations and evaluation thereof were performed by D. Wiechert and P. J. Schmidt. W. Schnick directed and supervised the work. All authors revised the manuscript.

6. **$Ba_3P_5N_{10}Br$:Eu^{2+}: A Natural-White-Light Single Emitter with a Zeolite Structure Type**

   A. Marchuk and W. Schnick

   published in: *Angew. Chem.* **2015**, *127*, 2413-2417. DOI: 10.1002/ange.201410528

   published in: *Angew. Chem. Int. Ed.* **2015**, *54*, 2383-2387. DOI: 10.1002/anie.201410528

   Writing of the manuscript, synthesis of the sample, structure elucidation from single-crystal X-ray diffraction data, Rietveld refinement, evaluation of the spectroscopic data, literature research, creation of graphical material and topological analysis were performed by A. Marchuk. Luminescence measurements were carried out by P. Huppertz (LDCA, Aachen). W. Schnick directed and supervised the work. All authors revised the manuscript.

7. **Nontypical Luminescence Properties and Structural Relation of $Ba_3P_5N_{10}X$:Eu^{2+} (*X* = Cl, I) — Nitridophosphate Halides with Zeolite-like Structure**

   A. Marchuk, S. Wendl, N. Imamovic, F. Tambornino, D. Wiechert, P. J. Schmidt and W. Schnick

published in: *Chem. Mater.* **2015**, *27*, 6432-6441. DOI: 10.1021/acs.chemmater.5b02668

Writing of the manuscript, structure elucidation from single-crystal X-ray diffraction data, Rietveld refinements, literature research, creation of graphical material and topological analysis were carried out by A. Marchuk. Synthesis of the samples was performed by A. Marchuk, S. Wendl, and N. Imamovic. Luminescence investigations and evaluation thereof were performed by D. Wiechert and P. J. Schmidt. W. Schnick directed and supervised the work. All authors revised the manuscript.

H.2 Contributions to Conferences

1. **$Ba_3P_5N_{10}X:Eu^{2+}$ (*X* = Cl, Br, I) — Luminescent Nitridophosphate with Zeolite-like Framework Structure** (poster presentation, poster award)

   A. Marchuk, W. Schnick

   European Conference On Solid State Conference, Vienna, Austria **2015**

2. **Combination of TEM and Microfocus Synchrotron Diffraction for the Structure Determination of Micro- and Nanocrystalline Materials**

   F. Fahrnbauer, T. Rosenthal, A. Marchuk, P. Urban, G. Wagner, W. Schnick, O. Oeckler

   22. Jahrestagung der Deutschen Gesellschaft für Kristallographie, Berlin, Germany **2014**

3. **Kombination von TEM und Synchrotron-Mikrofokusdiffraktion**

   L. Neudert, G. Wagner, F. Fahrnbauer, T. Rosenthal, A. Marchuk, P. Urban, T. Schmutzler, W. Schnick, O. Oeckler

   Hirschegg-Seminar für Festkörperchemie, Hirschegg, Austria **2013**

4. **High-Pressure Synthesis and Characterization of Luminescent Nitridophosphates** (poster presentation)

   F. J. Pucher, A. Marchuk, W. Schnick

   The Freiberg High Pressure Symposium, Freiberg, Germany **2012**

H.3 Deposited Crystallographic Data

Crystallographic data for the compounds synthesized as part of this work were deposited at the Fachinformationszentrum (FIZ) Karlsruhe, Germany (fax: +49-7247-808-666, e-mail: crysdata@fiz-karlsruhe.de) and are available on quoting the following CSD depository numbers.

Compound	**CSD-Number**
α-HPN_2	426003
Ca_2PO_3N (average structure)	430221
Ca_2PO_3N (modulated structure)	430215
Sr_2PO_3N (300 K)	430220
Sr_2PO_3N (250 K)	430219
Sr_2PO_3N (200 K)	430218
Sr_2PO_3N (150 K)	430217
Sr_2PO_3N (100 K)	430216
$MgH_4P_6N_{12}$	427952
$CaH_4P_6N_{12}$	427953
$CaMg_2P_6O_3N_{10}$	427175
$Ba_3P_5N_{10}Cl$	429689
$Ba_3P_5N_{10}Br$	428381
$Ba_3P_5N_{10}I$	429688